NEW INSIGHTS INTO THE MILKY WAY MAGNETIC FIELDS THROUGH RADIO BROADBAND SPECTRO-POLARIMETRY

Dissertation

zur

Erlangung des Doktorgrades (*Dr. rer. nat.*)

der

Mathematisch-Naturwissenschaftlichen Fakultät

der

Rheinischen Friedrich–Wilhelms–Universität Bonn

vorgelegt von

Yik Ki MA

aus

Hong Kong

Bonn 2019

Angefertigt mit Genehmigung der Mathematisch-Naturwissenschaftlichen Fakultät
der Rheinischen Friedrich–Wilhelms–Universität Bonn

1. Referent: Prof. Dr. Michael Kramer
2. Referent: Prof. Dr. Pavel Kroupa
Tag der Promotion: 16.12.2019
Erscheinungsjahr: 2020

Diese Dissertation ist auf dem Hochschulschriftenserver der ULB Bonn unter
https://nbn-resolving.org/urn:nbn:de:hbz:5-57732 elektronisch publiziert.

RHEINISCHE FRIEDRICH–WILHELMS–UNIVERSITÄT BONN

Abstract

by Yik Ki Ma

for the degree of

Doctor rerum naturalium

Magnetic field is an essential ingredient of the interstellar medium of galaxies. In particular, an accurate characterisation of the magnetic field strength and structure of the Milky Way is crucial for complete understanding of many Galactic astrophysical processes. The Faraday rotation effect can be exploited to reveal the strength and direction of the magnetic field component parallel to the line of sight, which are imprinted in the rotation measure (RM) or Faraday depth (FD) values obtained from radio polarisation observations.

In this thesis, I utilised the broadband spectro-polarimetric capability of the Karl G. Jansky Very Large Array (VLA) in L-band (1–2 GHz) to gain new insights into the magnetic fields of the Milky Way in two ways. Firstly, I investigated in the reliability of the NRAO VLA Sky Survey (NVSS) RM catalogue, which is the largest RM catalogue to date with 37,543 RM values north of declination of -40° (more than one RM per deg^2). The wide sky coverage combined with the high RM density have made the NVSS RM catalogue a potent data set for the study of Galactic magnetism, including modelling of the global Milky Way magnetic fields. A full understanding of systematics of the NVSS RM catalogue is therefore indispensable to our knowledge of the magnetism of the Milky Way. In particular, I have quantified the effects of $n\pi$-ambiguity and off-axis instrumental polarisation in the NVSS RM catalogue. Secondly, I performed new radio observations for a direct study of the magnetic fields in the mid-plane of the Milky Way in the first Galactic quadrant. This specific region hosts a complex magnetic field structure being referred to as the large-scale field reversal, which has its details such as the field strength and the exact location poorly constrained owing to the lack of reliable RM values of background polarised extragalactic radio sources (EGSs). My new observations have led to a drastic increase in the number of lines of sight with probed magnetic fields by a factor of five, from which I have discovered new features in the Galactic magneto-ionic medium that were previously unnoticed.

Chapter 1 of this thesis summarises the essential information relevant to the study of magnetic fields of the Milky Way, including astrophysical motivations, our current knowledge of the Galactic magnetic fields, and the properties of synchrotron radiation and Faraday rotation that are crucial for the magnetic field measurements conducted in this thesis. In the subsequent Chapter 2, I

outline the details of radio broadband spectro-polarimetric observations that enabled the works in this thesis, including a review of the RM-Synthesis and Stokes QU-fitting algorithms.

In Chapter 3, I break the $n\pi$-ambiguity problem in the NVSS RM catalogue, where multiple RM values can satisfy the same measured polarisation position angles (PAs) from these narrowband NVSS observations. The $n\pi$-ambiguity can severely impact the reported NVSS RM values, with deviations from the true RM by $\pm 652.9\,\mathrm{rad\,m^{-2}}$. New broadband spectro-polarimetric observations with the Jansky VLA, which is immune to $n\pi$-ambiguity, were performed on 23 $n\pi$-ambiguity candidates. Upon comparing my newly derived FD values with the respective NVSS RMs, nine sources that are affected by $n\pi$-ambiguity and 11 with reliable NVSS RM values have been identified. Furthermore, I noted two targets that are unpolarised. Careful comparisons in the statistical properties of the two main classes of sources allowed the identification of a good diagnostic of $n\pi$-ambiguity, leading to my estimate of at least 50 sources out of the entire NVSS RM catalogue suffering from $n\pi$-ambiguity.

In Chapter 4, I utilised the same data set to quantify the effects of off-axis instrumental polarisation on the RM values reported in the NVSS RM catalogue. The new on-axis observations were compared with the NVSS results in identical frequency ranges, and I found differences between the two that cannot be explained by measurement uncertainties alone. This discrepancy, along with the two unpolarised sources identified in Chapter 3, have been attributed to the off-axis instrumental polarisation of the NVSS observations. I performed simulations to quantify the effects of off-axis instrumental polarisation on NVSS RM measurements, and found that the NVSS RM uncertainties have to be increased on average by approximately 10 per cent to account for the off-axis instrumental polarisation effect. Furthermore, this effect has been found to be more significant for sources with lower polarisation fraction, is a function of the true RM values of the sources, and results in RM uncertainties with highly non-Gaussian distributions. By incorporating this extra RM uncertainty into the 21 polarised target sources, the discrepant RM values of 18 sources have been successfully reconciled. The remaining three sources may exhibit RM time variabilities, and have been followed up by further observations.

In Chapter 5, I examined the magnetic fields in the mid-plane of the Milky Way in the first Galactic quadrant. FD values of 196 polarised EGSs within Galactic longitudes of 20°–52° and latitudes of ±5° have been determined using new broadband spectro-polarimetric observations with the Jansky VLA. A joint analysis with the FD values of pulsars at various distances in the same sky region has led to the discovery of complex magneto-ionic structures that were not noted before. This feature produces a clear FD asymmetry across the Galactic plane within longitudes of about 40°–52° at a distance of about 5 kpc, coinciding with the Sagittarius arm that was also known to host a large-scale magnetic field

reversal. The FD asymmetry can be explained by (1) an odd-parity Galactic disk field in the Sagittarius arm, (2) a significant contribution of an odd-parity Galactic halo field to FD at low Galactic latitudes, or (3) contaminations by ionised structures that cannot be identified in Hα, H I, or radio continuum maps. Furthermore, I concluded that none of the major Galactic magnetic field models considered can adequately reproduce my newly derived FD values. This calls for a new global model of the Milky Way magnetic fields that can capture my newly discovered FD asymmetry.

In Chapter 6, I summarise the scientific findings of this thesis. Additionally, I outline the exciting prospects in the research field of Galactic magnetism in the coming years from on-going and future polarisation surveys, as well as from parallel efforts using other magnetic field tracers and studies of external spiral galaxies. I conclude by stating the future research projects that I am leading in. These projects are motivated by the results of this thesis, and will further extend our knowledge in the magnetic fields in the Milky Way and in the Universe in general.

To my parents and grandparents.

"There is no magic. There is only knowledge, more or less hidden."

Gene Wolfe

Acknowledgements

It has been an amazing journey through the field of cosmic magnetism. This thesis serves as a conclusion to the current stage of my academic career, and has been made possible thanks to the help and support from the following individuals.

My biggest thank goes to my advisor (or, *Doktormutter*), **Dr. Sui Ann Mao**, for her excellent guidance. She gave invaluable and critical comments on my work, and provided me with the freedom and encouragement to pursue my own research direction, allowing me to truly develop into an independent researcher. Off work, she made sure my smooth transition to living in a new country upon my arrival, and has been caring to me throughout my PhD study. I cannot be more thankful for having met and worked with her.

I would like to also thank my supervisor, **Prof. Dr. Michael Kramer**, for his insightful suggestions to my work as well as his help along the way for my professional development. His sharing of his views and experiences with students have not only been helpful, but also reassuring that we are not alone when facing the many challenges along our paths.

Next on the list would be **Dr. Aritra Basu**, who I often discussed with about techniques in radio astronomy and the physics of the interstellar medium. As a collaborator, he gave many helpful comments on my work. I have also learnt so much from him about coding in `python`, which is not only essential for my study presented in this thesis, but also quite possibly for the rest of my research career. A huge thank to him!

Also thanks to my other collaborators: **Sarah Betti**, **Prof. Dr. Carl Heiles**, **Dr. Alex Hill**, **Dr. Jeroen Stil**, and **Dr. Jennifer West** for our work presented in Chapters 3 and 4, and **Dr. Jo-Anne Brown** for our study presented in Chapter 5. They all have provided valuable suggestions to my work. Special thanks to **Dr. Jeroen Stil** for providing me with cutout images of the NVSS RM catalogue, and to **Dr. Jennifer West** for assisting me in implementing the NE2001 free electron density model. Both of these are vital to my work presented in this thesis.

Many thanks to my senior colleagues, especially **Dr. Rainer Beck**, **Dr. David Champion**, **Dr. Andreas Horneffer**, **Dr. Marita Krause**, **Dr. Aristeidis Noutsos**, **Dr. Shane O'Sullivan**, **Dr. Dominic Schnitzeler**, and **Dr. Xiaohui Sun**. They helped me get a firm grasp on cosmic magnetism, provided me with helpful feedbacks on my writings and presentations, and gave me invaluable suggestions on my career developments.

I would like to express my gratitude to **Prof. Dr. Pavel Kroupa** for his suggestions and comments on my work as a Thesis Advisory Committee member, and for being my *Zweitgutachter*. Also thanks to **Prof. Dr. Klaus Desch** and **Prof. Dr. Dietmar Quandt** for agreeing to be my *Fachnahes Mitglied* and *Fachfremdes Mitglied*, respectively.

Thanks to my academic sister, **Dr. Maja Kierdorf**. Together we have discussed and shared about our works, progressed through the ups and downs of our PhD studies,

and travelled to other continents to attend international conferences and workshops. She is also always willing to help me understand the German documents that are essential to my living in Bonn.

I am grateful to have met so many friends who have been encouraging and have motivated me to push through the many challenges that I faced. It is unfortunately impossible to list all of them here. Special thanks to **Madhuri Gaikwad**, who has been so supportive through my difficult and stressful times, and has put up with my rants. The laughters we shared have made this journey memorable. Also thanks to **Bessy Chan**, **Weiwei Chen**, **Marilyn Cruces**, **Tasha Gautam**, **Alison Ip**, **Arshia Jacob**, and **Dr. Gigi Leung** for their supports.

In addition, I would like to thank **Kira Kühn**, **Dr. Rainer Mauersberger**, **Barbara Menten**, **Dr. Simone Pott**, and **Tuyet-Le Tran** for their patience in helping me through the administrative procedures throughout my residence in Bonn and study at the MPIfR.

Last but not least, I would like to express my heartfelt gratitudes to my parents, **Hak Kin Ma** and **Lai Yee Chau**. They have been so understanding and encouraging to my choice of pursuing PhD overseas. There is no way I could have achieved what I have without their continued support.

I acknowledge financial supports from the International Max Planck Research School (IMPRS) for Astronomy and Astrophysics, the Bonn-Cologne Graduate School (BCGS) of Physics and Astronomy, the International Astronomical Union (IAU), and the Newcastle University for my travels throughout my PhD study.

Contents

List of Figures

List of Tables

Nomenclature

Frequently Used Symbols

l	Galactic longitude
b	Galactic latitude
δ	Declination
B	Magnetic field strength
$B_\parallel$	Magnetic field strength along sight line
$B_\perp$	Magnetic field strength perpendicular to sight line
$N_{\rm HI}$	Neutral hydrogen column density
f	Volume filling factor
L, l	Path length
z	Redshift (Chapters 1, 3, and 4); Galactic height (Chapter 5)
ν	Frequency
λ	Wavelength
S	Total intensity
α	Spectral index ($S \propto \nu^\alpha$)
ϕ	Faraday depth
$\overline{\phi}$	Polarisation-weighted Faraday depth
p	Polarisation fraction
$\mathbf{p}$	Complex polarisation fraction ($= q + iu$)
$\mathbf{P}$	Complex polarisation ($= Q + iU$)
$\tilde{\mathbf{P}}$	Measured complex polarisation
$\mathbf{F}$	Complex Faraday spectrum
$\tilde{\mathbf{F}}$	Measured (dirty) Faraday spectrum
$\mathbf{R}$	Rotation Measure Transfer Function (RMTF)
$\delta\phi_0$	Resolution of Faraday spectrum
$\delta\phi$	FWHM of Faraday spectrum
$\Delta\lambda^2$	Bandwidth in λ^2-space
$\delta\lambda^2$	Channel width in λ^2-space
$\lambda^2_{\rm min}$	Minimum observed λ^2
W	Weight function
S/N	Signal-to-noise ratio

Physical Constants

Speed of light	c	$=$	$2.99792458 \times 10^{10}\,{\rm cm\,s^{-1}}$
Elementary charge	e	$=$	$4.80320 \times 10^{-10}\,{\rm esu}$
Mass of electron	m_e	$=$	$9.10938 \times 10^{-28}\,{\rm g}$
Mass of proton	m_p	$=$	$1.67262 \times 10^{-24}\,{\rm g}$
Boltzmann constant	$k_{\rm B}$	$=$	$1.38065 \times 10^{-16}\,{\rm erg\,K^{-1}}$

Astrophysical Constants

Astronomical Unit	$1\,\mathrm{AU}$	$=$	$1.49598 \times 10^{13}\,\mathrm{cm}$
Parsec	$1\,\mathrm{pc}$	$=$	$3.08568 \times 10^{18}\,\mathrm{cm}$
Jansky	$1\,\mathrm{Jy}$	$=$	$10^{-23}\,\mathrm{erg\,s^{-1}\,cm^{-2}\,Hz^{-1}}$
Rayleigh	$1\,\mathrm{R}$	$=$	$(10^6/4\pi)\,\mathrm{cm^{-2}\,s^{-1}\,sr^{-1}}$

Frequently Used Acronyms

AGN	Active galactic nucleus
EGS	Extragalactic radio source
PWN	Pulsar wind nebula
IGM	Intergalactic medium
ISM	Interstellar medium
ASKAP	Australian Square Kilometre Array Pathfinder
ATCA	Australia Telescope Compact Array
SKA	Square Kilometre Array
VLA	Very Large Array
MPIfR	Max-Planck-Institut für Radioastronomie
NRAO	National Radio Astronomy Observatory
DM	Dispersion measure
EM	Emission measure
RM	Rotation measure
FD	Faraday depth
PI	Polarised intensity
PA	Polarisation position angle
RMTF	Rotation Measure Transfer Function
CGPS	Canadian Galactic Plane Survey
SGPS	Southern Galactic Plane Survey
FIRST	Faint Images of the Radio Sky at Twenty-Centimeters
NVSS	NRAO VLA Sky Survey
POSSUM	Polarisation Sky Survey of the Universe's Magnetism
VLASS	Very Large Array Sky Survey
WHAMSS	Wisconsin H-Alpha Mapper Sky Survey
EBHIS	Effelsberg-Bonn H I Survey
GASS	Galactic All-Sky Survey
BIC	Bayesian information criterion
FWHM	Full-width at half-maximum
IF	Intermediate frequency
MHD	Magnetohydrodynamic
RFI	Radio frequency interference
VLBI	Very Long Baseline Interferometry

Chapter 1

Introduction

Contents

1.1 The Magnetised Universe

Magnetic fields are crucial to our daily lives. They are needed to drive motors in appliances such as electric fans and vehicles, and the magnetic induction phenomenon has been harnessed for applications including cooking with induction stoves and wireless charging of mobile phones. Even for medical uses, magnetic fields have been applied in techniques such as magnetic resonance imaging. One of the earliest applications of magnetic fields is for navigation by exploiting the magnetic field of the Earth. Compasses are sensitive to the direction of the geomagnetic field, and have been used by humanity for thousands of years. In modern times, they are even partially involved in the navigation of commercial aircrafts.

The magnetic field of the Earth has a strength of $\approx 0.5\,\mathrm{G}$ as measured on its surface (Finlay et al. 2010). As we lift off from the Earth and ascend into the astrophysical

realm, magnetic fields are ubiquitous within the solar system. The vast interplanetary space is filled with magnetic fields dragged from the Sun by solar wind (e.g., Owens & Forsyth 2013), with the typical solar magnetic field strength being $\approx$ 2–5 G on the photosphere (the "surface" of the Sun; e.g., de Wijn et al. 2009). Solar active regions such as sunspots can host magnetic fields with immense strengths of $\approx$ 1–5 kG (e.g., Charbonneau 2014). Magnetic fields can also be found on planets such as Jupiter (e.g., Ness et al. 1979, with *Voyager 1*) and Saturn (e.g., Dougherty et al. 2018, with *Cassini*). In the last decade, both *Voyager 1* and *2* have left the heliosphere[1] and thus escaped from the solar system's confinement into the interstellar medium[2], allowing for direct probes of the $\sim 4\,\mu$G interstellar magnetic fields at the immediate vicinity of the solar system with the magnetometers onboard (Opher et al. 2009; Burlaga & Ness 2014).

Within a galaxy, almost all astrophysical objects are known to be magnetised, including (but certainly not limited to) pulsars (Lorimer & Kramer 2012) pulsar wind nebulae (PWNe; Kothes 2017), supernova remnants (SNRs; Reynolds et al. 2012), supershells (e.g., Thomson et al. 2018), H II regions (e.g., Harvey-Smith et al. 2011), molecular clouds (Crutcher 2012), and high velocity clouds (e.g., McClure-Griffiths et al. 2010). If we zoom out further and consider the galaxy as a whole, magnetic fields can be found in dwarf and irregular galaxies (e.g., Gaensler et al. 2005; Chyży et al. 2011), and can be seen forming coherent (over $\sim$ 10 kpc), spectacular spiral patterns following the arms of spiral galaxies with strengths of $\approx 10\,\mu$G (Beck 2016). The magnetic fields of the Milky Way, which is the focus of this thesis, are expected to be qualitatively similar to those in external spiral galaxies (see Chapter 1.3.4).

Finally, recent efforts in the research field have revealed the omnipresent magnetic fields in the intergalactic space. The enormous neutral hydrogen (H I) structure of the Magellanic Bridge spanning $\gtrsim$ 15 kpc between the Large and Small Magellanic Clouds has been found to host a regular magnetic field of $\approx 0.3\,\mu$G along the sight line (Kaczmarek et al. 2017). In the outskirt of the interacting Antennae galaxies, regular magnetic fields spanning $\sim$ 20 kpc has been discovered (Basu et al. 2017). Radio relics, being the shock fronts of colliding galaxy clusters, were found to contain regular magnetic fields of $\sim 1\,\mu$G stretching over Mpc (Kierdorf et al. 2017). There have also been hints of detections of the magnetic fields in filaments of the cosmic web (O'Sullivan et al. 2018) and the intergalactic medium (IGM) in general (Vernstrom et al. 2019).

Clearly, we are living in a magnetised Universe. The importance of magnetic fields in many astrophysical processes is now widely agreed upon (see Chapter 1.2). To measure cosmic magnetic fields, excluding the use of spacecrafts to study the solar neighbourhood, one has to rely on measuring the electromagnetic waves[3] originating from astrophysical systems and eventually arriving at our telescopes on or close to

[1] The extent of the heliosphere is $\approx$ 120 AU towards the Sun's direction of travel, and possibly $\gtrsim 10,000$ AU in the Sun's trail (e.g., Zank 2015).

[2] See https://voyager.jpl.nasa.gov/mission/status/ for the current distances of both spacecrafts.

[3] Note the interesting prospects of using cosmic rays (Boulanger et al. 2018) or even gravitational waves (Kahniashvili et al. 2018) for the study of cosmic magnetism.

the Earth. In this Chapter, I will first state the importance of magnetic fields in astrophysics. Then, I will briefly review the magnetic field structures of spiral galaxies in general, as well as the specific case of the Milky Way. Next, I will describe the methods used in this thesis to measure astrophysical magnetic fields. Finally, I look back into the history of the developments and progresses in the rotation measure (RM) sky, which is a manifestation of the magnetic fields of the Milky Way.

1.2 The Role of Magnetic Fields in Astrophysics

The total magnetic field strength of a typical spiral galaxy is $\approx 10\,\mu$G (Beck 2016), corresponding to a magnetic energy density of $\approx 4 \times 10^{-12}\,\mathrm{erg\,cm^{-3}}$. This is comparable to the energy densities of other components of the interstellar medium (e.g., Heiles & Haverkorn 2012; Beck 2016, also Chapter 1 of Draine 2011), most notably the kinetic energy density of thermal gas ($\approx 8 \times 10^{-13}\,\mathrm{erg\,cm^{-3}}$), the turbulence energy density ($\approx 4 \times 10^{-13}\,\mathrm{erg\,cm^{-3}}$), and the cosmic ray energy density ($\approx 2 \times 10^{-12}\,\mathrm{erg\,cm^{-3}}$). It is evident that magnetic field is an important constituent of the interstellar medium. Although magnetic fields can only directly act on charged particles, namely ions, thermal electrons, and cosmic ray particles, they also influence the neutral phase of the interstellar medium via neutral-ion collision. This is because all but the densest portions of molecular clouds are sufficiently ionised (with ionisation fraction of $\gtrsim 0.04$ per cent) for magnetic fields to have a significant effect (e.g., Ferrière 2001). Below, I describe a few examples of astrophysical scenarios where magnetic fields are known to play significant roles.

1.2.1 Gas Dynamics in the Interstellar Medium

For plasma subjected to magnetic fields, a term known as the plasma beta can be defined (Krall & Trivelpiece 1973):

$$\beta \equiv \frac{p_{\mathrm{plasma}}}{p_B} = \frac{n_q k_{\mathrm{B}} T}{B^2/8\pi}, \tag{1.1}$$

where p_{plasma} and p_B are the gas pressure from the plasma and the magnetic pressure, respectively, n_q is the number density of the plasma particles, k_{B} is the Boltzmann constant, T is the plasma temperature, and B is the magnetic field strength. For cases where $\beta \gg 1$, the plasma dominates and drags along the magnetic fields; conversely when $\beta \ll 1$, the plasma is anchored to the magnetic fields (see, e.g., Chapter 5 of Chiuderi & Velli 2015). The value of β in the diffuse interstellar medium is typically low ($\lesssim 1$), except in H II regions ($\gtrsim 1$) and the hot ionised medium ($\gtrsim 10$) where the plasma pressure play more significant roles (e.g., Boulares & Cox 1990; Crutcher 1999; Heiles & Crutcher 2005; Harvey-Smith et al. 2011; Haverkorn & Spangler 2013; Beck 2016, also Chapter 12 of Biskamp 2008).

It has been determined from both observations (Beck et al. 2005) and numerical simulations (Kim & Stone 2012) that magnetic fields can be essential for the gas inflow in barred spiral galaxies. This can lead to the formation of the nuclear ring, and can fuel

the central active galactic nucleus (AGN). Furthermore, the orientation of molecular cloud structures appear to be parallel or perpendicular to the magnetic fields for low or high column densities, respectively, with the cutoff at $N_{\mathrm{H}} \approx 10^{21.7}\,\mathrm{cm}^{-2}$ (Planck Collaboration et al. 2016a). This is indicative of a highly magnetised environment (Soler et al. 2013), meaning that magnetic fields are important for the gas dynamics in molecular clouds (Planck Collaboration et al. 2016a).

1.2.2 Star Formation Processes

Stars account for more than 80 per cent of the baryonic mass of galaxies (Kalberla & Kerp 2009; Licquia & Newman 2015, see also Chapter 1 of Draine 2011), and are central to many galactic astrophysical processes. Heavy elements are manufactured from hydrogen through stellar (and supernova) nucleosynthesis, and are then dispersed to the interstellar medium as stellar outflows or supernova ejecta. The ionising radiation of the heaviest (O- and early B-type) stars can convert surrounding H I or molecular clouds into H II regions (see, e.g., Chapter 1 of Osterbrock & Ferland 2006). The evolution of massive stars can end as spectacular supernova explosions, which is one of the main drivers of turbulence in the interstellar medium (e.g., MacLow 2004), and in turn contributes to the amplification and ordering of the galactic-scale magnetic fields (see Chapter 1.3.2.3). Clearly, a deep understanding of the factors affecting star formation is essential to galactic astrophysics.

The importance of magnetic fields in star formation has been widely appreciated. Numerical simulations have demonstrated that the presence of magnetic fields can suppress star formation processes (Price & Bate 2008; Birnboim et al. 2015). This can be at least partially attributed to the pressure support by the magnetic fields against gravitational collapses of molecular clouds (Price & Bate 2008). The inclusion of the effects of magnetic fields, along with cosmic rays and turbulence, can lead to a delayed gas depletion in the galactic interstellar medium from $\sim 100\,\mathrm{Myr}$ to $\sim 1\,\mathrm{Gyr}$, with the latter better match observational results (Birnboim et al. 2015, see also Girichidis et al. 2018). On the other hand, the accretion of matter within the context of star formation requires an effective mechanism to transport angular momentum away from the system. This can be achieved through magneto-rotational instabilities under the presence of even weak magnetic fields (Balbus & Hawley 1998).

1.2.3 Cosmic Ray Propagation

The propagation of cosmic ray particles are heavily influenced by magnetic fields (see, e.g., Amenomori et al. 2006; Aab et al. 2015, see also Chapters 7, 15, and 16 of Longair 2011). The Larmor radius of a relativistic charged particle about magnetic fields is given by (in cgs units)

$$R = \frac{\gamma m v_{\perp} c}{q \cdot B}, \tag{1.2}$$

where γ is the Lorentz factor, m is the mass of the particle, $v_{\perp}$ is the velocity component perpendicular to the magnetic field, and q is the electric charge of the particle. Cosmic ray particles with lower energies have smaller Larmor radii, and thus their propagations

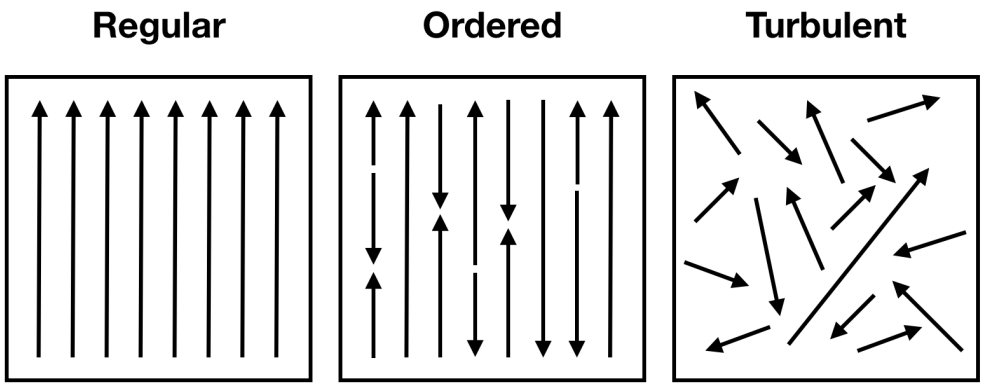

Figure 1.1: Illustration of regular, ordered, and turbulent magnetic fields.

are more affected by magnetic fields. It is generally accepted that the low energy cosmic ray particles, with energies of $\lesssim 10^{16}$–10^{18} eV, originated from within the Milky Way, as they are confined by the Galactic magnetic fields (see, e.g., Chapter 15 of Longair 2011). Furthermore, their arrival directions are nearly isotropic due to the heavy scattering by the turbulent magnetic fields of the Milky Way. On the other hand, ultra-high-energy cosmic rays (UHECRs), with energies of $\gtrsim 10^{18}$ eV, are most likely produced by extragalactic sources (Aab et al. 2015). Their arrival directions are anisotropic, meaning that the origins of these cosmic ray particles could be identified, but will first require a good knowledge in the magnetic fields of the Milky Way (Aab et al. 2015).

1.3 Magnetic Fields in Spiral Galaxies

1.3.1 Regular, Ordered, or Turbulent?

Before exploring the origin as well as the structure of magnetic fields in galaxies, I first narrate here the common descriptions of astrophysical magnetic fields, which is essential in the rest of the thesis.

Magnetic fields can be divided into three types depending on the degree of coherence (e.g., Haverkorn 2015; Beck 2016), as illustrated in Figure 1.1. The geometry of magnetic fields is said to be **regular** (sometimes referred to as uniform or coherent in the literature) if the field lines have the same direction on a certain scale (e.g. the left box of Figure 1.1, where the magnetic fields point upwards within the spatial confine of the box). Such a field configuration can be generated by α-Ω dynamo processes (see Chapter 1.3.2.3). If the fields change direction while preserving their orientation, the system is deemed as hosting **ordered** magnetic fields (also called anisotropic random, ordered random, or striated). An example would be the middle box of Figure 1.1, where the field directions switch between upwards and downwards, but maintain a vertical orientation. An ordered magnetic field can be created by compression (e.g. shocks) or shearing of an initially turbulent magnetic field. Finally, the magnetic fields are considered as **turbulent** (also called isotropic random, random, or tangled) if the field

directions are random within the spatial scale considered.

1.3.2 The Origin of Galactic Magnetic Fields

The generation of the magnetic fields observed in spiral galaxies at the present epoch (e.g. M51, see Chapter 1.4.2) can be divided into three stages (see review of Ruzmaikin et al. 1988a; Brandenburg & Subramanian 2005; Beck 2016, also Chapters 3, 5, and 13 of Kronberg 2016).

1.3.2.1 Seed Magnetic Fields

First, the seeding stage generates a weak magnetic field that is required in the subsequent amplification stages. One possible way to generate magnetic fields from zero is by the Biermann battery effect (Biermann 1950). This effect is based on the mass ratio of about 1836.2 between protons and electrons — when they are subjected to the same external force (e.g., electric, radiation, or thermal pressure), the two species will experience different amount of acceleration, leading to a charge separation and finally a net electric current. This electric current can then induce magnetic fields. The Biermann battery effect can occur in stellar interiors (Biermann 1950), with further magnetic field amplification by a stellar dynamo before being advected into the interstellar medium by stellar outflows. This battery effect can also operate in supernova explosions (Hanayama et al. 2005). Similar effects such as Weibel instability (e.g., Lazar et al. 2009) and plasma fluctuations (e.g., Schlickeiser 2012; Schlickeiser & Felten 2013) can also explain the generation of the weak seed fields. A cosmological origin of the seed field from the early Universe, predating or during the structure formation era, has also been proposed (Durrer & Neronov 2013).

1.3.2.2 Magnetic Field Amplification

The next stage is the amplification stage, which is achieved through the small-scale dynamo processes (also called the fluctuation dynamo in the literature). The random motion of turbulence driven by supernova explosions (Ferrière 1996) or spiral shocks (Kim et al. 2006) can stretch, twist, and fold the magnetic fields, leading to a rapid amplification of the field strength (but with unchanged magnetic flux). This stage results in turbulent magnetic fields of $\sim \mu$G in $\lesssim 10^8$ yr (e.g., Schleicher et al. 2010; Beck et al. 2012).

1.3.2.3 Large-scale Field Ordering (α-Ω Dynamo)

Finally, the magnetic fields have to undergo ordering processes that can result in the observed *regular* magnetic fields over galactic scales (~ 10 kpc). The turbulent motion of gas (α) from energetic events such as supernova explosions (or superbubbles created by multiple supernovae) and the differential rotation (Ω) of a galaxy can amplify and order magnetic fields in $\sim 10^9$ yr (e.g., Arshakian et al. 2009; Pakmor et al. 2014; Rodrigues et al. 2015) by the α-Ω dynamo mechanism (see Ruzmaikin et al. 1988a).

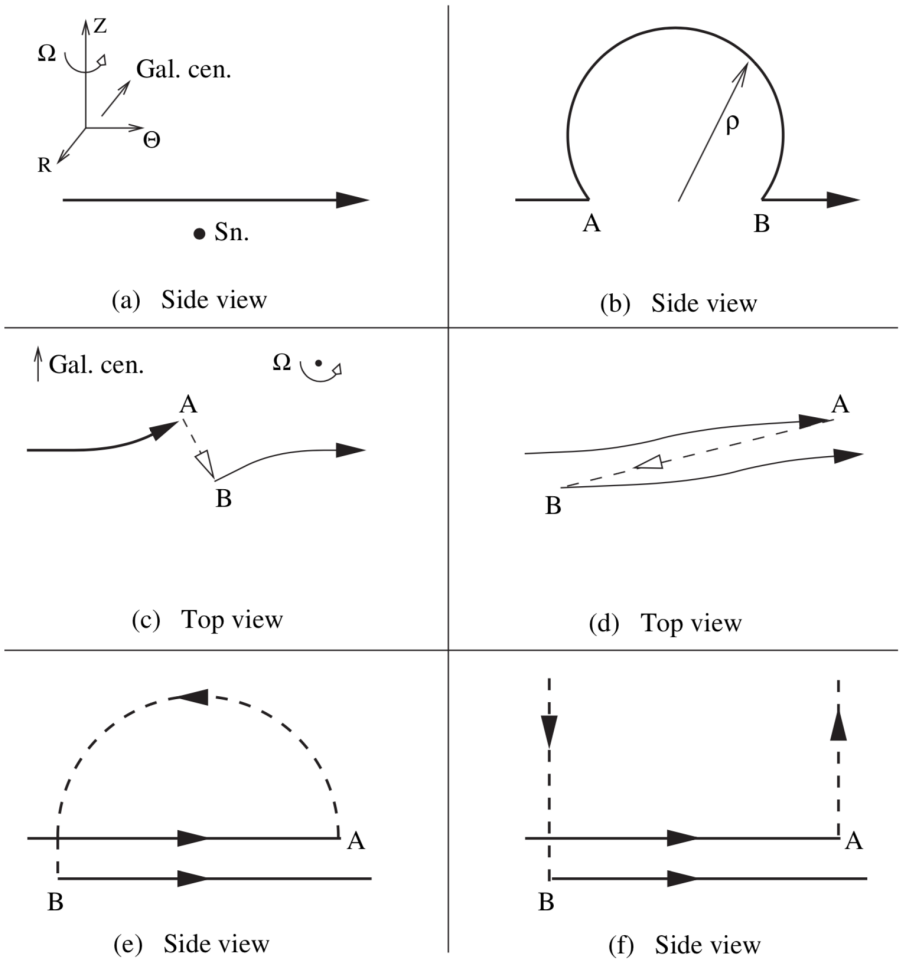

Figure 1.2: Illustration of the α-Ω dynamo in galaxies. See text for details. Image courtesy of Kulsrud (2005).

If the magnetic field strength has already reached saturation level from small-scale dynamo above, the α-Ω dynamo will then only be needed for the ordering processes.

A full treatment of the relevant 3D magnetic induction equations would require numerical simulations (see, e.g., Brandenburg 2015). Alternatively, analytical solutions of the large-scale magnetic fields can be obtained by adopting the mean-field approximation — spatial and temporal averages of the velocity and magnetic fields are considered, ignoring the fluctuations on small scales. In this case, the mean-field dynamo equation is given by

$$\frac{\partial \mathbf{B}}{\partial t} = \nabla \times (\mathbf{v} \times \mathbf{B}) + \nabla \times \alpha \mathbf{B} + \eta \nabla^2 \mathbf{B}, \tag{1.3}$$

with $\mathbf{B}$ here represents the large-scale regular magnetic field, $\mathbf{v}$ denotes the large-scale velocity field, and $\eta = c^2/(4\pi\sigma)$ is the magnetic diffusivity (with σ in turn being the electric conductivity).

The α-Ω dynamo processes can be intuitively understood with the illustration in

Figure 1.2 (Kulsrud 2005). Let there be an azimuthal magnetic field at the beginning (panel a), which is disrupted by a supernova explosion (denoted as Sn.). This will result in the magnetic field lines being pushed upwards / downwards away from the galactic plane, with this stretching process resulting in a half loop with radius ρ (panel b). As the supernova remnant grows in size, the effect of differential rotation of the galaxy becomes appreciable. This causes the remnant to rotate in the opposite sense to the global galactic rotation. The magnetic fields are also dragged along by this local rotation, with this twisting of magnetic fields causing the fields closer to the galactic rotation centre advancing forward and vice versa (panels c and d). Eventually, the originally single field line is folded back to itself (panel e), with the magnetic flux doubled in the process. However, the vertical component of the magnetic fields must be expelled from the system (panel f), since otherwise the return of the vertical fields would lead to magnetic reconnection and the magnetic flux will return to its original value.

1.3.3 The Structure of Galactic Magnetic Fields

The large-scale magnetic field structure of spiral galaxies are determined by the α-Ω dynamo, and therefore we shall look into simple solutions of the mean-field dynamo equation (see, e.g., Brandenburg & Subramanian 2005; Beck 2016, also Chapter 5 of Kronberg 2016). Note that the actual magnetic field structure of galaxies can be represented by the superposition of multiple magnetic field modes.

The large-scale magnetic fields from α-Ω dynamo is modulated by the $e^{im\theta}$ term, with m denoting the azimuthal field mode (see below) and θ being the azimuthal angle. Field configuration of the lowest mode ($m = 0$) is called the axisymmetric spiral structure (ASS), and is the most readily excited mode with the largest field amplitude (see below). Magnetic fields of $m = 1$ correspond to the bisymmetric spiral structure (BSS), which predicts two large-scale magnetic field reversals across azimuthal angles. These field reversals are essentially inversions of the magnetic field direction. Higher field modes also exist and are occasionally hinted by observations of galaxies (see Beck & Wielebinski 2013, for a summary), but is outside of the scope of this thesis.

Along galactic height, the large-scale magnetic fields can have two forms of symmetry. In flat objects such as galactic disks, the resulting magnetic fields from α-Ω dynamo is expected to have even parities (symmetric about the galactic plane), i.e. the plane-parallel magnetic fields have the same direction above and below the galactic disk, while the vertical fields (if any) change direction across the galactic plane. On the other hand, magnetic fields of nearly spherical objects are expected to have odd parities (anti-symmetric about the galactic plane), i.e. the plane-parallel fields reverse in direction across the galactic disk, while the vertical fields have the same direction in the two hemispheres.

Currently, the magnetic field structures of upwards of 117 external galaxies have been investigated with radio polarimetric observations (Beck & Wielebinski 2013)[4].

[4]According to the updated version on February 2018, available from: http://www.mpifr-bonn.mpg.de/staff/rbeck/PSSS18.pdf.

Studies of face-on systems have revealed that the large-scale disk field of almost all spiral galaxies have ASS configuration as the dominant component, with no large-scale azimuthal field reversals (see also Fletcher 2010). The only known possible exception is M81, which was suggested to host a dominant BSS configuration and hence two large-scale azimuthal field reversals (Krause et al. 1989). However, their polarimetric observations with the legacy Very Large Array (VLA) at 21 cm suffered from the missing flux issue of radio interferometers, which could have affected the interpretation of the data on the large-scale magnetic field geometry of this galaxy. A recent study of the edge-on spiral galaxy NGC4666 has shown hints of radial magnetic field reversal of its large-scale fields (Stein et al. 2019).

1.3.4 Magnetic Fields in the Milky Way

The knowledge of the Milky Way magnetic field strength and structure is clearly of critical importance, but is challenging to obtain given our perspective of the Milky Way from within. Numerous observational tracers can be, and indeed have been, used to probe the Galactic magnetic fields (see Chapters 1.4.2, 1.4.4, and 6.4.1; also see review of Haverkorn 2015). The current general picture is that the magnetic field structure of the Milky Way appears more complex than those found in other spiral galaxies. This can be because of our unique vantage point, or the Milky Way indeed hosts magnetic fields with a distinctive geometry.

There is a variety of phenomenological models of the Galactic magnetic fields in the literature, as summarised recently by Haverkorn (2015). These models generally agree on a predominantly clockwise large-scale magnetic field in the disk when seen from the Galactic north pole, with a strength of $\approx 2\,\mu$G and an orientation roughly following the spiral arms. Furthermore, it is clear that there is at least one large-scale radial field reversal towards the inner Galaxy, first noted by Thomson & Nelson (1980) and Simard-Normandin & Kronberg (1980) from rotation measure (RM) measurements of pulsars and extragalactic radio sources (EGSs), respectively (see Chapter 1.4.5). This is a rare feature of the Milky Way amongst spiral galaxies (Beck & Wielebinski 2013). However, the exact details including the location(s) and the number of such reversal(s) remain controversial, and therefore it warrants new observational data to better constrain these parameters (see Chapter 5). On the other hand, the geometry of the Galactic halo field is also under active research, with a general preference of adopting anti-symmetric fields in models to explain the anti-symmetry in the all-sky RM maps about the Galactic plane (see Chapter 1.5 below).

1.4 Measurement of Astrophysical Magnetic Fields

Magnetic fields in galaxies, and in many other astrophysical objects, can be measured by exploiting the properties of synchrotron radiation, particularly in the radio wavelengths. This will be the primary methodology adopted in this thesis, and is discussed below. Other methods to measure cosmic magnetic fields, such as starlight polarisation and polarised dust emission, will be briefly discussed in Chapter 6.4.1.

1.4.1 Synchrotron Emission — A Quick Overview

By measuring the synchrotron radiation emitted by high energy particles, the magnetic fields in both the emitting volume (see Chapter 1.4.2) and the intervening medium (see Chapter 1.4.4) can be inferred. The physics involved in the synchrotron emission mechanism have been covered by, e.g., Ginzburg & Syrovatskii (1965), Pacholczyk (1970), Rybicki & Lightman (1986), Govoni & Feretti (2004), and will be briefly discussed here.

Charged particles are sent into spiral trajectories when subjected to magnetic fields due to the Lorentz force. The acceleration experienced by the particles result in the production of electromagnetic waves. For cases where the particles are relativistic ($\gamma \gg 1$, where γ is the Lorentz factor), synchrotron radiation will be emitted. Consider a particle with charge q, rest mass m, and Lorentz factor γ influenced by magnetic fields of strength B. The emission coming from this particle will peak at a frequency of (in cgs units)

$$\nu_c = \frac{3q}{4\pi mc}\gamma^2(B\sin\theta), \tag{1.4}$$

where θ is the pitch angle between the magnetic field vector and the particle's velocity vector. Furthermore, the power of the emission is given by (again in cgs units)

$$P = \frac{2q^4}{3m^2c^3}\gamma^2(B\sin\theta)^2. \tag{1.5}$$

From this equation, one can realise that astrophysical synchrotron emission can be almost completely attributed to the relativistic electrons in cosmic rays, since the synchrotron power is proportional to m^{-2} and is negligible for other constituents of cosmic ray particles.

In radio observations for astrophysical studies, we almost always measure the combined emission from an ensemble of particles rather than the emission from each individual particle. The same holds for synchrotron-emitting objects. It was found empirically that the radio spectrum of a typical synchrotron-emitting object follows a power law, as given by

$$S(\nu) \propto \nu^{\alpha}, \tag{1.6}$$

where $S(\nu)$ is the measured flux density at frequency ν, and α is the spectral index of the emission. This implies that the energy distribution of the responsible relativistic electrons also follows a power law:

$$N(\varepsilon)\,\mathrm{d}\varepsilon \propto \varepsilon^{\delta}\,\mathrm{d}\varepsilon, \tag{1.7}$$

where $N(\varepsilon)$ is the number density of electrons with energy between ε and $\varepsilon+\mathrm{d}\varepsilon$, and δ is the particle distribution index. This is consistent with the energy spectrum of electrons derived from direct cosmic ray detection experiments (e.g., Adriani et al. 2017). The two indices are related by $\alpha = (1+\delta)/2$.

An important property of synchrotron radiation is that it is intrinsically linearly polarised, with the polarisation plane perpendicular to the magnetic fields in the emission region. This can be exploited to measure the magnetic field orientation of astrophysical

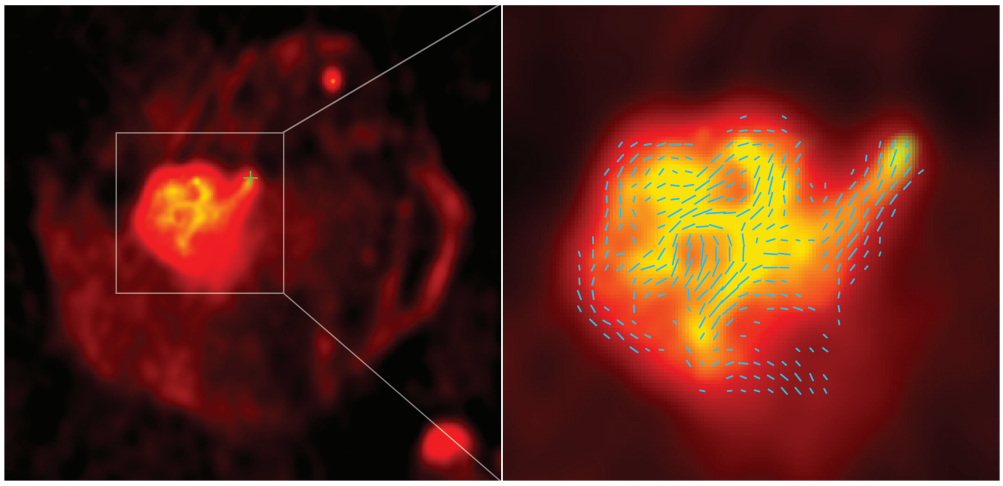

Figure 1.3: Radio images of the Snail PWN in the supernova remnant G327.1−1.1. Red and yellow show the radio maps at 36 cm with the Molonglo Observatory Synthesis Telescope and at 6 cm with the Australia Telescope Compact Array, respectively. The overlaid cyan vectors in the right panel trace the magnetic fields in the PWN, with the lengths proportional to the polarised intensities at 6 cm. The green cross in the left panel marks the location of an X-ray point source presumed to be the neutron star powering the PWN (Temim et al. 2015). The extent of the PWN is $\approx 4' \approx 10$ pc. Image courtesy of Ma et al. (2016).

objects (see Chapter 1.4.2). Furthermore, the intrinsic fractional polarisation of the emission is given by

$$p = \frac{3\delta - 3}{3\delta - 7} = \frac{3\alpha - 3}{3\alpha - 5}, \tag{1.8}$$

with typical value of ≈ 70 per cent. Usually, the actual observed polarisation fraction of astrophysical sources is much lower ($\lesssim 10$ per cent), because the magnetic field structures of astrophysical systems are often not ordered. In other words, within the angular resolution of the telescope, different volumes can have magnetic fields with varying orientations, and therefore the sum of the polarised emission can lead to depolarisation, resulting in a lower observed polarisation fraction.

1.4.2 Probing the Synchrotron-emitting Volume

The polarisation signature of synchrotron radiation can be exploited to probe the magnetic fields in the emitting volume. As mentioned in Chapter 1.4.1, the intrinsic polarisation plane of synchrotron emission is perpendicular to the local magnetic field orientation, meaning that it can directly trace the geometry of the regular and/or ordered magnetic fields of synchrotron-emitting objects (see below for examples). Note that in practice, the Faraday rotation effect must first be corrected for, as it causes the observed polarisation plane orientation to deviate from the intrinsic orientation (see Chapter 1.4.3). This technique is only limited to measuring the magnetic field component in the plane of the sky but not to that along the sight line, can only probe

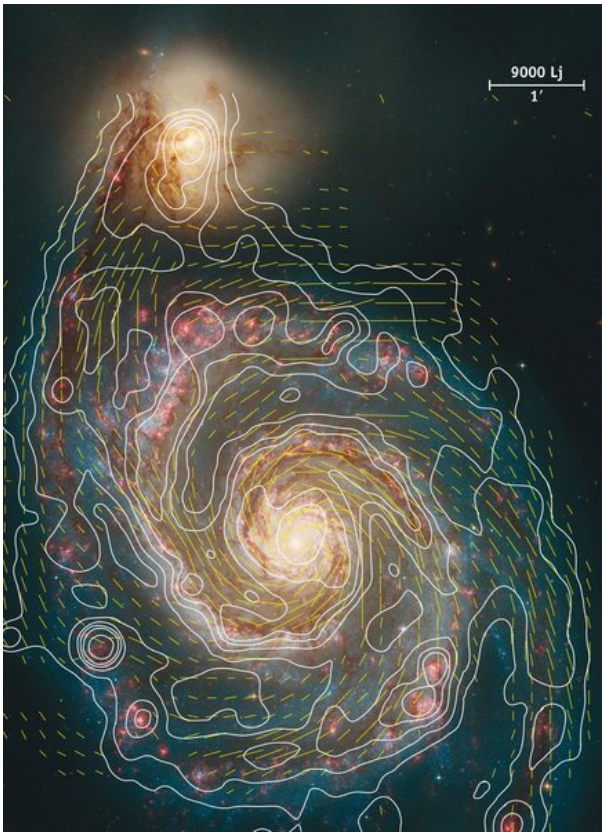

Figure 1.4: Images of the nearby face-on spiral galaxy M51. The background colour map shows a *Hubble Space Telescope* optical image of M51 [Credit: NASA, ESA, S. Beckwith (STScI) and the Hubble Heritage Team (STScI/AURA)], and the contours outline the total intensities measured with the Effelsberg 100-m telescope and the Very Large Array (VLA) at 6 cm. The magnetic fields are traced by the yellow vectors overlaid. The scale of the image is shown in the upper right corner (Lj = *Lichtjahre* = Light years). Image courtesy of Fletcher et al. (2011).

the orientation but not the direction of the magnetic field (i.e., cannot distinguish between regular and ordered fields), and can only be used for objects populated with sufficient cosmic ray electrons to emit synchrotron radiation at detectable levels.

Furthermore, the total magnetic field strength (including the regular, ordered, and turbulent field components) in the synchrotron-emitting object can be estimated from radio observations, though this analysis will not be performed in this thesis and therefore is only mentioned here briefly for completeness. The synchrotron emissivity is determined by three factors — the particle distribution index δ, the energy density of cosmic ray electrons, and the local magnetic field strength. Although δ is readily available from radio observations through the spectral index α (see above), it is less straightforward to determine the other two factors independently. One way to circumvent this degeneracy to enable magnetic field estimation is to invoke the assumption of energy equipartition (Beck & Krause 2005) — the cosmic ray electrons and magnetic

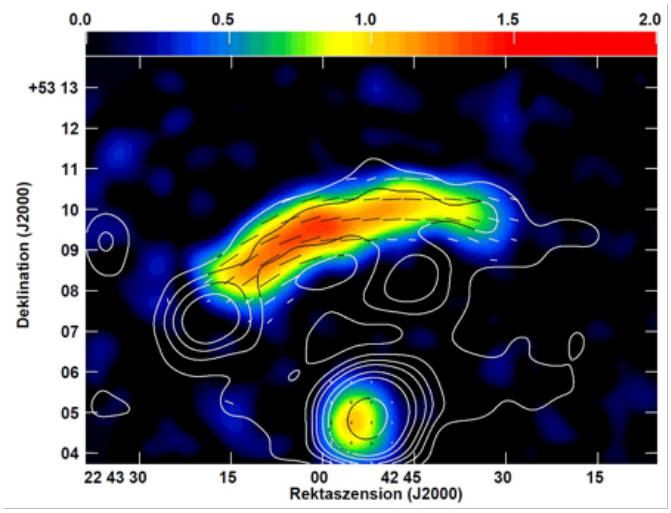

Figure 1.5: Radio images of the Sausage radio relic. The colour map shows the polarised intensities measured with the Effelsberg 100-m telescope at 3.6 cm, and the contours outline the total intensities at the same wavelength. The magnetic fields are represented by the vectors overlaid. For this object, $1'$ translates to a physical scale of 195 kpc. Image courtesy of Kierdorf et al. (2017).

fields are coupled and the energy exchanges between these two components lead to an eventual equilibrium in which the energy densities of the two are equal. This assumption allows the two factors to be combined for an estimation of the magnetic field strengths from radio observations. Independent estimation of the Galactic magnetic field strengths through γ-ray observations of inverse Compton processes were found to show consistent results with those from equipartition (Strong et al. 2000; Shukurov 2004). However, recent simulation studies have shown that the energy densities of cosmic rays and magnetic fields are not correlated at spatial scales of $\lesssim 100$ pc, meaning that the equipartition assumption likely does not hold at such scales (Seta et al. 2018; Seta & Beck 2019).

Regular / ordered magnetic fields can be found in a broad range of astrophysical scenarios, and can be mapped by radio observations of their associated synchrotron emission. I show here a few examples at vastly different physical scales that have had their magnetic fields inferred from their intrinsic synchrotron emission. Starting from smaller scales, the Snail PWN has a physical dimension of ≈ 10 pc, and its magnetic fields were found to closely align with the internal filamentary structures (Ma et al. 2016, see Figure 1.3). On a larger scale of ≈ 10 kpc, spiral galaxies such as M51 exhibit spiral magnetic fields spanning the entire galaxy (Fletcher et al. 2011, see Figure 1.4), as mentioned above in Chapter 1.1. Finally at Mpc scales, ordered magnetic fields have been found in radio relics such as the Sausage (Kierdorf et al. 2017, see Figure 1.5).

1.4.3 Physics of Faraday Rotation

Faraday rotation of synchrotron emission (Faraday 1846) is the primary phenomenon exploited for magnetic field measurements in this thesis. Linearly polarised electromagnetic waves are the sums of right- and left-handed circularly polarised waves, with the phase difference between the two circular components determining the orientation of the linear polarisation plane. In a magnetised plasma, the phase velocities of the two circular polarisation components are given by

$$v_p = c \cdot \left(1 - \frac{{\omega_p}^2}{\omega(\omega \pm \omega_c)}\right)^{-\frac{1}{2}}, \tag{1.9}$$

where ω is the angular frequency of the circularly polarised waves, and ω_p and ω_c are the plasma and cyclotron frequencies, respectively, given in cgs units by

$$\omega_p = \sqrt{\frac{4\pi n_q q^2}{m}}, \text{ and} \tag{1.10}$$

$$\omega_c = \frac{qB_\parallel}{mc}, \tag{1.11}$$

where n_q is the number density of plasma, and $B_\parallel$ is the magnetic field strength along the direction of wave propagation, with a positive (negative) value meaning the field direction is parallel (anti-parallel) to the direction of propagation. The choice of plus $(+)$ or minus $(-)$ sign for the plus-minus sign $(\pm)$ in Equation 1.9 correspond to the case of right- and left-handed circular polarisation, respectively. The right- and left-handed circularly polarised waves propagate through magnetised plasma at different phase velocities, leading to a phase shift between the two and an eventual rotation of the linear polarisation plane. This effect is called Faraday rotation.

The orientation of the polarisation plane of a linearly polarised electromagnetic wave can be quantified by its polarisation position angle (PA), defined as the angle of the electric field plane measured from north through east (see Chapter 2.1.2 for illustration). Under this notion, the change in PA due to the Faraday rotation effect is given by (again in cgs units)

$$\Delta\text{PA} = \frac{q^3}{2\pi m^2 c^4}\lambda^2 \int_\ell^0 n_q(s) B_\parallel(s)\,\mathrm{d}s, \tag{1.12}$$

where λ is the wavelength of the polarised emission, and ℓ is the distance to the synchrotron emitting source from us along the line of sight (s). Similar to the conclusion from Equation 1.5, the effect of Faraday rotation is predominantly caused by free electrons in the interstellar medium since $\Delta\text{PA} \propto m^{-2}$. Substituting the elementary charge (e), the mass of electron (m_e), and the number density of free electrons (n_e) gives

$$\Delta\text{PA} = \left[0.81 \int_\ell^0 n_e(s) B_\parallel(s)\,\mathrm{d}s\right] \cdot \lambda^2 \equiv \phi \cdot \lambda^2, \tag{1.13}$$

where ϕ [rad m^{-2}] is the Faraday depth (FD) of the emitting object, and ℓ, $B_\parallel$, and λ here are instead in units of pc, μG, and m, respectively. Note that traditionally,

the FD in this formula is instead replaced by rotation measure (RM), with the subtle differences between them explained in Chapter 2.2. Before so, the two terms are used interchangeably.

The first reported measurement of astrophysical Faraday rotation is that of Cooper & Price (1962) observing Centaurus A. Their observations with the Parkes radio telescope at multiple frequencies within 970–3000 MHz have revealed an RM of $\approx -70\,\mathrm{rad\,m^{-2}}$ towards this radio galaxy.

1.4.4 Probing the Intervening Volume

As can be seen from Equation 1.13, by measuring the FD values of background polarised sources, the magnetic field strength integrated along the line of sight in the foreground magneto-ionic medium, weighted by n_e, can be derived. FD values can be determined from polarisation measurements at multiple frequencies, with the exact methods used explained in details in Chapter 2.2.

Within the context of Galactic astrophysics, as is the case in this thesis, n_e along a certain sight line can be independently determined from other observables. For example, the n_e in H II regions can be inferred from their Hα intensities, as the two are related by (Reynolds 1988)

$$\frac{n_e}{\mathrm{cm^{-3}}} = \sqrt{1.375 \cdot \left(\frac{T}{10,000\,\mathrm{K}}\right)^{0.9} \cdot \frac{I_{\mathrm{H}\alpha}}{\mathrm{Rayleighs}} \cdot e^{\tau} \cdot \left(\frac{fL}{\mathrm{pc}}\right)^{-1}}, \tag{1.14}$$

where T is the plasma temperature, $I_{\mathrm{H}\alpha}$ is the Hα intensity, τ is the optical depth to the H II region due to dust extinction, f is the volume filling factor, and L is the path length through the entire H II region. The values of τ can be estimated by measuring the reddening of the ionising star embedded in the H II region, $E(B-V)$ (see Reynolds 1988; Finkbeiner 2003; Harvey-Smith et al. 2011), and T can be obtained from optical emission line ratios (e.g., Madsen et al. 2006). The values of f and L often have to be assumed. Another method is to adopt models of the n_e distribution within our Milky Way (e.g., Cordes & Lazio 2002; Yao et al. 2017). These models rely on pulsar dispersion measure (DM; $[\mathrm{cm^{-3}\,pc}]$) values, which can be determined from the delay in the time of arrival ($\Delta\tau_{\mathrm{a}}$ [ms]) of their pulses (e.g., Lorimer & Kramer 2012):

$$\Delta\tau_{\mathrm{a}} = \frac{4.15 \times 10^{18}}{\nu^2} \cdot \int_0^{\ell} n_e(s)\,\mathrm{d}s \equiv \frac{4.15 \times 10^{18}}{\nu^2} \cdot \mathrm{DM}, \tag{1.15}$$

where ν [Hz] is the observed frequency. The Galactic free electron density models above were built utilising pulsars with known DMs and distances. With such independently obtained n_e values, the magnetic field strength of the intervening volume can be extracted from the measured FD values.

The amount of Faraday rotation experienced by linearly polarised emission in the Galactic interstellar medium is often significant at centi- and deci-metre wavelengths. For example, if one were to observe a polarised extragalactic source behind the disk of the Milky Way (e.g., Chapter 5), the expected ΔPA can be estimated by substituting

typical values of $\ell \sim 10\,\mathrm{kpc}$, $n_e \sim 0.05\,\mathrm{cm}^{-3}$, and $B_{\parallel} \sim 1\,\mu\mathrm{G}$ on the Galactic disk (e.g., Cordes & Lazio 2002; Van Eck et al. 2011) to yield an $|\phi|$ of $\sim 400\,\mathrm{rad\,m}^{-2}$. The polarised emission from this extragalactic source at 3, 6, 13, and 20 cm would then experience $|\Delta\mathrm{PA}|$ of about 20°, 80°, 390°, and 920°, respectively.

Magnetic field measurements from Faraday rotation and from the intrinsic synchrotron radiation can complement each other. This is because the former is sensitive to the foreground magnetic fields *along* the sight line, while the latter probes the magnetic fields in the emission region *perpendicular to* the line of sight. However, the Faraday rotation method is advantageous in two aspects. First, FD values can distinguish the directions of the average magnetic fields along the sight lines, with the magnetic fields pointing towards the observer leading to a positive FD by definition and vice versa. This allows us to differentiate between regular and ordered magnetic fields originating from different astrophysical mechanisms (see Chapter 1.3.1). In contrast, intrinsic synchrotron radiation only gives the orientation but not the direction of magnetic fields. Furthermore, the magnetic fields of astrophysical entities without sufficient cosmic ray electrons to emit synchrotron radiation at detectable levels, such as H II regions (e.g., Harvey-Smith et al. 2011; Purcell et al. 2015) and H I structures like the Magellanic Bridge (Kaczmarek et al. 2017) and high velocity clouds (e.g., Betti et al. 2019), can instead be measured from the amount of Faraday rotation experienced by the polarised synchrotron emission coming from background sources.

1.4.5 Faraday Depth Grid Experiments

The magnetic fields in a volume of magnetised plasma, for example an H II region or an external galaxy, can be measured by observing multiple polarised sources behind it ("on-source" targets), along with nearby polarised sources that are outside of its projected sky location ("off-source" targets). The FD contribution of the volume can then be determined by subtracting the off-source FD from the on-source FD. The multiple background polarised sources observed essentially form a grid in the sky, and therefore such studies are commonly called FD-grid experiments. Most FD-grid experiments utilise extragalactic radio sources (EGSs) and/or Galactic pulsars as the background sources, and they are individually discussed below.

1.4.5.1 FD Grids with Extragalactic Radio Sources

Polarised EGSs are often used to construct FD grids in cosmic magnetism studies. Most of these EGSs are likely active galactic nuclei (AGNs). As expressed in Equation 1.13, the observed FD value is the integrated magnetic field strength along the sight line, weighted by n_e. For the case of an FD-grid study of a discrete astrophysical object (e.g., an external galaxy, or a Galactic H II region), the observed FD (ϕ_{obs}) can be decomposed into multiple components[5]:

$$\phi_{\mathrm{obs}} = \phi_{\mathrm{EGS}} + \phi_{\mathrm{IGM}} + \phi_{\mathrm{MW}} + \phi_{\mathrm{src}}, \tag{1.16}$$

[5]It is implicitly assumed here that Faraday rotation does not occur in the synchrotron-emitting volume (see also Chapter 2.2.4).

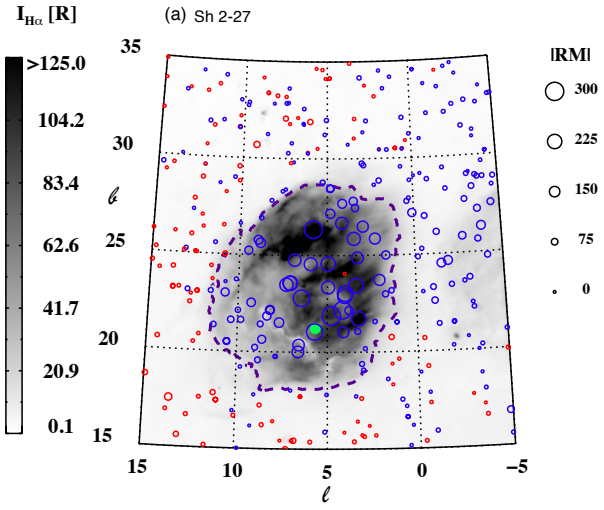

Figure 1.6: FD-grid experiment of the H II region Sh 2-27. The background greyscale map shows the Hα intensity (Haffner et al. 2003), while each open circle represents the FD value from a background polarised EGS (Taylor et al. 2009), with positive and negative values shown as red and blue, respectively. The green filled circle denotes the pulsar J1643−1224 situated behind Sh 2-27. Image courtesy of Harvey-Smith et al. (2011).

where $\phi_{\rm EGS}$, $\phi_{\rm IGM}$, $\phi_{\rm MW}$, and $\phi_{\rm src}$ denote the FD contributions from the EGS, the intergalactic medium (IGM), the Milky Way, and the target source itself, respectively. The contribution of $\phi_{\rm EGS}$ is typically small, with amplitudes of $\sim 10\,{\rm rad\,m^{-2}}$ (e.g., Schnitzeler 2010; Oppermann et al. 2015, see also Rudnick 2019) but can sometimes be significant ($\sim 10^3\,{\rm rad\,m^{-2}}$; e.g. Pasetto et al. 2018). The contamination by this component can be reduced by averaging the FD values of EGSs in close spatial proximities (e.g., Gaensler et al. 2005; Mao et al. 2010). The contribution of $\phi_{\rm IGM}$ is expected to be even smaller ($\lesssim 10\,{\rm rad\,m^{-2}}$; e.g., Vallee 1990; O'Sullivan et al. 2018; Vernstrom et al. 2019). Meanwhile, $|\phi_{\rm MW}|$ highly depends on the Galactic region considered, ranging from $\approx 0\,{\rm rad\,m^{-2}}$ at the Galactic poles (Mao et al. 2010) to $\gtrsim 100\,{\rm rad\,m^{-2}}$ on the Galactic plane (e.g., Simard-Normandin & Kronberg 1980; Brown et al. 2003, 2007; Van Eck et al. 2011). Maps of this Galactic FD contribution have been estimated at $\sim 1^\circ$ scale (e.g., Oppermann et al. 2012, 2015), and can be subtracted from $\phi_{\rm obs}$ to better recover $\phi_{\rm src}$.

EGS FD grids have been used to uncover the magnetic fields in a wide variety of astrophysical objects, and two notable examples are given here. The case of the Milky Way, being the focus of this thesis, is separately covered in Chapters 1.3.4 and 1.5. The magnetic fields in five Galactic H II regions, including that of Sh 2-27 (Figure 1.6), have been studied with FD grids formed with ~ 10 EGSs each (Harvey-Smith et al. 2011). It was found that the on-source $|\phi|$ values are systematically offset from the off-source values, indicating the presence of regular magnetic fields with strengths of

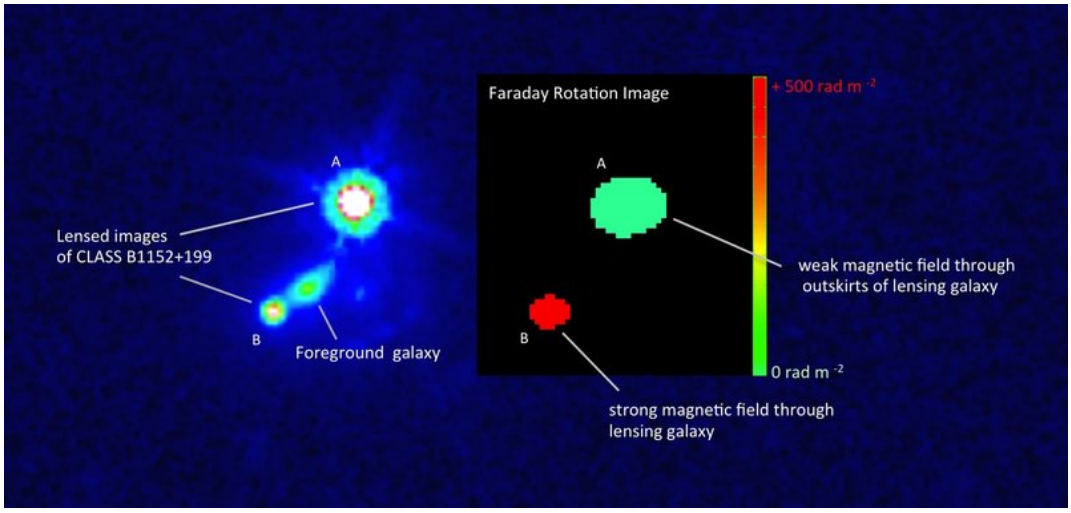

Figure 1.7: FD-grid experiment of a galaxy at $z = 0.439$, marked as the "foreground galaxy" in the *Hubble Space Telescope* image (Rusin et al. 2002) shown in colour. The two gravitational lensing images of the same background EGS, CLASS B1152+199, are used as the FD grid to reveal the large-scale magnetic fields present in the foreground galaxy. Image courtesy of Mao et al. (2017).

2–6 μG along the sight lines. On the other hand, the magnetic fields in a distant galaxy at $z = 0.439$ have recently been measured with a unique FD-grid design — using two polarised sources only (Figure 1.7; Mao et al. 2017). These two background polarised sources are in fact two gravitationally lensed images of the same EGS, meaning that their $\phi_{\rm EGS}$ values should be identical. The redshift-corrected difference in the two FD values of $1040 \pm 60\,{\rm rad\,m^{-2}}$ is a clear indication of a regular magnetic field in the foreground galaxy.

1.4.5.2 FD Grids with Galactic Pulsars

FD-grid experiments can also be performed by using Galactic pulsars (e.g., Thomson & Nelson 1980; Han et al. 2002; Noutsos et al. 2008; Han et al. 2018), which are well suited for studying the Galactic magnetic fields because (1) they are often highly polarised, (2) their pulsations allow dispersion measures (DMs) to be determined from multi-frequency observations (Equation 1.15), (3) the distances to nearby pulsars can be constrained with reasonable accuracy (≈ 20 per cent), and (4) they are believed to have minimal intrinsic FD contributions[6] (see, e.g., Lorimer & Kramer 2012; Han 2017).

The DM value of a pulsar can be utilised to decouple the free electron column density from the FD value of the same pulsar to yield the mean magnetic field strength

[6]The FD contribution from pulsar magnetosphere has been suggested to be negligible (Wang et al. 2011). However, note that supernova remnants can have significant FD values (e.g., Piro & Gaensler 2018), which can affect young pulsars (with age $\lesssim 40$ kyr; e.g. Gaensler & Slane 2006) still residing in their associated supernova remnants.

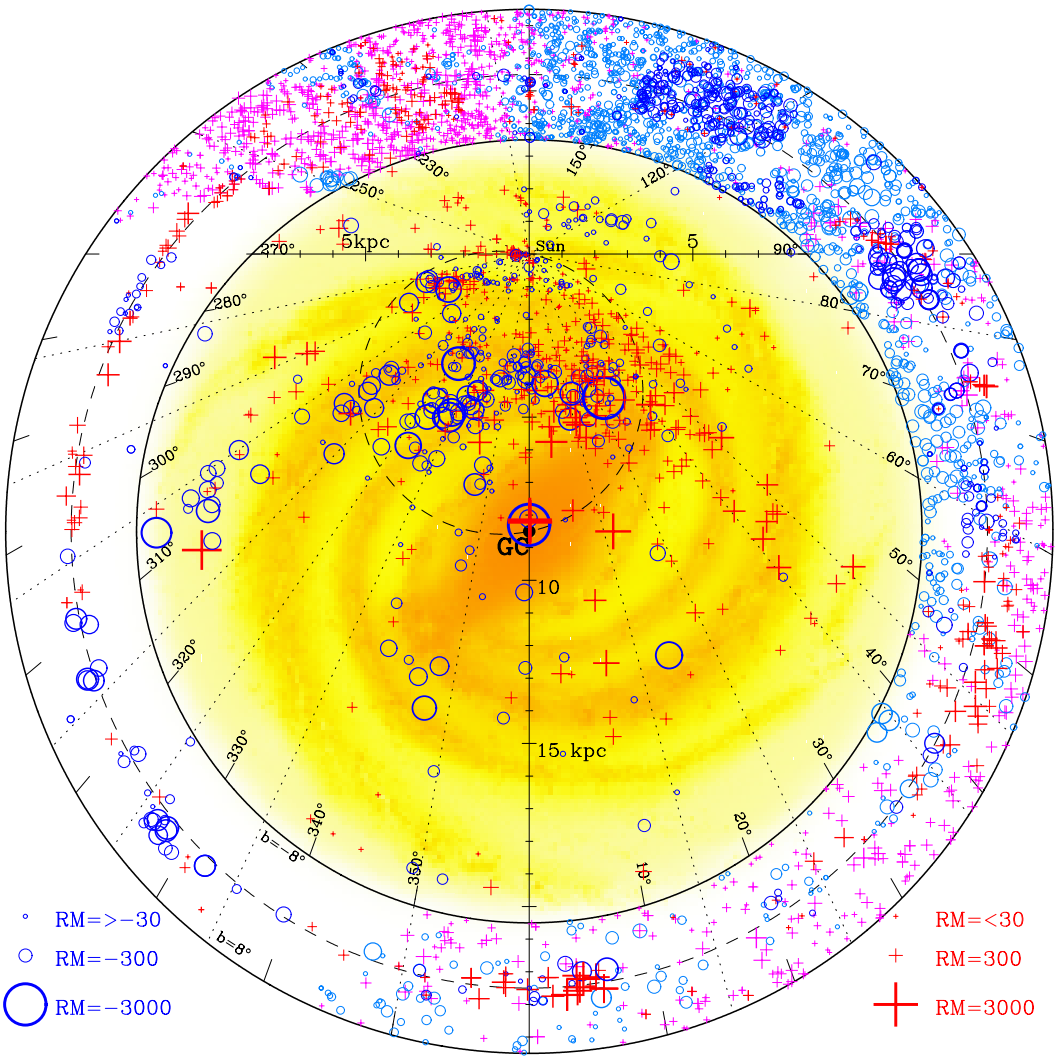

Figure 1.8: Spatial distribution of 787 pulsars and 3933 EGSs on the Galactic plane ($|b| < 8°$). The FD values are represented by red crosses and blue circles for positive and negative values, respectively, except for RM measurements from Taylor et al. (2009) which are shown as light red and light blue instead. The sizes of the markers are proportional to $\sqrt{|\phi|}$. The locations of pulsars, along with the Galactic centre (GC) and the Sun, are marked in the central part where an artist's impression of Galactic structures of Hou & Han (2014) is shown as the background heat map [Credit: NASA/JPL/R. Hurt]. The EGS measurements are shown in the outer ring, where the radial distances represent Galactic latitudes with scales shown at the lower left. Image courtesy of Han et al. (2018).

along the sight line (e.g., Lorimer & Kramer 2012; Han 2017):

$$\langle B_{\parallel} \rangle = \frac{\int_0^{\ell} n_e B_{\parallel} \, \mathrm{d}s}{\int_0^{\ell} n_e \, \mathrm{d}s} = 1.232 \cdot \frac{\phi}{\mathrm{DM}}, \tag{1.17}$$

with $B_{\parallel}$ in units of μG. This assumes that $B_{\parallel}$ and n_e are uncorrelated (e.g., Beck et al. 2003). Furthermore, the DM values of pulsars can be used to estimate their distances by assuming a free electron density model of the Galaxy, such as the NE2001 (Cordes & Lazio 2002) or the YMW16 (Yao et al. 2017) models. By considering hundreds or even thousands of pulsars with known distances, the 3D magnetic field geometry of the Milky Way can be mapped (e.g., Han et al. 2018, see Figure 1.8). In this thesis, I have performed pulsar FD analysis in Chapter 5.5.3.1 to investigate the complex magnetic fields in the first Galactic quadrant.

1.5 Evolution of the Rotation Measure Sky

To study the global magnetic field of the Milky Way, we need to set up an RM grid covering the entire sky. This is because of our perspective of the Galaxy from within. I therefore review here the progresses of our knowledge of the RM sky in the last decades.

One of the earliest all-sky RM maps was constructed with 543 polarised EGSs by Simard-Normandin & Kronberg (1980), as shown in Figure 1.9. With roughly one polarised source per 76.0 deg^2, the effective angular resolution of the RM sky was only $\approx 20^\circ$. Nonetheless, the authors suggested from the measured RM values the presence of large-scale field reversals in the Galactic disk.

Until the 2000s, our knowledge of the RM sky did not see significant improvements (Figure 1.10), with only 801 EGSs (one source per 51.5 deg^2) with reliable RM values in the literature by year 2003 (Tabara & Inoue 1980; Simard-Normandin et al. 1981; Lawler & Dennison 1982; Rudnick & Jones 1983; Broten et al. 1988; Hennessy et al. 1989) as summarised by Johnston-Hollitt (2003).

Since the turn of the millennium, there have been various observational projects focusing on smaller sections of the sky, with the most notable of which being described here. The Southern Galactic Plane Survey (SGPS; Gaensler et al. 2001; Brown et al. 2007) was conducted with the Australia Telescope Compact Array (ATCA) at 1336–1432 MHz covering the sky region of 253°–358° in Galactic longitude (ℓ) and within $\pm 1\overset{\circ}{.}5$ in Galactic latitude (b). This has resulted in 148 RMs (about one source per 2 deg^2) from polarised EGSs in the southern Galactic plane. The northern Galactic plane has been covered by the Canadian Galactic Plane Survey (CGPS; Taylor et al. 2003; Brown et al. 2003), with the observations performed with the Dominion Radio Astrophysical Observatory (DRAO) Synthesis Telescope at ≈ 1420 MHz. Their survey covered 380 polarised sources (one source per 1.1 deg^2) in two longitudinal slices on the Galactic plane at $82^\circ \leq \ell \leq 96^\circ$ and $115^\circ \leq \ell \leq 146^\circ$, both confined within $-3\overset{\circ}{.}6 \leq b \leq +5\overset{\circ}{.}6$. As can be noted, there are Galactic longitude ranges that are covered by neither the SGPS nor the CGPS. The majority of such gaps are filled by

the legacy VLA observations of Van Eck et al. (2011) at $\approx 1420\,\mathrm{MHz}$, which covered longitudes of 17°–63° and 205°–253°. They combined their 194 EGS RMs (one source per $3.3\,\mathrm{deg}^2$) together with the SGPS and CGPS RM values above to construct a model of the Galactic disk fields (see Chapter 5.5.4.1).

Moving away from the Galactic plane, the halo fields above / below the Perseus arm, as well as the disk fields inside of it, have been studied with legacy VLA observations at $\approx 1420\,\mathrm{MHz}$ by Mao et al. (2012). Their observations covering $100° < \ell < 117°$ and $|b| < 30°$ have resulted in 641 RM values (one source per $1.4\,\mathrm{deg}^2$), with which they concluded that the disk fields in the Perseus arm have an even parity, estimated a disk-halo transition height of $|z| \sim 540\,\mathrm{pc}$, and constructed a model for the halo fields there. Finally, the vertical halo fields pointing towards the Galactic poles have been measured with the Westerbork Synthesis Radio Telescope (WSRT) for $b > +77°$ and the ATCA for $b < -77°$ (Mao et al. 2010). They have concluded from the total of 813 derived RM values (one source per $1.3\,\mathrm{deg}^2$) that there is no evidence of regular vertical fields towards the Galactic north pole, while a regular vertical field with strength of $0.31 \pm 0.03\,\mu\mathrm{G}$ has been found pointing from the Galactic south pole towards the Galactic plane.

Apart from the improved knowledge of the RM sky in specific Galactic regions described above, the last decade has seen major advances in the all-sky RM from polarisation surveys. The combined RM map of the two polarisation surveys covered in this paragraph is shown in Figure 1.11, which is representative of our current knowledge of the RM sky. North of $\delta = -40°$, Taylor et al. (2009) has reported 37,543 RM values (one source per $0.9\,\mathrm{deg}^2$) derived by re-analysing the NRAO VLA Sky Survey (NVSS; Condon et al. 1998) data at $\approx 1400\,\mathrm{MHz}$. The high source density combined with large sky coverage of this NVSS RM catalogue have been shown to be potent for the study of cosmic magnetism (e.g., McClure-Griffiths et al. 2010; Harvey-Smith et al. 2011; Purcell et al. 2015; Vernstrom et al. 2019), especially for the global magnetic fields in the Milky Way (e.g., Stil et al. 2011; Jansson & Farrar 2012; Oppermann et al. 2015; Terral & Ferrière 2017). Nonetheless, in contrast to the RM measurements above, the Taylor et al. (2009) RM catalogue was built from polarisation measurements at only two narrow frequency bands, which can potentially be affected by the $n\pi$-ambiguity that will lead to erroneous RM values for some individual sources (see Chapter 2.2.2 for details). The reliability of this Taylor et al. (2009) RM catalogue has been investigated in Chapters 3 and 4. On the other hand, the RM sky south of $\delta = 0°$ has recently been uncovered by the S-PASS/ATCA survey (Schnitzeler et al. 2019) using the ATCA at 1.3–3.1 GHz. Their broadband observations of 3811 polarised EGSs (one source per $5\,\mathrm{deg}^2$) have not only provided us with a drastic improvement in our knowledge of the RM sky south of $\delta = -40°$, but have also demonstrated the power of broadband polarisation surveys (see Chapters 2.2.3 and 2.2.4 for detailed explanation).

We can certainly expect the RM sky to continue to evolve. The improved sensitivities of on-going and future polarisation surveys (Chapter 6.2.1) are anticipated to bring order(s) of magnitude increase in the polarised source densities, and their broadband capabilities will allow us to investigate the potential complex physical conditions in the Faraday rotating medium (see Chapters 2.2.3 and 2.2.4).

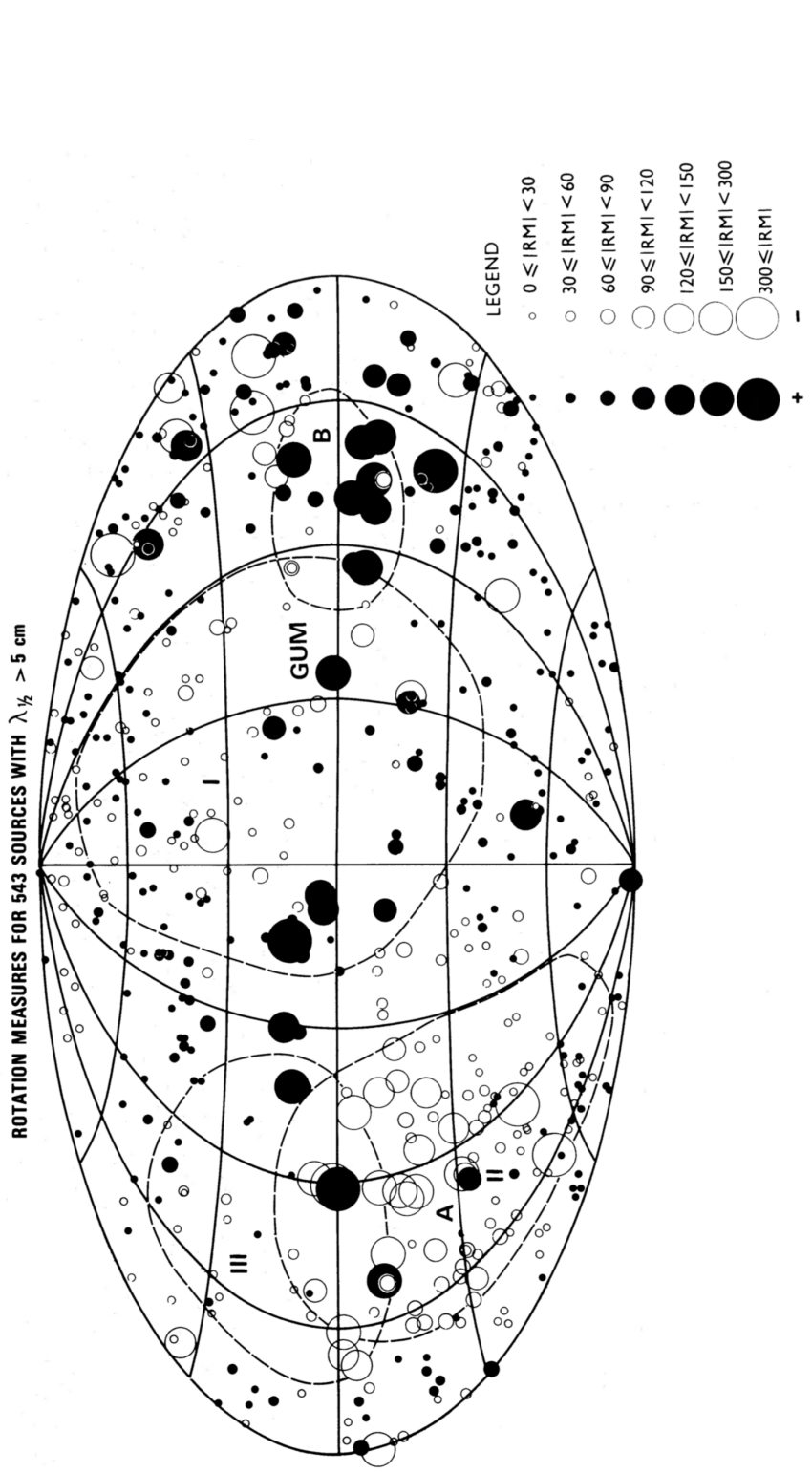

Figure 1.9: The Simard-Normandin & Kronberg (1980) RM map, constructed with 543 EGSs. The RM values are plotted in the sky map in Galactic coordinates, with positive and negative RM values represented by filled and open circles, respectively. Image courtesy of Simard-Normandin & Kronberg (1980).

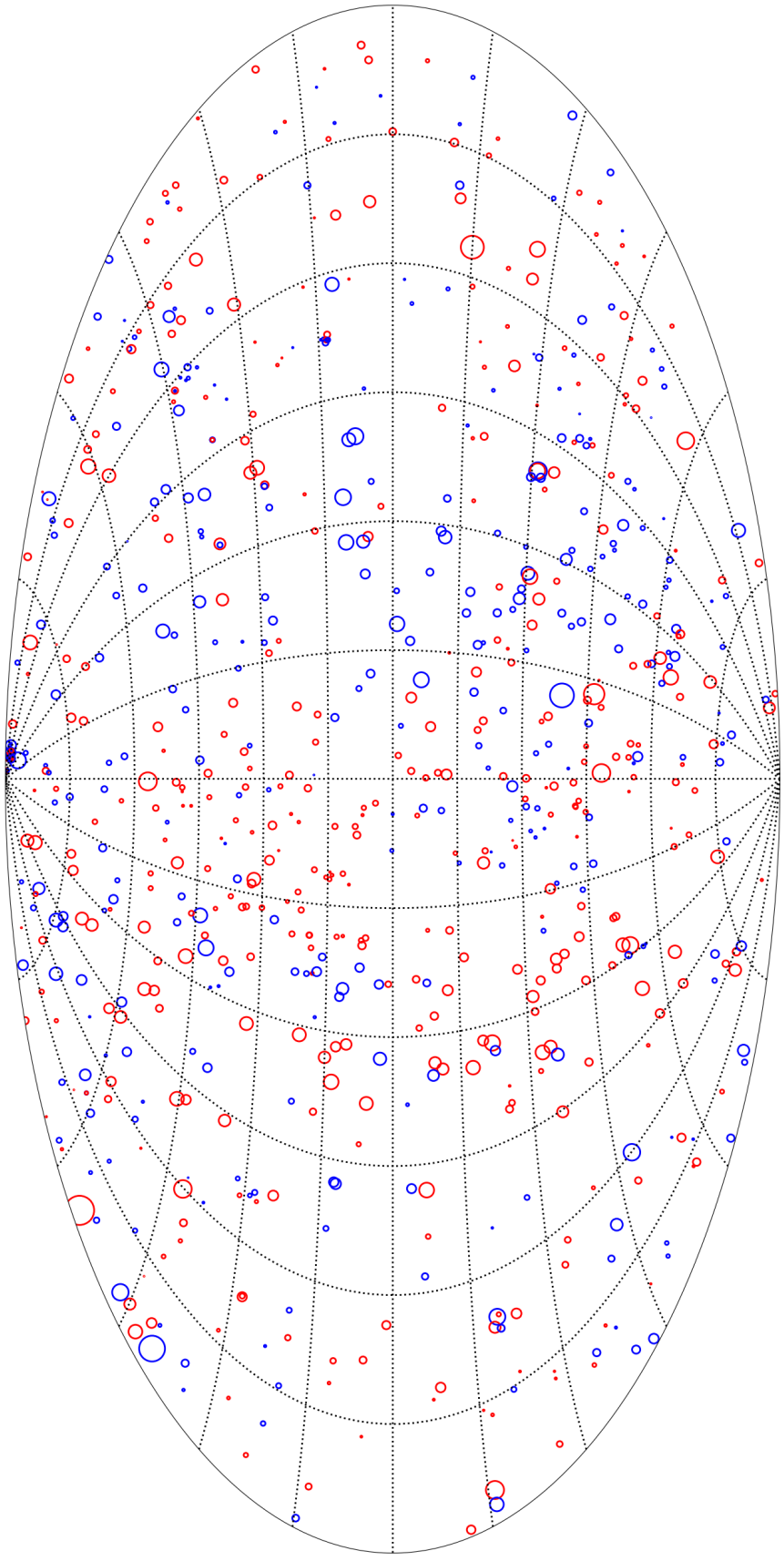

Figure 1.10: The RM map compiled by Johnston-Hollitt (2003), showing the 801 EGSs with reliable RM values. The RM values are plotted in the sky map in Galactic coordinates, with positive and negative RM values represented by red and blue circles, respectively. Image courtesy of Sui Ann Mao.

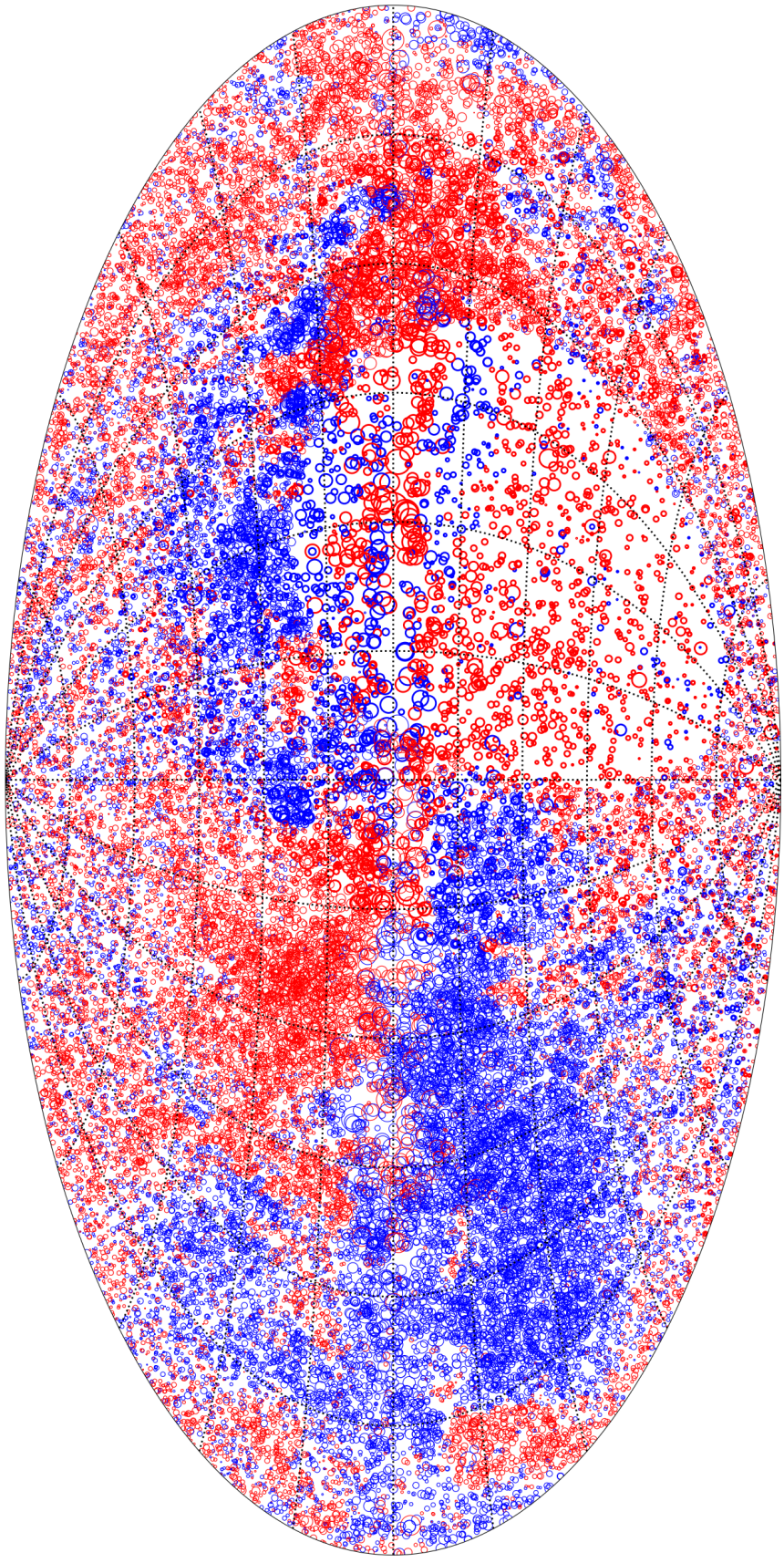

Figure 1.11: The NVSS (Taylor et al. 2009) and S-PASS/ATCA (Schnitzeler et al. 2019) RM map, constructed with over 40,000 polarised radio sources. The RM values are plotted in the sky map in Galactic coordinates, with positive and negative RM values represented by red and blue circles, respectively. Image courtesy of Sui Ann Mao.

Chapter 2

Methods in Broadband Spectro-polarimetry

As established in Chapter 1.4, astrophysical magnetic fields can be probed by measuring the polarised synchrotron emission from the object in question and/or from background sources. In most cases, such observations are best carried out at radio wavelengths within which (1) we have highly sensitive instruments (i.e. radio telescopes) to detect such emission, (2) synchrotron is usually the dominant emission mechanism, and (3) the amount of Faraday rotation experienced by the polarised emission reaches a measurable level. These are the reasons that this thesis primarily involves measurements of astrophysical magnetic fields in the radio regime. The working principles of radio telescopes are already well documented, and readers can refer to e.g. Taylor et al. (1999); Wilson et al. (2013); Thompson et al. (2017) for details. Here, I shall outline the journey to extracting the physical conditions of magnetised astrophysical objects starting from calibrated radio images. The necessary technical definitions and important instrumental effects will also be covered.

Contents

2.1 Measurements of Radio Polarisation

2.1.1 Definition of Bandwidths and Channel Widths

Radio telescopes are designed to be simultaneously sensitive to incoming radio waves within finite frequency ranges, since within an infinitesimal frequency range the

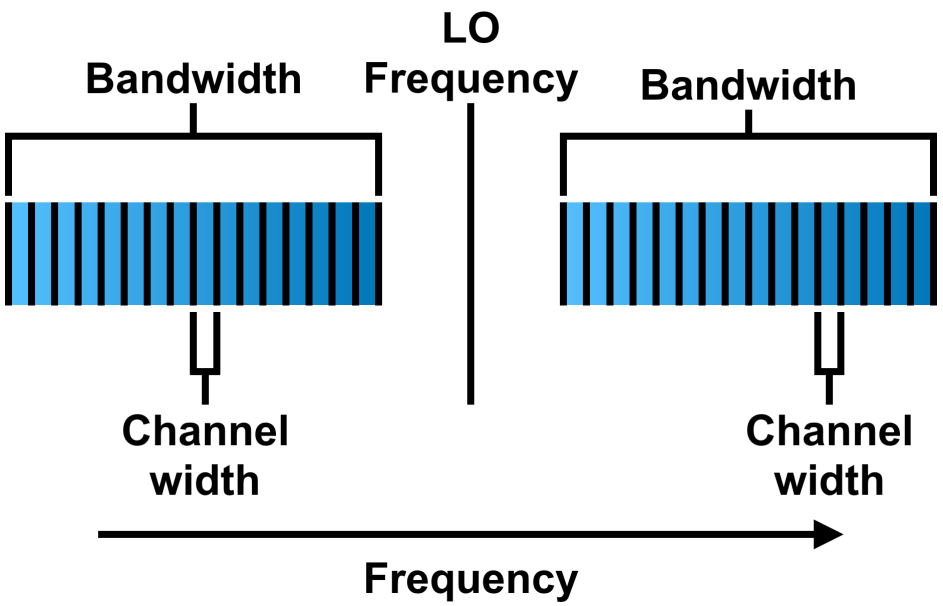

Figure 2.1: Illustration of the concept of bandwidths and channel widths. The two blue blocks represent the two IF bands in which a radio telescope is observing at.

power carried by the radio waves would be zero and is undetectable. Due to technical considerations, the incoming radio waves are first mixed with the signals from the local oscillator (LO) to convert the original radio frequency ($\nu_{\rm RF}$) of the radio waves down to a much lower "intermediate frequency" ($\nu_{\rm IF}$), such that the subsequent signal processing procedures would be more convenient and economical. The three frequencies mentioned above are related by

$$\nu_{\rm RF} = \nu_{\rm LO} \pm \nu_{\rm IF}, \tag{2.1}$$

since essentially the resulting IF signals are determined by the beating of the two input signals at RF and LO. Note that $\nu_{\rm LO}$ is single valued, while $\nu_{\rm RF}$ and $\nu_{\rm IF}$ each spans a range of frequencies known as the bandwidth (see below). Evidently, from Equation 2.1 we can see that our radio telescopes would be sensitive to two frequency sidebands (IF bands hereon) simultaneously.

Now, let's consider one of the two IFs that a radio telescope is observing at. The width in frequency space within which this IF is sensitive to is called the bandwidth (see Figure 2.1). However, note that for modern radio telescopes such as the Karl G. Jansky Very Large Array (VLA) the two IFs are often placed side-by-side on the frequency axis to provide a continuous frequency coverage. For such cases, bandwidths can be somewhat confusingly referring to the *total* bandwidths spanned by the two IFs combined. For example, the NRAO VLA Sky Survey (NVSS; Condon et al. 1998) observations, which have been closely investigated in this thesis (Chapters 3 and 4), were conducted with the legacy VLA system[1] with bandwidths of 42 MHz per IF, while

[1]The legacy system had been used since the inauguration of the VLA in 1980 until the receiver and correlator upgrades in the early 2010s (Perley et al. 2009).

for broadband observations with the upgraded Jansky VLA the *total* bandwidths at L- (1–2 GHz) and S-bands (2–4 GHz) are about 1 and 2 GHz, respectively.

Finally, some radio telescopes operated under certain observing modes allow each individual IF to be further split into finer frequency channels (see Figure 2.1), with data taken within each of them. This is an important feature for polarisation studies, since (1) the resulting data would be far less susceptible to bandwidth depolarisation (Chapter 2.1.3.2), (2) spectro-polarimetric studies would be made possible by providing a continuous sampling of the polarisation properties of the astrophysical source over a range of λ^2 (Chapters 2.2.3 and 2.2.4), and (3) data corruption by radio frequency interference (RFI) can be mitigated by discarding only the affected channels instead of the entire IF. Such capability of separating an IF into constituent channels were not available with the legacy VLA system operated in the continuum mode (thus, not provided by the NVSS data) but could be exploited by observing in the spectral line mode (e.g., Van Eck et al. 2011; Mao et al. 2012)[2]. Advances in radio receiver technologies along with computational power have enabled radio telescopes to perform wide-band narrow-channel observations (e.g., Perley et al. 2009). For instance, the upgraded VLA operates with native channel widths of 1 and 2 MHz in L- and S-bands, respectively. This is invaluable to the study of cosmic magnetism by utilising spectro-polarimetric observations (see above).

2.1.2 Stokes Parameters

The Stokes parameters (I, Q, U, and V) are a convenient and complete description of polarised electromagnetic radiation (Stokes 1851). The total intensity (including both the polarised and unpolarised components of the emission) is represented by Stokes I. Both Stokes Q and U together describes the linearly polarised component, with the orientations in astrophysical contexts defined by the International Astronomical Union (see Figure 2.2; Contopoulos & Jappel 1974). A polarisation position angle (PA) of the electric field plane is defined from north through east, and is related to Stokes Q and U by[3]

$$\mathrm{PA} = \frac{1}{2}\tan^{-1}\left(\frac{U}{Q}\right). \tag{2.2}$$

For example, a linearly polarised emission oriented along north-south has $Q > 0$ and $U = 0$, while that oriented along northwest-southeast has $Q = 0$ and $U < 0$. The linear polarised intensity (PI) is further given by

$$\mathrm{PI} = \sqrt{Q^2 + U^2}. \tag{2.3}$$

Under this scheme, we can define the complex polarisation as

$$\mathbf{P} = Q + iU = \mathrm{PI} \cdot e^{2i\cdot\mathrm{PA}}, \tag{2.4}$$

[2]See, e.g., https://science.nrao.edu/facilities/vla/docs/manuals/alloss/oct06.pdf for the capabilities of the legacy VLA.

[3]Technically, the function `arctan2` is used instead. This function preserves the quadrant in which the complex polarisation vector $\mathbf{P}$ is in on the QU-plane. The domain of the normal $\tan^{-1}$ function is $[-\pi/2, +\pi/2]$, while that of `arctan2` is $[-\pi, +\pi]$.

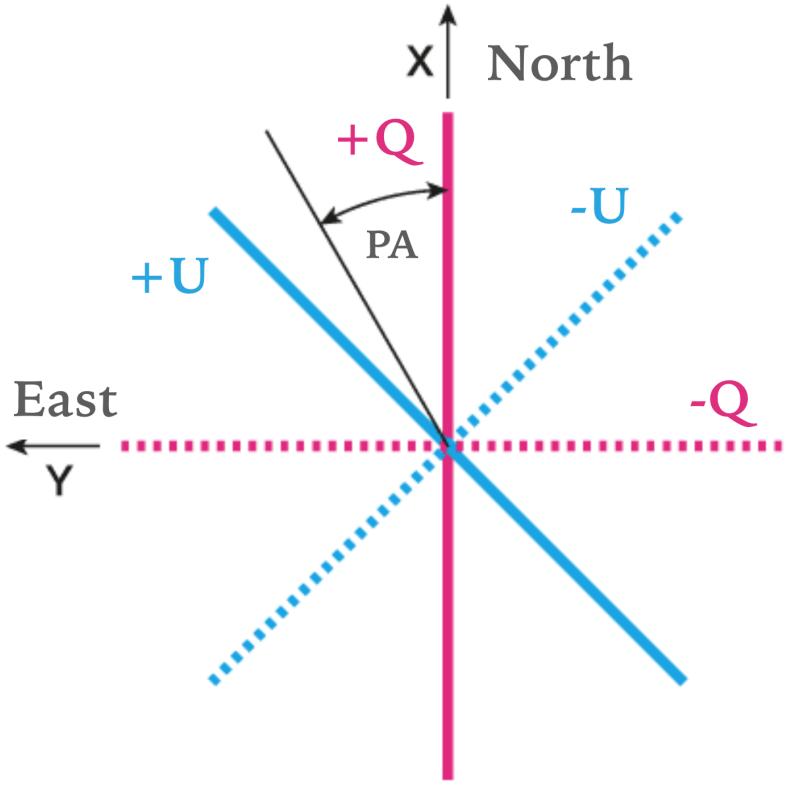

Figure 2.2: The definition of Stokes Q and U parameters according to the International Astronomical Union definition (Contopoulos & Jappel 1974). Image courtesy of NASA/LAMBDA.

which conveniently behaves like vectors. Finally, the circular polarisation is characterised by Stokes V, with positive (negative) V representing right- (left-) handed circular polarisation as per the definition of the Institute of Electrical and Electronics Engineers (IEEE)[4] endorsed by the International Astronomical Union.

The Stokes values of an astrophysical source can be extracted from the respective radio images (see, e.g., Figure 2.3). Note that in general, the Stokes parameters are functions of the observed wavelength. This is in part because of the emission spectrum of typical synchrotron-emitting objects (see Chapter 1.4.1), and for Stokes Q and U also because of Faraday rotation (see Chapter 1.4.3).

2.1.3 Instrumental Effects

As outlined above in Chapter 2.1.2, we can obtain the PI of our target astrophysical source from the Stokes Q and U images, combined with Equation 2.3. However, it is critical to note the instrumental effects that can corrupt this measured PI, as they can significantly alter our scientific conclusions.

[4]See http://ieeexplore.ieee.org/document/7370739.

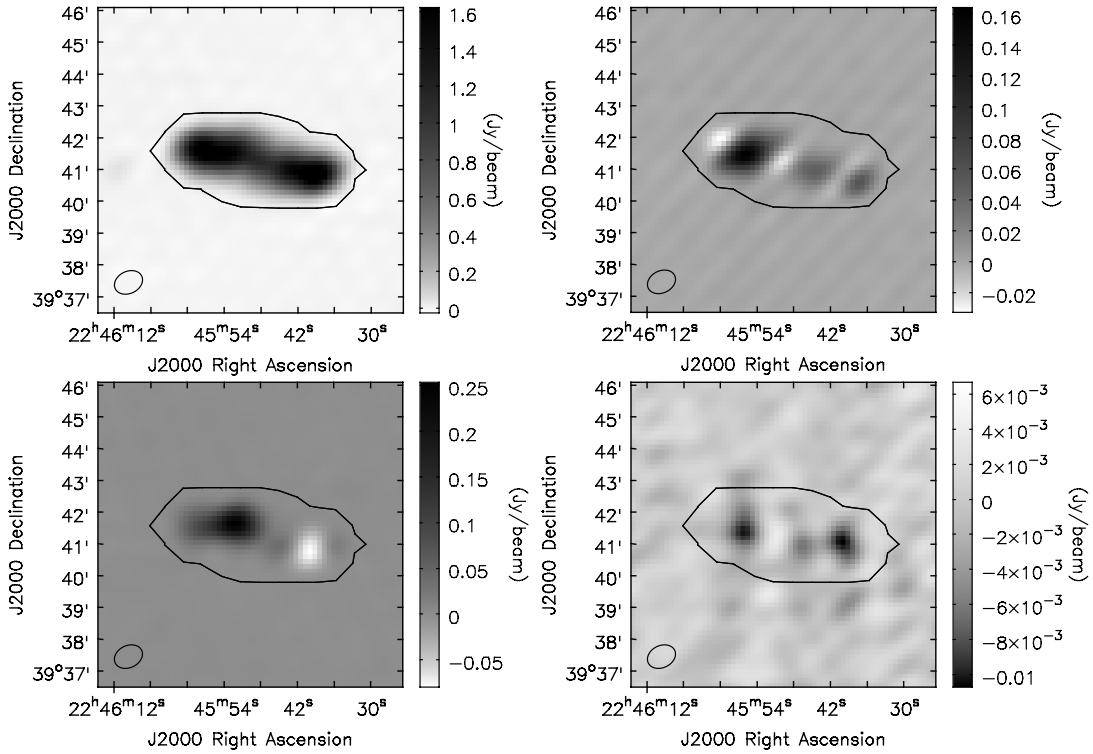

Figure 2.3: Radio images of an FR II radio galaxy NVSS J224549+394122 (3C 452) at 1421.5 MHz in **(Top left)** Stokes I, **(Top right)** Stokes Q, **(Bottom left)** Stokes U, and **(Bottom right)** Stokes V. The synthesised beam (or, the angular resolution) of the observation is shown as the ellipse in the bottom left of each panel. The black contours enclosing the radio galaxy are the flux density integration region, with which the Stokes values of this object can be extracted. Note that the apparent detection in Stokes V is likely an instrumental artefact due to the beam squint effect[5].

2.1.3.1 Wavelength-independent Beam Depolarisation

The first such effect is called wavelength-independent beam depolarisation (or simply beam depolarisation hereon), caused by the depolarisation among the polarised emission originating from different emitting volumes at the same FD within the radio beam[6]. Consider the simple case of two discrete synchrotron-emitting volumes within our beam, named volumes 1 and 2. I denote the complex polarisation from these two volumes as, respectively,

$$\mathbf{P}_1 = \mathrm{PI}_1 \cdot e^{2i \cdot \mathrm{PA}_1}, \tag{2.5}$$

$$\mathbf{P}_2 = \mathrm{PI}_2 \cdot e^{2i \cdot \mathrm{PA}_2}. \tag{2.6}$$

[5]See http://www.aoc.nrao.edu/evla/geninfo/memoseries/evlamemo113.pdf.

[6]Cases where the emitting volumes are at different FDs would lead to wavelength-dependent polarisation signatures that will allow separation of those discrete volumes by spectro-polarimetric observations. These situations are referred to as Faraday depolarisation, and I delay the discussion of such cases to Chapter 2.2.4.

As our radio telescope cannot spatially distinguish these two components, the complex polarisation signals of them are simply added together, resulting in the final measured complex polarisation as

$$\mathbf{P}_{\rm out} = \mathbf{P}_1 + \mathbf{P}_2 = {\rm PI}_1 \cdot e^{2i\cdot{\rm PA}_1} + {\rm PI}_2 \cdot e^{2i\cdot{\rm PA}_2} = {\rm PI}_{\rm out} \cdot e^{2i\cdot{\rm PA}_{\rm out}}. \tag{2.7}$$

Evidently, this would in general lead to a reduction in PI compared to that by adding the two together as scalars:

$${\rm PI}_{\rm out} \leq {\rm PI}_1 + {\rm PI}_2, \tag{2.8}$$

with the equality holding if and only if ${\rm PA}_1 = {\rm PA}_2$ for non-zero ${\rm PI}_1$ and ${\rm PI}_2$. The beam depolarisation can only be eradicated by increasing the angular resolution of the radio observations.

2.1.3.2 Bandwidth Depolarisation

Another notable instrumental effect is bandwidth depolarisation, caused by the difference in the change in PA due to Faraday rotation within a frequency band (or channel, for the case of spectro-polarimetric observations). Given the inevitable finite bandwidths of our instruments, the incoming polarisation planes at slightly different frequencies would in general be smeared across the frequency band (see Figure 2.4 for the specific case of the NVSS observational setup, and with ${\rm RM} = +400\,{\rm rad\,m^{-2}}$). Assuming a continuous frequency coverage and a constant polarisation fraction across the frequency band, the amount of bandwidth depolarisation is given by (e.g., Gardner & Whiteoak 1966; Gaensler et al. 2001):

$$\frac{p_{\rm obs}}{p_0} = \left|\frac{\sin\Delta\Theta}{\Delta\Theta}\right|, \tag{2.9}$$

with $\Delta\Theta = 2{\rm RM}c^2\nu^{-3}\Delta\nu$ (in SI units), where $\Delta\nu$ is the bandwidth and ν is the centre frequency of the band. From this Equation, it is apparent that the effect of bandwidth depolarisation is more severe for (1) higher |RM|, (2) wider bandwidth, and (3) lower observing frequency, as all these three changes would lead to more significant in-band Faraday rotation within the given $\Delta\nu$.

I further illustrate this with Figure 2.5, where I plot the bandwidth depolarisation (defined as the ratio of the detected PI to the intrinsic PI) as a function of the source RM for the NVSS, as well as for the VLA in L-band. I have adopted the bandwidth of 42 MHz for each of the NVSS IFs (with IF1 and IF2 centred at 1364.9 and 1435.1 MHz, respectively; Condon et al. 1998), and assumed a channel width of 4 MHz for the VLA to be in-line with my spectro-polarimetric analysis in this thesis. By combining the two NVSS IFs (as is the case for the original NVSS; Condon et al. 1998), bandwidth depolarisation halves the PI at a mere $|{\rm RM}| = 220\,{\rm rad\,m^{-2}}$, while with the two IFs considered separately (as is the case for the NVSS RM catalogue; Taylor et al. 2009) the same occurs at a considerably higher |RM| of $640\,{\rm rad\,m^{-2}}$ for IF1 and $750\,{\rm rad\,m^{-2}}$ for IF2. Thanks to the narrow channel widths, the Jansky VLA in L-band, which I have observed in for the studies presented in this thesis, is much more robust against

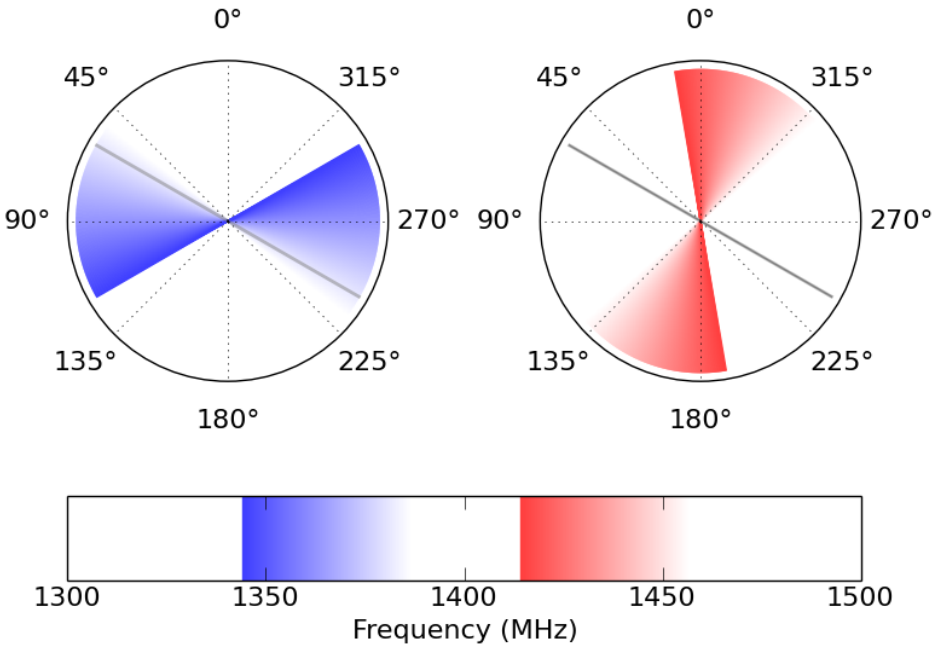

Figure 2.4: Illustration of bandwidth depolarisation for the specific case of NVSS observational setup. The upper two panels show the observed polarisation planes in IF1 (blue) and IF2 (red), with the intrinsic polarisation plane (with $PA_0 = 60°$) shown as the grey solid lines. The smearing in polarisation planes in both IFs is caused by an RM of $+400\,\mathrm{rad\,m^{-2}}$, leading to bandwidth depolarisation. The different shades of colours represent different frequencies within an IF, as presented in the lower panel.

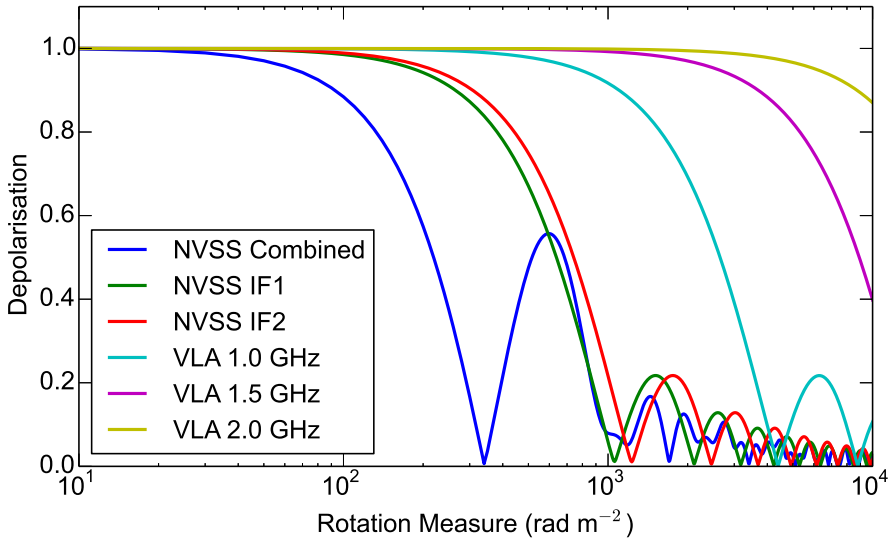

Figure 2.5: Bandwidth depolarisation as a function of RM with the NVSS observational setup, as well as with the VLA in L-band at 1.0, 1.5, and 2.0 GHz with an assumed channel width of 4 MHz.

bandwidth depolarisation, with the PI halved at |RM| of 2660, 8910, and 21030 rad m^{-2} at 1.0, 1.5, and 2.0 GHz, respectively.

Bandwidth depolarisation can affect all radio polarisation measurements, and is highly relevant to this thesis. The Taylor et al. (2009) RM catalogue has exploited this effect to resolve the $n\pi$-ambiguity of their RM measurements (see Chapter 3.4.1.1), while the goal of my study in Chapter 3 is to investigate the severity of the $n\pi$-ambiguity issue in their state-of-the-art RM catalogue. I further quantify the effect of off-axis instrumental polarisation in Taylor et al. (2009) in Chapter 4, which involved careful comparisons between the polarisation properties from the NVSS (Condon et al. 1998), Taylor et al. (2009), and my new observations, each affected by bandwidth depolarisation to different extents (see above). Finally, I have studied the magnetic fields in the first Galactic quadrant with new observations in Chapter 5, with the target sources selected from the NVSS and Taylor et al. (2009) catalogues. Bandwidth depolarisation in their observations can have imposed a selection bias to the targets (see Chapter 5.2).

2.1.3.3 Instrumental Polarisation

Finally, the observed polarisation signal can also be corrupted by instrumental polarisation (also commonly referred to as polarisation leakage). In the ideal case, the two polarised feeds of radio telescopes should be independent of each other, with each of them being sensitive to one of the two orthogonal polarisation states. Unfortunately, imperfections of telescopes can lead to the polarised feeds having non-zero responses to their orthogonal polarisations, producing artificial instrumental polarisation signals.

The instrumental polarisation of radio telescopes can be separated into two constituents — the on-axis and the off-axis components. The calibration solution to the on-axis component can be determined from one of the two common ways (see, e.g., Hales 2017). The first method involves observing an unpolarised calibrator to determine the instrumental polarisation by relying on the fact that the entirety of the detected polarisation signal is due to instrumental effects. With this calibrator placed on the pointing axis of the telescope, the amount of instrumental polarisation at the pointing centre can be characterised and removed. This is the method used in my thesis project. Another method is to use a calibrator with unknown polarisation properties, given that (1) the telescope is driven by altitute-azimuthal (alt-az) mounts, and (2) the calibrator has been observed over a range of parallactic angles. This exploits the field rotation effect of alt-az mounts: the sky rotates with respect to the telescope as the parallactic angle changes, meaning that the polarisation signal from the calibrator rotates with respect to the telescope while the instrumental polarisation remains fixed. In other words, the calibrator's true contribution to the observed polarisation would change sinusoidally across parallactic angle, while the instrumental contribution remains constant. This allows simultaneous determination of the calibrator's polarisation properties along with the on-axis instrumental polarisation. The typical on-axis leakage amplitude for the VLA is a few per cent[7], while the residual value after calibration can reach $\lesssim 0.02$ per cent (see, e.g., Chapter 3).

[7] See http://library.nrao.edu/public/memos/evla/EVLAM_201.pdf.

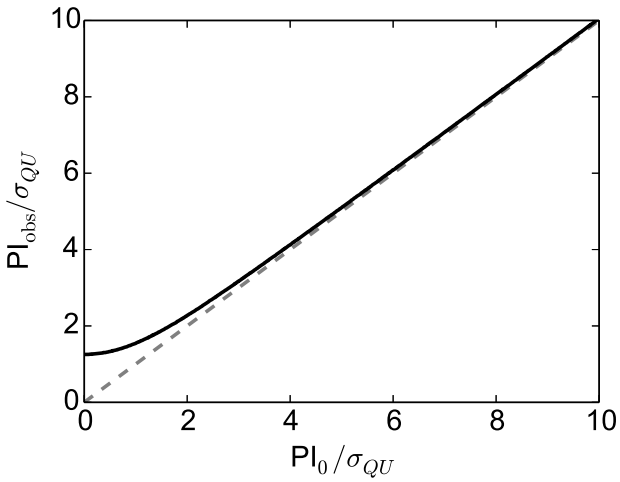

Figure 2.6: The effect of Ricean polarisation bias, showing the most likely $\mathrm{PI}_{\mathrm{obs}}$ at any given PI_0, with both normalised by the measurement uncertainty of Stokes Q and U. The grey dashed line shows where x- and y-values are equal.

However, after applying the on-axis calibrations described above, residual polarisation leakage would still remain for positions away from the pointing axis within the primary beam. This is the off-axis component of instrumental polarisation, and can be caused by imperfections in optical alignments or standing waves within optical parts (e.g., Popping & Braun 2008). Off-axis instrumental polarisation can be determined by holography scans (e.g. for the NVSS; Cotton 1994; Condon et al. 1998), which essentially creates a map of the off-axis polarisation leakage within the primary beam by placing an unpolarised calibrator at various positions with respect to the pointing axis. Alternatively, the off-axis response of the telescope can be obtained by ray-tracing models of the antenna optics (e.g., Jagannathan et al. 2018), or even by employing full electromagnetic simulations of the antenna (e.g., Young et al. 2013).

There has been on-going work to further improve the A-projection algorithm (Bhatnagar et al. 2008, 2013) for applications on correcting for the off-axis instrumental polarisation (e.g., Jagannathan et al. 2017, 2018), and this would require a detailed model of the off-axis response of the antenna. The uncorrected off-axis instrumental polarisation of the NVSS observations can be up to about 2.5 per cent (Cotton 1994), and its effects on the reported RM values in the Taylor et al. (2009) catalogue constitute a substantial part of this thesis (see Chapter 4).

2.1.4 Ricean Polarisation Bias

Apart from the instrumental effects above that can affect polarisation measurements, one must also take great care of the statistical bias in polarisation signals, especially for cases where the polarisation signal-to-noise (S/N) ratio is low. In the ideal case, our measurements should have Gaussian noises — given an observed value of

$X_{\rm obs}$ for the quantity of interest X, the probability that the true value of this quantity being X_0 is given by

$$P(X_0|X_{\rm obs}) = \frac{1}{\sigma_X\sqrt{2\pi}} e^{-(X_0-X_{\rm obs})^2/2\sigma_X^2}, \tag{2.10}$$

where σ_X is commonly called the measurement uncertainty of X. For such quantities with Gaussian noises the most likely value of X_0 is $X_{\rm obs}$. Indeed, most radio telescopes (such as the VLA) have been designed such that the measured Stokes values follow such Gaussian distributions.

The same, however, does not hold for PI (see Wardle & Kronberg 1974). Given that both Stokes Q and U have Gaussian noises of σ_{QU} (both assumed to be equal), the resulting observed PI (Equation 2.3) would follow a Ricean distribution:

$$P({\rm PI}_{\rm obs}|{\rm PI}_0) = \frac{{\rm PI}_{\rm obs}}{\sigma_{QU}^2} e^{-({\rm PI}_{\rm obs}^2+{\rm PI}_0^2)/2\sigma_{QU}^2} \cdot J_0\left(\frac{{\rm PI}_{\rm obs}\cdot{\rm PI}_0}{\sigma_{QU}^2}\right), \tag{2.11}$$

where J_0 is the zeroth-order Bessel function of the first kind. I plot in Figure 2.6 the relationship between ${\rm PI}_0$ and the corresponding most likely value of ${\rm PI}_{\rm obs}$. For the case of PI, the most likely value of ${\rm PI}_0$ deviates from ${\rm PI}_{\rm obs}$, especially for low S/N cases. This discrepancy is called the Ricean polarisation bias, and corrections known as debiasing have to be made to convert ${\rm PI}_{\rm obs}$ to the most likely ${\rm PI}_0$ (see e.g., Wardle & Kronberg 1974; George et al. 2012). The Ricean polarisation bias has been corrected for in the original NVSS catalogue (Condon et al. 1998), while in both the Taylor et al. (2009) RM catalogue and my new observations (Chapters 3–5) it is expected to have negligible effects at the high S/N regime considered, and therefore have not been removed from the data.

2.2 Extraction of Polarisation Properties from Observations

In Chapter 2.1, I have established the general pathway to obtain the polarisation properties (Stokes Q and U, and the derived PI, p, and PA) as a function of λ^2 for the astrophysical sources of interest. These can then be used to derive the magnetic fields in the emitting volumes as well as in the intervening medium. Below I describe the commonly used algorithms to achieve this.

2.2.1 Faraday Simple versus Faraday Complex

Before discussing the different algorithms to convert the measured polarisation signals into information about astrophysical magnetic fields, it is worth first pointing out the difference between Faraday simple and Faraday complex cases. Consider an astrophysical source that emits at a single FD only. This source would be called Faraday simple, with the observational signatures being (1) linear PA against λ^2 ($\Delta{\rm PA} \propto \lambda^2$; see Equation 1.13), and (2) a constant polarisation fraction across λ^2. On the other

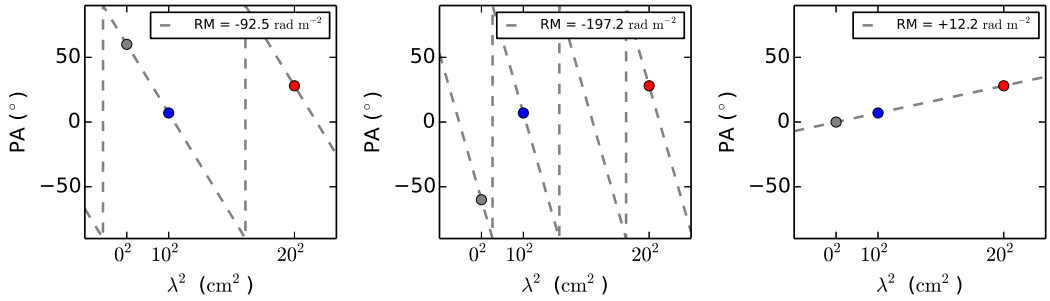

Figure 2.7: The traditional λ^2-fitting to PA to extract the RM and intrinsic PA. The blue and red data points (identical for the three panels) are the observed PAs at the two observed λ^2. The grey dashed lines in the three panels show three different ways to join the two data points due to $n\pi$-ambiguity, and the grey data point marks the extrapolated intrinsic PA resulting from the three different fits.

hand, a source can emit at multiple (or over a range of) FDs corresponding to discrete emitting volumes (e.g., the two radio lobes of an FR II radio galaxy), a gradient in FD either along or perpendicular to the line of sight, or due to turbulence in the Faraday rotating medium that leads to spatial fluctuations in FD (see Chapter 2.2.4 for more details). Such Faraday complex cases can be observationally distinguished by (1) non-linear PA against λ^2, and/or (2) a varying polarisation fraction across λ^2.

Recent studies have unravelled the wide spread Faraday complexities in essentially all astrophysical objects, such as pulsar wind nebulae (PWNe; e.g., Kothes et al. 2008), the Milky Way (e.g., Dickey et al. 2019), nearby spiral galaxies (e.g., Heald et al. 2009; Fletcher et al. 2011; Mao et al. 2015; Basu et al. 2017), active galactic nuclei (AGNs; e.g., Law et al. 2011a; O'Sullivan et al. 2012, 2015, 2017, 2018; Anderson et al. 2018; Kaczmarek et al. 2018; Pasetto et al. 2018), and extragalactic radio sources (EGSs) in general (e.g., Farnsworth et al. 2011; Anderson et al. 2015, 2016; Schnitzeler et al. 2019, see also Chapters 3 and 5). A complete picture of the magneto-ionic medium in the emitting as well as the intervening astrophysical objects can only be acquired by applying algorithms that do not implicitly assume Faraday simplicities, such as RM-Synthesis and Stokes QU-fitting (see Chapters 2.2.3 and 2.2.4).

2.2.2 Traditional λ^2-fitting

Early radio polarisation studies involved limited numbers of polarisation measurements across λ^2-space — source properties often have to be derived from very limited ($\ll 10$; sometimes even just two) number of data points (e.g., Simard-Normandin et al. 1981; Krause et al. 1989; Minter & Spangler 1996; Gaensler et al. 2005; Taylor et al. 2009; Ma et al. 2016). The traditional algorithm applied to such sparsely sampled data is least-square fit to PA across λ^2, assuming a linear relationship between the two (and thus Faraday simplicity). Figure 2.7 illustrates the simplest case of fitting to two data points only. For such cases, we obtain the RM of the target astrophysical source, which is defined as the slope of the resulting fit. This is in contrast to

FD, which is a measure of the amount of Faraday rotation experienced by polarised emission (Equation 1.13). The two are indeed identical for Faraday simple cases, but for Faraday complex sources (i.e., sources emitting at more than a single FD) the two can be different. In this thesis, the term "RM" is used to highlight cases where traditional λ^2-fitting has been performed, while the more general term "FD" is used for all cases. The RM value contains information about the magnetic fields in the intervening medium (see Chapters 1.4.3 and 1.4.4), while the intrinsic PA (which can be inferred by extrapolating the linear fit to $\lambda^2 = 0$) tells us the projected magnetic field geometry of the emitting source (see Chapters 1.4.1 and 1.4.2).

A major issue associated with a scarce number of polarisation measurements across λ^2 is $n\pi$-ambiguity. PA values determined from Stokes Q and U according to Equation 2.2 are confined in $[-\pi/2, +\pi/2]$, and therefore does not automatically take into account the potential wrapping of PA from $\pm\pi/2$ to $\mp\pi/2$. This leads to an ambiguity in the true RM as well as PA_0 if the number of data points available is limited. Figure 2.7 shows three different ways to join the same two observed PAs, leading to three different values of RM and PA_0. For this specific case of RM determination from two measurements, the RM is given by

$$\mathrm{RM} = \frac{\mathrm{PA}_1 - \mathrm{PA}_2 + n\pi}{\lambda_1^2 - \lambda_2^2}, \tag{2.12}$$

where the subscripts denote the two observed bands, and $n\pi$ introduces the possibility of PA wraps between the two observed bands. This is known as the $n\pi$-ambiguity in RM measurements, and can be best mitigated by additional polarisation measurements at other frequencies (such as with broadband spectro-polarimetric observations; see Chapter 3)[8]. The NVSS RM catalogue (Taylor et al. 2009) was constructed based on two-point PA measurements only, and hence their RM values can be susceptible to this $n\pi$-ambiguity. This has motivated the study in Chapter 3 of this thesis, where I have tested the reliability of the $n\pi$-ambiguity mitigation algorithm of Taylor et al. (2009) using new broadband data.

2.2.3 Faraday Rotation Measure Synthesis

Since 2005, we see a shift in the algorithm used for radio polarimetric analysis. The RM-Synthesis algorithm (Brentjens & de Bruyn 2005) was developed to fully exploit broadband spectro-polarimetric data, which are consisted of hundreds or even thousands of data points across λ^2 as individual frequency channels. Given that the input data have a sufficient λ^2-coverage, RM-Synthesis allows the study of Faraday complexities of target astrophysical objects and straightforward eradication of the $n\pi$-ambiguity. In a nutshell, this algorithm converts the input polarisation data (i.e. complex polarisation as a function of λ^2) into complex Faraday dispersion function ($\mathbf{F}$; also called a Faraday spectrum, and is essentially the complex polarisation as a function of ϕ).

[8] Most algorithms in the literature that tackle the $n\pi$-ambiguity, such as the Polarization Angle CorrEcting Rotation Measure ANalysis (PACERMAN; Dolag et al. 2005), can only be applied to spatially resolved sources with PA measurements at three or more frequencies, and are outside of the scope of this thesis.

To understand the working principle of RM-Synthesis, first consider the complex polarisation ($\mathbf{P}$) at a given λ^2:

$$\mathbf{P}(\lambda^2) = \int_{-\infty}^{+\infty} \mathbf{F}(\phi) e^{2i\phi\lambda^2} \, \mathrm{d}\phi. \tag{2.13}$$

This equation encapsulates the observed polarisation as a sum of emission from different FDs, with the Faraday rotation effect incorporated by the exponential term. To represent the actual measured complex polarisation ($\tilde{\mathbf{P}}$), a weight function (W) can be introduced:

$$\tilde{\mathbf{P}}(\lambda^2) = W(\lambda^2)\mathbf{P}(\lambda^2) = W(\lambda^2) \int_{-\infty}^{+\infty} \mathbf{F}(\phi) e^{2i\phi\lambda^2} \, \mathrm{d}\phi. \tag{2.14}$$

In the simplest case, one can set $W = 1$ for λ^2 ranges where observations were made, and $W = 0$ otherwise. However, one can also adopt more sophisticated weighting schemes (see, e.g., Heald et al. 2009; Schnitzeler & Lee 2017) that can slightly affect the FD resolution and the S/N ratio of the final results. An inverse Fourier transform to Equation 2.14 would yield the observed Faraday dispersion function ($\tilde{\mathbf{F}}$) as

$$\tilde{\mathbf{F}}(\phi) = \mathbf{F}(\phi) \circledast \mathbf{R}(\phi) = \frac{\displaystyle\int_{-\infty}^{+\infty} \tilde{\mathbf{P}}(\lambda^2) e^{-2i\phi\lambda^2} \, \mathrm{d}\lambda^2}{\displaystyle\int_{-\infty}^{+\infty} W(\lambda^2) \, \mathrm{d}\lambda^2}, \tag{2.15}$$

where $\circledast$ denotes a convolution, and $\mathbf{R}$ is called the Rotation Measure Transfer Function (RMTF) and is given by

$$\mathbf{R}(\phi) = \frac{\displaystyle\int_{-\infty}^{+\infty} W(\lambda^2) e^{-2i\phi\lambda^2} \, \mathrm{d}\lambda^2}{\displaystyle\int_{-\infty}^{+\infty} W(\lambda^2) \, \mathrm{d}\lambda^2}. \tag{2.16}$$

Evidently, the right side of Equation 2.15 consists of only observed or defined quantities, which means $\tilde{\mathbf{F}}$ can be readily obtained. However, this also mean the quantity of interest, namely $\mathbf{F}$, is corrupted by the instrumental artefact $\mathbf{R}$. Deconvolution schemes (e.g. the RM-Clean algorithm; Heald et al. 2009) can be applied to $\tilde{\mathbf{F}}$ to recover the desired $\mathbf{F}$.

The λ^2-coverage of an observation plays a critical role in determining the shape of $\mathbf{R}$ and the detectability of certain complex Faraday polarisation features. The full-width at half-maximum (FWHM) of the main peak of the RMTF is approximately given by (equation 61 of Brentjens & de Bruyn 2005)

$$\delta\phi \approx \frac{2\sqrt{3}}{\Delta\lambda^2}, \tag{2.17}$$

where $\Delta\lambda^2$ is the width of the observed frequency band in λ^2-space. This equation sets the FD resolution granted by an observation. For example, VLA observations in L- (1–2 GHz), S- (2–4 GHz), and LS-bands combined (1–4 GHz) would respectively grant

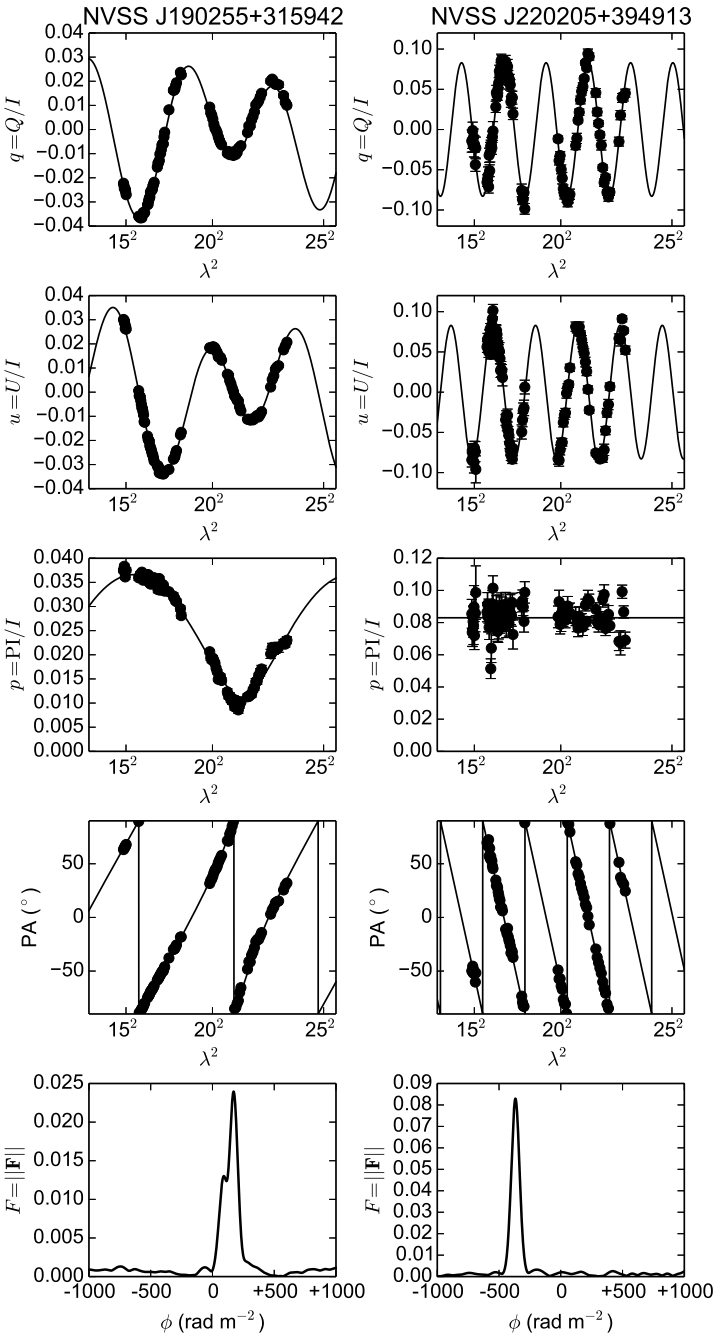

Figure 2.8: Examples of RM-Synthesis and QU-fitting for two polarised radio sources (one per column). The data points represent the observed values from broadband VLA observations in L-band (1–2 GHz), and the solid lines in the top four rows represent the best-fit results from QU-fitting. Error bars are not shown for the PA data points. The final row shows the Faraday spectra from RM-Synthesis for the two sources.

Table 2.1: Analogies between Synthesis Imaging and RM-Synthesis

Synthesis Imaging	RM-Synthesis
uv-plane	λ^2-space
Visibility data	$\tilde{\mathbf{P}}(\lambda^2)$
Dirty beams	$\mathbf{R}(\phi)$
Dirty images	$\tilde{\mathbf{F}}(\phi)$
Sky brightness	$\mathbf{F}(\phi)$

$\delta\phi$ of 51, 206, and 41 rad m^{-2}, assuming that no frequency channels are discarded and the entirety of the frequency bands are used. This highlights the suitability of the VLA L-band for scenarios where accurate FD determinations are required, as are the cases for my thesis projects. The λ^2-coverage also determines the largest detectable scale in ϕ-space (equation 62 of Brentjens & de Bruyn 2005):

$$\text{max-scale} \approx \frac{\pi}{\lambda^2_{\text{min}}}, \tag{2.18}$$

where λ^2_{min} is the lower end of the frequency band in λ^2-space. This scale in L- and S-bands observations are approximately 140 and 559 rad m^{-2}, respectively, meaning that Faraday structures spanning over FDs of wider than these values would not be satisfactorily recovered by the observations. It is crucial to keep these numbers in mind when one analyses spectro-polarimetric data and to acknowledge such limits imposed by the observational parameters. Lastly, the maximum detectable FD (due to bandwidth depolarisation) is given by (equation 63 of Brentjens & de Bruyn 2005)

$$||\phi_{\text{max}}|| \approx \frac{\sqrt{3}}{\delta\lambda^2}, \tag{2.19}$$

where $\delta\lambda^2$ is the width of frequency channels in λ^2 space. Assuming a binned channel width of 4 MHz as are the cases for my thesis projects, the maximum detectable FDs at 1.0 GHz, 1.5 GHz, and 2.0 GHz are 2409 rad m^{-2}, 8130 rad m^{-2}, and 19272 rad m^{-2}, respectively, at which the measured PI is approximately halved due to bandwidth depolarisation. Finally, significant gaps in λ^2-space will lead to undesirably high sidelobes in the RMTF.

Analogies can be drawn between synthesis imaging and RM-Synthesis. Table 2.1 shows translations of the key technical terms between the two. The main differences between the two algorithms are (1) synthesis imaging almost always sample the 2D uv-plane and result in 2D radio images, while RM-Synthesis samples the 1D λ^2-space to give 1D $\tilde{\mathbf{F}}$, and (2) although it is possible to sample the negative uv-space in synthesis imaging[9], the counterpart in RM-Synthesis is not possible as we cannot make measurements at negative λ^2 values.

[9]That is because (u, v) of a baseline is the displacement from an antenna to its pair, and therefore u and v can be negative. In addition, the visibility function is Hermitian, i.e. the visibility at $(-u, -v)$ is the complex conjugate of the visibility at (u, v).

In Figure 2.8, I show examples of RM-Synthesis results for two polarised radio sources from Chapter 3 of this thesis. Essentially, Stokes q ($= Q/I$) and u ($= U/I$) as shown in the top two rows are used as the input, and $F = ||\mathbf{F}||$ (in units of polarisation fraction per RMTF) shown in the last row is the resulting output from the RM-Synthesis algorithm. It is customary, as I also do throughout this thesis, to use q and u as the inputs to RM-Synthesis (and also QU-fitting below) instead of Stokes Q and U, so as to remove the spectral effects of Stokes I (e.g., Anderson et al. 2015; Mao et al. 2015; Kaczmarek et al. 2017). The effect of Stokes I spectral index on Stokes Q and U, if not taken care of, can be mistaken as re-/de-polarisation signatures associated with Faraday complexities.

2.2.4 Stokes QU-fitting

Stokes QU-fitting (e.g., Farnsworth et al. 2011; O'Sullivan et al. 2012) is an algorithm that performs direct least-square fits to the measured $Q(\lambda^2)$ and $U(\lambda^2)$ (or $q = Q/I$ and $u = U/I$). Typically, an array of astrophysical models describing the synchrotron-emitting as well as the Faraday rotating volumes are considered to determine the best-fit model and the best-fit parameters. These models can consist of multiple polarised components combined together. In the following paragraphs, I will first describe the most commonly considered polarised components (see also, e.g., Burn 1966; Sokoloff et al. 1998; O'Sullivan et al. 2012), and then show how one can combine these components to form the polarisation models. For simplicity, I assume in the following discussion that the emitting astrophysical sources are spatially unresolved from the observations.

The simplest system that one can consider is composed of a purely synchrotron-emitting volume (with no internally embedded thermal electrons that can cause Faraday rotation) and an external Faraday rotating screen (with a homogeneous thermal electron density and a uniform magnetic field configuration) between the observer and the emitting volume. I shall call such polarised component a ***thin*** component, with its complex polarisation fraction [$\mathbf{p}(\lambda^2) = q(\lambda^2) + iu(\lambda^2)$] given by

$$\mathbf{p}_j(\lambda^2) = p_{0,j} e^{2i(\mathrm{PA}_{0,j} + \phi_j \lambda^2)}, \tag{2.20}$$

where the subscript j is an index for the polarised components for when I combine multiple of them below, and the subscript 0 denotes the intrinsic values describing the polarised components.

The ***Burn slab*** component consists of a simultaneously synchrotron-emitting and Faraday rotating volume. The cosmic rays and thermal electron densities are both homogeneous, and the magnetic fields are set to be uniform in this volume. This means the source suffers from differential Faraday rotation, with the far side experiencing more Faraday rotation than the near side. The resulting complex polarisation fraction is given by

$$\mathbf{p}_j(\lambda^2) = p_{0,j} \frac{\sin(\phi_j \lambda^2)}{\phi_j \lambda^2} e^{2i(\mathrm{PA}_{0,j} + \frac{1}{2}\phi_j \lambda^2)}. \tag{2.21}$$

A generalised form of the Burn slab component is the ***Burn slab with foreground screen*** component, for which there is an additional homogeneous Faraday rotating screen between the emitting volume and the observer. Such a foreground screen can represent the FD contributions from, e.g., the intergalactic medium and the interstellar medium of the Milky Way. For this case, the complex polarisation fraction is given by

$$\mathbf{p}_j(\lambda^2) = p_{0,j}\frac{\sin(\phi_j\lambda^2)}{\phi_j\lambda^2}e^{2i[\mathrm{PA}_{0,j}+(\frac{1}{2}\phi_j+\phi_{\mathrm{fg}})\lambda^2]}, \tag{2.22}$$

where ϕ_{fg} is the FD contribution by the foreground Faraday screen.

We can also take into account the turbulent nature (due to spatial fluctuations of thermal electron density and/or magnetic fields) of the Faraday rotating media. In the following polarised components, Gaussian turbulence has been invoked (i.e., the probability density function of the thermal electron density and/or magnetic fields are Gaussian). This will cause a dispersion of FD along different lines of sight to the source within the telescope beam, leading to different wavelength-dependent polarisation signatures as compared to the polarised components discussed above. It is important that the telescope beam encompasses a considerable number of turbulence cells ($\gg 10$; e.g. Sokoloff et al. 1998) for the observed polarisation signatures to converge to the predictions below. If the foreground Faraday screen in the thin component above is instead turbulent, we will have an ***external Faraday dispersion*** component with the complex polarisation fraction given by

$$\mathbf{p}_j(\lambda^2) = p_{0,j}e^{-2\sigma^2_{\phi,j}\lambda^4}e^{2i(\mathrm{PA}_{0,j}+\phi_j\lambda^2)}, \tag{2.23}$$

where $\sigma_{\phi,j}$ represents the dispersion in FD due to turbulence. The λ^4 term in the first exponent means that even a mild turbulence can cause severe depolarisation at long wavelengths, and is one of the explanations to the low source densities found in low frequency polarisation surveys (e.g., Van Eck et al. 2018). Similarly, if the embedded Faraday rotating medium in the Burn slab model is turbulent, we will have an ***internal Faraday dispersion*** component with complex polarisation fraction given by

$$\mathbf{p}_j(\lambda^2) = p_{0,j}e^{2i\mathrm{PA}_{0,j}}\left(\frac{1-e^{i\phi_j\lambda^2-2\sigma^2_{\phi,j}\lambda^4}}{2\sigma^2_{\phi,j}\lambda^4-i\phi_j\lambda^2}\right). \tag{2.24}$$

Finally, if there is an extra external homogeneous (i.e., no turbulence) Faraday screen to the internal Faraday dispersion component, we will have an ***internal Faraday dispersion with foreground screen*** component, with complex polarisation fraction given by

$$\mathbf{p}_j(\lambda^2) = p_{0,j}e^{2i(\mathrm{PA}_{0,j}+\phi_{\mathrm{fg}}\lambda^2)}\left(\frac{1-e^{i\phi_j\lambda^2-2\sigma^2_{\phi,j}\lambda^4}}{2\sigma^2_{\phi,j}\lambda^4-i\phi_j\lambda^2}\right). \tag{2.25}$$

The above polarised components are the building blocks to the actual polarisation models applied in QU-fitting. In my thesis projects, I assume that the polarised components are spatially distributed perpendicular to the line of sight within the telescope beam (i.e. the polarised emission from one polarised component does not traverse

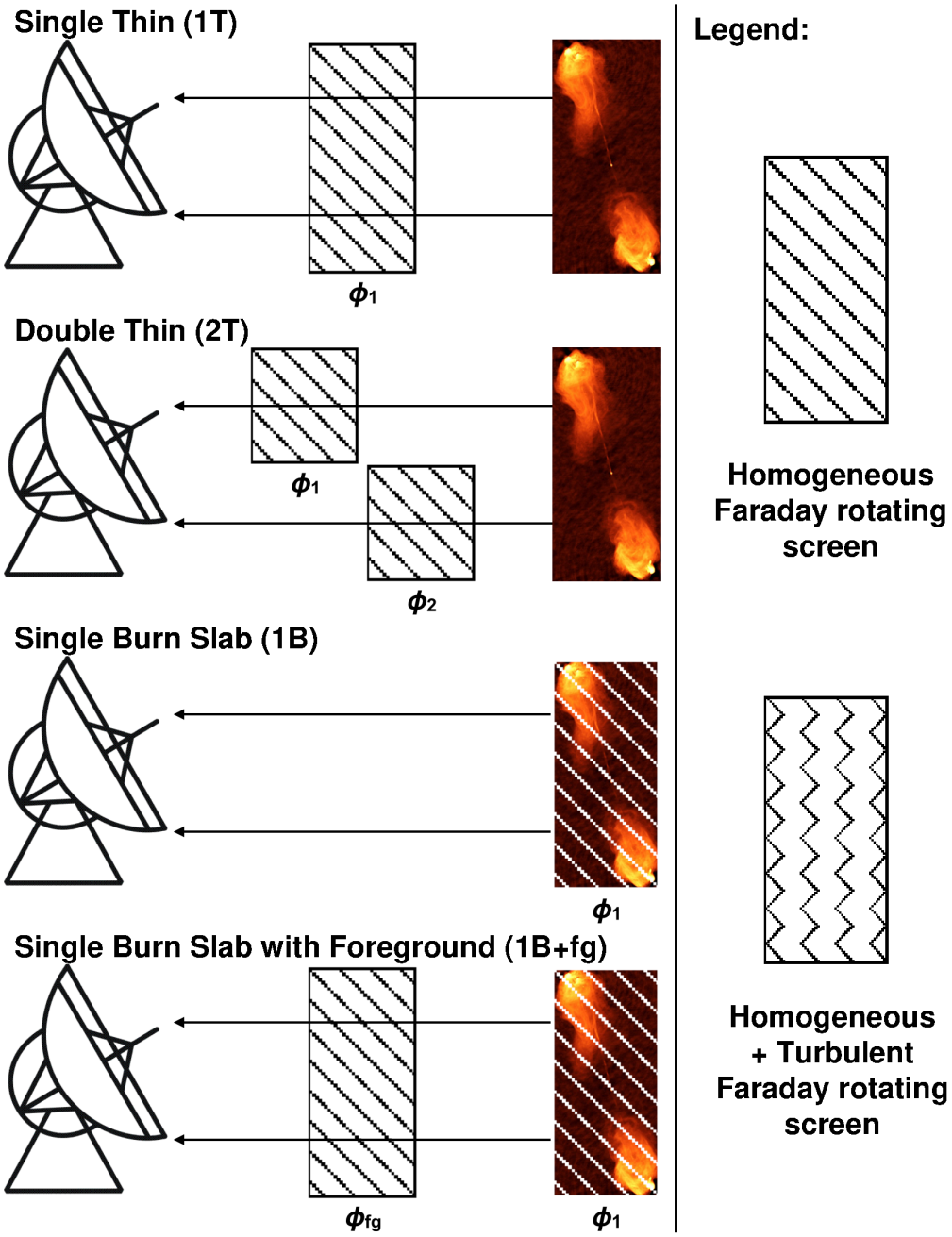

Figure 2.9: Schematics for Stokes QU-fitting models as labelled. The heat map of the radio galaxy Cygnus A represents here the synchrotron-emitting target, with the Faraday rotation occurring in the homogeneous Faraday rotating screen (block with diagonal stripes) and/or the Faraday rotating screen with intermixed homogeneous and turbulent components (block with zig-zag pattern). Image courtesy of NRAO/AUI (Cygnus A image) and MPIfR (MPIfR logo).

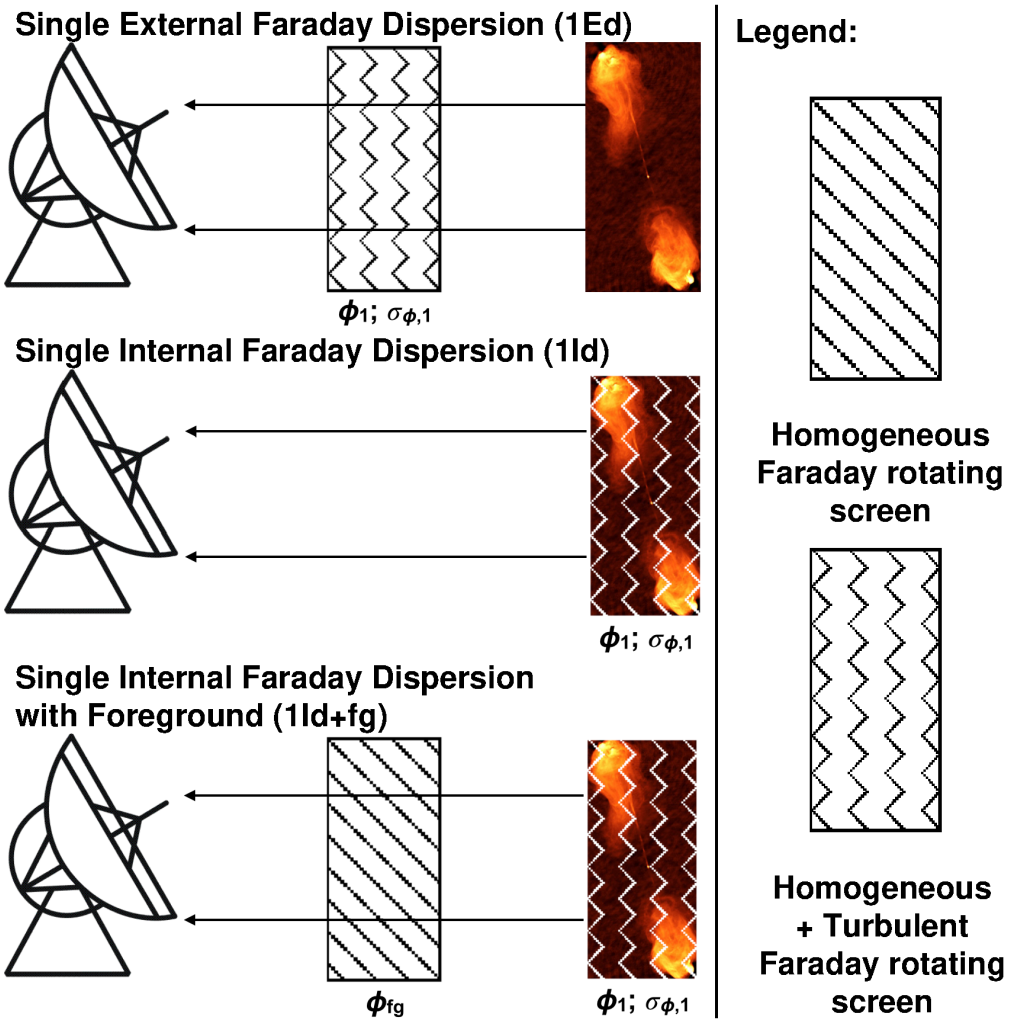

Figure 2.9: (Continued) Schematics for Stokes QU-fitting models as labelled. Image courtesy of NRAO/AUI (Cygnus A image) and MPIfR (MPIfR logo).

through the emitting volume of the other components before reaching our telescope)[10]. In this case, the final observed complex polarisation fraction is just a sum of that of the constituent polarised components:

$$\mathbf{p}(\lambda^2) = \sum_j \mathbf{p}_j(\lambda^2). \tag{2.26}$$

For example, consider a polarisation model consisting of two thin components (denoted

[10]One can consider, given an appropriate astrophysical system, cases where the polarised components are placed along the same line of sight. This would mean that the internal Faraday rotating medium in the foreground component(s) would act as an external Faraday rotating screen to the background component(s). Detailed explorations of such cases are outside of the scope of my thesis.

as $j = 1, 2$). Their complex polarisation fractions are given by

$$\mathbf{p}_1(\lambda^2) = p_{0,1} e^{2i(\mathrm{PA}_{0,1} + \phi_1 \lambda^2)}, \tag{2.27}$$

$$\mathbf{p}_2(\lambda^2) = p_{0,2} e^{2i(\mathrm{PA}_{0,2} + \phi_2 \lambda^2)}. \tag{2.28}$$

Therefore, following Equation 2.26, the final complex polarisation for this double thin polarisation model is given by

$$\mathbf{p}(\lambda^2) = \mathbf{p}_1(\lambda^2) + \mathbf{p}_2(\lambda^2) = p_{0,1} e^{2i(\mathrm{PA}_{0,1} + \phi_1 \lambda^2)} + p_{0,2} e^{2i(\mathrm{PA}_{0,2} + \phi_2 \lambda^2)}. \tag{2.29}$$

I consider a total of 10 different polarisation models for the QU-fitting analysis in my work (with the degree of freedom, dof, listed for each case): single thin (1T; dof = 3), double thin (2T; dof = 6), triple thin (3T; dof = 9), single Burn slab (1B; dof = 3), double Burn slab (2B; dof = 6), single Burn slab with foreground screen (1B+fg; dof = 4), double Burn slab with foreground screen (2B+fg; dof = 7), single external Faraday dispersion (1Ed; dof = 4), single internal Faraday dispersion (1Id; dof = 4), and single internal Faraday dispersion with foreground screen (1Id+fg; dof = 5). Specifically for the double Burn slab with foreground screen model, I have further imposed a limit that the foreground FD (ϕ_{fg}) of the two components are identical. The single thin model corresponds to the Faraday simple case as mentioned in Chapter 2.2.1, while all others are Faraday complex. Schematics of some of these models (namely, 1T, 2T, 1B, 1B+fg, 1Ed, 1Id, and 1Id+fg) are shown in Figure 2.9. For each source, the best-fit parameters for each polarisation model are determined by minimising the chi-squared (χ^2) values of the fit, while the individual models are ranked by the Bayesian information criterion (BIC) values (see, e.g., O'Sullivan et al. 2012; Schnitzeler 2018):

$$\mathrm{BIC} = -2 \log L + k \log N, \tag{2.30}$$

where L is the maximum likelihood of the model fit, k is the degree of freedom of the polarisation model, and N is the number of data points (i.e. Stokes Q and U measurements). The best model is determined as the one with the lowest BIC value.

In principle, one can develop more sophisticated polarisation models best suited for specific classes of sources. For example, Shneider et al. (2014) has put forward a model predicting the wavelength dependent depolarisation behaviour of face-on spiral galaxies[11] by considering the galaxy as individual layers that are distributed along the sight line. Furthermore, there are on-going efforts to test the validity of Stokes QU-fitting models with Gaussian turbulence by using magnetohydrodynamic (MHD) simulations (e.g., Basu et al. in prep.), which can eventually lead to even more physically sound models for Stokes QU-fitting analysis.

Finally, I show in Figure 2.8 the QU-fitting results for two target sources in my thesis projects as examples. NVSS J190255+315942 and NVSS J220205+394913 are best represented by the double thin and single thin models, respectively. The best-fit

[11] They have only presented the predicted p (i.e. amplitude of $\mathbf{p}$) as a function of λ^2, though their mathematical derivations can be repeated to recover the predicted PA as a function of λ^2 for a full wavelength dependent representation of the complex polarisation.

parameters are listed in Chapter 3. Evidently, for both cases the best-fit models can well capture the complicated wavelength dependent polarisation behaviours, including the varying p and non-linear PA of J190255+315942. Moreover, the best-fit QU-fitting models are in great correspondence with the RM-Synthesis results also shown in the same Figure.

2.2.5 Rotation Measure Synthesis or QU-fitting?

The two algorithms suited for spectro-polarimetric analysis are based on vastly different philosophies. RM-Synthesis is non-parametric, meaning that no prior assumptions of the observed astrophysical system have to be made. In contrast, QU-fitting requires an initial selection of astrophysical models that will be considered, and naturally this algorithm will not perform satisfactorily if none of the models adequately represent the actual astrophysical system. Nonetheless, simulations evaluating the effectiveness of both algorithms have shown that, specifically for the double thin model observed in the frequency range of 1.1–1.4 GHz (matching that of the POSSUM and GALFACTS surveys), QU-fitting demonstrated a higher consistency in recovering the parameters describing the model than RM-Synthesis (Sun et al. 2015). This may suggest that QU-fitting is more robust than RM-Synthesis in general given that the correct polarisation model has been considered, but a more definitive conclusion would require further extensive tests including other models and a wider range of λ^2-coverages (see Chapter 6.2.2). The RM-Synthesis results can also be used as the initial guesses to QU-fitting to help the algorithm converge to the best-fit parameters (e.g., Mao et al. 2015). In this thesis, I performed both RM-Synthesis and Stokes QU-fitting in Chapter 3 for a complementary analysis of my new spectro-polarimetric data, while in Chapter 5 I follow the common scheme of considering the main peaks of the Faraday spectra from RM-Synthesis only (e.g., Mao et al. 2017; Betti et al. 2019) to study the magnetic fields in the first Galactic quadrant.

Chapter 3

Breaking the $n\pi$-ambiguity in the NVSS Rotation Measure Catalogue

---

This Chapter is based on an article titled **"A Broad-band Spectro-polarimetric View of the NVSS Rotation Measure Catalogue — I. Breaking the nπ-ambiguity"**, which has been published in the Monthly Notices of the Royal Astronomical Society (2019; Volume 487, Issue 3, Pages 3432–3453), published by Oxford University Press on behalf of the Royal Astronomical Society, available on https://doi.org/10.1093/mnras/stz1325. Edits are done solely to maintain a consistent style within the entirety of this thesis. As the lead author of this publication, I have conducted all the data reduction and analysis in this Chapter, and was responsible for the writing of the manuscript. The full list of authors is: **Yik Ki Ma**, Sui Ann Mao, Jeroen Stil, Aritra Basu, Jennifer West, Carl Heiles, Alex S. Hill, and Sarah K. Betti.

The NRAO VLA Sky Survey (NVSS) Rotation Measure (RM) catalogue is invaluable for the study of cosmic magnetism. However, the RM values reported in it can be affected by $n\pi$-ambiguity, resulting in deviations of the reported RM from the true values by multiples of $\pm 652.9\,\mathrm{rad\,m^{-2}}$. We therefore set off to observationally constrain the fraction of sources in the RM catalogue affected by this ambiguity. New broadband spectro-polarimetric observations were performed with the Karl G. Jansky Very Large Array (VLA) at 1–2 GHz, with 23 $n\pi$-ambiguity candidates selected by their peculiarly high |RM| values. We identified nine sources with erroneous RM values due to $n\pi$-ambiguity and 11 with reliable RM values. In addition, we found two sources to be unpolarised and one source to be inconsistent with neither $n\pi$-ambiguity nor reliable RM cases. By comparing the statistical distributions of the above two main classes, we devised a measure of how much a source's RM deviates from that of its neighbours: Δ/σ, which we found to be a good diagnostic of $n\pi$-ambiguity. With this, we estimate that there are at least 50 sources affected by $n\pi$-ambiguity among the 37,543 sources in the catalogue. Finally, we explored the Faraday complexities of our sources revealed by our broadband observations.

Contents

3.1 Introduction

Magnetic fields are ubiquitous in the Universe. For astrophysical processes such as star formation, cosmic ray propagation, galactic outflows, and galactic evolution, magnetic fields are critical and must be considered (see review by Beck & Wielebinski 2013; Beck 2016). Magnetic field structures of astrophysical objects can be directly measured through their polarised synchrotron diffuse emission (e.g., Kothes et al. 2008; Heald et al. 2009; Ma et al. 2016; Basu et al. 2017). However, this technique is limited to probing volumes filled with synchrotron-emitting cosmic ray electrons. Polarised emission from background sources can illuminate the foreground magneto-ionic media through the Faraday rotation effect, allowing the study of physical conditions in the intervening magnetised plasma.

Radio polarimetric observations of background extragalactic radio sources (EGSs) have been successful in revealing the magnetic fields in foreground astrophysical objects, such as discrete H II regions in the Milky Way (Harvey-Smith et al. 2011; Purcell et al. 2015; Costa et al. 2016), Galactic high velocity clouds (McClure-Griffiths et al. 2010; Hill et al. 2013; Betti et al. 2019), the Galactic disk (Van Eck et al. 2011), the Galactic halo (Mao et al. 2010, 2012; Terral & Ferrière 2017), the Magellanic system (Gaensler et al. 2005; Mao et al. 2008; Kaczmarek et al. 2017), nearby galaxies such as M31 (Han et al. 1998; Gießübel et al. 2013), and cosmologically distant galaxies (Mao et al. 2017). As the polarised radiation traverses through the foreground media, its polarisation position angle (PA; [rad]) will be rotated by

$$\Delta\mathrm{PA} = \left[0.81 \int_{\ell}^{0} n_e(s) B_{\parallel}(s)\,\mathrm{d}s\right] \cdot \lambda^2 \equiv \phi \cdot \lambda^2, \tag{3.1}$$

where ℓ [pc] is the (physical) distance of the emitting volume from the observer, n_e [cm^{-3}] is the electron density, $B_\parallel$ [μG] is the strength of the magnetic field component along the line of sight (s [pc]; increasing away from the observer), λ [m] is the wavelength of the electromagnetic wave, and ϕ [$\mathrm{rad\,m}^{-2}$] is the Faraday depth (FD) of the emission region. This Faraday rotation effect encodes the physical conditions of the foreground magneto-ionic media, in particular n_e and $B_\parallel$, into FD. The traditional way to extract the FD values of polarised sources is by PA measurements at two or more distinct frequency bands and perform a linear fit to PA against λ^2. In this case, FD is commonly referred to as Rotation Measure (RM) instead, which is the slope of the resulting fit. For situations where PA measurements are only available at two frequencies, the resulting FD (or RM) values can be ambiguous because wrapping(s) of PA can occur between the two bands. This is the so-called $n\pi$-ambiguity problem, and can be best mitigated by additional PA measurements at other frequency bands.

Modern radio telescopes equipped with broadband backends, such as the Karl G. Jansky Very Large Array (VLA), have started a new era in the study of cosmic magnetism. They opened up the possibility of spectro-polarimetric observations with unprecedented bandwidths (e.g. 1–2 GHz in L-band and 2–4 GHz in S-band for the Jansky VLA) and fine frequency resolutions (1–2 MHz in the above-mentioned bands). This allows a simple eradication of $n\pi$-ambiguity in FD (or RM) measurements, since PAs at hundreds or even thousands of closely spaced frequencies can be measured simultaneously, ensuring no wrappings of PA between the channels. The even more important aspect of broadband spectro-polarimetric studies is the possibility to apply analysis methods such as RM-Synthesis (Brentjens & de Bruyn 2005) and Stokes QU-fitting (e.g. Farnsworth et al. 2011; O'Sullivan et al. 2012). The former makes use of the Fourier-like behaviour of polarisation signal, such that input complex polarisation ($\mathbf{P} = Q + iU$) as a function of λ^2 can be transformed into output Faraday spectrum ($\mathbf{F}$; which is the complex polarisation as a function of ϕ):

$$\mathbf{P}(\lambda^2) = \int_{-\infty}^{+\infty} \mathbf{F}(\phi) e^{2i\phi\lambda^2}\, \mathrm{d}\phi, \tag{3.2}$$

$$\mathbf{F}(\phi) = \int_{-\infty}^{+\infty} \mathbf{P}(\lambda^2) e^{-2i\phi\lambda^2}\, \mathrm{d}\lambda^2. \tag{3.3}$$

The latter technique is to fit the observed Stokes Q and U values as a function of λ^2 by using models of magnetised plasma along the line of sight. Both of the techniques allow exploration of Faraday complex sources (e.g. Burn 1966; Sokoloff et al. 1998), which emit at multiple FDs. These sources have varying polarisation fractions as a function of λ^2, and sometimes deviate from the linear relationship between PA and λ^2. Given sufficient λ^2 coverage, these sources would exhibit multiple peaks and/or extended component(s) in Faraday spectra. In contrast, Faraday simple sources emit at a single FD only, with constant polarisation fractions across λ^2, and have PA values varying linearly with λ^2. RM-Synthesis and QU-fitting are widely used in broadband radio polarisation studies, with a growing success in revealing the Faraday complexities of a significant number of the observed EGSs (e.g. Law et al. 2011a; Anderson et al.

2015, 2016; Kim et al. 2016; O'Sullivan et al. 2017; Kaczmarek et al. 2018; Pasetto et al. 2018; Schnitzeler et al. 2019).

The largest RM catalogue of polarised radio sources to date is the Taylor et al. (2009, hereafter TSS09) catalogue, which contains RM values of 37,543 radio sources north of $\delta = -40°$ at a source density of higher than one per square degree. This makes it invaluable for the study of cosmic magnetism (e.g. Stil et al. 2011; Oppermann et al. 2012; Purcell et al. 2015; Terral & Ferrière 2017). TSS09 constructed the catalogue by re-analysing the NRAO VLA Sky Survey (NVSS; Condon et al. 1998) data, and thus it is also called the NVSS RM catalogue. While in the original NVSS catalogue the two intermediate frequencies (IFs; centred at 1364.9 and 1435.1 MHz with bandwidths of 42 MHz each) were combined, TSS09 processed data from the two IFs independently, allowing determination of RM from these two frequency bands. However, these RM values could then be susceptible to $n\pi$-ambiguity as discussed above. For each of the sources in their catalogue, the authors compared the observed amount of depolarisation with that expected from bandwidth depolarisation at the different allowed RM values, and also used the RM values of neighbouring sources within 3°, to minimise $n\pi$-ambiguity. However, it is not clear how effective this method really is at picking the correct RM values. Understanding the limits of the NVSS RM catalogue is vital to the study of cosmic magnetism. While upcoming polarisation surveys such as Polarization Sky Survey of the Universe's Magnetism (POSSUM; Gaensler et al. 2010) at 1130–1430 MHz and VLA Sky Survey (VLASS; Myers et al. 2014) at 2–4 GHz are expected to bring vastly higher RM densities compared to TSS09, the two surveys either do not have exact sky or frequency coverage as TSS09. This means the NVSS RM catalogue will remain a unique data set for studying the magnetised Universe, complementing the VLASS in the frequency domain and POSSUM in the sky domain, in addition to both in the time domain. A prior deeper understanding in the systematics of TSS09 will facilitate future robust comparisons among these surveys. The focus of our work here is to effectively test the reliability of the TSS09 RM values by validating a small sample of TSS09 sources using broadband polarimetry, which provides us with $n\pi$-ambiguity-free FD.

In this Chapter, we report the results from new broadband observations of 23 candidates from the NVSS RM catalogue which could suffer from $n\pi$-ambiguity. The observational setup and data reduction procedures are described in Chapter 3.2, and the results are presented in Chapter 3.3. In Chapter 3.4, we discuss the implications of the results on the $n\pi$-ambiguity in the TSS09 catalogue, and also explore the Faraday complexities of the targets revealed by the new broadband observations. Finally, we conclude this work in Chapter 3.5. In Chapter 4, we further compare this data set with the TSS09 catalogue in matching frequency ranges to quantify the effects of the off-axis instrumental polarisation on the TSS09 RM measurements. Throughout the Chapter, we adopt a cosmology in accordance to the latest *Planck* results (i.e., $H_0 = 67.8\,\mathrm{km\,s^{-1}\,Mpc^{-1}}$ and $\Omega_m = 0.308$; Planck Collaboration et al. 2016c).

Table 3.1: Summary of the Jansky VLA Observations on 2014 July 03

Start Time (UTC)	End Time (UTC)	Flux and Bandpass Calibrator	Leakage Calibrator	Phase Calibrator	Target Source (NVSS)	Target Source (Other Name)	Angular Resolution[a]
03:25:53	04:25:48	3C 286	J1407+2827	J1549+2125	J154936+183500	4C +18.45	$43'' \times 40''$
				J1623−1140	J162706−091705	—	$59'' \times 43''$
					J163927−124139	—	$64'' \times 42''$
				J1733−1304	J170934−172853	—	$84'' \times 41''$
				J1924+3329	J190255+315942	3C 395	$52'' \times 44''$
13:44:31	14:44:23	3C 138	J0319+4130	J0238+1636	J022915+085125	—	$52'' \times 37''$
				J2202+4216	J220205+394913	—	$56'' \times 39''$
					J220927+415834	—	$57'' \times 38''$
					J224412+405715	—	$53'' \times 38''$
					J224549+394122	3C 452	$51'' \times 38''$
				J2340+1333	J234033+133300	4C +13.88	$49'' \times 41''$
					J235728+230226	4C +22.65	$46'' \times 38''$
22:28:10	23:57:59	3C 286	J0713+4349	J0837−1951	J083930−240723	—	$102'' \times 41''$
					J084600−261054	—	$109'' \times 40''$
					J084701−233701	—	$101'' \times 42''$
				J0921−2618	J090015−281758	—	$116'' \times 40''$
					J091145−301305	—	$127'' \times 39''$
					J092410−290606	—	$114'' \times 38''$
					J093349−302700	—	$124'' \times 38''$
				J1018−3144	J093544−322845	—	$139'' \times 38''$
					J094750−371528	—	$177'' \times 36''$
					J094808−344010	—	$148'' \times 36''$
				J1120+1420	J111857+123442	4C +12.39	$50'' \times 40''$

[a] From channel maps at 1.5 GHz

3.2 Observations and Data Reduction

3.2.1 New Observations and Calibration

We selected the 23 target sources from the TSS09 catalogue. They have high $|\mathrm{RM}_{\mathrm{TSS09}}| \gtrsim 300\,\mathrm{rad\,m^{-2}}$ and are situated away from the Galactic plane ($|b| > 10°$)[1]. In this region, the Galactic FD (or RM) contributions are less significant, with ≈ 99 per cent of the TSS09 sources with $|\mathrm{RM}_{\mathrm{TSS09}}| < 150\,\mathrm{rad\,m^{-2}}$. The peculiar population we selected, with high $|\mathrm{RM}_{\mathrm{TSS09}}|$, could be statistical *outliers* from the generally low $|\mathrm{RM}_{\mathrm{TSS09}}|$ population, either because they have high intrinsic FD (or RM) values or they are positioned along special lines of sight with high foreground FD (or RM) contributions. On the other hand, our target sources could also be *out-liars* with erroneous $\mathrm{RM}_{\mathrm{TSS09}}$ values, deviating from the true RM by multiples of $\pm 652.9\,\mathrm{rad\,m^{-2}}$ due to $n\pi$-ambiguity (TSS09) and causing them to stand out from the majority. However, we note that our selection criteria does not allow us to study sources with high true |RM| having low reported $|\mathrm{RM}_{\mathrm{TSS09}}|$ due to $n\pi$-ambiguity, and thus our study here only focuses on cases where sources with low true |RM| are "boosted" to high $|\mathrm{RM}_{\mathrm{TSS09}}|$ due to $n\pi$-ambiguity. We further selected only bright sources with NVSS total intensities larger than 100 mJy to ensure that sufficient signal-to-noise ratio could be achieved.

Our new broadband data were acquired using the Jansky VLA in L-band (1–2 GHz)

[1] Except for J234033+133300, which has $\mathrm{RM}_{\mathrm{TSS09}} = +56.7 \pm 6.3\,\mathrm{rad\,m^{-2}}$. This source was also observed because it was thought to have a high emission measure (EM; $\sim 140\,\mathrm{cm^{-6}\,pc}$) but low |RM|, which could be another manifestation of $n\pi$-ambiguity. However, upon close examination after the observation was conducted, we found that the EM along this sightline is actually $\lesssim 10\,\mathrm{cm^{-6}\,pc}$, thus disqualifying this source as an $n\pi$-ambiguity candidate. This source will not be included in the statistical analysis on $n\pi$-ambiguity in this work. However, we later found that this source is unpolarised, which leads to implications on the residual off-axis polarisation leakage of TSS09 (see Chapter 4).

in D array configuration. The observations were carried out on 2014 July 03 in three observing blocks, and are summarised in Table 3.1 where the observing time, calibrators, target sources, and angular resolutions are listed. For each of the target sources, the integration time is about 3–4 minutes. We used the Common Astronomy Software Applications (`CASA`) package (version 4.4.0; McMullin et al. 2007) for all of the data reduction procedures.

The three measurement sets were calibrated independently. Hanning smoothing is first applied to all the visibilities in frequency domain to remove the Gibbs phenomenon, and the antenna position calibration is applied to the data set. Then, we flagged out times when the antennas were not performing as intended or when prominent radio frequency interference (RFI) was seen. Next, we determined the delay, bandpass, and gain solutions using the flux and/or phase calibrators, with the absolute flux densities following the Perley & Butler (2013a) scales. The PA calibration was done by using the previously determined PAs of the flux calibrators 3C 286 and 3C 138 (Perley & Butler 2013b), while the on-axis instrumental leakage was corrected for by observing standard unpolarised leakage calibrators (see Table 3.1). Finally, we applied one round of phase self calibration to all our target sources to further improve the gain solution.

3.2.2 Full L-Band Images

With the calibrated visibilities, we formed a series of Stokes I, Q, and U images for each target source at different frequencies across L-band, combining 4 MHz of visibility data to form the images for each step in the frequency axis. The Clark deconvolution algorithm in `CASA` task `CLEAN` was adopted, with Briggs visibilities weighting of `robust` = 0 (Briggs 1995). We did not further smooth the resulting images, as it would only be necessary if we directly combine images at different frequencies. We list the angular resolution at 1.5 GHz of each pointing in Table 3.1. At the spatial resolution of our observations, our targets can be divided into three morphology classes — single (unresolved), double (resolved into two unresolved components), and extended. The typical root-mean-square (rms) noise of each 4 MHz image is about 1.6 mJy beam^{-1} in Stokes I, and 1.0 mJy beam^{-1} in Stokes Q and U.

We measured the Stokes I, Q, and U values of our target sources per frequency step. We used different methods depending on whether the sources are spatially resolved with our observational setup. For spatial singles and doubles, we used the `CASA` task `IMFIT` to extract the flux densities and their uncertainties. The full-width at half-maximum (FWHM) of the Gaussian components are fixed as that of the synthesised beam at each frequency step, and the fitted source locations in Stokes I are also used for Stokes Q and U. The positions of the individual components of the five double sources in our sample are listed in Table 3.2. For extended sources (J094750−371528 and J224549+394122), we used the multi-frequency synthesis (MFS) algorithm with `nterms` = 2 (which incorporates the spectral indices of the sources) to form Stokes I images using the entire L-band for each of the sources, from which 6σ contours in Stokes I enclosing the target sources are defined. The `CASA` task `IMSTAT` is then used to integrate the Stokes I, Q, and U flux densities within the contour for each channel

Table 3.2: Positions of Individual Components of the Spatial Doubles

Source (NVSS)	Right Ascension (J2000; h m s)	Declination (J2000; ° ′ ″)
J091145−301305		
··· a	09 11 42.47 ± 0.04	−30 13 19.26 ± 1.45
··· b	09 11 46.33 ± 0.02	−30 12 58.63 ± 0.74
J092410−290606		
··· a	09 24 10.09 ± 0.02	−29 05 45.36 ± 0.79
··· b	09 24 11.44 ± 0.02	−29 06 26.66 ± 0.75
J093544−322845		
··· a	09 35 43.98 ± 0.02	−32 28 48.51 ± 0.65
··· b	09 35 43.79 ± 0.02	−32 29 40.03 ± 0.60
J162706−091705		
··· a	16 27 04.53 ± 0.02	−09 16 55.99 ± 0.64
··· b	16 27 06.78 ± 0.01	−09 17 06.50 ± 0.20
J163927−124139		
··· a	16 39 27.09 ± 0.01	−12 41 26.41 ± 0.15
··· b	16 39 28.20 ± 0.01	−12 42 09.07 ± 0.27

map. We note that using integrated flux densities discards all the spatial information we have of these two sources, and may increase Faraday complexity and/or cause beam depolarisation. A detailed spatial analysis of them is included in Appendix B.1. The radio spectra of our targets are reported in Chapter 4, in which we address the potential Stokes I and RM time variabilities of our sample.

3.3 Broadband Spectro-polarimetric Analysis

3.3.1 Rotation Measure Synthesis

Using the extracted Stokes I, Q, and U values for every 4 MHz channel map (Chapter 3.2.2), we performed RM-Synthesis (Brentjens & de Bruyn 2005) on all our target sources. For double sources, each of the spatial components are analysed independently. We used the `python`-based RM-Synthesis code, `pyrmsynth`[2], to perform this analysis, including RM-Clean algorithm (e.g. Heald et al. 2009) to deconvolve the Faraday spectra. The $q = Q/I$ and $u = U/I$ values are used as the inputs, and therefore the resulting complex Faraday spectra (sometimes referred to as Faraday dispersion functions in the literature) are in units of polarisation fraction (p) per Rotation Measure Transfer Function (RMTF). With our observational setup, the resolution of Faraday spectrum, maximum detectable scale, and maximum detectable FD are (equations 61–

[2] Available on `http://www.github.com/mrbell/pyrmsynth`.

Table 3.3: Results of RM-Synthesis on Broadband Jansky VLA Data

Source (NVSS)	p (%)	PA_0 (°)	ϕ (rad m^{-2})	$\overline{\phi}$ (rad m^{-2})	$\mathrm{RM}_{\mathrm{TSS09}}$ (rad m^{-2})	$\lvert\overline{\phi} - \mathrm{RM}_{\mathrm{TSS09}}\rvert$ (rad m^{-2})	$\delta\phi$ (rad m^{-2})	$\delta\phi_0$ (rad m^{-2})
Outliers (Reliable $\mathrm{RM}_{\mathrm{TSS09}}$)								
J083930−240723	$4.54^{+0.06}_{-0.05}$	$+5.8^{+2.2}_{-2.2}$	$+325.9 \pm 1.0$	$+325.9 \pm 1.0$	$+345.2 \pm 10.5$	19.3	128.0	128.0
J084701−233701	$3.12^{+0.10}_{-0.10}$	$-88.5^{+4.4}_{-4.4}$	$+384.8 \pm 2.0$	$+384.8 \pm 2.0$	$+429.5 \pm 15.3$	44.7	128.0	128.0
J090015−281758	$4.44^{+0.02}_{-0.02}$	$+6.8^{+0.5}_{-0.5}$	$+352.1 \pm 0.2$	$+352.1 \pm 0.2$	$+320.6 \pm 4.2$	31.5	76.0	76.0
J092410−290606**	—	—	—	$+527.6^{+0.3}_{-0.3}$	$+472.9 \pm 6.2$	54.7	—	76.0
··· a	$8.23^{+0.06}_{-0.06}$	$+60.1^{+0.6}_{-0.6}$	$+526.1 \pm 0.3$	—	—	—	76.0	—
··· b	$3.80^{+0.09}_{-0.09}$	$+74.8^{+1.9}_{-1.9}$	$+530.8 \pm 0.8$	—	—	—	76.0	—
J093349−302700	$6.03^{+0.08}_{-0.08}$	$-33.6^{+1.7}_{-1.7}$	$+341.6 \pm 0.8$	$+341.6 \pm 0.8$	$+313.4 \pm 7.7$	28.2	112.0	112.0
J093544−322845**	—	—	—	$+390.9^{+0.3}_{-0.3}$	$+368.1 \pm 9.3$	22.8	—	76.0
··· a	$7.68^{+0.07}_{-0.07}$	$-50.2^{+0.7}_{-0.7}$	$+393.8 \pm 0.3$	—	—	—	76.0	—
··· b	$5.16^{+0.08}_{-0.08}$	$+74.2^{+1.3}_{-1.3}$	$+387.2 \pm 0.6$	—	—	—	76.0	—
J094750−371528⊙‡	$3.90^{+0.25}_{-0.24}$	$-8.7^{+5.2}_{-5.2}$	$+328.8 \pm 2.2$	$+328.8 \pm 2.2$	$+311.0 \pm 7.2$	17.8	113.6 ± 0.4	77.0
J162706−091705**	—	—	—	-327.8 ± 0.7	-297.2 ± 12.8	30.6	—	104.0
··· a	—	—	—	—	—	—	—	—
··· b	$11.32^{+0.16}_{-0.15}$	$+4.4^{+1.4}_{-1.4}$	-327.8 ± 0.7	—	—	—	104.0	—
J163927−124139**	—	—	—	$-331.4^{+0.3}_{-0.3}$	-313.5 ± 3.6	17.9	—	104.0
··· a	$9.11^{+0.06}_{-0.06}$	$+32.1^{+0.8}_{-0.8}$	-328.4 ± 0.3	—	—	—	104.0	—
··· b	$10.10^{+0.07}_{-0.07}$	$+68.6^{+0.8}_{-0.8}$	-336.0 ± 0.4	—	—	—	104.0	—
J220205+394913	$8.39^{+0.10}_{-0.10}$	$+59.1^{+1.0}_{-1.0}$	-367.2 ± 0.4	-367.2 ± 0.4	-349.1 ± 6.6	18.1	76.0	76.0
J220927+415834	$6.92^{+0.04}_{-0.04}$	$-12.5^{+0.5}_{-0.5}$	-338.1 ± 0.2	-338.1 ± 0.2	-336.0 ± 5.4	2.1	76.0	76.0
Out-*liars* ($n\pi$-ambiguity)								
J022915+085125!‡	—	—	—	$+13.6 \pm 1.0$	$+521.2 \pm 8.0$	507.6	—	124.0
··· PC 1	$0.27^{+0.03}_{-0.03}$	$+63.2^{+12.9}_{-13.1}$	-246.8 ± 5.9	—	—	—	74.7 ± 4.8	—
··· PC 2	$4.05^{+0.07}_{-0.07}$	$-24.2^{+2.2}_{-2.2}$	$+13.6 \pm 1.0$	—	—	—	187.3 ± 0.2	—
··· PC 3	$0.27^{+0.03}_{-0.03}$	$+69.7^{+12.9}_{-12.8}$	$+272.8 \pm 5.8$	—	—	—	72.6 ± 4.4	—

×Unpolarised sources
?Special case compared to TSS09 catalogue (see Chapter 3.4.1.8)
**Double point sources
⊙Extended sources
!Polarised components (PCs) 1 and 3 may be artefacts corresponding to RMTF sidelobes (see text)
‡Faraday complex from RM-Synthesis

Table 3.3: (Continued) Results of RM-Synthesis on Broadband Jansky VLA Data

Source (NVSS)	p (%)	PA_0 (°)	ϕ (rad m^{-2})	$\overline{\phi}$ (rad m^{-2})	$\mathrm{RM}_{\mathrm{TSS09}}$ (rad m^{-2})	$\lvert\overline{\phi} - \mathrm{RM}_{\mathrm{TSS09}}\rvert$ (rad m^{-2})	$\delta\phi$ (rad m^{-2})	$\delta\phi_0$ (rad m^{-2})
Out-*liars* ($n\pi$-ambiguity)								
J091145−301305**	—	—	—	$+246.9^{+0.3}_{-0.3}$	-426.1 ± 3.5	673.0	—	76.0
··· a	$8.68^{+0.21}_{-0.20}$	$-27.5^{+2.1}_{-2.1}$	$+245.0 \pm 0.9$	—	—	—	76.0	—
··· b	$17.15^{+0.11}_{-0.11}$	$-15.3^{+0.6}_{-0.6}$	$+247.4 \pm 0.3$	—	—	—	76.0	—
J094808−344010‡	—	—	—	$+382.7^{+2.6}_{-2.4}$	-327.9 ± 10.6	710.6	—	76.0
··· PC 1	$4.20^{+0.08}_{-0.08}$	$+53.8^{+2.0}_{-2.0}$	$+364.7 \pm 0.9$	—	—	—	76.0	—
··· PC 2	$0.73^{+0.11}_{-0.10}$	$-71.6^{+10.7}_{-11.0}$	$+486.0 \pm 5.2$	—	—	—	76.0	—
J111857+123442‡	—	—	—	$+79.4^{+2.6}_{-2.8}$	-465.4 ± 5.7	544.8	—	76.0
··· PC 1	$0.15^{+0.02}_{-0.02}$	$-59.8^{+10.3}_{-10.8}$	-2.5 ± 5.2	—	—	—	76.0	—
··· PC 2	$0.63^{+0.02}_{-0.02}$	$+51.7^{+2.5}_{-2.5}$	$+98.8 \pm 1.2$	—	—	—	76.0	—
J170934−172853‡	—	—	—	$+106.2^{+1.8}_{-1.9}$	-490.0 ± 12.7	596.2	—	76.0
··· PC 1	$0.43^{+0.06}_{-0.05}$	$-3.6^{+10.1}_{-10.2}$	-26.5 ± 4.8	—	—	—	76.0	—
··· PC 2	$3.86^{+0.05}_{-0.05}$	$-37.9^{+1.1}_{-1.1}$	$+120.9 \pm 0.5$	—	—	—	76.0	—
J190255+315942‡	—	—	—	$+142.2^{+1.1}_{-1.1}$	-424.3 ± 2.6	566.5	—	76.0
··· PC 1	$1.34^{+0.05}_{-0.05}$	$-25.2^{+3.0}_{-3.0}$	$+84.9 \pm 1.4$	—	—	—	76.0	—
··· PC 2	$2.45^{+0.05}_{-0.05}$	$+17.4^{+1.6}_{-1.6}$	$+173.4 \pm 0.8$	—	—	—	76.0	—
J224412+405715	$3.55^{+0.05}_{-0.05}$	$+84.5^{+1.3}_{-1.3}$	-320.4 ± 0.6	-320.4 ± 0.6	$+345.8 \pm 14.4$	666.2	76.0	76.0
J224549+394122⊙‡	—	—	—	$-278.6^{+0.8}_{-1.0}$	$+373.3 \pm 6.4$	651.9	—	76.0
··· PC 1	$0.20^{+0.04}_{-0.03}$	$+72.3^{+15.9}_{-15.9}$	-407.3 ± 6.3	—	—	—	110.9 ± 9.6	—
··· PC 2	$5.37^{+0.02}_{-0.02}$	$+4.5^{+0.4}_{-0.4}$	-273.8 ± 0.2	—	—	—	80.5 ± 0.0	—
J235728+230226	$0.20^{+0.02}_{-0.02}$	$+46.5^{+13.6}_{-13.6}$	$+42.3 \pm 6.1$	$+42.3 \pm 6.1$	-556.7 ± 13.8	599.0	124.0	124.0
Others								
J084600−261054×	—	—	—	—	$+481.0 \pm 11.4$	—	—	128.0
J154936+183500?‡	—	—	—	$-119.3^{+7.5}_{-7.4}$	-426.8 ± 14.6	307.5	—	76.0
··· PC 1	$0.50^{+0.03}_{-0.03}$	$+23.2^{+4.9}_{-4.9}$	-315.3 ± 2.1	—	—	—	87.9 ± 0.3	—
··· PC 2	$0.31^{+0.03}_{-0.03}$	$+77.1^{+8.3}_{-8.3}$	-31.8 ± 3.5	—	—	—	90.8 ± 3.1	—
··· PC 3	$0.35^{+0.03}_{-0.03}$	$-48.2^{+6.6}_{-6.6}$	$+81.3 \pm 2.8$	—	—	—	84.4 ± 1.7	—
J234033+133300×	—	—	—	—	$+56.7 \pm 6.3$	—	—	124.0

×Unpolarised sources
?Special case compared to TSS09 catalogue (see Chapter 3.4.1.8)
**Double point sources
⊙Extended sources
!Polarised components (PCs) 1 and 3 may be artefacts corresponding to RMTF sidelobes (see text)
‡Faraday complex from RM-Synthesis

63 in Brentjens & de Bruyn 2005)

$$\delta\phi_0 \approx \frac{2\sqrt{3}}{\Delta\lambda^2} \approx 76\text{–}128\,\mathrm{rad\,m^{-2}}, \tag{3.4}$$

$$\text{max-scale} \approx \frac{\pi}{\lambda^2_{\mathrm{min}}} \approx 143\,\mathrm{rad\,m^{-2}}, \text{ and} \tag{3.5}$$

$$||\phi_{\mathrm{max}}|| \approx \frac{\sqrt{3}}{\delta\lambda^2} \approx (4\text{–}20) \times 10^3\,\mathrm{rad\,m^{-2}}, \tag{3.6}$$

respectively. The quoted range for $\delta\phi_0$ is due to the slightly different λ^2 coverage for each source as the result of flagging (individual values listed in Table 3.3), and that for $||\phi_{\mathrm{max}}||$ is because of the difference in widths of the 4 MHz channels in λ^2 space across L-band. We adopted a normalised inverse noise variance weighting function of (e.g. Schnitzeler & Lee 2017)

$$W(\lambda^2) \propto \frac{1}{\sigma_q^2(\lambda^2) + \sigma_u^2(\lambda^2)}, \tag{3.7}$$

where σ_q and σ_u are the uncertainties in q and u respectively. The Faraday spectra were formed within $-2000 \leq \phi\ (\mathrm{rad\,m^{-2}}) \leq +2000$ with a step size of $2\,\mathrm{rad\,m^{-2}}$. We first perform trial cleans to determine the rms noise (denoted as σ here) in the source-free FD ranges of $|\phi| \geq 1000\,\mathrm{rad\,m^{-2}}$ from the q_ϕ and u_ϕ Faraday spectra. The final Faraday spectra are cleaned down to 6σ only so as to avoid over-cleaning, which can introduce artefacts to the resulting spectra.

The Faraday spectra amplitudes ($||\mathbf{F}|| = |F_\phi| = \sqrt{q_\phi^2 + u_\phi^2}$) are shown in Figure 3.1. For each amplitude spectrum, we counted the number of peaks higher than 6σ, and then we fitted the spectrum with the corresponding number of Gaussian components plus a y-offset to extract the FD values and widths of the peaks. This 6σ cutoff grants us an insignificant false detection rate of $\lesssim 0.5$ per cent (e.g. George et al. 2012), and a negligible Ricean polarisation bias ($\lesssim 1.5$ per cent; Wardle & Kronberg 1974). If the fitted FWHM ($\delta\phi$) of a peak is within 10 per cent from the theoretical RMTF FWHM value (i.e. $\delta\phi_0$; obtained from `pyrmsynth` output), we re-fit the spectrum with $\delta\phi$ being fixed at $\delta\phi_0$. The uncertainties in FD are obtained by (e.g. Mao et al. 2010; Iacobelli et al. 2013)

$$\frac{\delta\phi}{2 \cdot (S/N)}, \tag{3.8}$$

where S/N is the signal-to-noise ratio of the peak. The FD and $\delta\phi$ of the peaks are then fixed and used to fit the q_ϕ and u_ϕ Faraday spectra to extract the complex polarisation fraction of the polarised components that they correspond to. The obtained values, namely ϕ, $\delta\phi$, and complex polarisation fraction, are then used to calculate p and intrinsic PA ($\mathrm{PA_0}$) of each polarised component. The uncertainties are propagated by Monte Carlo simulations with 10^6 realisations per source, starting from assuming that q, u, ϕ, and $\delta\phi$ obtained from RM-Synthesis above follow Gaussian statistics. We evaluated the 68.3 per cent confidence interval (corresponding to 1σ under normal distribution), which are listed as the asymmetric errors in Table 3.3. Such an error propagation method is needed, since strictly speaking the uncertainties of both p and

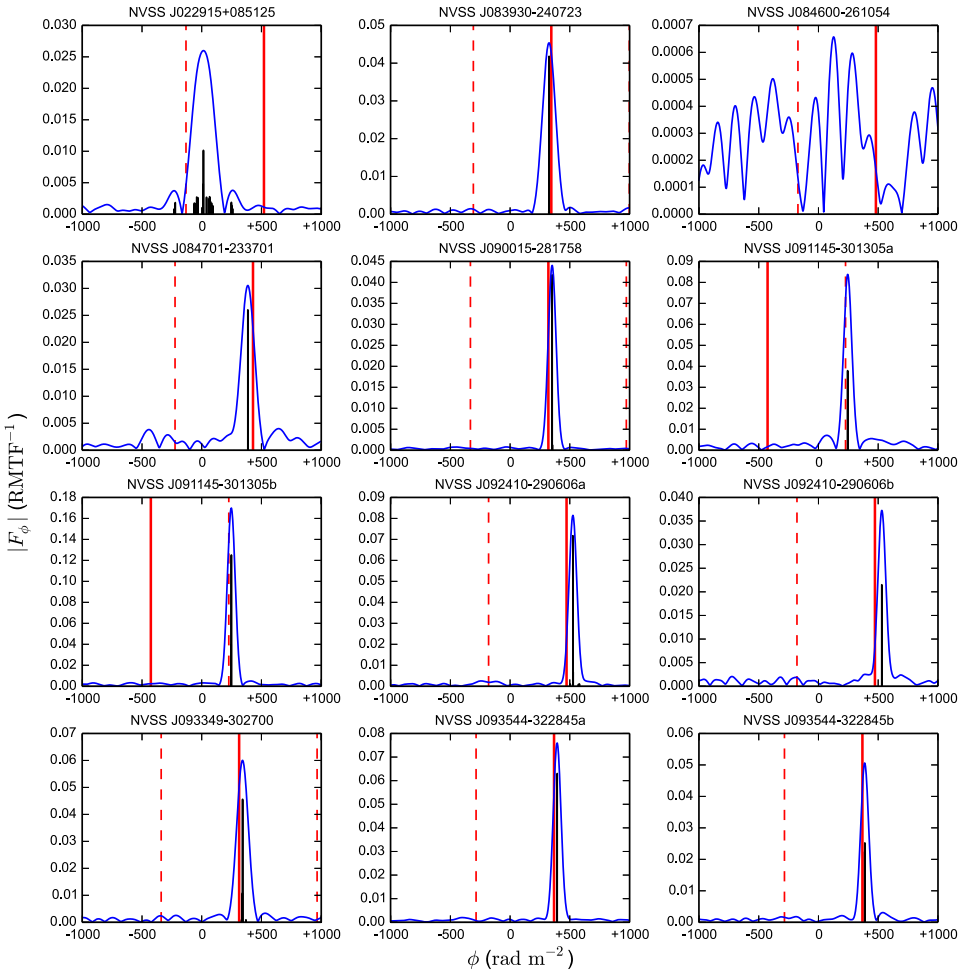

Figure 3.1: Faraday spectra of our target sources. Blue lines show the amplitude of the complex Faraday spectra after deconvolution, with the black bars representing the clean components. The RM values from the NVSS RM catalogue (TSS09) are represented by the red vertical solid lines, while those RM values corresponding to $\pm 1\pi$-ambiguity are indicated by red vertical dashed lines. We only show the spectra within the FD range of -1000 to $+1000\,\mathrm{rad\,m^{-2}}$, as significant polarised components are not found outside of this range.

PA_0 do not follow Gaussian distributions. A caveat to the results here is that the polarisation fraction p is the polarised intensity of the polarised component divided by the total intensity of the entire spatial component. The Ricean polarisation bias is not corrected for because it is insignificant at our signal-to-noise levels (see above).

We also formed Faraday spectra for the leakage calibrators J0319+4130, J0713+4349, and J1407+2827, in order to constrain the remaining instrumental polarisation leakage of our observations. Their spectra are also shown in Figure 3.1, with peak values of 0.003 ± 0.001, 0.019 ± 0.006, and 0.010 ± 0.003 per cent, respectively.

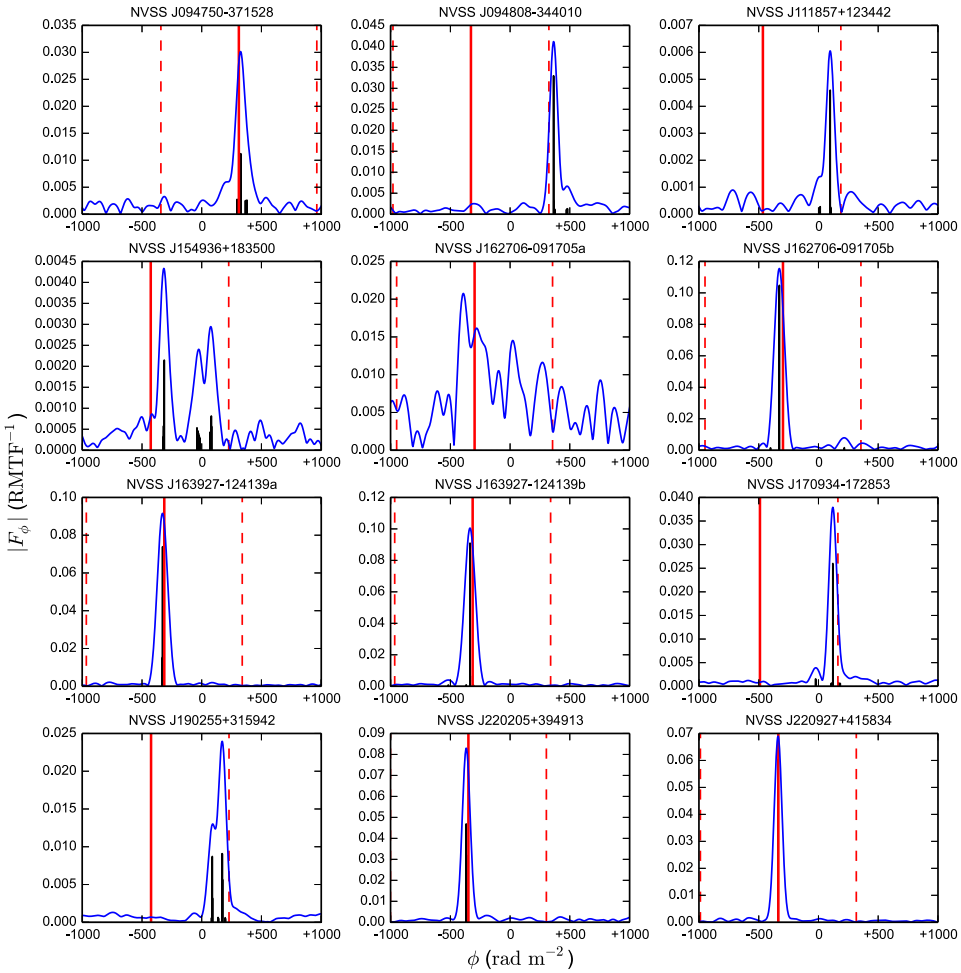

Figure 3.1: (Continued) Faraday spectra of our target sources.

Note that these values could be due to random noise fluctuations leading to polarisation bias (e.g. George et al. 2012) instead of due to residual instrumental polarisation leakage, and are therefore upper limits to the actual remaining leakage levels of our calibrated data. We conclude that the residual polarisation leakage in our data is at < 0.02 per cent level.

One point to note is that for one of our sources, J022915+085125, polarised components (PCs) 1 and 3 are likely artefacts corresponding to the sidelobes of the RMTF (see Table 3.3), most likely because the main (physical) peak is Faraday thick, leading to sub-optimal deconvolution with RM-Clean. The two components are symmetric about the prominent polarised component 2, having the same polarisation fraction of 0.27 per cent, PA_0 and ϕ offsets from component 2 by about 90° and 260 rad m^{-2} respectively, and $\delta\phi \approx 73\,\mathrm{rad\,m^{-2}}$, less than the theoretical value of 124 rad m^{-2}. Upon inspection of the (complex) RMTF of this source, we find that the secondary maxima are offset from the primary by 161 rad m^{-2}, phase offset by 180° (i.e. 90° in PA), and

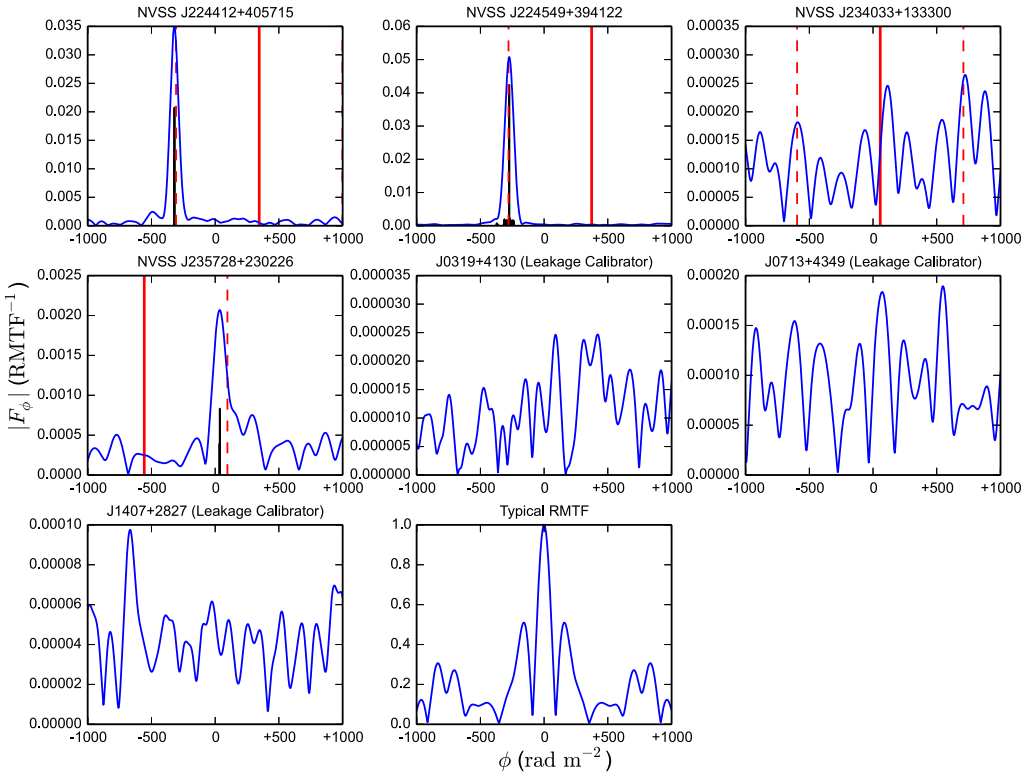

Figure 3.1: (Continued) Faraday spectra of our target sources, as well as that of the leakage calibrators. The typical RMTF of our L-band observations is shown in the last panel.

have FWHM of about 108 rad m^{-2}. We have therefore ignored these two components in the remainder of this Chapter.

For the six sources that can be decomposed into multiple spatial or Faraday components, it is not trivial to directly compare the multiple FD values against the single $\mathrm{RM}_{\mathrm{TSS09}}$ value of each source. Therefore, we define a polarisation-weighted FD as

$$\overline{\phi} = \sum_i \frac{p_i \cdot S_{1.4\,\mathrm{GHz},i} \cdot \phi_i}{\sum_j p_j \cdot S_{1.4\,\mathrm{GHz},j}}, \tag{3.9}$$

where i and j are indices representing the spatial and/or polarised components, and $S_{1.4\,\mathrm{GHz}}$ is the flux density of the corresponding spatial component at 1.4 GHz (listed in Chapter 4). This formulation is a modified version of that from O'Sullivan et al. (2017), where the FDs were weighted by p instead. The uncertainties in $\overline{\phi}$ are again propagated by Monte Carlo simulations as above. We will compare the $\overline{\phi}$ values against the TSS09 RM values to determine whether the source suffers from $n\pi$-ambiguity. The results are listed in Table 3.3.

We find that two of our target sources (J084600−261054 and J234033+133300) are unpolarised (less than the 6σ cutoff levels at 0.07 and 0.06 per cent, respectively),

and therefore are excluded in the subsequent stages of our study in this Chapter[3]. Furthermore, the spatial double J162706−091705 hosts one unpolarised component (a) and a polarised component (b). Out of the remaining 21 sources (five being spatial doubles) with reliable polarisation signals, nine have $\overline{\phi}$ disagreeing with the TSS09 RM values by about $\pm 652.9\,\mathrm{rad\,m^{-2}}$, and 11 have the two sets of values agreeing within $60\,\mathrm{rad\,m^{-2}}$. The only remaining source J154936+183500 is a special case, with $\overline{\phi}$ and $\mathrm{RM_{TSS09}}$ values deviating by $307.5\,\mathrm{rad\,m^{-2}}$ (see Chapter 3.4.1.8 for discussion on this source).

We further performed a per-pixel RM-Synthesis analysis to the extended sources J094750−371528 and J224549+394122 (also known as 3C 452), presented in Appendix B.1. This allows the Faraday complexities of these two sources to be resolved spatially, leading to interesting comparisons with the RM-Synthesis results above and QU-fitting results in Chapter 3.3.2.

3.3.2 Stokes QU-fitting

We complement our RM-Synthesis results in Chapter 3.3.1 with Stokes QU-fitting analysis (e.g. Farnsworth et al. 2011; O'Sullivan et al. 2012). Tests with synthetic data have shown that QU-fitting can perform better than RM-Synthesis for sources composed of two Faraday thin components (Sun et al. 2015). The main difference between these two techniques is that the former is non-parametric, while the latter requires input astrophysical models. These models consist of one or more polarised components added together, which can correspond to discrete astrophysical sources or emitting volumes with different physical parameters within our telescope beam or flux integration region. For our study, we considered the following polarised components (Burn 1966; Sokoloff et al. 1998; O'Sullivan et al. 2012):

1. *Thin:* A purely synchrotron-emitting volume, with Faraday rotation occurring in a foreground screen with a homogeneous magnetic field and thermal electron density. The complex polarisation fraction is given by

$$\mathbf{p}_j(\lambda^2) = p_{0,j} e^{2i(\mathrm{PA}_{0,j} + \phi_j \lambda^2)}. \tag{3.10}$$

2. *Burn slab:* This depicts a volume that is simultaneously synchrotron-emitting and Faraday rotating, with no foreground Faraday rotating screens. The magnetic fields, thermal electron densities, and cosmic rays densities in the slab are all uniform. The complex polarisation fraction is given by

$$\mathbf{p}_j(\lambda^2) = p_{0,j} \frac{\sin(\phi_j \lambda^2)}{\phi_j \lambda^2} e^{2i(\mathrm{PA}_{0,j} + \frac{1}{2}\phi_j \lambda^2)}. \tag{3.11}$$

3. *Burn slab with foreground screen:* This is the same as a Burn slab component, except there is a homogeneous foreground rotating screen giving rise to an extra

[3]We believe this discrepancy with TSS09 in polarisation level is due to the off-axis polarisation leakage in the NVSS data, and we shall investigate this in detail in Chapter 4.

FD of $\phi_{\rm fg}$. The complex polarisation fraction is given by

$$\mathbf{p}_j(\lambda^2) = p_{0,j}\frac{\sin(\phi_j\lambda^2)}{\phi_j\lambda^2}e^{2i[\mathrm{PA}_{0,j}+(\frac{1}{2}\phi_j+\phi_{\rm fg})\lambda^2]}. \tag{3.12}$$

4. *External Faraday dispersion:* In addition to the homogeneous Faraday screen for a thin component, an external turbulent Faraday screen lies in front of the synchrotron-emitting volume. This turbulent screen leads to a dispersion in FD (σ_ϕ) through different lines of sight to the emitting volume (within the telescope beam or the flux integration region), causing depolarisation effects. The complex polarisation fraction is given by

$$\mathbf{p}_j(\lambda^2) = p_{0,j}e^{-2\sigma^2_{\phi,j}\lambda^4}e^{2i(\mathrm{PA}_{0,j}+\phi_j\lambda^2)}. \tag{3.13}$$

5. *Internal Faraday dispersion:* This is similar to the Burn slab above, except that in the simultaneously emitting and Faraday rotating volume there is also a turbulent magnetic field component. The complex polarisation fraction is given by

$$\mathbf{p}_j(\lambda^2) = p_{0,j}e^{2i\mathrm{PA}_{0,j}}\left(\frac{1-e^{i\phi_j\lambda^2-2\sigma^2_{\phi,j}\lambda^4}}{2\sigma^2_{\phi,j}\lambda^4-i\phi_j\lambda^2}\right). \tag{3.14}$$

6. *Internal Faraday dispersion with foreground screen:* This is the same as the internal Faraday dispersion component, but there is a homogeneous foreground rotating screen leading to an extra FD of $\phi_{\rm fg}$. The complex polarisation fraction is given by

$$\mathbf{p}_j(\lambda^2) = p_{0,j}e^{2i(\mathrm{PA}_{0,j}+\phi_{\rm fg}\lambda^2)}\left(\frac{1-e^{i\phi_j\lambda^2-2\sigma^2_{\phi,j}\lambda^4}}{2\sigma^2_{\phi,j}\lambda^4-i\phi_j\lambda^2}\right). \tag{3.15}$$

A caveat of the QU-fitting technique here is that, similar to RM-Synthesis in Chapter 3.3.1, the intrinsic polarisation fraction $p_{0,j}$ obtained from this analysis is the polarised intensity of the component j divided by the total intensity of the entire spatial component, since this analysis does not separate the total intensity into corresponding polarised components.

We deployed 10 different models to fit the observed q and u values of our target sources: single thin (1T), double thin (2T), triple thin (3T), single Burn slab (1B), double Burn slab (2B), single Burn slab with foreground screen (1B+fg), double Burn slab with foreground screen (2B+fg), single external Faraday dispersion (1Ed), single internal Faraday dispersion (1Id), and single internal Faraday dispersion with foreground screen (1Id+fg). The complex polarisation fraction of the models are constructed by adding together that of the constituent polarised components [$\mathbf{p}(\lambda^2) = \sum_j \mathbf{p}_j(\lambda^2)$]. In other words, the polarised components of each model are assumed to be spatially distributed perpendicular to the line of sight. For the double Burn slab with foreground screen model, both of the Burn slab components are subjected to the same foreground FD, instead of having individual $\phi_{\rm fg}$ values. The best-fit parameters and

Table 3.4: Results of QU-fitting on the New Broadband Jansky VLA Data

Source (NVSS)	Faraday Model	ϕ (rad m^{-2})	p (%)	PA$_0$ (°)	$\phi_{\rm fg}$ (rad m^{-2})	σ_ϕ (rad m^{-2})	$\chi^2_{\rm red}$	$\Delta{\rm PI}/\overline{\rm PI}^a$ (%)
Outliers (Reliable RM$_{\rm TSS09}$)								
J083930−240723	1T	$+325.9 \pm 0.7$	4.55 ± 0.05	$+4.6 \pm 1.5$	—	—	1.7	+4.5
J084701−233701	1T	$+385.5 \pm 1.5$	3.03 ± 0.08	$+87.8 \pm 3.5$	—	—	2.1	+1.2
J090015−281758	1T	$+352.0 \pm 0.3$	4.42 ± 0.02	$+6.9 \pm 0.6$	—	—	2.5	+3.5
J092410−290606a	2T	$+526.3 \pm 0.7$	8.22 ± 0.08	$+60.7 \pm 1.8$	—	—	1.5	+7.1
		$+582.9 \pm 12.2$	0.51 ± 0.08	$+69.4 \pm 30.1$	—	—	—	—
J092410−290606b	1Ed	$+530.6 \pm 0.6$	4.13 ± 0.15	$+75.3 \pm 1.4$	—	6.2 ± 0.9	1.2	+1.3
J093349−302700	1B+fg	$+24.9 \pm 1.5$	7.01 ± 0.15	-32.9 ± 1.1	$+328.8 \pm 1.0$	—	2.7	+0.1
J093544−322845a	1T	$+393.5 \pm 0.4$	7.61 ± 0.07	-49.5 ± 1.0	—	—	2.4	+3.8
J093544−322845b	1T	$+387.4 \pm 0.6$	5.07 ± 0.06	$+74.0 \pm 1.3$	—	—	2.7	+4.7
J094750−371528$^\odot$	1B+fg	$+50.3 \pm 1.5$	6.60 ± 0.31	-8.6 ± 3.6	$+303.7 \pm 2.0$	—	1.5	−27.4
J162706−091705b	2T	-330.4 ± 1.7	12.38 ± 0.52	$+8.1 \pm 3.4$	—	—	1.1	+10.9
		-376.2 ± 11.5	1.58 ± 0.52	-10.8 ± 21.3	—	—	—	—
J163927−124139a	1T	-328.3 ± 0.2	9.16 ± 0.04	$+31.8 \pm 0.5$	—	—	1.5	+4.1
J163927−124139b	1B+fg	$+16.1 \pm 1.3$	10.78 ± 0.14	$+68.3 \pm 0.6$	-343.8 ± 0.7	—	1.1	+2.3
J220205+394913	1T	-367.3 ± 0.4	8.30 ± 0.07	$+59.2 \pm 1.1$	—	—	1.6	+5.7
J220927+415834	1T	-338.3 ± 0.2	6.88 ± 0.04	-12.2 ± 0.5	—	—	0.9	+4.8
Out-*liars* ($n\pi$-ambiguity)								
J022915+085125	2T	$+70.3 \pm 0.7$	2.58 ± 0.03	$+44.0 \pm 1.5$	—	—	1.8	−191.5
		-44.2 ± 0.7	2.57 ± 0.03	$+89.8 \pm 1.5$	—	—	—	—
J091145−301305a	1T	$+244.8 \pm 1.0$	8.35 ± 0.17	-26.9 ± 2.2	—	—	1.9	+5.3
J091145−301305b	1T	$+247.5 \pm 0.3$	17.02 ± 0.09	-15.5 ± 0.6	—	—	2.3	+4.3
J094808−344010	2T	$+365.9 \pm 1.0$	4.30 ± 0.07	$+51.3 \pm 2.1$	—	—	2.8	−1.4
		$+466.4 \pm 5.0$	0.84 ± 0.07	-25.8 ± 10.9	—	—	—	—
J111857+123442	2T	$+99.4 \pm 1.7$	0.66 ± 0.01	$+49.7 \pm 3.7$	—	—	3.7	−4.9
		$+11.2 \pm 6.1$	0.20 ± 0.01	$+89.8 \pm 13.1$	—	—	—	—
J170934−172853	2B+fg	$+21.4 \pm 1.1$	3.82 ± 0.06	-31.6 ± 2.2	$+107.5 \pm 0.6$	—	1.6	+0.4
		-91.3 ± 4.3	2.46 ± 0.18	$+32.4 \pm 7.8$	$+107.5 \pm 0.6$	—	—	—
J190255+315942	2T	$+168.0 \pm 0.5$	2.39 ± 0.02	$+30.1 \pm 1.1$	—	—	6.5	+2.6
		$+96.5 \pm 0.9$	1.27 ± 0.02	-51.7 ± 2.2	—	—	—	—
J224412+405715	1Ed	-320.8 ± 0.5	3.86 ± 0.08	$+85.3 \pm 1.0$	—	5.7 ± 0.5	1.4	−2.8
J224549+394122$^\odot$	1Id+fg	-19.4 ± 4.4	7.40 ± 0.04	$+7.2 \pm 0.5$	-270.7 ± 0.8	13.9 ± 0.3	3.8	−2.7
J235728+230226	2T	$+36.0 \pm 7.6$	0.22 ± 0.02	$+54.3 \pm 17.1$	—	—	1.4	+18.5
		$+118.4 \pm 14.8$	0.11 ± 0.02	-68.9 ± 33.8	—	—	—	—
Others								
J084600−261054$^\times$	—	—	—	—	—	—	—	—
J154936+183500$^?$	3T	-318.4 ± 1.8	0.42 ± 0.02	$+30.1 \pm 4.3$	—	—	2.0	−30.9
		$+70.3 \pm 3.0$	0.31 ± 0.02	-27.3 ± 7.1	—	—	—	—
		-12.0 ± 4.2	0.23 ± 0.02	$+34.8 \pm 9.7$	—	—	—	—
J234033+133300$^\times$	—	—	—	—	—	—	—	—

NOTE — Key to the polarised components: T: Thin; B: Burn slab; B+fg: Burn slab with foreground screen; Ed: External Faraday dispersion; Id: Internal Faraday dispersion; Id+fg: Internal Faraday dispersion with foreground screen

[a] $\Delta{\rm PI} = {\rm PI}_1 - {\rm PI}_2$ and $\overline{\rm PI} = ({\rm PI}_1 + {\rm PI}_2)/2$, where PI$_1$ and PI$_2$ are the predicted polarised intensities at the two NVSS IFs according to the best-fit model and fitted $\alpha_{\rm L}$ (reported in Chapter 4), without taking bandwidth depolarisation into account

$^\times$Unpolarised sources

$^?$Special case compared to TSS09 catalogue (see Chapter 3.4.1.8)

$^\odot$Extended sources

their uncertainties of each of the models for each target source are obtained, along with the reduced chi squared values ($\chi^2_{\rm red}$) and the Bayesian information criterion (BIC; e.g. O'Sullivan et al. 2012; Schnitzeler 2018). We rejected models where the $p_{0,j}$ and/or $\sigma_{\phi,j}$ values are less than two times of the uncertainties. The remaining models for each source are ranked according to the BIC values (with a lower value signifying a better model), and the best for each source is listed in Table 3.4 and plotted in Figure B.3 in Appendix B.3.

3.4 Discussion

3.4.1 The $n\pi$-ambiguity in the NVSS RM Catalogue

In Chapter 3.3.1, we compared our $\overline{\phi}$ values from RM-Synthesis performed on the new broadband data with narrowband RMs from the NVSS RM catalogue (TSS09).

Nine out of 21 of our polarised target sources (43 per cent) have $\overline{\phi}$ values deviating by approximately $\pm 652.9\,\mathrm{rad\,m^{-2}}$ from the corresponding $\mathrm{RM_{TSS09}}$. The discrepancy is almost certainly due to $n\pi$-ambiguity in the TSS09 catalogue. In an attempt to unveil the cause(s) and possible diagnostic(s) of this, we divided our sources into the two classes — out-*liars* and outliers — and compared select observed quantities. Specifically, we investigated the distributions of spectral index from our L-band observations (α_L; reported in Chapter 4), NVSS flux density (S_NVSS), TSS09 polarised intensity ($\mathrm{PI_{TSS09}}$), TSS09 polarisation fraction (p_TSS09), $\mathrm{RM_{TSS09}}$, $\overline{\phi}$, $|\mathrm{RM_{TSS09}} - \mathrm{RM_{3^\circ}}|$, and $|\mathrm{RM_{TSS09}} - \mathrm{RM_{3^\circ}}|/\sigma_{3^\circ}$, with $\mathrm{RM_{3^\circ}}$ and σ_{3° defined below. For each parameter, we performed two-sample Kolmogorov–Smirnov test (KS-test) with the null hypothesis being that the two samples are drawn from the same population. The above parameters are plotted in Figure 3.2, with their corresponding KS-test p-values also reported. We adopted the standard p-value cutoff of 0.05 (a larger p-value favours the null hypothesis), and concluded that the two populations have different distributions in α_L, p_TSS09, $|\mathrm{RM_{TSS09}} - \mathrm{RM_{3^\circ}}|$, and $|\mathrm{RM_{TSS09}} - \mathrm{RM_{3^\circ}}|/\sigma_{3^\circ}$, which we will discuss in detail below. On the other hand, our KS-test results suggest that the two classes of sources likely originate from the same population in S_NVSS, $\mathrm{PI_{TSS09}}$, $\mathrm{RM_{TSS09}}$, and $\overline{\phi}$, with p-values of 0.168, 0.471, 0.058, and 0.085, respectively. However, note that given this small sample size (nine and 11 in the two classes), we cannot rule out the possibility that our statistical analysis here could be biased by random statistical anomalies. Below, we will also explore the effects of FD ranges and Faraday complexities (Table 3.5) on $n\pi$-ambiguity in TSS09 catalogue, and investigate the special case J154936+183500, which has a difference between $\overline{\phi}$ and $\mathrm{RM_{TSS09}}$ consistent with neither the outlier nor the out-*liar* cases.

3.4.1.1 The TSS09 $n\pi$-ambiguity Rejection Algorithm

Before looking into the dependence of $n\pi$-ambiguity on various parameters, we review the algorithm devised by TSS09 to minimise $n\pi$-ambiguity in their catalogue. This algorithm picks the most probable RM value for each source based on the following three constraints. First, they assumed that at most only a single PA wrap can occur between the two NVSS IFs. This imposes a limit of $|\mathrm{RM_{TSS09}}| \leq 1306\,\mathrm{rad\,m^{-2}}$ for all sources. Second, they introduced the parameter

$$R_0 = \frac{\mathrm{PI_1} + \mathrm{PI_2}}{2\mathrm{PI}_c}, \tag{3.16}$$

where $\mathrm{PI_1}$, $\mathrm{PI_2}$, and PI_c are the polarised intensities in NVSS IF1, IF2, and combined band, respectively. Since the measured PI is a function of the source |RM| due to bandwidth depolarisation in the NVSS observational setup, the parameter R_0 in turn is also a function of |RM| (Figure 3.3). TSS09 compared the observed R_0 of each source with the predicted R_0 values at the few possible RM values, with a likelihood assigned to each possible RM. This means TSS09 assumed that the differences among $\mathrm{PI_1}$, $\mathrm{PI_2}$, and PI_c are only due to bandwidth depolarisation, but not caused by other effects such as spectral indices and Faraday complexities. Lastly, they rejected candidate RM values

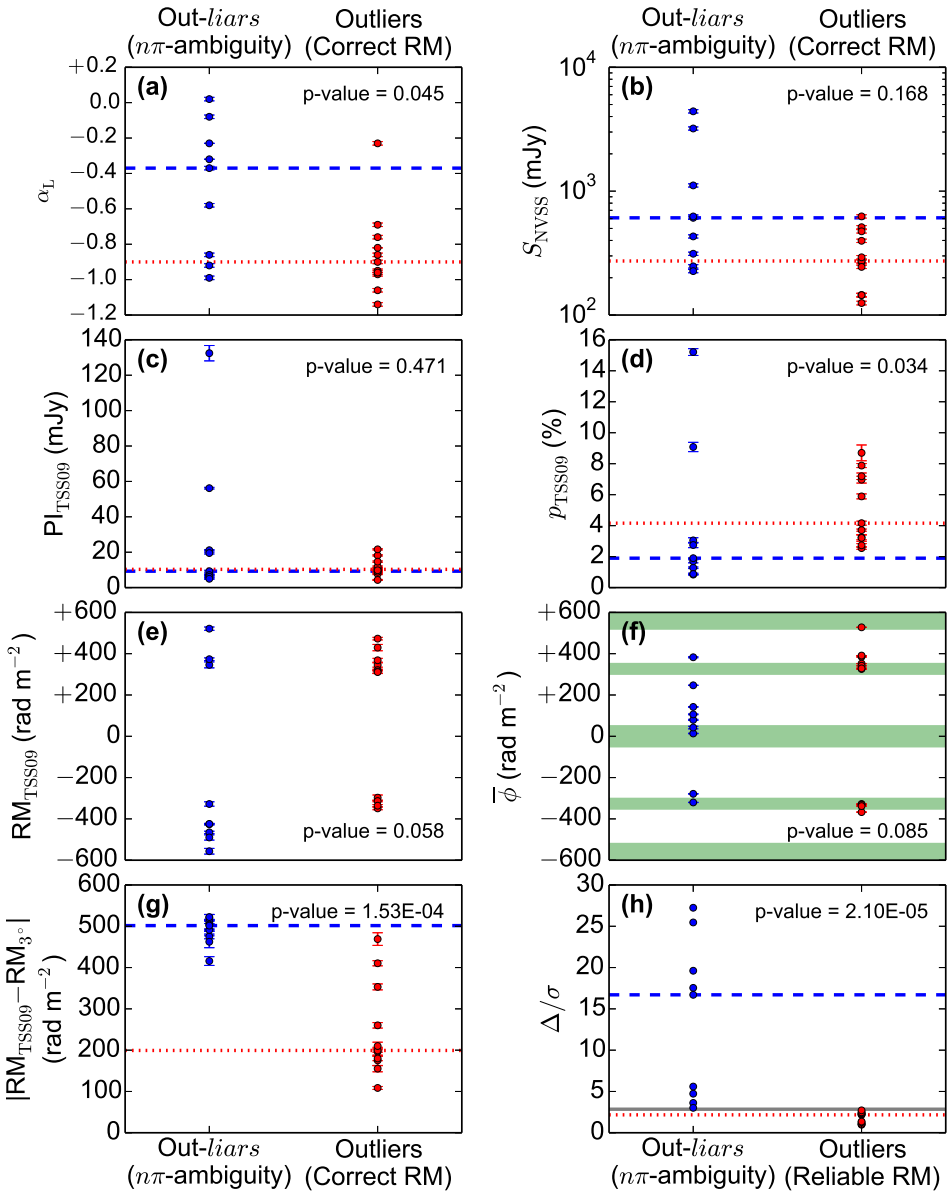

Figure 3.2: Select parameters of our 20 target sources separated into out-*liars* (left; in blue) and outliers (right; in red). The p-value from two-sample KS-test is reported in each panel. In relevant cases, the medians of the two populations are plotted as blue dashed (for out-*liars*) and red dotted (for outliers) lines. In panel (f), the areas highlighted in green corresponds to the |RM| ranges of < 50, > 520, and $\approx 326.5\,\mathrm{rad\,m^{-2}}$, within which the R_0 parameter has limited reliability (TSS09). The grey solid line in panel (h) indicates the cutoff level at 2.85 (see text).

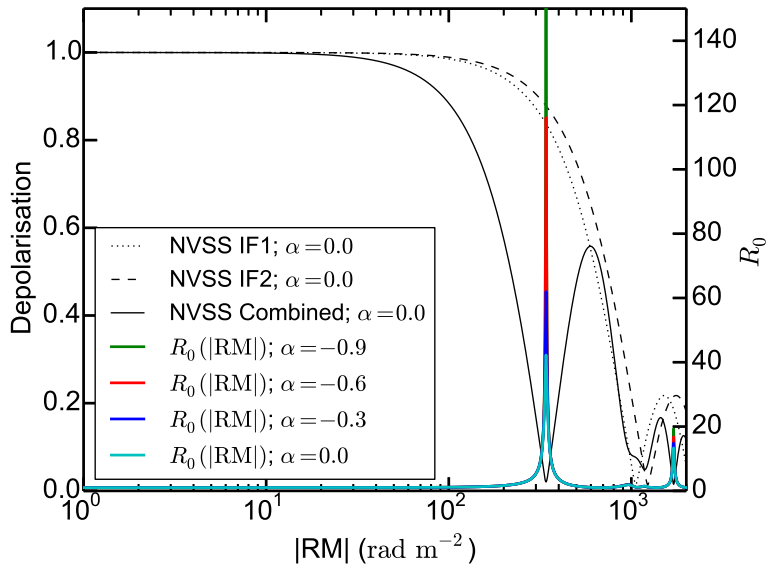

Figure 3.3: Bandwidth depolarisation and $R_0 = (\mathrm{PI}_1 + \mathrm{PI}_2)/2\mathrm{PI}_c$ of the NVSS observational setup, assuming a Faraday simple source with constant $p(\lambda^2)$. The bandwidth depolarisation of the two NVSS IFs, as well as that combining both bands, are shown as the black curves for the case with spectral index of $\alpha = 0.0$. R_0 with different α values are plotted as the coloured curves, with the y-axis truncated at $R_0 = 150$ because the peak of R_0 for $\alpha = -0.9$ at $|\mathrm{RM}| \approx 340\,\mathrm{rad\,m^{-2}}$ reaches about 900, which can have obscured the other lower peaks.

that deviated significantly from the RM values of surrounding sources. Specifically, for each source they computed the median $\mathrm{RM}_{\mathrm{TSS09}}$ of neighbouring sources within a radius of 3°, and only accepted candidate RM values within $520\,\mathrm{rad\,m^{-2}}$ from the median RM. This implicitly assumes that the RM of individual sources cannot deviate significantly from that of their neighbours due to intrinsic RM or spatial fluctuations of foreground RM. The most likely candidate RM remaining is then reported as the $\mathrm{RM}_{\mathrm{TSS09}}$.

3.4.1.2 Dependence on Spectral Index

As seen in panel (a) of Figure 3.2, the out-*liars* and outliers appear to exhibit different distributions in α_{L}. This is further supported by the KS-test p-value of 0.045. The out-*liars* have α_{L} spread evenly over a wide range from -0.99 to $+0.02$, with a median of -0.37, while the α_{L} of most (ten out of 11) of the outliers cluster between -1.14 and -0.69, with a median of -0.9. It would be natural to directly link this discrepancy to the R_0 parameter used in the TSS09 algorithm. This is because the change in PI across λ^2 caused by spectral index effects could be mistaken as bandwidth depolarisation by the R_0 algorithm, possibly leading to $n\pi$-ambiguity. To test this hypothesis, we simulated R_0 as a function of |RM| for several different α_{L} values

(0.0, −0.3, −0.6, and −0.9), assuming Faraday simplicity. The results are shown in Figure 3.3. We find that the R_0 values at any given |RM| are only weakly dependent on $\alpha_{\rm L}$ except near the peak at |RM| $\approx 340\,{\rm rad\,m^{-2}}$ where the predicted R_0 diverge. This means that R_0 could be less effective in distinguishing different RM values for sources with true |RM| $\approx 340\,{\rm rad\,m^{-2}}$. TSS09 also reached similar conclusion regarding this |RM| range but for different reasons (see Chapter 3.4.1.4). However, only two out of nine out-*liars* (J094808−344010 and J224412+405715) reside in this |RM| range, and therefore spectral index dependence cannot explain most of our $n\pi$-ambiguity sources.

3.4.1.3 Dependence on Polarised Intensity and Polarisation Fraction

We show in panel (c) of Figure 3.2 the distribution of the two classes in $\rm PI_{TSS09}$, which is the average PI in the two IFs [i.e. $({\rm PI_1} + {\rm PI_2})/2$]. The KS-test p-value of 0.471 suggests that the two samples have the same underlying distribution in $\rm PI_{TSS09}$. It is worth noting, however, that while a previous study of 37 radio sources with high $\rm PI_{TSS09}$ ($> 200\,{\rm mJy}$) also at 1–2 GHz with the Allen Telescope Array (ATA) found no $n\pi$-ambiguity in the TSS09 catalogue (Law et al. 2011a), we have identified J224549+394122, which is spatially extended with PI $\approx 557.8 \pm 1.1\,{\rm mJy}$ in our observation and $\rm PI_{TSS09} = 132.4 \pm 4.3\,mJy$ (the difference can be due to how TSS09 extracted Stokes Q and U values for spatially resolved sources), as an out-*liar*. This shows that not all sources with high PI have reliable TSS09 RM values.

The discrepancies between the two populations in the fractional polarisation reported in the TSS09 catalogue ($p_{\rm TSS09}$) is more apparent, with KS-test p-value of 0.034. The $p_{\rm TSS09}$ values are plotted in panel (d) of Figure 3.2. Most (79 per cent) out-*liars* are concentrated at 0.8–3.1 per cent, while the outliers spread more evenly between 2.6 and 8.7 per cent. The median $p_{\rm TSS09}$ of out-*liars* and outliers are respectively 1.9 and 4.2 per cent. As we show in Chapter 4, sources with lower fractional polarisation are more susceptible to instrumental effects, particularly off-axis polarisation leakage, which can diminish the effectiveness of the TSS09 algorithm. However, this alone cannot explain all the out-*liars* we identified, since two of them are highly polarised at 9.1 ± 0.3 (J224549+394122) and 15.2 ± 0.2 per cent (J091145−301305).

3.4.1.4 Dependence on FD and RM Ranges

TSS09 pointed out that R_0 (Equation 3.16) could be less effective in selecting the correct RM values for sources with true |RM| falling within ranges of $< 50\,{\rm rad\,m^{-2}}$, $> 520\,{\rm rad\,m^{-2}}$, and $\approx 326.5\,{\rm rad\,m^{-2}}$ (taken as 301–352 $\rm rad\,m^{-2}$ here). For the case of < 50 and $> 520\,{\rm rad\,m^{-2}}$, that is because for both cases $R_0 \approx 1$, making it difficult to discern the correct RM value. The |RM| value of $\approx 326.5\,{\rm rad\,m^{-2}}$ is also believed to be a challenge for the TSS09 algorithm, since (1) there is almost complete bandwidth depolarisation for the combined band, and (2) R_0 cannot distinguish between the case of +326.5 and $-326.5\,{\rm rad\,m^{-2}}$ as the predicted R_0 are the same.

We plotted $\overline{\phi}$ of the two samples in panel (f) of Figure 3.2, with the above ranges shaded in green. Out of our sample, ten sources fall into these ranges, with only three

Table 3.5: Number of Faraday Simple/Complex Sources

	RM-Synthesis		QU-fitting	
	Faraday Simple	Faraday Complex	Faraday Simple	Faraday Complex
Out-*liars* ($n\pi$-ambiguity)	3	6	1	8
Outliers (Reliable $\mathrm{RM_{TSS09}}$)	10	1	6	5

being out-*liars* — J022915+085125 with $+13.6 \pm 1.0\,\mathrm{rad\,m^{-2}}$, J224412+405715 with $-320.4 \pm 0.6\,\mathrm{rad\,m^{-2}}$, and J235728+230226 with $+42.3 \pm 6.1\,\mathrm{rad\,m^{-2}}$. It is apparent that out-*liars* do not preferentially fall into the above RM ranges, and our samples within those ranges are more likely to have correct $\mathrm{RM_{TSS09}}$ than suffer from $n\pi$-ambiguity.

3.4.1.5 Dependence on Faraday Complexity

Faraday complexity (formally defined in Chapter 3.4.3.1) could be one of the reasons for the presence of $n\pi$-ambiguity in the NVSS RM catalogue. As summarised in Table 3.5, six out of the nine (67 per cent) out-*liars* are Faraday complex from our RM-Synthesis results, while only one out of the 11 (9 per cent) outliers show Faraday complexities from the same analysis. We can draw similar conclusion from the QU-fitting results, with eight out of nine (89 per cent) and five out of 11 (45 per cent) sources being Faraday complex, respectively. This may be because the R_0 algorithm can be affected by both non-linear PA and varying p across λ^2.

We test the possibility of the latter by quantifying the amount of Faraday depolarisation due to Faraday complexities. For each source, we adopted the best-fit model from QU-fitting, as well as spectral index α_L from Chapter 4, to compute the PI at the two NVSS IFs ($\mathrm{PI_1}$ and $\mathrm{PI_2}$) *without* taking bandwidth depolarisation into account. A depolarisation parameter is defined as

$$\frac{\Delta\mathrm{PI}}{\overline{\mathrm{PI}}} = \frac{\mathrm{PI_1} - \mathrm{PI_2}}{(\mathrm{PI_1} + \mathrm{PI_2})/2}, \tag{3.17}$$

which is listed in Table 3.4 for each source. Note that the values for even sources best characterised by the single thin model are non-zero because of the effect of the spectral index, which leads to a positive $\Delta\mathrm{PI}/\overline{\mathrm{PI}}$ with negative α_L. Apart from J022915+085125 which has a large $|\Delta\mathrm{PI}/\overline{\mathrm{PI}}| = 191.5$ because $p(\lambda^2)$ at NVSS IF1 approaches zero, we do not see clear signs of out-*liars* having larger $|\Delta\mathrm{PI}/\overline{\mathrm{PI}}|$, as would be expected if the Faraday depolarisation affects the R_0 algorithm leading to $n\pi$-ambiguity.

3.4.1.6 Dependence on RM of Neighbouring Sources

For each of our target sources, we evaluated the medians ($\mathrm{RM_{3^\circ}}$) and standard deviations (σ_{3°) of $\mathrm{RM_{TSS09}}$ values of the neighbouring sources within a radius of 3°.

These values are listed in column 4 of Table 3.6. On average, there are 28 neighbours to our target sources within the 3° radius circles. Assuming that $\mathrm{RM_{TSS09}}$ values are correct for most of the neighbouring sources, $\mathrm{RM_{3^\circ}}$ and σ_{3° would respectively represent the RM contribution by large-scale Galactic and/or intergalactic component(s), and the spatial fluctuations of the above-mentioned foreground RM components superimposed on the statistical spread of intrinsic RM of the neighbouring sources.

The out-*liars* clearly deviate from the outliers in $|\mathrm{RM_{TSS09}} - \mathrm{RM_{3^\circ}}|$ values, as we show in panel (g) of Figure 3.2. The out-*liars* gather within 416–522 $\mathrm{rad\,m^{-2}}$, with a median of 502 $\mathrm{rad\,m^{-2}}$, while the outliers spread through 109 to 469 $\mathrm{rad\,m^{-2}}$, with a median of 199 $\mathrm{rad\,m^{-2}}$. The large values for out-*liars* are clearly due to $n\pi$-ambiguity, leading to discrepancies between the individual $\mathrm{RM_{TSS09}}$ and the respective $\mathrm{RM_{3^\circ}}$. Large values are also found for three outliers, which could stem from spatial variations of the foreground RM structures around the positions of those of our targets. If this is the case, we would expect high σ_{3° values from those outliers as well.

An even clearer diagnostic is therefore the deviation in RM in units of σ_{3°. We plotted this ($|\mathrm{RM_{TSS09}} - \mathrm{RM_{3^\circ}}|/\sigma_{3^\circ}$; shortened as Δ/σ in text below) in panel (h) of Figure 3.2. Indeed, we found that all outliers converged to 0.97–2.71 in Δ/σ, meaning that those with high $|\mathrm{RM_{TSS09}} - \mathrm{RM_{3^\circ}}|$ also have high σ_{3°, matching our expectation above. The out-*liars*, on the other hand, have Δ/σ spread over 3.02 to 27.24, since the large $|\mathrm{RM_{TSS09}} - \mathrm{RM_{3^\circ}}|$ are due to $n\pi$-ambiguity and not necessarily accompanied by high σ_{3° due to spatial variations of the foreground. There is an apparent cutoff between the two populations at about 2.85. Since this Δ/σ parameter can be computed from the listed information from the NVSS RM catalogue without any extra information, this could be useful for identification of $n\pi$-ambiguity sources in the TSS09 catalogue (see Chapter 3.4.1.7).

3.4.1.7 How Many TSS09 Sources Suffer from $n\pi$-ambiguity?

We apply our findings from Chapter 3.4.1.6 to estimate how many TSS09 sources suffer from $n\pi$-ambiguity. The Δ/σ values for all of the 37,543 TSS09 sources have been computed. There is an average of 33 neighbouring sources for each TSS09 source. Sources with Δ/σ larger than 2.70, 2.85, and 3.00 are identified, corresponding to loose, moderate, and strict cutoffs respectively according to Chapter 3.4.1.6. Although we found that 837, 701, and 603 sources satisfy the above lower limits in Δ/σ respectively, we also noted that some of such sources have low $|\mathrm{RM_{TSS09}} - \mathrm{RM_{3^\circ}}|$. These sources may be located at regions with smooth RM foreground leading to low σ_{3° and high Δ/σ, but not suffering from $n\pi$-ambiguity. We therefore imposed another constraint of $|\mathrm{RM_{TSS09}} - \mathrm{RM_{3^\circ}}| \geq 400\,\mathrm{rad\,m^{-2}}$. This results in 56, 49, and 48 $n\pi$-ambiguity candidates in the entire TSS09 catalogue, depending on whether we adopt the loose, moderate, or strict cutoffs as defined above, respectively. Note that this is a lower limit estimated by the Δ/σ parameter only, which may not exhaust the entire $n\pi$-ambiguity population of TSS09 (see below). On the other hand, EGSs with high intrinsic FD (or RM) magnitudes of $\gtrsim 400\,\mathrm{rad\,m^{-2}}$ might also be included under the above selection criteria.

We further compared our list of $n\pi$-ambiguity candidates with the literature to verify the accuracy of our Δ/σ criterion. The wrongly classified sources (if any) can be separated into two categories — false-positives ($n\pi$-ambiguity candidates that actually have reliable $\mathrm{RM_{TSS09}}$) and false-negatives (sources that actually suffer from $n\pi$-ambiguity but not picked up by our algorithm above). No false-positives have been identified after consulting catalogues of polarised sources verified to have reliable $\mathrm{RM_{TSS09}}$ (Mao et al. 2010; Law et al. 2011a; Van Eck et al. 2011; Mao et al. 2012; Rawes et al. 2018; Betti et al. 2019), suggesting that our list of $n\pi$-ambiguity candidates is accurate. We further compare our findings with the known TSS09 $n\pi$-ambiguity sources listed in the literature to look for the false-negatives. Van Eck et al. (2011) reported RM values of 194 EGSs on the Galactic plane ($|b| \leq 5°$) with their observations, of which 146 were cross-matched with TSS09. From this sample, 13 sources (9 per cent) were found to suffer from $n\pi$-ambiguity in TSS09. Most of these 13 sources are concentrated in the inner Galaxy ($35° \leq l \leq 52°$), with 11 out of the 15 cross-matches in that region suffering from $n\pi$-ambiguity. This is likely linked to the complex large-scale magnetic field structure of the Milky Way manifested as large |RM| and rapid changes in RM in small spatial scales of a few degrees (e.g., Sun et al. 2008; Van Eck et al. 2011; Jansson & Farrar 2012), ultimately leading to the concentration of $n\pi$-ambiguity sources there. However, using our Δ/σ parameter defined above only one out of those 11 $n\pi$-ambiguity sources found there is correctly classified as an $n\pi$-ambiguity candidate. This means that our $n\pi$-ambiguity candidates list from Δ/σ is conservative, i.e. there can be more than 50 $n\pi$-ambiguity sources in the entire TSS09 catalogue.

3.4.1.8 NVSS J154936+183500: A Special Case

Upon comparison between our broadband $\overline{\phi}$ with narrowband $\mathrm{RM_{TSS09}}$ (Chapter 3.3.1), we identified J154936+183500 which has the two values differing by $307.5\,\mathrm{rad\,m^{-2}}$. This source can neither be classified as an out-*liar* nor an outlier, as these two classes of sources should have deviating $\overline{\phi}$ and $\mathrm{RM_{TSS09}}$ by about 652.9 and $0\,\mathrm{rad\,m^{-2}}$ respectively. To rule out the possibility that this discrepancy of $307.5\,\mathrm{rad\,m^{-2}}$ is due to RM time variabilities, we compared the $\mathrm{RM_{TSS09}}$ of this source with $\mathrm{RM_{VLA}}$ from Chapter 4. This $\mathrm{RM_{VLA}}$ is obtained from our new observations within the NVSS frequency ranges only. We find that this source has $\mathrm{RM_{VLA}} = -473.5 \pm 14.4\,\mathrm{rad\,m^{-2}}$, similar to its $\mathrm{RM_{TSS09}} = -426.8 \pm 14.6\,\mathrm{rad\,m^{-2}}$. In other words, the difference of $307.5\,\mathrm{rad\,m^{-2}}$ above cannot be attributed to time variabilities.

This peculiar difference in $\overline{\phi}$ versus $\mathrm{RM_{TSS09}}$ is likely due to its Faraday complexity. Both RM-Synthesis and QU-fitting suggest that this source contains three polarised components at FDs of about -315, -20, and $+75\,\mathrm{rad\,m^{-2}}$, with p of about 0.46, 0.27, and 0.33 per cent respectively. Such a wide spread of polarised components over FD, combined with their similar fractional polarisation, results in highly non-linear PA across λ^2 in the NVSS bands, as well as in our broadband L-band. This leads to a poor agreement between $\overline{\phi}$ and $\mathrm{RM_{TSS09}}$.

J154936+183500 is an example of sources that might not be suitable for RM grid experiments (e.g. Gaensler et al. 2005; Mao et al. 2010; Van Eck et al. 2011). This

is because of the large spread in FD of the three polarised components within the telescope beam, suggesting that this source has large intrinsic FD ($\sim 100\,\mathrm{rad\,m^{-2}}$). For such case, narrowband RM values are clearly poor representations of the foreground magneto-ionic media, while techniques applied to broadband data such as extraction of absolute maxima in Faraday spectra (e.g. Mao et al. 2010; Betti et al. 2019) and using polarisation-weighted FD (e.g. O'Sullivan et al. 2017, and this work) also may not give satisfactory results. This highlights the power of broadband spectro-polarimetric observations, which have opened up the possibility to identify such sources for careful treatments in RM grid experiments and/or further studies of their intrinsic polarisation properties.

3.4.1.9 Summary of Chapter 3.4.1

In Chapter 3.4.1, we showed the differences in the statistical distributions for several parameters of out-*liars* ($n\pi$-ambiguity sources in TSS09) versus outliers (sources with reliable $\mathrm{RM_{TSS09}}$). We suggest that low p_{TSS09} could cause $n\pi$-ambiguity in TSS09 values. Also, out-*liars* are found to have larger spread in α_{L} and tends to be Faraday complex, while outliers are concentrated at steeper α_{L} and are more likely Faraday simple. However, there may not be a direct relationship between these and $n\pi$-ambiguity. Out-*liars* do not appear to preferentially fall within |FD| ranges of < 50, > 520, and $\approx 326.5\,\mathrm{rad\,m^{-2}}$. We further compared, for each of our target sources, their $\mathrm{RM_{TSS09}}$ with the median ($\mathrm{RM_{3^\circ}}$) and standard deviation (σ_{3°) of $\mathrm{RM_{TSS09}}$ of neighbouring sources within a radius of 3°. All out-*liars* cluster at $|\mathrm{RM_{TSS09}} - \mathrm{RM_{3^\circ}}| \approx 500\,\mathrm{rad\,m^{-2}}$, while outliers span a range between 110 to $470\,\mathrm{rad\,m^{-2}}$. Most interestingly, we found that $\Delta/\sigma = |\mathrm{RM_{TSS09}} - \mathrm{RM_{3^\circ}}|/\sigma_{3^\circ}$ is an excellent diagnostic for $n\pi$-ambiguity in TSS09 catalogue. This parameter is an indicator of how much the $\mathrm{RM_{TSS09}}$ value of each source deviates from the RM caused by foreground structures, in units of how much such foreground structures fluctuate spatially. There is a cutoff at ~ 2.85 between the two classes of sources, with out-*liars* being above this cutoff and outliers below. Using this Δ/σ parameter, combined with a further constraint of $|\mathrm{RM_{TSS09}} - \mathrm{RM_{3^\circ}}| \gtrsim 400\,\mathrm{rad\,m^{-2}}$ to discard sources situated behind smooth RM foregrounds with low σ_{3°, we estimate that at least 50 out of the 37,543 TSS09 sources can be affected by the $n\pi$-ambiguity effect.

3.4.2 The Origin of Large Faraday Depths

Out of our 21 polarised target sources, we found (from RM-Synthesis) that 15 of them have $|\overline{\phi}| > 200\,\mathrm{rad\,m^{-2}}$. Such high $|\overline{\phi}|$ values are peculiar for sources away from the Galactic plane, as is the case for our targets ($|b| > 10^\circ$). While the FD could originate from within the EGSs themselves or from their immediate ambient media, it is challenging to directly confirm this scenario with the available information. We therefore explore the possibility of explaining the FD values from Galactic contributions and/or from foreground galaxy clusters. For the former, as Galactic FD (or RM) structures are often associated with warm and/or cold phases of the interstellar medium

Table 3.6: Foreground Diagnostics to Our Target Sources

Source (NVSS)	$\overline{\phi}$ (rad m^{-2})	$\mathrm{RM_{TSS09}}$ (rad m^{-2})	$\mathrm{RM}_{3^\circ} \pm \sigma_{3^\circ}$ [a] (rad m^{-2})	$\mathrm{RM_{O15}}$ [b] (rad m^{-2})	$N_{\mathrm{H\,I}}$ [c] (10^{20} cm^{-2})	$I_{\mathrm{H}\alpha}$ [d] (Rayleighs)
J022915+085125†	$+13.6 \pm 1.0$	$+521.2 \pm 8.0$	$+0.9 \pm 19.1$	$+0.2 \pm 7.8$	6.15 [E]	0.78
J083930−240723	$+325.9 \pm 1.0$	$+345.2 \pm 10.5$	$+148.8 \pm 191.0$	$+123.4 \pm 32.3$	7.05 [G]	45.07
J084600−261054$^{\times}$	—	$+481.0 \pm 11.4$	$+168.9 \pm 169.2$	$+202.2 \pm 21.8$	7.67 [G]	48.05
J084701−233701	$+384.8 \pm 2.0$	$+429.5 \pm 15.3$	-39.5 ± 216.2	$+67.4 \pm 29.1$	8.17 [G]	49.93
J090015−281758	$+352.1 \pm 0.2$	$+320.6 \pm 4.2$	$+121.3 \pm 204.7$	$+162.8 \pm 23.7$	12.2 [G]	61.12
J091145−301305**†	$+246.9^{+0.3}_{-0.3}$	-426.1 ± 3.5	$+84.0 \pm 141.2$	$+81.5 \pm 28.6$	15.7 [G]	33.24
J092410−290606**	$+527.6^{+0.3}_{-0.3}$	$+472.9 \pm 6.2$	$+62.5 \pm 183.9$	$+95.7 \pm 24.5$	8.48 [G]	36.36
J093349−302700	$+341.6 \pm 0.8$	$+313.4 \pm 7.7$	$+158.1 \pm 144.1$	$+138.4 \pm 22.7$	9.64 [G]	29.90
J093544−322845**	$+390.9^{+0.3}_{-0.3}$	$+368.1 \pm 9.3$	$+158.1 \pm 92.7$	$+154.2 \pm 19.1$	8.57 [G]	35.46
J094750−371528$^{\odot}$	$+328.8 \pm 2.2$	$+311.0 \pm 7.2$	-42.2 ± 148.7	-2.2 ± 28.3	12.4 [G]	78.99
J094808−344010†	$+382.7^{+2.6}_{-2.4}$	-327.9 ± 10.6	$+87.9 \pm 137.8$	$+31.9 \pm 23.4$	11.4 [G]	48.90
J111857+123442†	$+79.4^{+2.6}_{-2.8}$	-465.4 ± 5.7	$+10.0 \pm 27.1$	$+11.8 \pm 4.0$	1.86 [E]	0.26
J154936+183500$^{?}$	$-119.3^{+7.5}_{-7.4}$	-426.8 ± 14.6	$+22.8 \pm 16.6$	$+21.3 \pm 6.9$	2.72 [E]	0.89
J162706−091705**	-327.8 ± 0.7	-297.2 ± 12.8	-122.0 ± 70.7	-154.3 ± 18.4	12.1 [G]	132.04
J163927−124139**	$-331.4^{+0.3}_{-0.3}$	-313.5 ± 3.6	-205.0 ± 85.4	-195.0 ± 21.6	14.3 [G]	92.15
J170934−172853†	$+106.2^{+1.8}_{-1.9}$	-490.0 ± 12.7	$+14.1 \pm 25.7$	-9.7 ± 26.6	16.5 [G]	4.65
J190255+315942†	$+142.2^{+1.1}_{-1.1}$	-424.3 ± 2.6	$+66.7 \pm 29.4$	$+77.2 \pm 24.2$	9.91 [E]	3.93
J220205+394913	-367.2 ± 0.4	-349.1 ± 6.6	-89.0 ± 95.9	-145.0 ± 12.5	13.8 [E]	11.57
J220927+415834	-338.1 ± 0.2	-336.0 ± 5.4	-156.1 ± 132.6	-193.9 ± 31.9	15.7 [E]	5.75
J224412+405715†	-320.4 ± 0.6	$+345.8 \pm 14.4$	-116.7 ± 97.8	-182.8 ± 24.3	10.8 [E]	26.40
J224549+394122$^{\odot\dagger}$	$-278.6^{+0.8}_{-1.0}$	$+373.3 \pm 6.4$	-149.0 ± 93.4	-259.2 ± 7.7	8.56 [E]	14.91
J234033+133300$^{\times}$	—	$+56.7 \pm 6.3$	-8.2 ± 18.1	$+4.7 \pm 6.8$	5.07 [E]	1.31
J235728+230226†	$+42.3 \pm 6.1$	-556.7 ± 13.8	-55.1 ± 19.7	-55.3 ± 11.2	4.23 [E]	0.85

[a] Median RM values of TSS09 sources within 3° radius, with the uncertainties being the standard deviations of those neighbouring sources
[b] Galactic contribution to RM from Oppermann et al. (2015)
[c] Neutral hydrogen column density from H I observations
[d] Velocity-integrated Hα intensity from the WHAMSS (Haffner et al. 2003, 2010)
† Suffers $n\pi$-ambiguity in the TSS09 catalogue
$^{\times}$ Unpolarised sources
$^{?}$ Special case compared to TSS09 catalogue (see Chapter 3.4.1.8)
** Double point sources
$^{\odot}$ Extended sources
[E] From the Effelsberg-Bonn H I Survey (EBHIS; Winkel et al. 2016)
[G] From the Galactic All-Sky Survey (GASS; McClure-Griffiths et al. 2009; Kalberla & Haud 2015)

(e.g. Heiles & Haverkorn 2012), we looked into their respective tracers (Hα and H I) as an attempt to unveil the origin of the FDs.

3.4.2.1 Comparison with Hα Maps

Upon inspection of the Wisconsin H-Alpha Mapper Sky Survey (WHAMSS; Haffner et al. 2003, 2010) images, we found that nine of our high $|\overline{\phi}|$ EGSs (J083930−240723, J084701−233701, J090015−281758, J091145−301305, J092410−290606, J093349−302700, J093544−322845, J094750−371528, and J094808−344010) lie behind the northern arc of the Gum Nebula, two (J162706−091705 and J163927−124139) lie behind Sh 2-27, two (J224412+405715 and J224549+394122) situated close to Sh 2-126, and one (J220205+394913) lies behind an H II filament. All of the above sources are positioned on lines of sight with high velocity-integrated Hα intensities ($I_{\mathrm{H}\alpha} > 10$ Rayleighs; see column 7 of Table 3.6). Thus, the high $|\overline{\phi}|$ values of these 14 sources could be attributed to foreground Galactic H II structures. The only remaining EGS (J220927+415834) does not appear to be situated behind prominent H II structures, with a foreground velocity-integrated Hα intensity of only 5.75 R. The high FD of this source may have originated from a foreground galaxy cluster (Chapter 3.4.2.3).

To assess the link between the H II structures and the high $|\overline{\phi}|$, we estimate the regular magnetic field strengths ($B_{\rm reg}$) in those H II clouds needed to produce the observed $\overline{\phi}$. We omit the Gum Nebula and Sh 2-27 here, as their magnetic field structures are already studied in detail in Purcell et al. (2015) and Harvey-Smith et al. (2011) respectively using many of the above-mentioned EGSs. Following Harvey-Smith et al. (2011), emission measure (EM) and $B_{\rm reg}$ are given by

$$\mathrm{EM} = 2.75 \left(\frac{T_e}{10^4\,\mathrm{K}}\right)^{0.9} \left(\frac{I_{\mathrm{H}\alpha}}{\mathrm{R}}\right) e^{\tau}\,\mathrm{cm}^{-6}\,\mathrm{pc}, \tag{3.18}$$

$$B_{\rm reg} \sim \sqrt{3} B_{\rm reg,\parallel} = \sqrt{3} \frac{\phi}{0.81\sqrt{\mathrm{EM}}\sqrt{fL}}\,\mu\mathrm{G}, \tag{3.19}$$

where T_e is the electron temperature, τ is the optical depth due to dust extinction, $B_{\rm reg,\parallel}$ is the strength of the regular magnetic field component parallel to the line of sight, f is the filling factor, and L is the integration path length through the H II filament (in pc). The relationship between $B_{\rm reg}$ and $B_{\rm reg,\parallel}$ stem from statistical argument, and it is implicitly assumed that n_e is homogeneous. Furthermore, $B_{\rm reg,\parallel}$ is assumed to be uniform in both strength and direction along the lines of sight. In particular, since EM is proportional to $<n_e^2>$ while FD is only proportional to $<n_e>$, clumps of free electrons can result in large EM values but only moderate FD values. We also assumed here that the observed $\overline{\phi}$ of our EGSs come entirely from the H II structures (i.e. zero intrinsic FD contributions). To get an upper limit of $B_{\rm reg}$, we assume a low T_e of 7000 K (e.g. Peimbert et al. 2017), a typical $f = 0.1$ (e.g. Harvey-Smith et al. 2011), and adopted a range of optical depth ($\tau = 0.5$–1.5) to obtain

$$B_{\rm reg} \lesssim 2.26\text{–}3.73 \left(\frac{\phi}{\mathrm{rad\,m^{-2}}}\right) \left(\frac{L}{\mathrm{pc}}\right)^{-\frac{1}{2}} \left(\frac{I_{\mathrm{H}\alpha}}{\mathrm{R}}\right)^{-\frac{1}{2}}\,\mu\mathrm{G}. \tag{3.20}$$

Here, a lower optical depth would lead to a larger coefficient in the above Equation. The only undetermined variable, L, can be approximated by simple modelling of the geometry of the individual H II filament. Sh 2-126 is located at a distance of about 370–600 pc from us (Chen & Lee 2008), and has an intriguing morphology consisting of filamentary/sheet-like structures with widths of about 50′, translating to $\sim$ 5–9 pc. Considering that both J224412+405715 and J224549+394122 lie at the outskirt of this H II structure, we adopt half of the lower limit in width (i.e. 2.5 pc) as the path length through Sh 2-126. The H II filament shrouding J220205+394913 has an angular width of about 20′. It has not been studied in detail and thus has an unknown distance, but its spatial proximity and similarity in radial velocity ($v_{\rm LSR} \approx -9.0\,\mathrm{km\,s^{-1}}$ from WHAMSS) with nearby H II structures Sh 2-118 and Sh 2-123 suggest physical associations among these objects. The latter two clouds have kinematic distances of 3.8 kpc (Russeil 2003), which if taken as the distance to the H II filament would yield a physical width of 22 pc. We adopt this as the path length through this filament. Note that $B_{\rm reg}$ is only weakly sensitive to L, as an over-/under-estimation of the latter by 10 times would only result in the former being weaker/stronger by a factor of 3.2, which would not affect our order-of-magnitude estimation here.

Substituting in the adopted values of L for each H II structure, as well as $I_{\mathrm{H}\alpha}$ from the WHAMSS (see Table 3.6) and ϕ as our $\overline{\phi}$ values into Equation 3.20, we obtain $B_{\mathrm{reg}} \lesssim 89$–$171\,\mu$G for Sh 2-126 and 52–$86\,\mu$G for the H II filament in front of J220205+394913. The field strengths here are an order of magnitude higher than that in typical Galactic H II regions (~ 1–$36\,\mu$G; e.g. Heiles et al. 1981; Gaensler et al. 2001; Harvey-Smith et al. 2011; Rodríguez et al. 2012), though note that these H II filaments might not be typical H II regions. Since our crude assumptions above would yield upper limits in field strengths, and for these two clouds we only have very rough estimates on the physical scales, we cannot draw a concrete conclusion on whether these two H II structures can contribute to the bulk of the observed $|\overline{\phi}|$ of the three target sources.

3.4.2.2 Comparison with H I Column Densities

We also looked into the Galactic H I column densities (N_{HI}) towards our target sources, using the result from the Effelsberg-Bonn H I Survey (EBHIS; Winkel et al. 2016) for the northern sky and the Galactic All-Sky Survey (GASS; McClure-Griffiths et al. 2009; Kalberla & Haud 2015) for the southern hemisphere. The foreground N_{HI} values for our target sources are listed in column 6 of Table 3.6. However, we do not see any clear trends between $|\overline{\phi}|$ and N_{HI}.

3.4.2.3 Foreground Galaxy Clusters

We explore the possibility of high FD stemming from the hot magnetised intra-cluster medium of foreground galaxy clusters (see Govoni & Feretti 2004), which can have |FD| contributions to embedded / background polarised sources of $\sim 100\,\mathrm{rad\,m^{-2}}$ (e.g. Taylor et al. 2001; Bonafede et al. 2009; Govoni et al. 2010). The NASA/IPAC Extragalactic Database (NED) was consulted for galaxy clusters within 2° of our 15 high $|\overline{\phi}|$ target sources, and we found matches for the six sources below.

1. J084701−233701 at $z = 0.0607 \pm 0.0001$ (Huchra et al. 2012) with $\overline{\phi} = +384.8 \pm 2.0\,\mathrm{rad\,m^{-2}}$ is situated at 34′.3 away from Abell S0613 and 96′.5 away from PSZ1 G246.45+13.16. The former galaxy cluster is background to our target ($z = 0.0740$; Chow-Martínez et al. 2014), and therefore cannot contribute to the high FD. The latter is a Sunyaev-Zel'dovich cluster candidate (Planck Collaboration et al. 2014b) with poorly constrained parameters.

2. J093349−302700 (z unknown) with $\overline{\phi} = +341.6 \pm 0.8\,\mathrm{rad\,m^{-2}}$ is accompanied by Abell 3421 at 92′.4 away and Abell S0618 at 92′.9 away. Both of the clusters do not have constrained z nor angular sizes.

3. J094808−344010 (z unknown) with $\overline{\phi} = +382.7^{+2.5}_{-2.4}\,\mathrm{rad\,m^{-2}}$ is 81′.1 away from Abell 3428. This cluster has a photometric redshift of $z = 0.0601$ (Coziol et al. 2009), but without any reported angular sizes.

4. J220205+394913 (z unknown) with $\overline{\phi} = -367.2 \pm 0.4\,\mathrm{rad\,m^{-2}}$ is situated next to ZwCl 2200.7+3752 at 103′.1 away. This cluster has a diameter of only 58′ (Zwicky et al. 1961), and therefore cannot contribute to the FD of our target.

5. J220927+415834 at $z = 0.512 \pm 0.029$ (photometric; Abolfathi et al. 2018) with $\overline{\phi} = -338.1 \pm 0.2\,\mathrm{rad\,m^{-2}}$ is neighbouring UGCL 467 (also known as ZwCl 2207.8+4114) at $30\farcm2$ away. This foreground cluster ($z = 0.0166$; $1' = 21\,\mathrm{kpc}$) has a diameter of $164'$ (Baiesi-Pillastrini et al. 1984), and could be the prime contributor to FD of J220927+415834 given that we could not identify any clear foreground Galactic structures from Hα nor H I above.

6. J224412+405715 at $z = 1.171$ (Ackermann et al. 2011) with $\overline{\phi} = -320.4 \pm 0.6\,\mathrm{rad\,m^{-2}}$ is accompanied by two galaxy clusters — 1RXS J223758.3+410109 ($70\farcm8$ away) and Sunyaev-Zel'dovich cluster candidate PSZ1 G097.52−14.92 ($77\farcm1$ away). Neither of them have reported z nor cluster diameter.

To summarise, J220927+415834 (for which we could not find any foreground Galactic Hα or H I structures to) may have attained its high FD from the foreground galaxy cluster UGCL 467. We cannot confidently attribute the high FD of the rest of our target sources to foreground clusters, given the ill-constrained parameters, particularly redshifts, to the sources themselves and/or to the foreground clusters.

3.4.3 The Nature of Faraday Complexity

3.4.3.1 Definition of Faraday Complex Sources

We find it necessary to formally define Faraday complex sources before proceeding further. The main reason is to facilitate comparisons with the literature, as a growing number of broadband spectro-polarimetric studies of EGSs choose to extract the flux densities of their samples by integrating within a source region (e.g., Anderson et al. 2016; O'Sullivan et al. 2017). While this would be similar to the strategies we adopted for our point sources and extended sources, it is in contrast to our spatial doubles, for which we fitted two Gaussian functions to each image (per frequency channel and per Stokes parameter; Chapter 3.2.2) and analysed the two spatial components independently. In other words, although we may be able to identify small differences in FD between two spatial components, the same source may be classified as Faraday simple when the spatial information is discarded. We therefore carefully define Faraday complexity for our target sources here to match the expected outcome if our sources were not spatially resolved. Also, in addition to angular resolution (see Appendix B.1), we note that whether the Faraday complexity of a source can be correctly identified can also depend on the S/N ratio (e.g. Anderson et al. 2015; O'Sullivan et al. 2017) and λ^2 coverage (e.g. Anderson et al. 2016).

We therefore define Faraday complex sources as follows. From RM-Synthesis, an unresolved or extended source is considered as Faraday complex if it is decomposed into multiple polarised components, or the only polarised component is Faraday thick. Here, we define "Faraday thick component" as one with the fitted FWHM ($\delta\phi$) at least 10 per cent more than the theoretical FWHM of the RMTF ($\delta\phi_0$), while "Faraday thin component" is one with $\delta\phi$ less than 1.1 times of $\delta\phi_0$. For a spatial double source, it is deemed Faraday complex if at least one of the spatial components is further divided into

multiple polarised components, or one/each of the spatial components hosts a Faraday thick component, or each spatial component contains one and only one Faraday thin component but the FDs of these two components are separated by more than 37 per cent of $\delta\phi_0$ (the choice of this factor is explained below). On the other hand, from QU-fitting a spatially unresolved or extended source is defined as Faraday complex if its best-fit model is not single thin (1T), while a double source is categorised as Faraday complex if either/both of the spatial components is/are best fitted by models other than single thin, or both spatial components are best characterised by the single thin model but the difference in FDs of the two Faraday simple components is larger than 37 per cent of the $\delta\phi_0$ from RM-Synthesis (again, the choice of this factor is explained below).

As mentioned above, the most critical part of this formal definition here is for spatial double sources, particularly for cases where each spatial component hosts a Faraday thin component. In such cases, the two spatially resolved polarised components could be indistinguishable from a single Faraday thin component if we discard the spatial information by combining them within a source integration region. While previous works showed by simulations that polarised components with FDs separated by less than $\approx$ 50–100 per cent of $\delta\phi_0$ cannot be confidently distinguished by RM-Synthesis and QU-fitting (e.g. Farnsworth et al. 2011; Sun et al. 2015; Schnitzeler 2018; Miyashita et al. 2019), we chose to adopt a smaller cutoff value of 37 per cent here. This is because although the two Faraday thin components cannot be separated if they are situated too close together in Faraday space, the two combined could be identified as a single Faraday thick component. We calculated for the simplest case of adding two Faraday thin components with equal amplitudes together, and found that when they are separated by about 37 per cent of $\delta\phi_0$ the combined function resembles a Gaussian function with $\delta\phi$ being 1.1 times of $\delta\phi_0$, satisfying our definition of Faraday thick component above. Nonetheless, the choice of this cutoff value would not affect the results of our work here, as the most extreme case we have is J093544−322845 in RM-Synthesis, with the two Faraday thin components separated by 8.7 per cent of $\delta\phi_0$ only.

3.4.3.2 The Physical Origin of Faraday Complexity

One of the major strengths of radio broadband spectro-polarimetric observations is the ability to decompose spatially unresolved sources (e.g. EGSs) into multiple polarised components. These components could be located anywhere in the volume traced by the telescope beam, both parallel or perpendicular to the line of sight. This opens up the possibility of identification or even study of discrete physical regions that are spatially unresolved by the observations, but this would require prior studies associating the polarised components with spatial components for a sample of spatially resolved sources. There appears to be some correspondences between the number of Faraday and spatial components of EGSs (e.g. Anderson et al. 2016; O'Sullivan et al. 2017, both with angular resolution of $\sim 1''$). This motivates us to carry out similar investigations to our sample of EGSs below.

We first look at sources that are spatially resolved with our $\sim 45''$ beam. The only such sources that are resolved into multiple polarised components are J224549+394122 from RM-Synthesis, and J092410−290606 and J162706−091705 from QU-fitting. All three of them host two polarised components each, with J224549+394122 being resolved into FR II morphology and the remaining two as double unresolved components. Interestingly, the two polarised components for each of the spatial doubles originate from just one of the two spatial components (J092410−290606a and J162706−091705b respectively). J092410−290606b is polarised, but its polarised component is indistinguishable from one of the two from J092410−290606a. On the other hand, J162706−091705a is not polarised (below 6σ limit of 3 per cent). For the remaining three spatial doubles (J091145−301305, J093544−322845, and J163927−124139), the sources are not resolved into multiple polarised components according to our definition above in Chapter 3.4.3.1. However, since we analysed the spatial components individually in both RM-Synthesis and QU-fitting, we can still obtain the difference in FD between the two components, and compute what λ^2 coverages are required to resolve them into two polarised components if these sources were spatially unresolved. From RM-Synthesis and QU-fitting, our spatial doubles have differences in FD of 2.4–7.6 rad m^{-2} and 2.7–15.5 rad m^{-2}, respectively. Assuming that in both analyses we can distinguish polarised components separated by more than 50 per cent of the theoretical $\delta\phi_0$ in RM-Synthesis (e.g. Schnitzeler 2018), a λ^2 coverage of more than 0.11–0.72 m^2 would be needed to resolve our spatial doubles into the multiple polarised components. These translate to frequency coverages from 1 GHz down to 660 and 330 MHz, respectively. From this, we argue that for spectro-polarimetric studies of EGSs in GHz regime, we should *not* combine multiple spatial components together with flux integration regions. This is because the spatially resolved polarised components would then become a single unresolved polarised component, leading to loss of physical information of the sources. We draw similar conclusions in Appendix B.1 for our spatially extended sources, where we found that the QU-fitting results after spatial flux integrations differs from our spatially resolved RM-Synthesis analysis.

Furthermore, we searched for Faint Images of the Radio Sky at Twenty-Centimeters (FIRST; angular resolution $\approx 5''$; Becker et al. 1995), as well as Very Long Baseline Interferometry (VLBI; angular resolution $\sim$ mas; Fey & Charlot 1997, 2000) total intensity images of all of our target sources. We found that four of them have existing higher angular resolution radio images. These sources are discussed individually below.

1. J111857+123442 (4C +12.39) is composed of two Faraday thin components in both of our analysis. In the FIRST image there is a hint of a fainter spatial component $10''$ to the northwest of the main component. At VLBI resolution the source is extended at 2.3 GHz, and is resolved into two spatial components at 8.6 GHz.

2. J154936+183500 (4C +18.45; the special case; Chapter 3.4.1.8) consists of three polarised components in both RM-Synthesis and QU-fitting. These polarised components have vastly different FD values (-315.3 ± 2.1, -31.8 ± 3.5, and $+81.3 \pm 2.8$ rad m^{-2} from RM-Synthesis; similar to that from QU-fitting). This

source is also spatially resolved into three components in the FIRST image — two bright blobs together resembling an FR II radio galaxy with an angular scale of about 15″ (corresponding to a projected physical scale of about 130 kpc at $z = 1.442$; Hewitt & Burbidge 1987), and a third faint point source situated about 40″ away to the southwest.

3. J170934−172853 is represented by two polarised components in our RM-Synthesis and QU-fitting analysis. The source appears in the VLBI image at 2.3 GHz as two spatial components, with the brighter one with flux density of about 500 mJy and the dimmer one situated about 10 mas away to the southeast with flux density of about 10 mJy. The brighter component can be further resolved into two components at 8.6 GHz, with component 1 at about 300 mJy and to the southeast by 3 mas component 2 at about 5 mJy.

4. J190255+315942 (3C 395) is found to have two Faraday thin components in our analysis. In the 2.3 GHz VLBI image it is consisted of two spatial components separated by about 15 mas (projected distance of about 100 pc at $z = 0.635$; Hewitt & Burbidge 1987), with a faint structure connecting the two. The two components can also be seen in the 8.6 GHz VLBI image.

From above, there appears to be a good association between the number of Faraday components identified from our 1–2 GHz observations and the number of spatial components resolved at 5″ (FIRST) or mas (VLBI) resolutions. A caveat here is that because of the missing short uv-spacing, there could be missing flux from structures on large angular scales, particularly in the VLBI images. Note that this suggested association between the number of spatial and polarised components is only speculative, and requires confirmation from high angular resolution spectro-polarimetric studies. Indeed, a more comprehensive study on the connection between polarised components and structures of EGSs at different angular and physical scales, as well as for different source types, would be necessary before we can confidently interpret their Faraday complexities from low angular resolution observations alone.

Finally, it has been suggested that lines of sight with Galactic H I column density of $1.4–1.65 \times 10^{20}$ cm^{-2} may pass through magnetised plasma in the Milky Way which could cause observed Faraday complexities in background EGSs (Anderson et al. 2015). This would imply that the turbulence scale of the magneto-ionic medium causing such complexities is less than ~ 5 pc assuming a distance to the far side of the Milky Way of 23.5 kpc with their angular resolution of $\sim 45''$. All of our target sources have foreground H I column densities higher than the above-mentioned range (Table 3.6), with J111857+123442 having the lowest of 1.86×10^{20} cm^{-2}. It is represented by double Faraday thin components in both RM-Synthesis and QU-fitting, with differences in FD of about 100 rad m^{-2}. This source is resolved into two spatial components separated by about 10″ in FIRST (see above). At such a small angular scale, the Milky Way contribution to FD is not expected to vary by such a large amount. We suggest that for this source, Faraday complexity is not caused by the magneto-ionic medium in the Milky Way.

3.4.3.3 Faraday Complexity Statistics

Our RM-Synthesis and QU-fitting results show respectively that eight (38 per cent) and 14 (67 per cent) out of the 21 polarised target sources are Faraday complex. We briefly discuss the difference between these two algorithms in Appendix B.2. The RM-Synthesis fraction is similar to the 29 per cent (12 out of 42) obtained from the RM-Synthesis analysis on ATA data of bright radio sources in 1–2 GHz (angular resolution $\sim 100''$; Law et al. 2011a). This similarity may be because of the similar λ^2 coverages, as well as the high signal-to-noise ratio in polarisation, in both studies. In contrast, Anderson et al. (2015) reported with their 1.3–2.0 GHz study at an angular resolution of $\sim 1'$ that only 12 per cent (19 out of 160) of their polarised sources appeared to be Faraday complex with their observational setup. This can be attributed to the lower signal-to-noise ratio in PI ($\lesssim 10$) of some of their target sources. As they suggested in their paper, sources that are genuinely Faraday complex might appear Faraday simple in the low S/N regime.

There are spectro-polarimetric studies of EGSs at other wavelengths that reported a much higher fraction of Faraday complex sources. Pasetto et al. (2018) found by QU-fitting analysis that, all of their 14 high RM sources are Faraday complex with their 4–12 GHz observations (angular resolution $\lesssim 1''$), though this could be biased due to their source selection criteria. They chose sources that are unpolarised in the NVSS at 1.4 GHz but polarised at higher frequencies, which could be due to bandwidth depolarisation in the NVSS at specific |RM| ranges (≈ 350 or $\gtrsim 1000\,\mathrm{rad\,m^{-2}}$) and/or Faraday depolarisation due to complexities. Nonetheless, O'Sullivan et al. (2017) reported that 90 per cent (90 out of 100) of their targets are Faraday complex from their 1–3 GHz observations with angular resolution of $\sim 10''$, also with QU-fitting analysis. This is similar to the findings of Anderson et al. (2016), who observed at 1.3–10 GHz (with angular resolution of ~ 1–$10''$) a total of 36 EGSs selected such that, based on archival narrowband 1.4 GHz data, half of the sample are Faraday simple and the other half are Faraday complex. Their broadband studies with RM-Synthesis concluded that 97 per cent (35 out of the 36) of their sample turns out to be Faraday complex in the observed λ^2 range, with the remaining one consistent with being unpolarised. By re-analysing their data at different λ^2 coverages, they suggested that the detection of Faraday complexity of EGSs could be hindered by limited λ^2 ranges. This suggests that many of our Faraday simple sources could become Faraday complex if they are observed at a wider λ^2 range with sufficient S/N ratio.

3.5 Conclusion

With new broadband spectro-polarimetric observations of 23 $n\pi$-ambiguity candidates with the Jansky VLA in L-band, we revealed nine out-*liars* (sources that suffer from $n\pi$-ambiguity in the NVSS RM catalogue). By comparing the statistics of their observed parameters with that of the 11 outliers (sources with reliable $\mathrm{RM_{TSS09}}$), we find noticeable differences between the two classes in α_L, p_TSS09, $|\mathrm{RM_{TSS09}} - \mathrm{RM_{3^\circ}}|$, $\Delta/\sigma = |\mathrm{RM_{TSS09}} - \mathrm{RM_{3^\circ}}|/\sigma_{3^\circ}$, and Faraday complexities. In particular, we find Δ/σ,

which is a measure of how much a source's RM deviates from the RMs of its surrounding sources, to be a good diagnostic for $n\pi$-ambiguity in the NVSS RM catalogue. There is an apparent cutoff at $\Delta/\sigma \approx 2.85$ between the two populations, which we used to estimate that there are at least 50 $n\pi$-ambiguity sources in the TSS09 catalogue out of the total of 37,543 sources. This is an important result for us to gauge the reliability of the TSS09 catalogue, and merits further studies to verify these $n\pi$-ambiguity candidates. We further identified two sources that are polarised in TSS09 at 0.5–0.6 per cent levels, but are unpolarised (below the 6σ cutoffs of ≈ 0.07 per cent) in our new broadband observations. These two sources have motivated a detailed study on the effects of the off-axis instrumental polarisation in the NVSS RM catalogue, presented in Chapter 4.

We found that 15 of our target sources have large $|\overline{\phi}| > 200\,\mathrm{rad\,m^{-2}}$ despite being situated away from the Galactic plane ($|b| > 10°$). 14 of them are found to be lying behind Galactic H II structures, which are likely the prime contributors to the observed high $|\overline{\phi}|$ of these sources. The only remaining source, J220927+415834, is found to be background to the galaxy cluster UGCL 467, which is the most likely explanation of its high $|\overline{\phi}|$.

Finally, we studied the Faraday complexities of our target sources with our broadband 1–2 GHz observations. We found good correspondence between the number of identified polarised components from our analysis with the number of spatial components in total intensities at $\approx 5''$ and milli-arcsecond resolutions in FIRST and VLBI images, respectively. However, this speculated associations between the Faraday and spatial components require confirmation from future polarisation studies at high angular resolution. In our sample of 21 polarised sources, eight (38 percent) and 14 (67 per cent) are Faraday complex from our RM-Synthesis and QU-fitting analysis respectively. The former value agrees with the 29 per cent reported by Law et al. (2011a) with their RM-Synthesis study of EGSs at similar frequency range. We noted that if our target sources are re-observed with a wider λ^2 coverage than that of our L-band observations here, many of our current Faraday simple sources will likely become Faraday complex at sufficient signal-to-noise ratio in polarisation.

Chapter 4

Effects of Off-axis Instrumental Polarisation in the NVSS Rotation Measure Catalogue

---

This Chapter is based on an article titled **"A Broad-band Spectro-polarimetric View of the NVSS Rotation Measure Catalogue — II. Effects of Off-axis Instrumental Polarization"**, which has been published in the Monthly Notices of the Royal Astronomical Society (2019; Volume 487, Issue 3, Pages 3454–3469), published by Oxford University Press on behalf of the Royal Astronomical Society, available on https://doi.org/10.1093/mnras/stz1328. Edits are done solely to maintain a consistent style within the entirety of this thesis. As the lead author of this publication, I have conducted all the data reduction and analysis in this Chapter, and was responsible for the development of the simulations presented and for the writing of the manuscript. The full list of authors is: **Yik Ki Ma**, Sui Ann Mao, Jeroen Stil, Aritra Basu, Jennifer West, Carl Heiles, Alex S. Hill, and Sarah K. Betti.

The NRAO VLA Sky Survey (NVSS) Rotation Measure (RM) catalogue has enabled numerous studies in cosmic magnetism, and will continue being a unique data set complementing future polarisation surveys. Robust comparisons with these new surveys will however require further understandings in the systematic effects present in the NVSS RM catalogue. In this Chapter, we make careful comparisons between our new on-axis broadband observations with the Karl G. Jansky Very Large Array and the NVSS RM results for 23 sources. We found that two unpolarised sources were reported as polarised at about 0.5 per cent level in the RM catalogue, and noted significant differences between our newly derived RM values and the catalogue values for the remaining 21 sources. These discrepancies are attributed to off-axis instrumental polarisation in the NVSS RM catalogue. By adopting the 0.5 per cent above as the typical off-axis instrumental polarisation amplitude, we quantified its effect on the reported RMs with a simulation, and found that on average the RM uncertainties in the catalogue have to be increased by ≈ 10 per cent to account for the off-axis instrumental polarisation effect. This effect is more substantial for sources with lower fractional polarisation, and is a function of the source's true RM. Moreover, the distribution of the resulting RM uncertainty is highly non-Gaussian. With the extra RM uncertainty incorporated, we found that the RM values from the two observations for most (18 out of 21) of our polarised targets can be reconciled. The remaining three are interpreted as showing hints of time variabilities in RM.

Contents

4.1 Introduction

Magnetic fields are known to be crucial for astrophysical processes such as star formation, cosmic ray propagation, galactic outflows, and galactic evolution (see, e.g., Beck & Wielebinski 2013; Beck 2016). While the magnetic field strength and structure of astrophysical objects can be probed by measurements of their polarised synchrotron emission (e.g., Fletcher et al. 2011; Gießübel et al. 2013; Mao et al. 2015; Kierdorf et al. 2017), this method is only sensitive to the magnetic field component in the plane of the sky in volumes populated with cosmic ray electrons. A complementary method is to use background polarised sources as probes to the foreground subjects of interest — polarised emission experiences the Faraday rotation effect as it traverses through the foreground intervening magnetised plasma, leading to a change in the polarisation position angle (PA; [rad]) given by

$$\Delta\mathrm{PA} = \left[0.81 \int_{\ell}^{0} n_e(s) B_{\parallel}(s)\,\mathrm{d}s\right] \cdot \lambda^2 \equiv \mathrm{RM} \cdot \lambda^2, \tag{4.1}$$

where ℓ [pc] is the (physical) distance to the source from the observer, n_e [cm^{-3}] is the thermal electron density, $B_{\parallel}$ [μG] is the strength of the magnetic field component along

the line of sight (s [pc]), λ [m] is the wavelength of the emission, and RM [rad m^{-2}] is the rotation measure of the source[1]. The integrated value of the magnetic field strength along the line of sight, weighted by n_e, is therefore encrypted in the RM values. The RM of any given sight line can be obtained by PA measurements at two or more frequency bands, followed by a linear fit to PA against λ^2. For example, the resulting RM from observations at two frequencies only is given by

$$\mathrm{RM} = \frac{\mathrm{PA}_1 - \mathrm{PA}_2 + n\pi}{\lambda_1^2 - \lambda_2^2}, \tag{4.2}$$

where the subscripts denote the two frequency bands, and n is an integer corresponding to $n\pi$-ambiguity resulting from the possible wrapping(s) of PA between the two bands (see Chapter 3 for more details).

Extragalactic radio sources (EGSs) have commonly been used to uncover the magnetic fields in foreground astrophysical objects. Such RM-grid experiments can be broadly divided into two categories: blind surveys and pointed observations. The NRAO VLA Sky Survey (NVSS) RM catalogue (Taylor et al. 2009, hereafter TSS09) is the largest RM catalogue to date, and is a notable example of blind surveys. This RM catalogue was built by re-analysing the original NVSS data (Condon et al. 1998), which were taken by scanning through a regularly spaced hexagonal grid in the northern sky ($\delta > -40°$). The wide sky coverage of the TSS09 catalogue has enabled numerous studies of cosmic magnetism (e.g., McClure-Griffiths et al. 2010; Harvey-Smith et al. 2011; Stil et al. 2011; Oppermann et al. 2012; Hill et al. 2013; Oppermann et al. 2015; Purcell et al. 2015; Terral & Ferrière 2017). Similar blind survey strategies were also adopted by other works for specific parts of the sky (e.g., Gaensler et al. 2005; Mao et al. 2008; Gießübel et al. 2013). With such surveying strategies, the target EGSs are in general not on the pointing axis of the telescopes, which means the resulting data can be affected by off-axis instrumental effects that need to be accounted for (see below). On the other hand, the strategy of pointed observations is also commonly used (e.g., Mao et al. 2010; Van Eck et al. 2011; Mao et al. 2012; Costa et al. 2016; Kaczmarek et al. 2017; Mao et al. 2017; Betti et al. 2019), where target EGSs are selected from existing catalogues of polarised radio sources. They are then observed with the EGSs placed on the pointing axis of the telescopes. Compared to blind surveys, the resulting data of the targets from these pointed observations are free of off-axis instrumental artefacts.

An ideal radio telescope with dual polarised feeds should have independent polarisation channels, each being insensitive to its orthogonal counterpart. In reality, however, imperfections of the telescopes allow these polarisation channels to "see" the orthogonally polarised components. This is known as the instrumental polarisation (also known as the polarisation leakage) of radio telescopes, which can alter the measured polarisation signals. The polarisation leakage can be seen as comprised of two distinct elements — the on-axis and the off-axis components. The former is routinely

[1] In this work, we investigate the narrowband results presented in Taylor et al. (2009), and therefore follow the traditional notion of RM instead of the more generalised notion of Faraday depth.

calibrated out in polarisation studies (see, e.g., Hales 2017), usually by either (1) observing a known unpolarised calibrator and attributing the measured polarisation signals as the instrumental response of the telescope, or (2) observing a calibrator over a range of parallactic angles to simultaneously determine the astrophysical and instrumental polarisation, given that the telescope is driven by altitude-azimuthal (alt-az) mounts. Both these strategies will remove the polarisation leakage at the pointing centre where the calibrator has been placed at (down to, e.g., $\lesssim 0.02$ per cent in our new Jansky VLA observations; see Chapter 3), but residual polarisation leakage remains for positions within the primary beam away from the pointing axis (thus "off-axis"). This off-axis instrumental polarisation can be determined by holography scans (e.g. in the NVSS; Cotton 1994; Condon et al. 1998) and subsequently be calibrated out. Alternatively, the A-projection algorithm (Bhatnagar et al. 2008, 2013) can be further developed to characterise and correct for the off-axis polarisation leakage (see, e.g., Jagannathan et al. 2017, 2018). This full Mueller A-projection requires an adequate knowledge of the antenna optics, and can be applied during the imaging step of data reduction.

The off-axis polarisation leakage present in the NVSS data, if completely uncorrected, can be up to 2.5 per cent (Cotton 1994). However, as calibrations for this off-axis leakage have been applied in the image domain, the residual leakage remaining in the data products of the original NVSS (namely, images and the source catalogue) is ≈ 0.3 per cent (Condon et al. 1998). As TSS09 constructed their RM catalogue by re-analysing the NVSS visibility data, the calibration for the off-axis leakage was *not* applied, though the mosaicking done to form their images could have smoothed out the off-axis leakage pattern with respect to the NVSS pointing centres. It is therefore likely that the reported RM values in the TSS09 catalogue have been affected by off-axis polarisation leakage, with its effect still remain unaccounted for.

It is crucial to fully understand the limits of this NVSS RM catalogue given its relevance. Although ongoing polarisation surveys such as Polarization Sky Survey of the Universe's Magnetism (POSSUM; Gaensler et al. 2010) in 1130–1430 MHz and VLA Sky Survey (VLASS; Myers et al. 2014) in 2–4 GHz will provide us with drastically higher RM densities than TSS09, these two surveys either do not have exact sky or frequency coverage, and both cover different time domains, compared to TSS09. This means the TSS09 catalogue will continue being a unique data set depicting the magnetised Universe.

In Chapter 3, we have explored the $n\pi$-ambiguity problem in TSS09 and concluded that there are likely more than 50 $n\pi$-ambiguity sources (with erroneous RM by $\pm 652.9\,\mathrm{rad\,m^{-2}}$) out of the total 37,543 in the NVSS RM catalogue. In addition, we found two sources that were reported as ≈ 0.5 per cent polarised in TSS09 but were unpolarised in our new broadband Jansky VLA observations. We attributed this discrepancy in polarisation levels to the off-axis polarisation leakage in the NVSS data, which has motivated our study here. In this Chapter, we perform a rigorous comparison between our new data of 23 sources with the results from TSS09. Our goal here is to identify and quantify systematic errors affecting RM measurements that were unaccounted for in the TSS09 catalogue. The observational setup and data reduction

procedures are outlined in Chapter 4.2, and the results are presented in Chapter 4.3. We discuss the discrepancies between our new results and TSS09 in Chapter 4.4. The effects of off-axis instrumental polarisation on RM measurements are quantified by simulations in Chapter 4.5. Finally, we make concluding remarks on this work in Chapter 4.6.

4.2 Observations and Data Reduction

4.2.1 New Observations

A total of 23 target sources were selected from the TSS09 catalogue, with the original primary goal of identifying $n\pi$-ambiguity sources (addressed in Chapter 3). These sources were selected based on their high $|\mathrm{RM}_{\mathrm{TSS09}}| \gtrsim 300\,\mathrm{rad\,m^{-2}}$, despite being situated away from the Galactic plane ($|b| > 10°$)[2]. Furthermore, all of our targets are bright with NVSS total intensities larger than 100 mJy.

Our new broadband observations were performed using the Jansky VLA in L-band (1–2 GHz) in D array configuration on 2014 July 03. The same array configuration as used by the NVSS means that our *uv*-coverages are similar to that of TSS09, and the observations from both works are sensitive to emission at the same ranges of angular scales. The typical integration time per source was about 3–4 minutes. Standard calibration procedures were followed using the Common Astronomy Software Applications (`CASA`) package (version 4.4.0; McMullin et al. 2007), and are described in detail in Chapter 3.2.

4.2.2 NVSS Band Images from New Observations

A careful comparison in polarisation properties between our new data and the NVSS RM catalogue requires that the two data sets have near identical frequency and *uv*-coverages, with the source properties extracted following the same method. We have therefore formed two sets of radio images using our calibrated broadband Jansky VLA data in the two NVSS intermediate frequency (IF) bands only. Although the original NVSS bands had frequency ranges of 1343.9–1385.9 MHz (IF1) and 1414.1–1456.1 MHz (IF2) respectively (Condon et al. 1998), parts of our data in these frequency ranges were unfortunately flagged because of corruption by radio frequency interferences (RFI) or because they lie at the edges of the new broadband Jansky VLA spectral windows where sensitivity drops rapidly. Therefore, we have instead used our new Jansky VLA data within frequency ranges of 1344.5–1373.5 MHz as IF1 and 1430.5–1445.5 MHz as IF2 uniformly for all the sources. These frequency ranges are the widest that we can get within the NVSS frequency bands, resulting in the best comparison that can be made between our data and TSS09 results.

[2]Except for J234033+133300, which has $\mathrm{RM}_{\mathrm{TSS09}} = +56.7 \pm 6.3\,\mathrm{rad\,m^{-2}}$. This included source turned out to be unpolarised in our new observations, and is pivotal to our study of off-axis instrumental polarisation in this Chapter.

Table 4.1: Comparison between New Jansky VLA and TSS09 Results

Source (NVSS)	$\mathrm{RM_{VLA}}^a$ (rad m^{-2})	$\mathrm{RM_{Tcut}}$ (rad m^{-2})	$\Delta\mathrm{RM}^b$ (rad m^{-2})	$\lvert\Delta\mathrm{RM}\rvert/\sigma^b$	$\Delta S/S_{1.4\,\mathrm{GHz}}{}^c$ (%)	α_L
J111857+123442†	$+81.3 \pm 13.5$	$+194.1 \pm 5.9$	-112.8 ± 14.7	7.67	-13.9^d	-0.232 ± 0.003
J084701−233701	$+353.2 \pm 9.2$	$+462.5 \pm 15.8$	-109.3 ± 18.3	5.99	$+7.5$	-0.233 ± 0.012
J170934−172853†	$+111.2 \pm 4.7$	$+193.7 \pm 14.7$	-82.4 ± 15.4	5.34	$+33.0$	-0.077 ± 0.007
J224549+394122$^{\dagger\odot}$	-269.7 ± 2.1	-279.4 ± 1.2	$+9.7 \pm 2.4$	4.12	$+7.0$	-0.988 ± 0.008
J094808−344010†	$+394.5 \pm 16.1$	$+330.1 \pm 11.6$	$+64.4 \pm 19.9$	3.24	-28.0	-0.373 ± 0.009
J090015−281758	$+350.1 \pm 2.9$	$+335.7 \pm 4.1$	$+14.4 \pm 5.0$	2.87	$+1.4$	-0.693 ± 0.006
J190255+315942†	$+261.0 \pm 5.3$	$+243.3 \pm 3.8$	$+17.7 \pm 6.5$	2.73	-9.0	-0.320 ± 0.003
J094750−371528$^\odot$	$+359.2 \pm 21.9$	$+293.1 \pm 23.4$	$+66.1 \pm 32.0$	2.07	-9.3	-0.755 ± 0.013
J220927+415834	-340.0 ± 5.2	-356.0 ± 6.0	$+16.0 \pm 8.0$	2.01	-5.3	-0.964 ± 0.006
J022915+085125†	-307.8 ± 102.3	-129.3 ± 8.3	-178.5 ± 102.7	1.74	$+3.9$	-0.581 ± 0.006
J092410−290606**	$+533.0 \pm 8.4$	$+513.5 \pm 9.1$	$+19.4 \pm 12.4$	1.57	-4.6	-0.955 ± 0.006
J154936+183500$^?$	-473.5 ± 14.4	-441.7 ± 14.9	-31.8 ± 20.7	1.54	-2.4	-0.797 ± 0.003
J091145−301305†**	$+237.6 \pm 5.5$	$+226.3 \pm 6.0$	$+11.2 \pm 8.1$	1.38	-4.4	-0.923 ± 0.011
J093349−302700	$+345.7 \pm 8.0$	$+331.5 \pm 10.0$	$+14.2 \pm 12.6$	1.12	-9.0	-0.972 ± 0.007
J220205+394913	-358.7 ± 5.8	-365.3 ± 6.7	$+6.6 \pm 8.9$	0.75	-2.3	-1.140 ± 0.009
J093544−322845**	$+440.5 \pm 25.8$	$+411.0 \pm 33.2$	$+29.6 \pm 42.0$	0.70	-4.3	-0.857 ± 0.006
J162706−091705**	-328.7 ± 9.8	-318.4 ± 15.9	-10.4 ± 18.7	0.55	$+0.9$	-1.061 ± 0.013
J235728+230226†	$+30.8 \pm 103.1$	$+82.0 \pm 13.1$	-51.2 ± 103.9	0.49	-0.6	-0.863 ± 0.007
J083930−240723	$+345.6 \pm 8.2$	$+351.7 \pm 13.1$	-6.1 ± 15.5	0.39	-5.2	-0.904 ± 0.010
J163927−124139**	-329.1 ± 4.7	-325.0 ± 9.6	-4.1 ± 10.7	0.38	$+0.5$	-0.822 ± 0.005
J224412+405715†	-325.9 ± 6.0	-325.7 ± 13.0	-0.2 ± 14.3	0.01	$+11.7$	$+0.015 \pm 0.008$
J084600−261054$^\times$	—	—	—	—	-2.9	-0.437 ± 0.007
J234033+133300$^\times$	—	—	—	—	$+2.8$	-1.252 ± 0.005

NOTE—Sorted by $|\Delta\mathrm{RM}|/\sigma$ in descending order
[a] Using our new data in the NVSS bands only
[b] $\Delta\mathrm{RM} = \mathrm{RM_{VLA}} - \mathrm{RM_{Tcut}}$
[c] $\Delta S = S_{1.4\,\mathrm{GHz}} - S_\mathrm{Ncut}$
[d] S_Ncut from the original NVSS has been replaced by S_Tcut from TSS09 instead (see Chapter 4.4.1)
† Out-*liars* ($n\pi$-ambiguity sources; see Chapter 3)
$^\times$ Unpolarised sources (less than the 6σ cutoff level)
$^?$ Special case compared to TSS09 catalogue (see Chapter 3)
** Double point sources
$^\odot$ Extended sources

Using our new Jansky VLA data, we created Stokes I, Q, and U images for each source in the NVSS IF1 and IF2 respectively. All the images were made with Briggs visibilities weighting of `robust`$= 0$ (Briggs 1995) with a common restoring beam of $60'' \times 60''$ matching that of the TSS09 images (see below). On the other hand, we obtained cutout images of our target sources from TSS09. The TSS09 images were formed using the calibrated NVSS visibility data, independently for NVSS IF1 and IF2. A mild *uv*-taper was applied and led to their resulting beam of $60'' \times 60''$. We decided to determine the RM values from the TSS09 images instead of directly adopting the listed $\mathrm{RM_{TSS09}}$ values in their catalogue to ensure that the most direct comparison is performed. The Stokes I, Q, and U values of our sources were extracted from the two observations in identical ways, with the flux densities of the unresolved sources determined from the `CASA` task `IMFIT`, and that of double and extended sources by integrating within 6σ contours in total intensity.

4.3 Results

4.3.1 Rotation Measure Comparison with Taylor et al. (2009)

We perform a rigorous comparison between the polarisation properties of our new Jansky VLA results and that in TSS09. By using the Stokes Q and U values obtained from our Jansky VLA data in NVSS bands and TSS09 cutout images, we computed

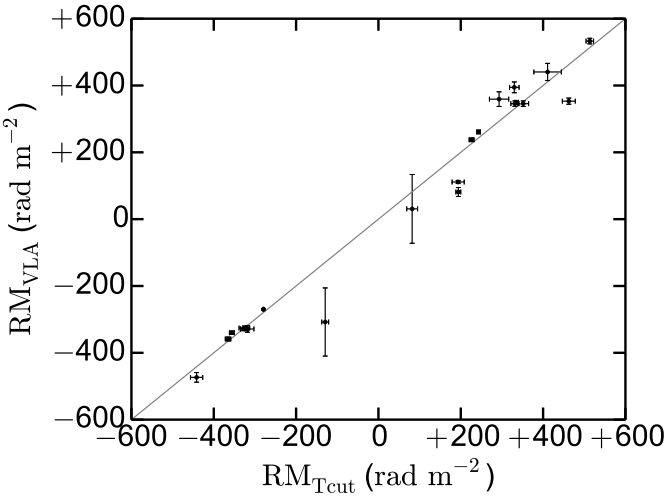

Figure 4.1: Narrowband RM from our observations against that from TSS09 cutout images. The $n\pi$-ambiguities have been corrected by using our broadband $\overline{\phi}$ values from RM-Synthesis. The solid line shows where the RM values of the two measurements are identical.

the PA values by

$$\mathrm{PA}_j = \frac{1}{2}\tan^{-1}\left(\frac{U_j}{Q_j}\right), \tag{4.3}$$

where the subscripts denote the IFs. Equation 4.2 is then used to compute the RM values. We used $\lambda_1 = 0.2196\,\mathrm{m}$ and $\lambda_2 = 0.2089\,\mathrm{m}$ for TSS09 cutouts, and $\lambda_1 = 0.2206\,\mathrm{m}$ and $\lambda_2 = 0.2085\,\mathrm{m}$ for our Jansky VLA data. The values of n were chosen such that the RM values would most closely match the broadband polarisation-weighted Faraday depths ($\overline{\phi}$) reported in Chapter 3, which is free of $n\pi$-ambiguity. The only exception is J154936+183500, since we did not find correspondence between our broadband $\overline{\phi}$ and the narrowband $\mathrm{RM}_{\rm TSS09}$ for this source[3], and therefore we chose n for this source such that the resulting RM values are the closest to its TSS09 value of $-426.8\,\mathrm{rad\,m^{-2}}$. As a sanity check, we further compared our RM values from TSS09 cutout images with the officially listed $\mathrm{RM}_{\rm TSS09}$ (corrected for $n\pi$-ambiguity as above) to ensure that these two sets of RM values agree with each other (within $\approx 1\sigma$), as would be expected since they were computed from the same data set.

The RM values obtained in the two data sets are shown in Figure 4.1, and listed in Table 4.1. The RM values from our new observations are denoted as $\mathrm{RM}_{\rm VLA}$, and that from TSS09 cutout images as $\mathrm{RM}_{\rm Tcut}$. We also listed the difference in RM ($\Delta\mathrm{RM} = \mathrm{RM}_{\rm VLA} - \mathrm{RM}_{\rm Tcut}$), as well as its magnitude divided by RM uncertainties (i.e., RM differences in units of σ; $|\Delta\mathrm{RM}|/\sigma$) in the same Table 4.1. It is found that nine (43 per cent) and five (24 per cent) out of our 21 polarised sources have deviating RM values by more than 2 and 3σ respectively. Assuming that the RM

[3]We determined in Chapter 3 that the disagreement between $\overline{\phi}$ and $\mathrm{RM}_{\rm TSS09}$ for this source is because of its highly non-linear PA across λ^2 resulting from its significant Faraday complexities.

Table 4.2: Total Flux Densities and Redshifts of the Targets

Source (NVSS)	$\alpha_{\rm L}$ ($S_\nu \propto \nu^{\alpha_{\rm L}}$)	$S_{1.4\,\rm GHz}$ (mJy)	$S_{\rm Ncut}$ [a] (mJy)	$S_{\rm NVSS}$ [b] (mJy)	z	Reference (z)
J022915+085125	-0.581 ± 0.006	649.2 ± 0.8	624.1 ± 2.4	609.0 ± 18.3	—	—
J083930−240723	-0.904 ± 0.010	261.6 ± 0.4	275.3 ± 1.9	268.3 ± 9.3	—	—
J084600−261054	-0.437 ± 0.007	1787.6 ± 2.0	1839.9 ± 2.1	1810.6 ± 54.3	—	—
J084701−233701	-0.233 ± 0.012	162.1 ± 0.3	150.0 ± 1.9	145.0 ± 4.4	0.0607 ± 0.0001^{s}	Huchra et al. (2012)
J090015−281758	-0.693 ± 0.006	530.8 ± 0.6	523.6 ± 2.6	511.6 ± 15.4	0.894^{s}	Perlman et al. (1998)
J091145−301305**	-0.923 ± 0.011	238.6 ± 0.5	249.2 ± 1.6	247.1 ± 7.8	—	—
··· a	-1.054 ± 0.022	81.0 ± 0.4	—	—	—	—
··· b	-0.858 ± 0.010	157.6 ± 0.3	—	—	—	—
J092410−290606**	-0.955 ± 0.006	590.2 ± 0.5	617.4 ± 1.9	625.4 ± 19.5	—	—
··· a	-1.011 ± 0.010	291.0 ± 0.5	—	—	—	—
··· b	-0.901 ± 0.009	299.2 ± 0.4	—	—	—	—
J093349−302700	-0.972 ± 0.007	253.6 ± 0.3	276.5 ± 2.1	273.0 ± 9.2	—	—
J093544−322845**	-0.857 ± 0.006	499.3 ± 0.7	521.0 ± 2.0	244.6 ± 7.4	—	—
··· a	-0.761 ± 0.010	227.5 ± 0.5	—	—	—	—
··· b	-0.941 ± 0.008	271.9 ± 0.5	—	—	—	—
J094750−371528⊙	-0.755 ± 0.013	602.3 ± 1.6	658.4 ± 2.0	473.9 ± 15.1	0.0412 ± 0.0002^{s}	Jones et al. (2009)
J094808−344010	-0.373 ± 0.009	245.6 ± 0.4	314.3 ± 2.2	312.4 ± 9.4	—	—
J111857+123442	-0.232 ± 0.003	2041.5 ± 1.0	1129.4 ± 0.9^{c}	1112.2 ± 33.4^{c}	2.125 ± 0.0003^{s}	Abolfathi et al. (2018)
J154936+183500	-0.797 ± 0.003	583.4 ± 0.4	597.4 ± 2.4	584.6 ± 20.6	1.442^{s}	Hewitt & Burbidge (1987)
J162706−091705**	-1.061 ± 0.013	130.8 ± 0.4	129.6 ± 1.6	125.0 ± 4.3	—	—
··· a	-0.730 ± 0.042	30.7 ± 0.3	—	—	—	—
··· b	-1.171 ± 0.015	100.2 ± 0.3	—	—	—	—
J163927−124139**	-0.822 ± 0.005	394.1 ± 0.4	392.0 ± 2.3	397.3 ± 12.5	—	—
··· a	-0.810 ± 0.006	247.5 ± 0.3	—	—	—	—
··· b	-0.843 ± 0.010	146.6 ± 0.3	—	—	—	—
J170934−172853	-0.077 ± 0.007	644.9 ± 0.9	432.2 ± 2.5	431.1 ± 12.9	—	—
J190255+315942	-0.320 ± 0.003	2923.5 ± 2.0	3186.9 ± 2.9	3203.8 ± 96.1	0.635^{s}	Hewitt & Burbidge (1987)
J220205+394913	-1.140 ± 0.009	143.8 ± 0.2	147.1 ± 1.7	144.8 ± 5.2	—	—
J220927+415834	-0.964 ± 0.006	283.5 ± 0.3	298.6 ± 1.7	292.4 ± 9.8	0.521 ± 0.029^{p}	Abolfathi et al. (2018)
J224412+405715	$+0.015 \pm 0.008$	260.4 ± 0.4	229.9 ± 2.4	226.2 ± 6.8	1.171^{s}	Ackermann et al. (2011)
J224549+394122⊙	-0.988 ± 0.008	11181.1 ± 16.0	10393.7 ± 5.5	4408.1 ± 136.4	0.081^{s}	Hewitt & Burbidge (1991)
J234033+133300	-1.252 ± 0.005	1868.0 ± 1.7	1815.9 ± 2.3	1829.1 ± 54.9	—	—
J235728+230226	-0.863 ± 0.007	634.9 ± 0.9	638.6 ± 2.3	624.7 ± 18.7	0.420 ± 0.120^{p}	Abolfathi et al. (2018)

[a] Our integrated flux densities from NVSS cutout images
[b] Listed integrated flux densities from the NVSS catalogue (Condon et al. 1998)
[c] Likely erroneous due to missing pointing in NVSS (see Chapter 4.4.1)
** Double point sources
⊙ Extended sources
[p] Photometric redshifts
[s] Spectroscopic redshifts

Table 4.3: Positions of Individual Components of the Spatial Doubles

Source (NVSS)	Right Ascension (J2000; h m s)	Declination (J2000; ° ′ ″)
J091145−301305		
··· a	09 11 42.47 ± 0.04	−30 13 19.26 ± 1.45
··· b	09 11 46.33 ± 0.02	−30 12 58.63 ± 0.74
J092410−290606		
··· a	09 24 10.09 ± 0.02	−29 05 45.36 ± 0.79
··· b	09 24 11.44 ± 0.02	−29 06 26.66 ± 0.75
J093544−322845		
··· a	09 35 43.98 ± 0.02	−32 28 48.51 ± 0.65
··· b	09 35 43.79 ± 0.02	−32 29 40.03 ± 0.60
J162706−091705		
··· a	16 27 04.53 ± 0.02	−09 16 55.99 ± 0.64
··· b	16 27 06.78 ± 0.01	−09 17 06.50 ± 0.20
J163927−124139		
··· a	16 39 27.09 ± 0.01	−12 41 26.41 ± 0.15
··· b	16 39 28.20 ± 0.01	−12 42 09.07 ± 0.27

NOTE — Identical to Table 3.2

uncertainties are Gaussian (which is approximately true given the high signal-to-noise ratio in polarisation of $\gtrsim 15$ for these sources), $|\Delta\mathrm{RM}|/\sigma$ should follow a folded normal distribution with $\mu = 0$ and $\sigma = 1$ (corresponding to the mean and standard deviation of the parent normal distribution, respectively). This distribution predicts much lower, namely, 4.6 and 0.3 per cent of the data deviating by more than 2 and 3σ respectively. It is evident that, with the entire sample of 21 sources considered as a whole, the RM values from TSS09 and our observations do not agree within their uncertainties.

4.3.2 Flux Densities and Spectral Indices

We report here the full-band (1–2 GHz) radio spectra of our targets. This has been deferred to here from Chapter 3 because of the relevance between Stokes I and RM time variabilities. The flux densities were extracted from 4 MHz channel images using the entire L-band (see Chapter 3.2.2), and were fitted for each source with a simple power law:

$$S_\nu = S_{1.4\,\mathrm{GHz}} \cdot \left(\frac{\nu}{1.4\,\mathrm{GHz}}\right)^{\alpha_\mathrm{L}}, \tag{4.4}$$

where S_ν is the flux density at frequency ν, and α_L is the spectral index in L-band. The values of $S_{1.4\,\mathrm{GHz}}$ and α_L are listed in Table 4.2, with the radio spectra shown in Figure C.1 in Appendix C.1. For double sources, apart from fitting the radio spectra of each of the spatial components (listed in Table 4.3), we also added the flux densities together (with uncertainties added in quadrature) to obtain a joint fit, which facilitates comparison with the integrated flux densities reported in the NVSS (S_NVSS;

also in Table 4.2), as well as other lower resolution radio studies. We do not see clear evidence of deviations of the radio spectra from the simple power law for any of the sources. We note the significant discrepancies between $S_{1.4\,\mathrm{GHz}}$ and S_{NVSS} for the double / extended sources J093544−322845, J094750−371528, and J224549+394122. The differences may be due to sub-optimal spatial fitting to these resolved sources in the NVSS catalogue. We therefore extracted the flux densities of our sample from NVSS cutout images (S_{Ncut}), also listed in Table 4.2. Indeed, we see much better agreement between $S_{1.4\,\mathrm{GHz}}$ and S_{Ncut} for the above three sources, but for four of our other targets (J094808−344010, J111857+123442, J170934−172853, and J224412+405715) we still see differences in flux densities by more than 10 per cent (see Chapter 4.4.1).

4.4 Comparisons with NVSS Results

4.4.1 Discrepancies in Total Intensities

Before comparing the flux densities between our 2014 observations and that of the NVSS in the 1990s, we note the different absolute flux density scales applied. The NVSS used 3C 295 as the flux calibrator adopting the Baars et al. (1977) scale, while we used 3C 286 and 3C 138 following the Perley & Butler (2013a) scale. It has been suggested that the systematic differences between these two scales at 1.4 GHz is less than 4 per cent (Perley & Butler 2013a), though they further noted flux density variations of $\lesssim 5$ per cent for 3C 138 over $\approx$ 10 yr at 1.4 GHz. We have therefore chosen a modest cutoff of 10 per cent in flux density variations above which we are confident that the differences are not due to errors in flux calibrations alone.

We compared our broadband $S_{1.4\,\mathrm{GHz}}$ with S_{Ncut} obtained from NVSS cutout images by introducing a parameter (see Table 4.1)

$$\frac{\Delta S}{S_{1.4\,\mathrm{GHz}}} = \frac{S_{1.4\,\mathrm{GHz}} - S_{\mathrm{Ncut}}}{S_{1.4\,\mathrm{GHz}}}. \tag{4.5}$$

Four of our sources (namely, J094808−344010, J111857+123442, J170934−172853, and J224412+405715) have differences in total intensities of more than 10 per cent. These cannot be explained by flux calibration errors alone, and are likely linked to Stokes I time variabilities between NVSS and our observations (over roughly 20 years). As all these four sources are listed as compact in the original NVSS catalogue (angular size $< 20''$)[4], this is consistent with the general picture that the variable radio emission originates from the core of AGNs. We gathered flux density measurements of these sources in the literature up to $\sim$ 10 GHz and plotted them in Figure 4.2 to facilitate comparisons.

J111857+123442 shows the most extreme Stokes I disparity of about 45 per cent when compared with its NVSS value. However, as seen in Figure 4.2 the NVSS flux density is inconsistent with others' as well as ours. We looked into the NVSS image containing this source (C1112P12), and noticed that at the centre of NVSS pointing

[4]The angular size of J111857+123442 was reported as $2'' \times 1''$ in the FIRST survey (Becker et al. 1995).

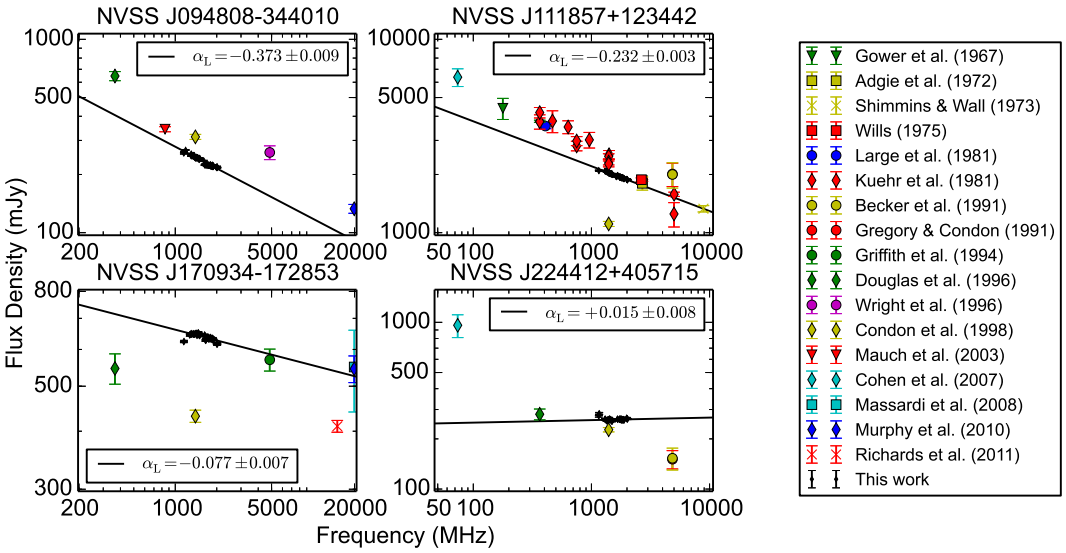

Figure 4.2: Radio spectra of the four sources with signs of Stokes I variabilities. Flux densities obtained from our new broadband measurements are shown as the black points, with the black solid line representing the best-fit power law spectra. The coloured data points represent flux densities from various studies.

11195+12260, which is the closest pointing to J111857+123442, there is a patch with radius of $2'$ where the intensity is exactly zero. Note that ($4° \times 4°$) NVSS images are weighted averages of their constituent snapshot images (one from each pointing; truncated at radius of $24'$), with the weights defined to be proportional to the square of the primary beam attenuation (Condon et al. 1998). Since individual NVSS pointings are separated by $26'$, the snapshot image of a missing pointing would result in a nearly circular area with $2'$ radius of zero pixel values, just as we found above. This suggests that the NVSS pointing 11195+12260 could be missing, and the NVSS flux density of J111857+123442 could be unreliable due to the weighted average algorithm. To further strengthen this argument, we computed the expected resulting flux density due to the missing pointing. There is a total of three NVSS pointings covering J111857+123442 (11195+12260, 11180+12392, and 11195+12524), with the source situated $11\farcm9$, $14\farcm6$, and $19\farcm4$ from the respective pointing centres, where the primary beam attenuation levels are 0.665, 0.541, and 0.338 respectively (equation 5 of Condon et al. 1998). If we replace the source flux density in the first pointing by zero, we obtain a weighted average flux density of 47.9 per cent of the true value, exactly matching the 47.9 per cent by comparing the NVSS value with that from TSS09 image. Even though the TSS09 images were also formed using the published NVSS visibility data, they were created by mosaicking with the primary beam response divided out, and any missing pointings would lead to an increase in root-mean-square (rms) noise instead of erroneous flux densities. Indeed, the flux density of 2042 ± 1 mJy from our broadband observation is much closer to the flux densities of 2324 ± 6 mJy from TSS09 cutout images and the integrated flux density of 2322.0 ± 0.4 mJy from the Faint Images of the Radio

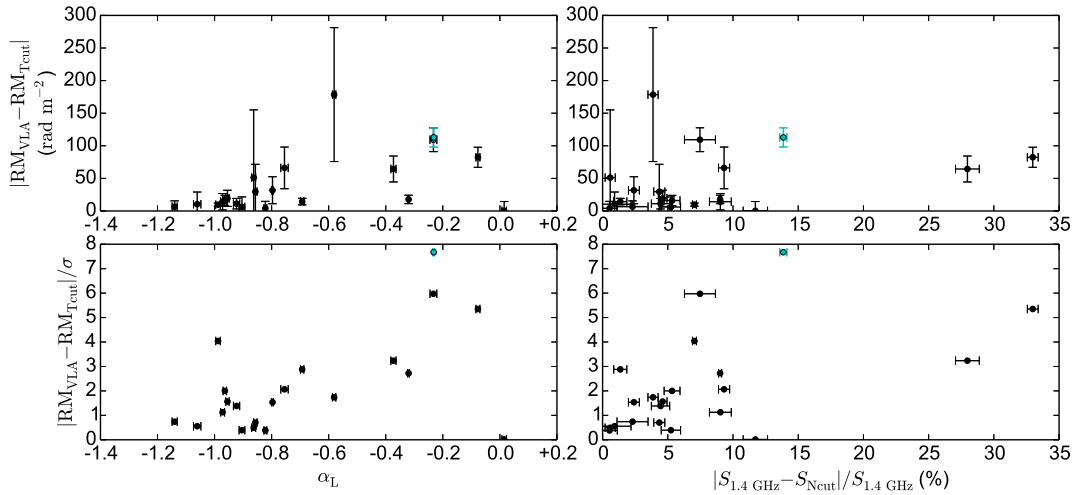

Figure 4.3: Plots of measures of RM time variabilities against that of Stokes I time variabilities of our 21 polarised sources. The cyan points represent J111857+123442, for which we used TSS09 cutout Stokes I value instead of that from NVSS cutout image (see Chapter 4.4.1).

Sky at Twenty-Centimeters (FIRST; Becker et al. 1995) catalogue. However, there is still a 13.9 per cent discrepancy which could be true Stokes I variability. In below, we compare our broadband $S_{1.4\,\mathrm{GHz}}$ with the flux density we obtained from TSS09 cutout for J111857+123442, instead of the S_{Ncut} from NVSS cutout images.

We first look into α_{L} of the four sources with significant Stokes I variabilities of more than 10 per cent. As expected, they all exhibit flat radio spectra ($-0.373 \leq \alpha_{\mathrm{L}} \leq +0.015$). We further compared the discrepancies in RM with Stokes I variabilities (Figure 4.3). It appears that flat spectrum sources are more likely to have significant RM discrepancies, though such differences in RM are not necessarily accompanied by Stokes I variabilities. Note that the RM differences between our new observations and TSS09 could be attributed to off-axis polarisation leakage instead of true RM time variabilities (see Chapter 4.4.2).

4.4.2 Discrepancies in Polarisation Properties

By comparing the polarisation properties of our sample in TSS09 with that from our new Jansky VLA observations (Chapter 3), we found that two of the sources are unpolarised. Furthermore, the RM values of our 21 polarised target sources from our new Jansky VLA observations do not agree with that from TSS09 within measurement uncertainties. As we will show below, both are likely linked to off-axis instrumental polarisation in the NVSS observations.

4.4.2.1 Unpolarised Sources

From the RM-Synthesis analysis on our new broadband (1–2 GHz) data in Chapter 3, we found that two of our targets (J084600−261054 and J234033+133300) have

polarisation fractions below our 6σ detection limits of 0.07 and 0.06 per cent, respectively. These polarisation levels are much lower than the respective values of 0.51 ± 0.02 and 0.59 ± 0.02 per cent reported in the TSS09 catalogue, as well as the 0.14 ± 0.03 and 0.09 ± 0.02 per cent in the original NVSS catalogue. Our on-axis broadband results are free of off-axis instrumental effects of the Jansky VLA, and are resilient against bandwidth depolarisation for sources with Faraday depths $\lesssim 10^4\,\mathrm{rad\,m^{-2}}$ (see Chapter 3). On the other hand, sources are in general placed significantly away from the pointing axis for surveys such as the NVSS, and therefore the off-axis polarisation leakage has to be taken care of for both the original NVSS catalogue (Condon et al. 1998) and TSS09. Corrections determined from holography scans were applied in the image plane in the original NVSS but not in TSS09, although the off-axis leakage pattern has been smoothed out by the mosaicking done to produce the TSS09 images. Therefore, the residual leakage level in the original NVSS (≈ 0.3 per cent; Condon et al. 1998) is significantly lower than in the NVSS RM catalogue (≈ 0.5 per cent; TSS09). However, the band-separated analysis of TSS09 has made them more robust against bandwidth depolarisation than the original NVSS.

Combining all the information above, we favour the interpretation that the polarisation signals detected from the two sources (J084600−261054 and J234033+133300) in the NVSS observations are dominated by off-axis polarisation leakage. In other words, we believe that these two sources are also unpolarised at the NVSS epoch, but were listed in the TSS09 catalogue just because the residual off-axis instrumental polarisation have made them appear polarised falsely. These two sources lie $10\farcm3$ and $12\farcm3$ away from the respective closest pointing centres of NVSS fields 08465−26188 and 23405+13453. At such angular distances, the (uncorrected) off-axis linear polarisation leakage is at ~ 1 per cent level (see Figure 14 of Condon et al. 1998), consistent with the measured values of these sources in the RM catalogue. However, we cannot completely rule out the possibility of changes in the observed polarisation fraction due to time variabilities (e.g. Aller 1970; Rudnick et al. 1985; Anderson et al. 2019).

4.4.2.2 Rotation Measure Discrepancies

By comparing our results from new Jansky VLA data in NVSS bands with TSS09, we found that the RM values derived from the two observations do not agree within their measurement uncertainties (see Chapter 4.3.1). We first rule out the possibility that the observed RM discrepancies are due to PA calibration errors, as we do not see systematic trends in ΔRM by grouping the target sources by the associated PA calibrators used in our observations. Another explanation to the RM disparity is genuine RM time variabilities, which can occur when a jet component near the AGN core is traversing along the jet and illuminating different parts of the foreground magnetised plasma near the jet at different epochs. Changes in RM of ≈ 100–$1000\,\mathrm{rad\,m^{-2}}$ have been noted for observations at $\gtrsim 10\,\mathrm{GHz}$ within as short as a few months (e.g. Zavala & Taylor 2001; Hovatta et al. 2012), and much lower values of $\approx 10\,\mathrm{rad\,m^{-2}}$ at 1.4 GHz have been reported over $\approx 20\,\mathrm{yr}$ (e.g. Anderson et al. 2016). This apparent variability for our targets will be further investigated with followup broadband polarisation observations

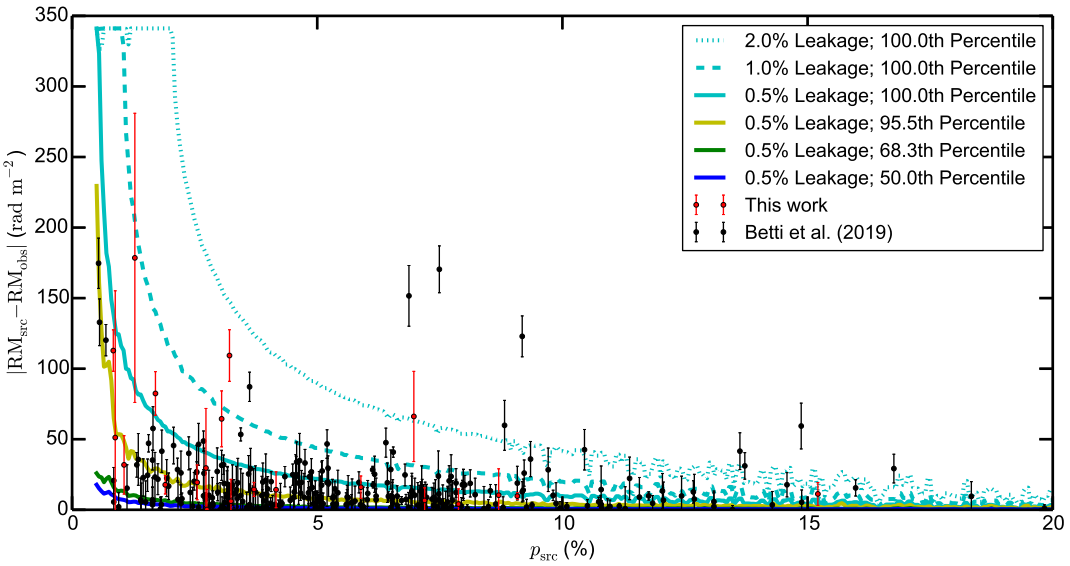

Figure 4.4: Simulation results of the off-axis polarisation leakage effects on the measured RM values reported in the TSS09 NVSS RM catalogue. The y-axis shows the difference between true and observed RM due to the added leakage, and x-axis is the true polarisation percentage. With injected leakage level of 0.5 per cent of the Stokes I flux densities, boxcar percentiles (with binning width of 0.1 per cent) from the 37,543,000 realisations were computed and shown as the colour solid lines. The 100.0th percentile (i.e. maximum) lines with leakage levels of 1.0 and 2.0 per cent are also shown for comparison. We also over-plot our 21 polarised target sources as red points, and the 282 Smith Cloud sources (Betti et al. 2019) as black points. For these sources, the y-values are the difference in RM between TSS09 and new Jansky VLA results.

(Ma et al. in prep; see Chapter 6.5.3). Finally, the discrepancies in measured RMs could also be attributed to some unaccounted systematic uncertainties in either or both of the observations, leading to underestimated uncertainties in RM. Here we propose that the disagreement in RM is mostly caused by residual off-axis polarisation leakage in the NVSS RM catalogue, as it can be thought of as adding a leakage vector[5] to the source polarisation vector, modifying the measured PA values and thus the resulting RM. In the following, we quantify the effect of off-axis leakage on RM_{TSS09} by simulations.

[5]Complex polarisations behave as vectors in the QU-plane, and can be simply added together. However, note that polarisation planes in the physical space do not add up as vectors (e.g. orthogonal polarisation planes cancel out each other).

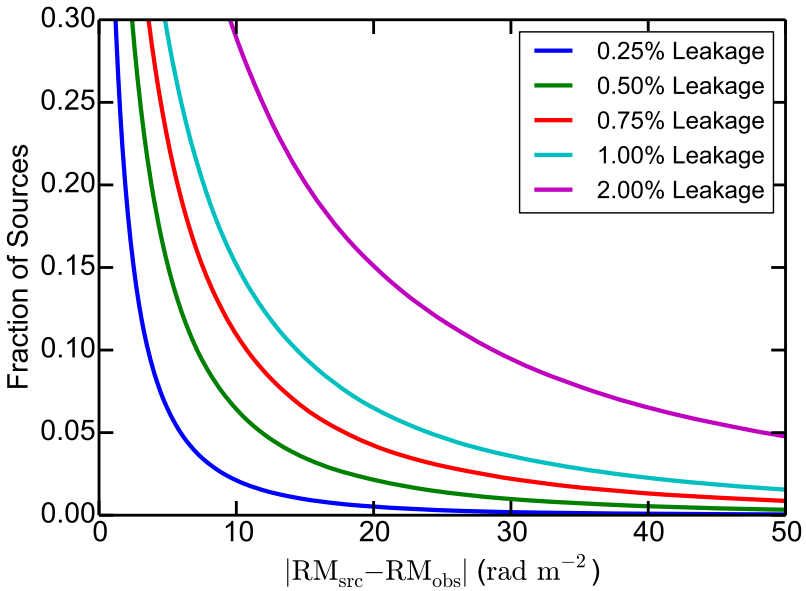

Figure 4.5: The inverse cumulative distribution function (1 − CDF) of the difference in RM due to off-axis polarisation leakage from our simulation. Injected leakage levels of 0.25, 0.50, 0.75, 1.00, and 2.00 per cent are adopted and shown here.

4.5 Simulating the Effects of Off-axis Instrumental Polarisation

4.5.1 Simulation Setup

We took the reported radio properties of the 37,543 sources in the NVSS RM catalogue to construct the source true polarisation vectors at the two NVSS bands by

$$\mathbf{P}_{j,\mathrm{src}} = Q_{j,\mathrm{src}} + iU_{j,\mathrm{src}} = \mathrm{PI}_{\mathrm{src}} \cdot e^{2i(\mathrm{PA}_0 + \mathrm{RM}_{\mathrm{src}} \cdot \lambda_j^2)}, \tag{4.6}$$

where the subscript j denotes the two NVSS IFs, and λ_{j} is the centre (in frequency space) wavelength of the two IFs with $\lambda_1 = 0.2196\,\mathrm{m}$ and $\lambda_2 = 0.2089\,\mathrm{m}$. We adopted the polarised intensity listed in the TSS09 catalogue as $\mathrm{PI}_{\mathrm{src}}$ and the RM from TSS09 as $\mathrm{RM}_{\mathrm{src}}$. Although we have set up the simulation by taking the listed TSS09 values as the source true values while in reality they should be taken as the observed values with polarisation leakage added in, we argue that our simulation results would still be representative of the general statistics of the TSS09 catalogue given its large sample size. A full treatment taking the listed TSS09 values as the observed values from our simulations will be presented in the future (see Chapter 6.5.2). It is assumed that all the sources have flat spectral indices ($\alpha_{\mathrm{L}} = 0$) and are Faraday simple. Since PA_0 were not reported in the TSS09 catalogue, we constructed 1,000 realisations for each source, each with a randomly picked PA_0 value within $[-\pi/2, +\pi/2]$ from a uniform distribution. This results in a total of 37,543,000 input realisations.

Then, we added leakage vectors ($\mathbf{P}_{\mathrm{leak}}$) to the true polarisation vectors to obtain

the observed polarisation vectors:

$$\mathbf{P}_{j,\mathrm{obs}} = \mathbf{P}_{j,\mathrm{src}} + \mathbf{P}_{\mathrm{leak}}, \tag{4.7}$$

$$\mathbf{P}_{\mathrm{leak}} = (S_{\mathrm{NVSS}} \times 0.5\,\%) \cdot e^{2i\mathrm{PA}_{\mathrm{leak}}}. \tag{4.8}$$

The leakage vector has an amplitude fixed at 0.5 per cent of the NVSS Stokes I values, and $\mathrm{PA}_{\mathrm{leak}}$ again randomly picked within $[-\pi/2, +\pi/2]$ from uniform distribution for each realisation, identical at IF1 and IF2. In other words, it is assumed that the leakage amplitude does not depend on the source position within the telescope primary beam with respect to the pointing centre, which is justifiable as the mosaicking done to produce the TSS09 images is expected to smooth out the leakage amplitude within the primary beam compared to the original leakage pattern of Cotton (1994). Furthermore, it is assumed that the instrumental polarisation (both amplitude and PA) is not frequency dependent, although the legacy VLA off-axis leakage pattern in the NVSS configurations are in reality weakly dependent of both direction and frequency (Condon et al. 1998; Cotton 1994). The 0.5 per cent leakage level we adopted is motivated by the TSS09 reported polarisation fractions of the two unpolarised sources that we identified (J084600−261054 and J234033+133300; see Chapter 4.4.2.1). As a reference, if the NVSS off-axis polarisation leakage is left completely uncorrected, sources will experience leakage levels of about 0.3, 0.6, 1.6, and 2.4 per cent at distances of $5'$, $10'$, $15'$, and $20'$ away from the pointing centre respectively (see Table 1 of Cotton 1994), and TSS09 sources have an average offset from the closest pointing centre by about $9\farcm5$. We therefore argue that an input leakage level of 0.5 per cent is a reasonable value to adopt, though note again that the residual leakage pattern in TSS09 is expected to be smoothed out from mosaicking.

With the resulting polarisation vectors after adding in polarisation leakages, we computed the observed RM values ($\mathrm{RM}_{\mathrm{obs}}$) for each of the 37,543,000 realisations by Equations 4.3 and 4.2. The $n\pi$-ambiguity is resolved by choosing the closest possible RM value to $\mathrm{RM}_{\mathrm{src}}$.

4.5.2 Unaccounted RM Uncertainties due to Off-axis Leakage

To quantify the effect of off-axis polarisation leakage on the measured RM, we compared $|\mathrm{RM}_{\mathrm{src}} - \mathrm{RM}_{\mathrm{obs}}|$ against the true polarisation fraction ($p_{\mathrm{src}} = \mathrm{PI}_{\mathrm{src}}/S_{\mathrm{NVSS}}$) for the 37,543,000 simulation realisations. The RM differences reflect how much the injected leakage vectors alter the source true RM values. To clearly see the underlying statistics, instead of plotting each of the realisations, we performed boxcar binning of these data points with a binning width of 0.1 per cent in p_{src}, with the results at the 50.0th, 68.3th, 95.5th, and 100.0th percentiles plotted as the colour solid lines in Figure 4.4. We also tested different binning widths (0.05, 0.2, and 0.5 per cent) to ensure that they all show consistent results. As expected, sources with lower fractional polarisation are more susceptible to changes in RM due to the injected polarisation leakage. At true polarisation level of 1 per cent, the RM difference at 50th percentile (i.e. median) is $7.3\,\mathrm{rad\,m^{-2}}$, while that at 68.3th percentile (corresponding to 1σ significance) is $13.5\,\mathrm{rad\,m^{-2}}$. These numbers are comparable to the median RM uncertainties

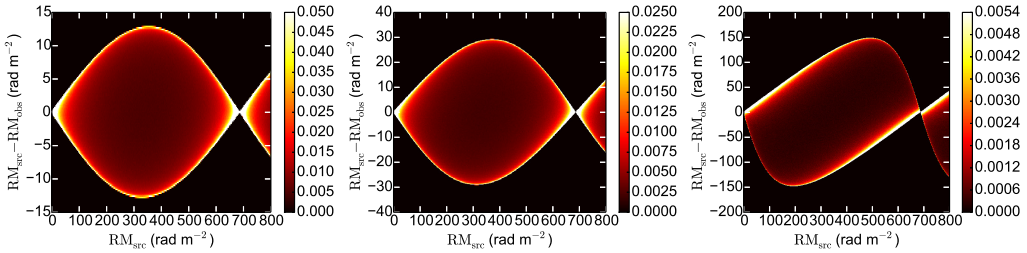

Figure 4.6: Simulation results showing the relationship between ($\mathrm{RM_{src}} - \mathrm{RM_{obs}}$) and $\mathrm{RM_{src}}$ as 2D-histograms (see Chapter 4.5.3). The left, middle, and right panels show the cases where the artificial target sources are strongly ($p = 8.5$ per cent), intermediately ($p = 3.8$ per cent), and weakly ($p = 0.8$ per cent) polarised, respectively. Each cut along the y-axis at a particular $\mathrm{RM_{src}}$ represents the artificial source with that corresponding $\mathrm{RM_{src}}$, chosen at a $1\,\mathrm{rad\,m^{-2}}$ interval from 0 to $+800\,\mathrm{rad\,m^{-2}}$. The same binning width of $0.2\,\mathrm{rad\,m^{-2}}$ along the y-axis has been used for all three panels, and we have normalised the histogram along each y-cut. Note that the y-axis and colour bar scales are different among the panels.

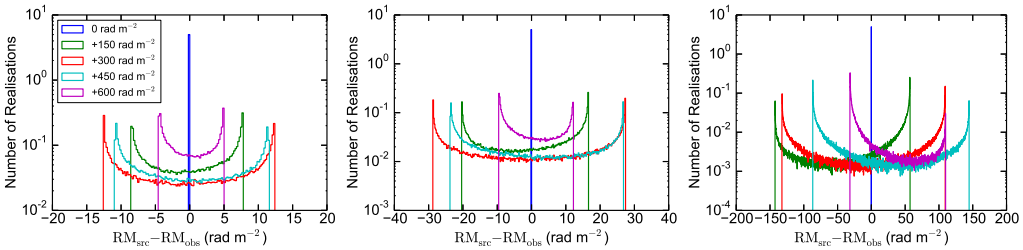

Figure 4.7: Simulation results showing the relationship between ($\mathrm{RM_{src}} - \mathrm{RM_{obs}}$) and $\mathrm{RM_{src}}$ (see Chapter 4.5.3), plotting cuts along the y-axis from Figure 4.6 at $\mathrm{RM_{src}}$ of 0, +150, +300, +450, and $+600\,\mathrm{rad\,m^{-2}}$ as the blue, green, red, cyan, and magneta lines, respectively. Note that the x- and y-axis scales are different among the panels, and the y-axis is in logarithmic scale.

of $10.8\,\mathrm{rad\,m^{-2}}$ reported in the TSS09 catalogue. This means the leakage effect introduces a significant extra RM uncertainty which has not been accounted for in the TSS09 RM catalogue, and therefore we suggest that care has to be taken when using the reported RM values of individual sources with $p \lesssim 1$ per cent.

The above simulation is also repeated by using different leakage levels (0.25, 0.75, 1.00, and 2.00 per cent). The 100.0th boxcar percentile lines for 1.00 and 2.00 per cent, which shows the maximum possible deviation of the observed RM from the true value at the respective leakage levels, are also shown in Figure 4.4. The flattening of these two curves at $p_{\mathrm{src}} \lesssim 2$ per cent are in the regime where the injected leakage overpowers the true polarisation signal, and should be ignored. We also show the inverse cumulative distribution function of $|\mathrm{RM_{src}} - \mathrm{RM_{obs}}|$ in Figure 4.5, from which we found that 2, 6, 11, 15, and 29 per cent of the NVSS RM sources have $|\mathrm{RM_{src}} - \mathrm{RM_{obs}}| \geq 10\,\mathrm{rad\,m^{-2}}$ at injected leakage levels of 0.25, 0.50, 0.75, 1.00, and 2.00 per cent respectively.

We further estimate how much TSS09 have underestimated their RM uncertainties

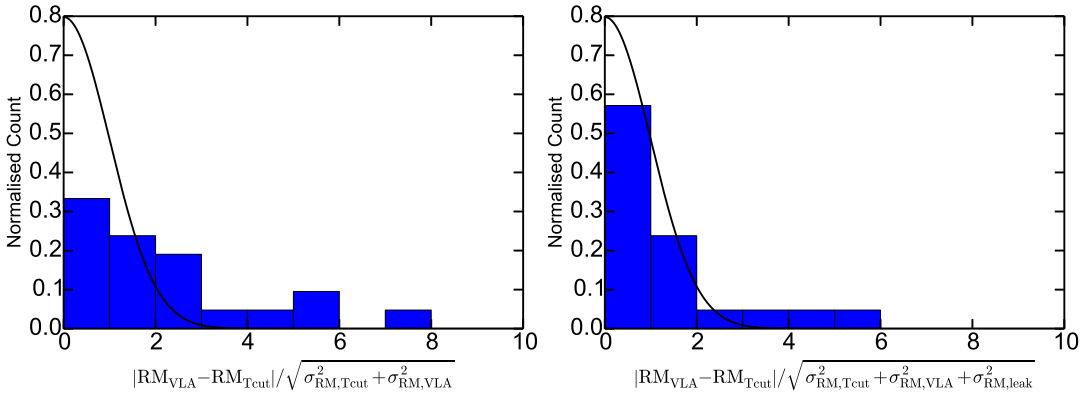

Figure 4.8: Histograms of RM differences between our new Jansky VLA observations and that from TSS09 cutout images, in units of RM uncertainties. The upper plot is in units of $\sqrt{\sigma^2_{\rm RM,Tcut} + \sigma^2_{\rm RM,VLA}}$ (i.e. without taking off-axis leakage into account), and the lower plot is in units of $\sqrt{\sigma^2_{\rm RM,Tcut} + \sigma^2_{\rm RM,leak} + \sigma^2_{\rm RM,VLA}}$ (i.e. with leakage taken into account). The black curves in both plots show a folded normal distribution with $\mu = 0$ and $\sigma = 1$.

for not having the off-axis leakage effect taken into account. To achieve this, we determined the rms value in $|{\rm RM_{src}} - {\rm RM_{obs}}|$ from the 1,000 simulation realisation for each of the 37,543 sources individually (denoted as $\sigma_{\rm RM,leak}$). This is then added in quadrature to the listed TSS09 RM uncertainties of the corresponding source ($\sigma_{\rm RM,TSS09}$) to yield the new RM uncertainties including the effect of off-axis leakage for each of the 37,543 sources ($\sigma_{\rm RM,new} = \sqrt{\sigma^2_{\rm RM,TSS09} + \sigma^2_{\rm RM,leak}}$). We calculated $\sigma_{\rm RM,new}/\sigma_{\rm RM,TSS09}$ at our default injected leakage level of 0.50 per cent, and obtained a median value of 1.09 out of the entire sample of 37,543 TSS09 sources. In other words, the TSS09 RM uncertainties should be increased by an average of nine per cent to incorporate the effect of off-axis polarisation leakage. Choosing different leakage levels of 0.25, 0.75, 1.00, and 2.00 per cent would yield median $\sigma_{\rm RM,new}/\sigma_{\rm RM,TSS09}$ of 1.03, 1.14, 1.19, and 1.39 instead.

Finally, we stress here that one should be cautious when applying the above results to individual TSS09 sources, since we find that the RM uncertainty from this off-axis polarisation leakage is also dependent on the actual RM of the source (Chapter 4.5.3). The statistics reported above are the average values out of the entire RM catalogue. Another point to note is that the distribution of $({\rm RM_{src}} - {\rm RM_{obs}})$ is found to be asymmetric, and is highly non-Gaussian (see Chapter 4.5.3).

4.5.3 Leakage RM Uncertainties Dependence on $\mathbf{RM_{src}}$

To investigate the relationship between the RM uncertainties due to off-axis leakage and the source true RM values, we repeated the simulation outlined in Chapter 4.5.1 but with manually selected $\rm RM_{src}$ values instead. In particular, we adopted the source properties of one of our targets, J091145−301305, as per TSS09 catalogue

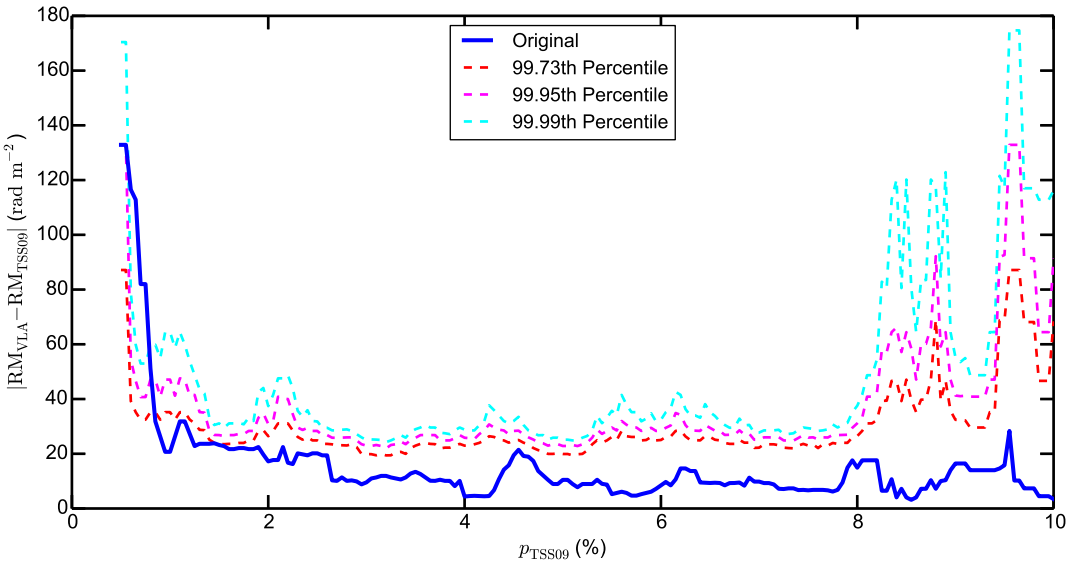

Figure 4.9: Difference in RM between TSS09 and new Jansky VLA observations. The boxcar median of the 303 sources (21 from this work, plus 282 from Betti et al. 2019) is shown by the blue solid line. The colour dashed lines are the 99.73th, 99.95th, and 99.99th percentile lines respectively from 10^7 shuffles of the y- with respective to the x-values (see Chapter 4.5.4). A boxcar binning width of 0.4 per cent is used here.

($S_{\mathrm{NVSS}} = 247.1\,\mathrm{mJy}$ and $\mathrm{PI} = 21.1\,\mathrm{mJy}$) *except* for the RM value. Instead, we have manually put in $\mathrm{RM_{src}}$ values of 0 to $+800\,\mathrm{rad\,m^{-2}}$ at $1\,\mathrm{rad\,m^{-2}}$ interval, resulting in 801 artificial sources. We chose J091145−301305 because it is strongly polarised ($p = 8.5$ per cent). We generated 10^5 simulation realisations for each artificial source (each with randomised $\mathrm{PA_0}$ and $\mathrm{PA_{leak}}$ as before; see Chapter 4.5.1), and plotted the distribution of the resulting $(\mathrm{RM_{src}} - \mathrm{RM_{obs}})$ individually for each artificial source as a 2D-histogram in the left panel of Figure 4.6. We further repeated the above by using the TSS09 source properties of two of our other targets — J093349−302700 ($S_{\mathrm{NVSS}} = 272.9\,\mathrm{mJy}$ and $\mathrm{PI} = 10.3\,\mathrm{mJy}$) as an intermediately polarised example ($p = 3.8$ per cent) and J235728+230226 ($S_{\mathrm{NVSS}} = 624.6\,\mathrm{mJy}$ and $\mathrm{PI} = 5.0\,\mathrm{mJy}$) as a weakly polarised example ($p = 0.8$ per cent). Both of these cases are also shown in Figure 4.6 as the middle and right panels, respectively.

From these simulations, we noted several interesting properties of the distribution of $(\mathrm{RM_{src}} - \mathrm{RM_{obs}})$ due to the injected off-axis polarisation leakage. Firstly, the distribution is a strong function of $\mathrm{RM_{src}}$, with the spread in $(\mathrm{RM_{src}} - \mathrm{RM_{obs}})$ being the widest at $\mathrm{RM_{src}} \sim 300\,\mathrm{rad\,m^{-2}}$, while it is identical to zero for the case of $\mathrm{RM_{src}} = 0$ and $\pm 682.3\,\mathrm{rad\,m^{-2}}$ (i.e., the injected leakage would not alter the RM value at all). These reported numbers, however, are only valid under the assumption that $\mathrm{PA_{leak}}$ are identical in the two IFs. Otherwise (i.e., if the off-axis leakage has a non-zero RM), the distributions shown in Figure 4.6 will be shifted horizontally by the leakage RM. Secondly, the distribution at any given $\mathrm{RM_{src}}$ (except for the identical zero cases mentioned above) is highly non-Gaussian, shaped as a double horn. This can be seen more

clearly in Figure 4.7 where we show cuts of the 2D-histograms at $\mathrm{RM_{src}}$ of 0, +150, +300, +450, and +600 rad m^{-2}. An interesting implication of this is that, the listed $\mathrm{RM_{TSS09}}$ values are in general *not* the most likely true RM of the sources, even for the highly polarised example with $p = 8.5$ per cent. Nonetheless, we find that the mean of the $(\mathrm{RM_{src}} - \mathrm{RM_{obs}})$ distribution at any given $\mathrm{RM_{src}}$ is almost identical to 0 rad m^{-2} for all cases. Finally, it can be seen that the distributions are asymmetric, with this property being more pronounced for sources with lower fractional polarisation. We will briefly explore the underlying causes of these properties in Appendix C.2.

4.5.4 Comparing Simulation with Our New Observations

We return to comparing the RM from our new observations ($\mathrm{RM_{VLA}}$) with that from TSS09 cutout images ($\mathrm{RM_{Tcut}}$) after taking this leakage effect into account. For each of our polarised target sources, we computed the RM uncertainty due to this off-axis leakage ($\sigma_{\mathrm{RM,leak}}$) by repeating the simulation (Chapter 4.5.1) but only considering our targets one at a time, and with a much higher number of simulation realisation of 10^5 per source. The rms of the resulting $|\mathrm{RM_{src}} - \mathrm{RM_{obs}}|$ values is taken as the $\sigma_{\mathrm{RM,leak}}$ of that source. We reiterate here that the distribution of $(\mathrm{RM_{src}} - \mathrm{RM_{obs}})$ is highly non-Gaussian (see Chapter 4.5.3).

The RM discrepancies between the two observations are plotted in the form of histograms in Figure 4.8, in units of $\sqrt{\sigma^2_{\mathrm{RM,Tcut}} + \sigma^2_{\mathrm{RM,VLA}}}$ (i.e. without taking leakage into account), as well as $\sqrt{\sigma^2_{\mathrm{RM,Tcut}} + \sigma^2_{\mathrm{RM,VLA}} + \sigma^2_{\mathrm{RM,leak}}}$ (i.e. with leakage taken into account), with $\sigma_{\mathrm{RM,Tcut}}$ and $\sigma_{\mathrm{RM,VLA}}$ being the RM uncertainties in TSS09 cutout and our Jansky VLA observations, respectively. If the difference in RM is only due to random Gaussian noise, the histogram should follow a folded normal distribution with $\mu = 0$ and $\sigma = 1$, which is shown as the black curves in both plots. Indeed, the histogram follows the expected distribution much more closely after taking into consideration the effect of the off-axis leakage. This means the RM discrepancies between our new Jansky VLA observations with that from TSS09 can be largely explained by the off-axis instrumental polarisation leakage at about 0.5 per cent level. The three sources still with significant RM discrepancies even after considering the off-axis leakage are J084701−233701 (at 5.0σ), J111857+123442 (at 4.8σ), and J170934−172853 (at 3.5σ). This could be due to genuine RM time variabilities, and will be investigated in a forthcoming paper (Ma et al. in prep; see Chapter 6.5.3).

4.5.5 Additional Evidence from the Betti et al. (2019) RM

To further confirm that the RM discrepancies are due to off-axis polarisation leakage, we supplemented our 21 sources with the 282 Smith Cloud sources from Betti et al. (2019) that are cross-matched with the TSS09 catalogue. Their sources were also placed on-axis in their broadband Jansky VLA observations in L-band and are thus unaffected by off-axis polarisation leakage. However, there are significant differences between their data and that of TSS09, namely (1) they used broadband 1–2 GHz data while TSS09 used narrowband observations, (2) their observations were conducted in

A array configuration instead of D array as did NVSS, and (3) their RM values were taken as the peak from RM-Synthesis analysis, while TSS09 performed two-point λ^2 fit to PA. Such differences in λ^2 coverage, *uv*-coverage, and analysis method can lead to disagreements between their RM values and the corresponding TSS09 RM values, which could be mistaken as caused by the off-axis polarisation leakage of TSS09 and/or RM time variabilities. A detailed, quantitative comparison between Betti et al. (2019) and TSS09 is therefore outside the scope of this work.

The combined 303 sources are plotted in Figure 4.4. We computed the boxcar median line for these 303 observed sources, as shown in Figure 4.9 (denoted as "original"). A boxcar binning width of 0.4 per cent is used here instead of the 0.1 per cent we used in Figure 4.4 because of the lack of observed sources in some p bins. We do not quantitatively compare this observed median line with the simulation results (Figure 4.4) directly, because the selection biases of the two observations preclude meaningful conclusions to be drawn. In particular, our target sources were selected to have $|\mathrm{RM_{TSS09}}| \gtrsim 300\,\mathrm{rad\,m^{-2}}$, while the Betti et al. sources are in close proximity to the Smith Cloud and therefore have a different RM distribution than that of the entire sample of TSS09. As the distribution of RM uncertainties due to off-axis leakage is a function of the source RM (Chapter 4.5.3), it would not be surprising if the median line here does not closely match the simulation results presented above in Chapter 4.5.2.

We focus here on the qualitative trend of the observed median line, from which we find a peak at the lower end of p ($\lesssim 1$ per cent). This is similar to what we see from our simulation, and is an important indicator that the discrepancies in RM are mainly due to off-axis polarisation leakage. However, this peak may also simply be a result of small number statistics — sources with larger $|\mathrm{RM_{VLA}} - \mathrm{RM_{TSS09}}|$ might just have low p coincidentally. In such case, $|\mathrm{RM_{VLA}} - \mathrm{RM_{TSS09}}|$ would actually have no correlation with p. We test this hypothesis with the bootstrapping method. With the 303 observed sources, we shuffle the $|\mathrm{RM_{VLA}} - \mathrm{RM_{TSS09}}|$ values with respect to p, and then construct a new boxcar median line (also at binning width of 0.4 per cent). This shuffling process is repeated for 10^7 times, yielding 10^7 median lines. As the final step, for each p value we evaluated the 99.73th, 99.95th, and 99.99th percentiles of $|\mathrm{RM_{VLA}} - \mathrm{RM_{TSS09}}|$ of the 10^7 median lines.

These percentile lines are plotted in Figure 4.9 together with the original observed median line. The percentile lines peak at several p values — at 0.5 per cent and between 8.0 and 10.0 per cent. These peaks are due to the scarcity of data points there, as can be seen in Figure 4.4. The original line is mostly featureless and lie well below the 99.73th percentile line for $p \gtrsim 1$ per cent, while for $p \lesssim 1$ per cent it peaks to a level close to the 99.95th percentile line. This suggests that the trend of higher $|\mathrm{RM_{VLA}} - \mathrm{RM_{TSS09}}|$ at lower p is statistically robust (at about 99.95 per cent confidence level), and that residual off-axis polarisation leakage is indeed introducing extra RM uncertainties to TSS09.

4.5.6 Comparing the Simulation Results with Stil et al. (2011)

When Stil et al. (2011) compared the RM structure function of the Galactic poles they derived from TSS09 results with that from Mao et al. (2010), they suggested that the RM uncertainties in TSS09 catalogue could be underestimated by a factor 1.22. This would explain the discrepancies between the two studies, though the authors did not explore the cause of such underestimated uncertainties. As we have shown above, off-axis polarisation leakage can introduce extra RM uncertainties to TSS09 results, and can potentially explain the factor 1.22 that they suggested.

To test this, we compiled the list of sources taken as the North Galactic Pole (NGP; 1,019 sources) and South Galactic Pole (SGP; 752 sources) samples by Stil et al. (2011), and investigated the $\sigma_{\rm RM,new}/\sigma_{\rm RM,TSS09}$ ratio of these sources. This ratio quantifies by what factor we should increase the TSS09 RM uncertainties in order to incorporate the effects of off-axis polarisation leakage, and were obtained in Chapter 4.5.2. Using our default leakage level of 0.5 per cent, we find that the median values of $\sigma_{\rm RM,new}/\sigma_{\rm RM,TSS09}$ for the NGP and SGP sources are both 1.02, much lower than the factor of 1.22 suggested by Stil et al. (2011). This suggests that there can be other sources of TSS09 RM uncertainties that have not been accounted for yet.

4.6 Conclusion

From our new broadband spectro-polarimetric observations of 23 NVSS RM sources with the Jansky VLA, we identified two unpolarised sources that are listed as ≈ 0.5 per cent polarised in the TSS09 catalogue. Moreover, we found significant discrepancies in RM for the remaining 21 sources by carefully comparing our new data with that from TSS09 using the same analysis methods and in almost identical frequency ranges. We attributed both of these effects to the residual off-axis instrumental polarisation in the TSS09 catalogue. We quantified its effects on the measured RM using simulations, and found that it is more significant for sources with lower fractional polarisation, leading to extra RM uncertainties of about $13.5\,{\rm rad\,m^{-2}}$ for TSS09 sources with $p \lesssim 1$ per cent. This is comparable to the median RM uncertainties of $10.8\,{\rm rad\,m^{-2}}$ reported in the TSS09 catalogue. For a typical TSS09 source, the RM uncertainties should be increased by nine per cent in order to incorporate the effects of off-axis leakage. We further demonstrated that the probability distribution of this extra RM uncertainty is asymmetric, highly non-Gaussian, and is a function of the source RM value. These properties must be carefully taken into account if one wishes to incorporate the off-axis leakage effects to individual sources, which will be the goal of our forthcoming Paper III.

The RM discrepancies of our sources can be largely explained by taking the extra RM uncertainties due to leakage into account, though three sources still show hints of RM time variabilities. Furthermore, by supplementing our data set with the 282 Smith Cloud sources from Betti et al. (2019), we confirmed (at confidence level of about 99.95 per cent) that sources with lower fractional polarisation have larger RM discrepancies between new on-axis Jansky VLA observations and that from TSS09. This is almost

certainly due to the residual off-axis polarisation leakage in TSS09 catalogue.

Chapter 5

The Complex Large-scale Magnetic Fields in the First Galactic Quandrant as Revealed by the Faraday Depth Profile Disparity

---

The Milky Way is one of the very few galaxies that exhibit large-scale magnetic field reversals. The existence of the field reversal in the first Galactic quadrant has been well established, but current models of the Galactic magnetic field diverge on its basic parameters, including the exact location, the field strength, and the geometry of the reversal region. Such discrepancies can be attributed to the lack of sight lines with reliably determined Faraday Depths (FDs) from extragalactic radio sources (EGSs) through the reversal region. An accurate characterisation of this feature in the Galactic magnetic field geometry is useful to the study of various branches of Galactic astrophysics, and can shed light on the details of the generation processes of the Galactic magnetic fields. We have therefore performed broadband (1–2 GHz) spectro-polarimetric observations with the Karl G. Jansky Very Large Array (VLA) to determine the FD values of 196 EGSs within ±5° of the Galactic mid-plane in the longitude range of 20°–52°, covering the aforementioned field reversal region and increasing the number of EGSs with robust FDs by a factor of five. Our joint analysis of the FD values of EGSs and pulsars resulted in the discovery of complex magneto-ionic structures in the field reversal region in the Sagittarius arm. This feature manifests as a clear FD disparity across the Galactic mid-plane within longitudes of 40°–52°, and can be explained by (1) an odd-parity disk field, (2) a significant FD contribution of an odd-parity halo field, or (3) contaminations by ionised structures that cannot be identified in Hα, H I, or radio continuum maps. We further compared our newly derived EGS FDs with the predictions of three major Galactic magnetic field models, and concluded that none of them can adequately reproduce our observational results. This shows the necessity of constructing a new Galactic magnetic field model that can capture our newly discovered FD disparity across the Galactic mid-plane.

Contents

5.1 Introduction

The magnetic fields of galaxies, including that of the Milky Way, can be decomposed into multiple components (see e.g., Haverkorn 2015; Beck 2016). The galactic magnetic fields can be divided according to the physical scales into the large-scale fields with coherence length of the order of the galactic scale ($\sim$ 1–10 kpc) and the small-scale fields with coherence length of $\lesssim$ 0.1 kpc. One can also divide the magnetic fields of galaxies by the spatial volumes in which they dominate in, with the disk fields occupying the galactic disk and the halo fields occupying the galactic halo. The current leading theory for the generation of the large-scale disk fields of galaxies is the α-Ω dynamo mechanism developed from the pioneering works in the 1970s (e.g., Parker 1971; Stix 1975; White 1978), while the small-scale disk fields are believed to originate from small-scale dynamo (Kazantsev 1968, see also Beresnyak & Lazarian 2015), or from tangling of the large-scale fields, both caused by violent astrophysical phenomena such as supernova explosions (e.g., Norman & Ferrara 1996; Mac Low & Klessen 2004; Haverkorn et al. 2008) or spiral shocks (e.g., Kim et al. 2006). The origin of the magnetic fields in galactic halos is still subjected to debates. Such fields could have emerged from the galactic disks and transported into the galactic halos by outflows (e.g., Brandenburg et al. 1993; Heald 2012; Krause 2019), or dynamo could be operating in the halos and generates the halo fields (Sokoloff & Shukurov 1990).

One way to measure the magnetic fields of the Milky Way is by polarisation observations of background extragalactic radio sources (EGSs; e.g., Simard-Normandin & Kronberg 1980; Brown et al. 2007; Taylor et al. 2009; Stil et al. 2011; Van Eck et al. 2011; Mao et al. 2012). As the polarised emission traverses through the foreground magneto-ionic media (including those in the Milky Way), it will experience the Faraday rotation effect, leading to a change in the polarisation position angle (PA; [rad])

by

$$\Delta\mathrm{PA} = \left[0.81 \int_{\ell}^{0} n_e(s) B_{\parallel}(s)\, \mathrm{d}s\right] \cdot \lambda^2 \equiv \phi \cdot \lambda^2, \tag{5.1}$$

where ℓ [pc] is the distance to the EGS, n_e [cm^{-3}] and $B_{\parallel}$ [μG] are the free electron density and magnetic field along the sight line (s), respectively, λ [m] is the observed wavelength, and ϕ [$\mathrm{rad\,m}^{-2}$] is the Faraday depth (FD) to the polarised source. The FD of a polarised source has been traditionally referred to as the rotation measure (RM) if it has been determined by a linear λ^2 fit to the measured PA (Chapter 2.2.2). The above equation shows that FD measurements from polarisation observations allow us to quantify the magnetic fields (both the strength and the direction along the sight lines) in the foreground. In particular, as FD contains information of the direction of the foreground magnetic fields (either pointing towards or away from the observer, which leads to positive and negative FD values, respectively), it allows identifications of magnetic field reversals (see below). Note, however, that the Milky Way is often not the only contributor to the FD of EGSs, since the intervening intergalactic medium (Vallee 1990; Vernstrom et al. 2019), cosmic filaments (O'Sullivan et al. 2019), galaxy clusters (Taylor et al. 2001; Bonafede et al. 2009; Govoni et al. 2010), and even the EGSs themselves (Zavala & Taylor 2001; Anderson et al. 2019) can also cause Faraday rotation. The FD values can be determined from broadband spectro-polarimetric observations by algorithms such as RM-Synthesis (Brentjens & de Bruyn 2005, see Chapter 2.2.3) or Stokes QU-fitting (Farnsworth et al. 2011; O'Sullivan et al. 2012, see Chapter 2.2.4).

By determining the FD values along numerous lines of sight passing through the astrophysical object of interest, one has effectively set up an FD grid with which the magnetic fields within the object can be measured (e.g., Gaensler et al. 2005; Harvey-Smith et al. 2011; Van Eck et al. 2011; Mao et al. 2017; Betti et al. 2019). For the case of the Milky Way, the large-scale magnetic fields can be recovered by spatial averaging of the FD values at an angular scale of $\sim 1^\circ$ in such FD-grid experiments (e.g., Sun et al. 2008; Mao et al. 2010; Van Eck et al. 2011; Mao et al. 2012, see Chapter 5.5.4.5 for details), while the small-scale fields can be studied by quantifying the spatial fluctuations of FD by structure function analysis (e.g., Minter & Spangler 1996; Haverkorn et al. 2008; Mao et al. 2010; Stil et al. 2011). Similar studies of the Galactic magnetic fields can be conducted using Galactic pulsars as well (e.g., Thomson & Nelson 1980; Noutsos et al. 2008; Han et al. 2018), with pulsars at different distances, as obtained from parallax measurements, H I kinematics, or dispersion measure (DM) values (see Lorimer & Kramer 2012), offering a direct tomographic view of the Galactic magnetic field geometry. Such studies, however, are usually bound to the Galactic disk where the pulsar number density is high, and are currently limited by the number of available pulsars with both measured FD (or RM) values and reliable distance estimates (see Chapter 6.4.1.1).

An accurate characterisation of the structure of the magnetic fields of the Milky Way has been difficult, primarily because our view from within the Milky Way makes it challenging to interpret the observational results. Nonetheless, it is generally believed

that the Milky Way hosts a unique magnetic field geometry among spiral galaxies — large-scale reversals of the disk field directions have been found between spiral arms (e.g., Thomson & Nelson 1980; Simard-Normandin & Kronberg 1980; Rand & Lyne 1994; Han et al. 2006; Sun et al. 2008; Van Eck et al. 2011; Jansson & Farrar 2012), and are rarely seen in external galaxies (Krause et al. 1989; Beck & Wielebinski 2013; Beck 2016; Stein et al. 2019). The exact details of such large-scale field reversals, including the number, the location(s), and the field strength, are not yet confidently determined, with Galactic magnetic field models in the literature suggesting diverging results (see Haverkorn 2015, for summary). In particular, most studies agree that a large-scale field reversal can be found in the Sagittarius arm in the first Galactic quadrant (Thomson & Nelson 1980; Simard-Normandin & Kronberg 1980; Rand & Lyne 1994; Sun et al. 2008; Van Eck et al. 2011), but it is unclear whether it continues to the fourth Galactic quadrant into the Carina arm (Frick et al. 2001) or the Scutum-Crux arm (Van Eck et al. 2011). Numerical simulations have suggested that such large-scale field reversals can be generated from α-Ω dynamo given that the initial turbulent field has a considerable strength (approximately equipartition; plausibly amplified by small-scale dynamo), combined with an efficient α-Ω dynamo (e.g. from a strong differential rotation), and these reversals can survive for $\gtrsim$ Gyr (Moss et al. 2012; Moss & Sokoloff 2013). A detailed characterisation of the large-scale field reversals of the Milky Way can allow further understanding in the physical conditions at the infancy stages of the magnetic field evolution of the Milky Way (see e.g. Moss & Sokoloff 2013), and an accurate understanding of the global Galactic magnetic field geometry is critical for many Galactic astrophysical studies (see Boulanger et al. 2018, see also Chapter 1.2).

The past decade has seen substantial efforts in improving the Galactic magnetic field models (e.g., Sun et al. 2008; Van Eck et al. 2011; Jansson & Farrar 2012). These field models are phenomenological, meaning that they were not derived from numerical simulations nor from analytical solutions of the α-Ω dynamo. Instead, their features are motivated by previous knowledge of the Milky Way (e.g., the presence of large-scale field reversals and the locations of the spiral arms) or other spiral galaxies (e.g. the pitch angles of magnetic fields and the presence of an X-shaped halo field for the Jansson & Farrar 2012 model), and the free parameters are then fitted to match observables such as the FD of EGSs and pulsars, and the diffuse synchrotron maps of the Milky Way (see Chapter 5.5.4.1 for more details). The aforementioned three Galactic magnetic field models all agree on a primarily clockwise magnetic field as viewed down from the Galactic north pole, with at least one large-scale field reversal (with anti-clockwise fields) required to explain the observations. However, as mentioned above, they all differ on the exact details such as the magnetic field strengths, the exact location(s) of the large-scale field reversal, and the geometries of the distinctly defined field regions.

The deviating results of the field models can at least be partially attributed to the lack of reliable FD (or RM) measurements towards Galactic volumes hosting complex magnetic field structures such as the large-scale field reversals. In particular, we identified the sky region of 20°–52° in Galactic longitude (ℓ) and within $\pm5°$ in Galactic latitude (b) that we will focus on in this study. The sight lines through this region intercept a large-scale field reversal in the Sagittarius arm according to the Sun et al. (2008)

and Van Eck et al. (2011) models, but have only 43 reliable RM measurements (one RM per 7.3 deg^2) from Van Eck et al. (2011). Specifically, the Van Eck et al. (2011) observations were performed with the legacy Very Large Array (VLA) at 1.4 GHz in spectral line mode, which allowed eradication of the $n\pi$-ambiguity but the bandwidth was insufficient for detailed studies in the sources' Faraday complexities. Although there are 106 reported RM values in that sky area (one RM per 3.0 deg^2) from the Taylor et al. (2009, hereafter TSS09) catalogue, their RM values in that particular region are especially susceptible to the $n\pi$-ambiguity[1] and thus can be unreliable (see Chapter 3.4.1.7). A new survey of polarised EGSs in this region is clearly necessary.

We performed broadband spectro-polarimetric observations with the Karl G. Jansky Very Large Array to determine the FD values of 196 EGSs in $20^\circ \leq \ell \leq 52^\circ$ and $-5^\circ \leq b \leq +5^\circ$ at a source density of one per 1.6 deg^2. The new polarised source density is almost a factor of five increase from that of Van Eck et al. (2011) in the same region. The goal is to form a dense FD grid for an accurate characterisation of the complex Galactic magnetic field structures there, which includes the large-scale magnetic field reversal in the Sagittarius arm. In this Chapter, we report the results from this study. The source selection criteria are presented in Chapter 5.2, and the details of the observations and the data reduction procedures are described in Chapter 5.3. The results from the RM-Synthesis analysis are shown in Chapter 5.4. Subsequently, we present our interpretation of the newly derived FD values in Chapter 5.5. Finally, we conclude our findings in the magnetic field configuration in the region of interest in Chapter 5.6.

5.2 Target Source Selection Criteria

In this study, we focus on the large-scale magnetic fields near the disk of the Milky Way in its first quadrant, where at least one large-scale magnetic field reversal has been identified (e.g., Thomson & Nelson 1980; Rand & Lyne 1994; Sun et al. 2008; Van Eck et al. 2011; Jansson & Farrar 2012; Han et al. 2018, see Figure 5.1). The field reversal region spans a wide range in Galactic longitude starting from $\ell = 0^\circ$ and, depending on the field model considered, can have noticeable effects on the EGS FDs to large longitudes. Following the Sun et al. (2008) and Van Eck et al. (2011) magnetic field models, the large-scale field reversals have the most significant contributions to FD at $\ell \approx 40^\circ$–60°, since these lines of sight pass almost tangentially to their field reversal rings. We have therefore determined a region of interest of $20^\circ \leq \ell \leq 52^\circ$ and $|b| \leq 5^\circ$ in Galactic coordinates. The lower limit in Galactic longitude was chosen to exclude the highly complex Galactic centre region (e.g., Law et al. 2011b, see also Han 2017), while the upper limit coincides with the lower limit of the Canadian Galactic Plane Survey (CGPS; Taylor et al. 2003), which has allowed studies of the magnetic fields in the $\ell \geq 52^\circ$ region (Brown et al. 2003; Ordog et al. 2017). The choice of the Galactic latitude range ensures a complete coverage of the Galactic disk fields — at a distance of 28.5 kpc to the far side of the Milky Way, a Galactic latitude of $|b| = 5^\circ$

[1] With their observational setup, sources suffering from the $n\pi$-ambiguity have listed RM values deviating from the true values by $\pm 652.9\,\mathrm{rad\,m^{-2}}$.

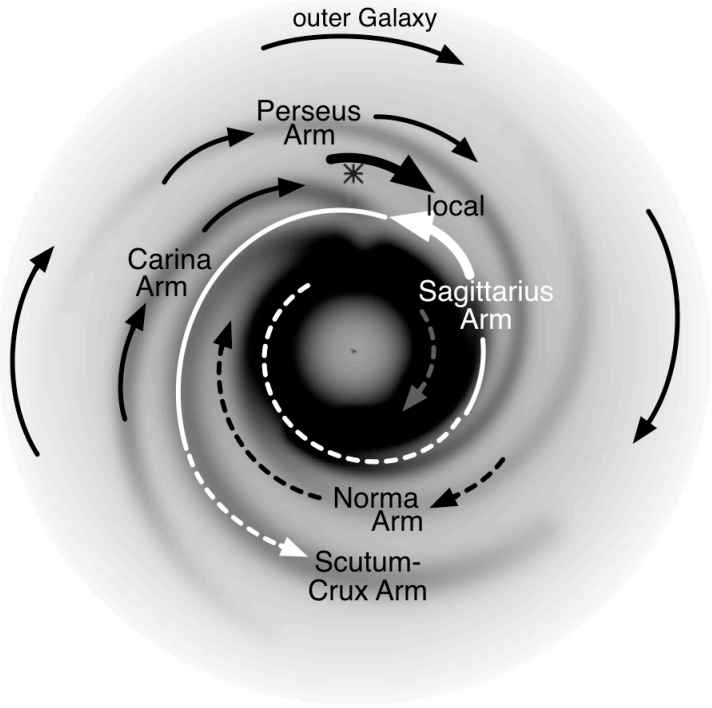

Figure 5.1: A schematic picture of the large-scale magnetic fields in the Galactic disk according to the Van Eck et al. (2011) model, looking down from the Galactic north pole. The arrows show the directions of the magnetic fields, with the white arrows depicting the large-scale field reversal. The dashed arrows represent regions where the magnetic field geometries are less certain given the available data. The location of the Sun is marked by the black asterisk. Image courtesy of Van Eck et al. (2011).

translates to an upper limit in the probed Galactic height of $|z| = 2.5\,\mathrm{kpc}$, well covering the free electron scale height of the Galactic thick disk of $\approx 1.8\,\mathrm{kpc}$ (Gaensler et al. 2008) as well as the Galactic disk magnetic field scale height of $\approx 1.5\,\mathrm{kpc}$ (Kronberg & Newton-McGee 2011).

Our target EGSs were selected from two criteria. First, we have chosen sources from the original NVSS catalogue (Condon et al. 1998) based on their listed polarisation properties: (1) NVSS (debiased) PI of more than 4σ, and (2) NVSS polarisation fraction of more than 0.5 per cent. The first criterion was imposed to ensure that a sufficient signal-to-noise (S/N) ratio in polarisation can be obtained within a modest amount of observing time, while the second criterion ensures that unpolarised sources that appear polarised as the result of the residual off-axis instrumental polarisation are not included (see Chapters 2.1.3.3 and 4.4.2.1). These targets will be referred to as the **NVSS targets** from hereon. However, by only considering these NVSS targets, a significant selection bias will be present in our sample as the original NVSS catalogue is highly susceptible to bandwidth depolarisation, which can reduce the observed PI by 50 per cent at $|\phi| \approx 220\,\mathrm{rad\,m^{-2}}$ owing to their wide bandwidths (see Chapter 2.1.3.2). This

would significantly impact this study, since within the region of interest the expected $|\phi|$ of the EGSs can reach $\gtrsim 600\,\mathrm{rad\,m^{-2}}$ (e.g., Van Eck et al. 2011). Using NVSS targets alone would lead to a bias against these expected large $|\phi|$ values. To recover and include these EGSs, we further selected all sources in the region of interest in the TSS09 RM catalogue that were not selected as NVSS targets. These targets will be referred to as the **TSS09 targets** in this Chapter. Finally, known Galactic sources, along with sources that lie within $2'$ from other nearby targets, are identified and excluded from the observations. The former class of sources are outside of the scope of this work which aims to measure the FD of EGSs only, while the polarisation properties of the latter class of sources can be recovered from the images of their neighbouring targets. Covering two or more close-by targets with a single pointing can allow a more optimised use of the granted observing time, given that the off-axis polarisation leakage would not affect the final results (see below). All these excluded sources are listed in Table 5.1. This results in a list of 177 targets, which we shall call the **on-axis targets** (when referring to the sources themselves) or the **target fields** (when referring to the pointings which can cover multiple targets at once).

An interesting point we noted about the excluded Galactic objects that appear to be polarised is that many of them are associated with H II regions or planetary nebulae, both with bremsstrahlung as the dominant emission mechanism at $\approx 1\,\mathrm{GHz}$ and are therefore expected to be completely unpolarised. A quick check (see Table 5.1) has revealed that most of such objects (10 out of 15) were initially selected by the TSS09 targets criteria in our study. This means the sources are correctly reported as unpolarised in the original NVSS, and the apparent polarisation signals from these sources in the TSS09 catalogue can be attributed to off-axis instrumental polarisation, which we have shown in Chapter 4 that the TSS09 catalogue suffers from. On the other hand, five out of 15 of the above objects were selected through the NVSS targets criteria, meaning that they are falsely listed as being polarised in the original NVSS. It would be interesting to explore further for the reason behind this, but such investigations are outside of the scope of this thesis.

5.3 Observations and Data Reduction

New broadband spectro-polarimetric observations of the 177 target fields were performed with the Jansky VLA in L-band (1–2 GHz) in D-array configuration under project code 18A-332. The observations took place on 2018 September 1–10 in seven observing blocks for a total of 15 hours. In each observing block, 3C 286 was observed and was used as the absolute flux, bandpass, and PA calibrator, and J1407+2827 was observed as the unpolarised leakage calibrator. Depending on the observing block, either J1822−0938, J1859+1259, J1941+1026, or J1942+1026 was observed as the phase calibrator. On-axis observations of the 177 target fields were conducted, with an integration time of 3–5 minutes per source.

The Common Astronomy Software Applications (`CASA`) package (version 5.3.0; McMullin et al. 2007) was used for all data reduction procedures. Measurement sets from

Table 5.1: List of Sources Excluded from the Observations

Excluded Source (NVSS)	Reason	Note
J182530−093521^N	Galactic	PSR B1822−09
J183333−103405^N	Galactic	PSR J1833−1034 or SNR G21.5−0.9
J183353−080726^T	Galactic	H II region PMN J1833−0807
J183513−080644^T	Galactic	H II region PMN J1835−0806
J183813−064847^T	Galactic	Part of PN G025.4−00.2
J183815−064750^T	Galactic	Part of PN G025.4−00.2
J183820−064703^N	Galactic	Part of PN G025.4−00.2
J184735−020143^N	Galactic	Part of SNR PKS 1844−02?
J184736−015632^T	Galactic	Part of SNR PKS 1844−02
J184737−015856^N	Galactic	Part of SNR PKS 1844−02
J184741−015441^N	Galactic	Part of SNR PKS 1844−02
J184746−015451^N	Galactic	Part of SNR PKS 1844−02
J185250+005527^N	Galactic	H II region G033.9+00.1
J185612+075340^T	Galactic	H II region G040.5+02.5
J185618+070726^T	Galactic	PN G039.8+02.1
J191421+110913^T	Galactic	H II region G045.5+00.1
J192214+140319^T	Galactic	H II region G048.9−00.3
J192223+142856^N	Galactic	Part of H II region G049.4−00.3?
J192234+153010^T	Galactic	H II region G050.2+00.3
J192312+142654^T	Galactic	Part of H II region G049.4−00.3
J192318+142915^N	Galactic	Part of H II region G049.4−00.3
J192353+143545^N	Galactic	Part of H II region G049.4−00.3
J193214+105931^N	Galactic	PSR B1929+10
J183417+004939^N	Nearby Field	Covered by J183418+004852
J183515+014611^N	Nearby Field	Covered by J183511+014620
J183842−013105^T	Nearby Field	Covered by J183840−012957
J184422−041746^N	Nearby Field	Covered by J184415−041757
J185731+111053^N	Nearby Field	Covered by J185728+111021
J192922+095901^N	Nearby Field	Covered by J192922+095808

NOTE — PN: planetary nebula; PSR: pulsar; SNR: supernova remnant.

^{N} Originally selected by the NVSS targets criteria.

^{T} Originally selected by the TSS09 targets criteria.

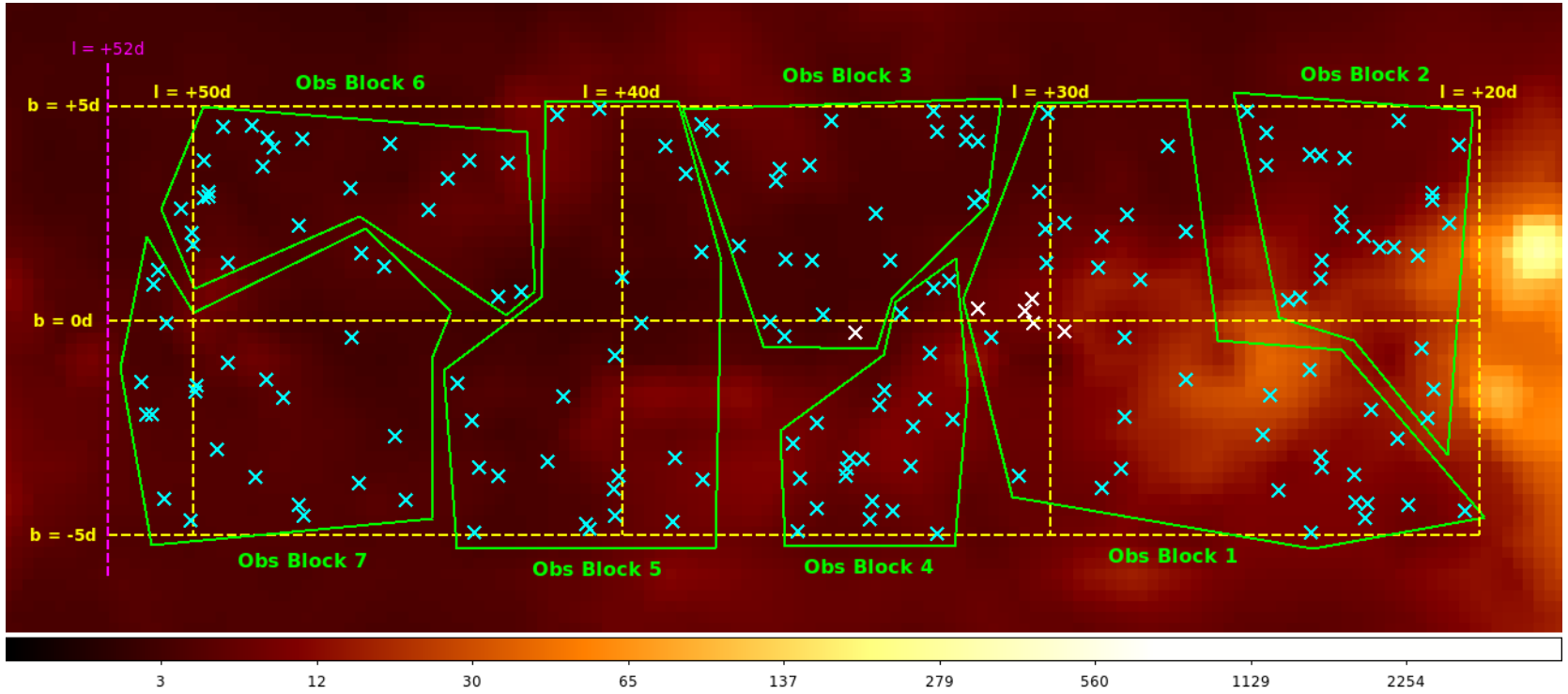

Figure 5.2: The spatial distribution of the 177 on-axis EGS targets shown as cyan crosses. The six sources discarded after the observations (Table 5.2) are marked in white. The groupings of the target sources into the seven observing blocks are demonstrated by the green polygons. The background heat map shows the Hα intensities from the WHAMSS (Haffner et al. 2003, 2010) in units of Rayleighs. The yellow vertical (horizontal) lines mark the Galactic longitudes (latitudes) in 10° (5°) interval, and the magenta line shows the upper limit in Galactic longitude of 52° sampled by this project.

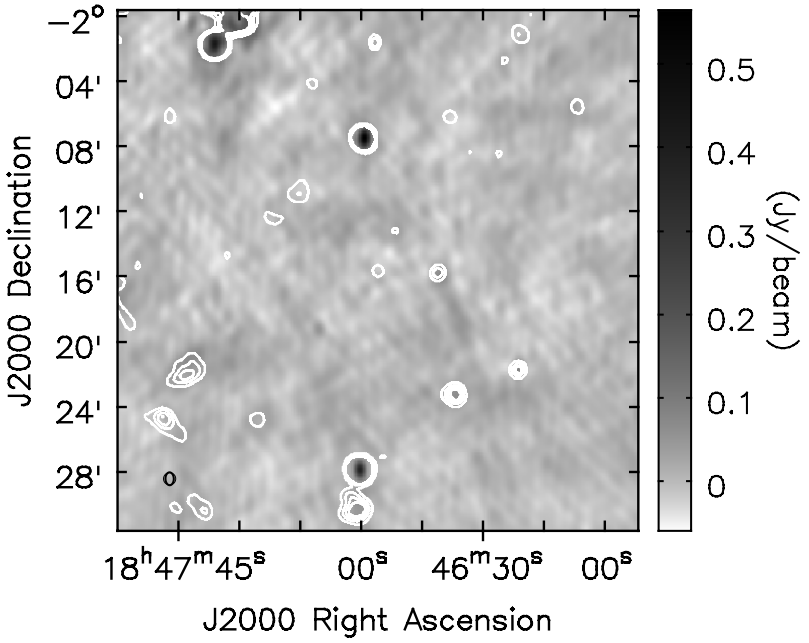

Figure 5.3: Stokes I image of NVSS J184655−021535 from our new Jansky VLA observations, an example of undetected sources that have been discarded. The size of the synthesised beam is shown as the black open ellipse at the lower left corner. The white contours represent the NVSS Stokes I image at $[3, 6, 9, 12] \times \sigma$ levels, with $\sigma = 3.8\,\mathrm{mJy\,beam^{-1}}$ being the rms noise of the NVSS image.

the seven observing blocks were calibrated independently. Firstly, Hanning smoothing in frequency space was applied to all visibility data to remove the Gibbs phenomenon, and the antenna position calibrations were applied. It is followed by flagging to remove the corrupted data due to RFI or phase instabilities. Afterwards, delay, flux, bandpass, gain, on-axis instrumental polarisation, and the polarisation position angle calibrations were performed using the appropriate calibrators as stated above. Lastly, one iteration of phase self calibration solutions were determined for all target fields independently. They were applied only if significant improvements (reduction by more than 10 per cent) to the image rms noises were achieved.

Channel images of the target fields in Stokes I, Q, and U across L-band were then formed. Instead of using the native 1 MHz channel widths, visibility data in 4 MHz channels were combined to form each binned channel image. This was chosen to lower the noise level in individual channel images (by a factor of two), and is not expected to cause significant loss of information since the Hanning smoothing procedure above has already degraded the effective spectral resolution by a factor of two. The `CASA` task `TCLEAN` was used to form the images, adopting a Briggs visibilities weighting with `robust` $= 0$ (Briggs 1995) for an optimisation between the final angular resolution and the image rms noise. Deconvolution of the dirty images were performed using the Clark algorithm, with no further smoothing done to the resulting images since the channel images will not be directly combined. Finally, primary beam corrections were applied

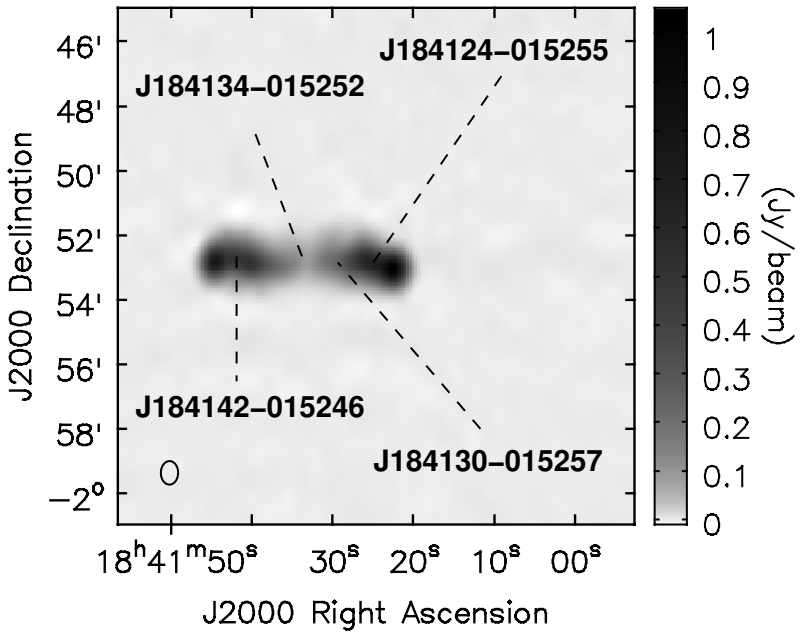

Figure 5.4: Stokes I image of NVSS J184124−015255 from our new Jansky VLA observations, an example of spatially spatially blended targets within a target field. The positions of the on-axis target J184124−015255, along with the three off-axis targets (J184130−015257, J184134−015252, and J184142−015246), are labelled. The size of the synthesised beam is shown as the black open ellipse at the lower left corner.

to all images. The typical angular resolution of the images is $50'' \times 42''$ at 1.5 GHz, and the typical rms noise of the Stokes I, Q, and U channel images (per 4 MHz) near pointing centres are 4.3, 1.4, and 1.5 mJy beam^{-1}, respectively.

For each of the target fields, we further identified nearby **off-axis targets** by consulting the NVSS catalogue (Condon et al. 1998) to complement the on-axis sample. Some, but not all, of these sources are the ones excluded due to their spatial proximities to other target fields (see Table 5.1). All sources that (1) are within $5'$ from at least one of the pointing centres and (2) have reported NVSS flux densities of ≥ 20 mJy are considered. At $5'$ from the pointing centre, the primary beam attenuation level is still close to unity (0.86 at 2 GHz), meaning that the image rms noise level is still at a reasonable level after the primary beam correction. Moreover, the off-axis instrumental polarisation is not expected to significantly corrupt the polarisation signals within this $5'$ radius. Specifically, the off-axis instrumental polarisation of the Jansky VLA in L-band can reach ≈ 5 per cent at the half-power point of the primary beam ($\approx 15'$ from the pointing centre), and is expected to manifest as an instrumental polarised component with $\phi \approx 0$ rad m^{-2} (Jagannathan et al. 2017). If we approximate the off-axis instrumental polarisation pattern as a second-order polynomial centred at the pointing centre of the Jansky VLA where the leakage level is set to be zero, then the expected off-axis leakage level at $5'$ away from the pointing centre would be ≈ 0.5 per cent. We will carefully examine the results from these off-axis targets to ensure that

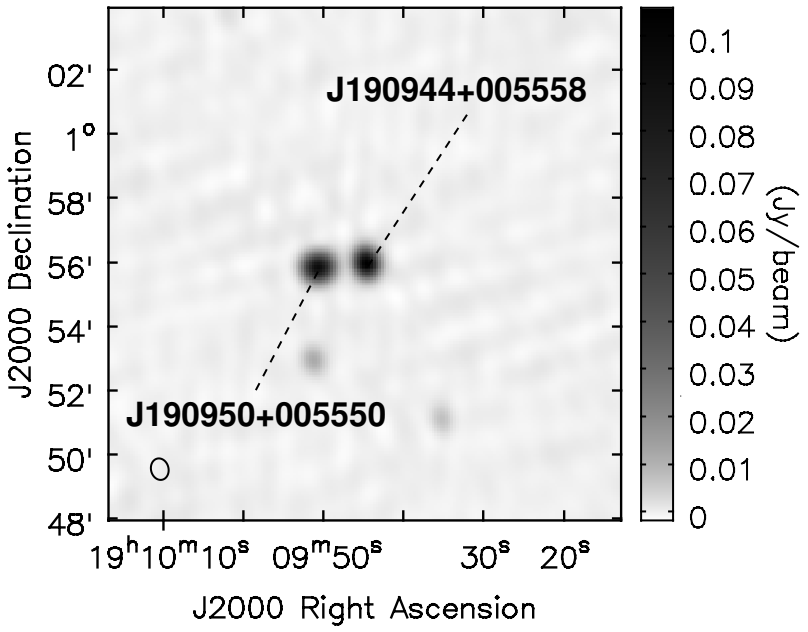

Figure 5.5: Stokes I image of NVSS J190944+005558 from our new Jansky VLA observations, an example of spatially spatially blended targets within a target field. The positions of the on-axis target J190944+005558, along with the off-axis target J190950+005550, are labelled. The size of the synthesised beam is shown as the black open ellipse at the lower left corner.

the off-axis instrumental polarisation does not affect the conclusions of this work (see Chapter 5.4).

Before proceeding to extracting the Stokes values of our on-axis and off-axis targets from the channel images, we further discarded 16 of the target sources either because they are not confidently detected in even the Stokes I images, or they are identified as Galactic objects after the observations were conducted. The reason that some sources are not detected is because of their low Stokes I values, or because they are situated close to some bright Galactic objects and therefore have higher than typical image rms noise or even have poor image fidelity with prominent image artefacts. These sources are listed in Table 5.2, and the Stokes I image of J184655−021535 from our new observations is shown in Figure 5.3 as an example. Furthermore, some of the off-axis targets cannot be clearly distinguished spatially from the corresponding on-axis targets at the angular resolution of our D-array observations. The Stokes I images of two such target fields, namely J184124−015255 and J190944+005558, are shown as examples in Figures 5.4 and 5.5, respectively. For such spatially blended sources (listed in Table 5.3), we extracted their combined flux densities (in Stokes I, Q, and U) below instead of attempting to separate them.

Next, we divided all the target sources (both on- and off-axis) into two morphological classes: unresolved or extended, and extracted their Stokes I, Q, and U values using two different strategies. For unresolved sources, the `CASA` task `IMFIT` was used

Table 5.2: List of Manually Discarded Sources After the Observations

Discarded Source (NVSS)	Target Field (NVSS)	Reason
Discarded On-axis Targets		
J184500−015838	—	Undetected
J184622−015654	—	Undetected
J184622−025943	—	Galactic (PWN Kes 75)
J184655−021535	—	Undetected
J184809−005748	—	Undetected
J185521+011951	—	Poor image fidelity
Discarded Off-axis Targets		
J183205−103701	J183220−103510	Undetected
J183207−103648	J183220−103510	Undetected
J185529+052003	J185513+052158	Diffused; poor image fidelity
J190352+054926	J190343+055256	Undetected
J190359+055501	J190343+055256	Undetected
J190402+055410	J190343+055256	Undetected
J190743+090552	J190741+090717	Undetected
J192508+135801	J192517+135919	Undetected
J192511+135653	J192517+135919	Undetected
J192519+135819	J192517+135919	Undetected

to obtain the integrated flux densities. Specifically, for each target and each frequency channel we used a Gaussian function with size and orientation fixed to that of the image's synthesised beam, and fitted for the source's position in the Stokes I map. This position (along with the size and the orientation) is then fixed to fit for the amplitude of Stokes I, Q, and U to obtain the integrated flux densities. For extended sources (naturally including the "spatially blended sources" listed in Table 5.3), we first created a Stokes I image utilising the entire L-band using the multi-frequency synthesis (MFS) algorithm for each of the targets. A 3σ contour is then defined enclosing each extended source using the newly generated image, and with those contours the flux densities of the sources are extracted with the `CASA` task `IMSTAT`.

5.4 Rotation Measure Synthesis Results

With the extracted lists of Stokes I, Q, and U values across frequency for the 204 sources (171 on-axis plus 33 off-axis), the RM-Synthesis algorithm (described in detail in Chapter 2.2.3; Brentjens & de Bruyn 2005) has been applied to determine the FD values of the target EGSs. The `python` script `RM-tools`[2] was utilised. The $q = Q/I$ and $u = U/I$ values were used as the inputs to remove the effect of spectral

[2]Available on https://github.com/crpurcell/RM-tools; the implementation by Cormac Purcell was used.

Table 5.3: List of Off-axis Sources Spatially Blended with On-axis Targets

On-axis Source (NVSS)	Blended Off-axis Source (NVSS)
J181931−091059	J181937−090914
J183409−071802	J183408−071904
	J183414−071628
J183511+014620	J183515+014611
J183840−012957	J183842−013105
J184124−015255	J184130−015257
	J184134−015252
	J184142−015246
J184249−075604	J184245−075613
J184415−041757	J184413−041938
	J184422−041746
	J184422−041848
J184718+055022	J184711+054948
J184821+001108	J184824+001158
J185030−090659	J185037−090633
J185239−101324	J185230−101410
J185728+111021	J185731+111053
J185744−052527	J185748−052631
J190655+000339	J190651+000113
	J190653+000213
J190944+005558	J190950+005550
J191025+140125	J191028+140019
	J191031+135810
	J191033+135653
J191325+034308	J191331+034218
J192458+130033	J192501+130143
J192922+095808	J192922+095901
J193939+134604	J193943+134652

index, and a normalised inverse noise variance weighting function (e.g., Schnitzeler & Lee 2017, see also Chapter 3.3.1) was used to obtain the dirty Faraday spectra ($\tilde{\mathbf{F}}$) within $|\phi| \leq 2000\,\mathrm{rad\,m^{-2}}$ at a step size of $2\,\mathrm{rad\,m^{-2}}$. The dirty spectra are subsequently deconvolved with the RM-Clean algorithm (e.g., Heald et al. 2009) until the residuals fell below 6σ. As a check, we also formed a set of Faraday spectra within $|\phi| \leq 20000\,\mathrm{rad\,m^{-2}}$ to ensure that no extremely high FD polarised components are missed. For reference, the resolution of Faraday spectrum, the maximum detectable scale, and the maximum detectable FD for our observational setup are (equation 61–63

Table 5.4: RM-Synthesis Results from New Broadband Observations

Target Source (NVSS)	ℓ (°)	b (°)	ϕ (rad m^{-2})	RM$_{\rm TSS09}$ (rad m^{-2})	$p_{\rm VLA}$ (%)	$p_{\rm TSS09}$ (%)	$p_{\rm NVSS}$ (%)
On-axis Targets							
J184415−131243	20.34	−4.42	−96.0 ± 2.4	—	3.35 ± 0.13	—	2.54 ± 0.54
J181343−090743	20.49	+4.11	+11.6 ± 6.1	—	4.42 ± 0.44	—	9.67 ± 2.19
J182038−094716	20.71	+2.29	—	—	(0.02)	—	0.58 ± 0.08
J183519−111559	21.08	−1.59	−60.3 ± 1.5	−23.4 ± 17.6	2.31 ± 0.06	3.02 ± 0.20	2.70 ± 0.22
J181851−090659	21.10	+3.00	+237.6 ± 2.5	—	4.07 ± 0.16	—	2.13 ± 0.48
J181931−091059	21.12	+2.82	+186.5 ± 2.6	+204.3 ± 12.5	4.81 ± 0.20	4.85 ± 0.28	2.17 ± 0.33
J183759−112627	21.23	−2.25	−91.0 ± 1.2	−75.7 ± 6.0	11.49 ± 0.23	10.10 ± 0.29	8.41 ± 0.47
J183220−103510	21.35	−0.63	—	−27.0 ± 10.4	(0.04)	1.01 ± 0.05	0.21 ± 0.07
J182443−092933	21.44	+1.54	+54.3 ± 3.6	—	5.81 ± 0.34	—	3.52 ± 0.46
J184606−115808	21.66	−4.26	−182.1 ± 1.5	−206.1 ± 11.9	2.23 ± 0.05	1.72 ± 0.09	1.36 ± 0.08
J181419−073733	21.88	+4.69	+69.4 ± 2.6	—	15.93 ± 0.68	—	12.15 ± 2.73
J184059−110139	21.93	−2.72	−19.6 ± 1.6	—	3.91 ± 0.10	—	2.85 ± 0.51
J182503−085445	22.00	+1.74	+164.8 ± 1.1	+148.0 ± 9.1	9.88 ± 0.18	9.37 ± 0.41	6.19 ± 0.61
J182542−083723	22.33	+1.73	+42.9 ± 1.9	+56.3 ± 11.9	3.25 ± 0.10	2.49 ± 0.15	2.58 ± 0.19
J183942−101038	22.54	−2.05	+127.8 ± 1.9	+146.9 ± 14.1	8.87 ± 0.27	7.97 ± 0.52	6.96 ± 0.82
J184750−110658	22.61	−4.25	−47.2 ± 1.3	−71.2 ± 7.7	7.32 ± 0.15	6.80 ± 0.25	5.87 ± 0.33
J184911−111241	22.68	−4.59	−0.7 ± 2.6	—	2.24 ± 0.09	—	2.14 ± 0.33
J182530−080945	22.71	+1.99	−150.1 ± 4.4	—	3.30 ± 0.23	—	1.83 ± 0.39
J184812−105133	22.88	−4.22	+33.5 ± 2.4	—	16.61 ± 0.65	—	10.79 ± 2.47
J184552−103126	22.93	−3.56	−1.2 ± 1.7	—	13.08 ± 0.37	—	4.23 ± 0.93
J181949−065524	23.15	+3.81	+126.1 ± 4.7	+77.4 ± 19.4	2.44 ± 0.18	2.10 ± 0.17	1.28 ± 0.25
J182537−073729	23.20	+2.21	−58.0 ± 1.3	−81.1 ± 13.7	2.20 ± 0.05	2.18 ± 0.13	1.92 ± 0.19
J182431−072714	23.23	+2.53	+27.7 ± 1.0	+13.9 ± 5.7	6.43 ± 0.11	6.88 ± 0.18	6.05 ± 0.30
J182920−073400$^{\odot}$	23.68	+1.42	+360.4 ± 3.0	+332.6 ± 16.6	7.48 ± 0.37	7.03 ± 0.49	−0.30 ± 0.77
J184644−094654	23.68	−3.41	+90.5 ± 1.7	+96.5 ± 10.1	5.60 ± 0.16	5.13 ± 0.25	4.30 ± 0.30
J184547−093821	23.70	−3.14	+190.4 ± 6.3	—	5.60 ± 0.57	—	2.16 ± 0.36
J183052−074402$^{\odot}$	23.71	+1.01	+517.8 ± 1.8	+518.1 ± 18.9	11.37 ± 0.33	6.90 ± 0.60	3.61 ± 1.08
J182043−062415	23.71	+3.86	−14.3 ± 2.3	—	6.41 ± 0.24	—	6.51 ± 0.79
J185239−101324	23.95	−4.91	+65.5 ± 1.5	+45.8 ± 9.5	4.35 ± 0.11	5.84 ± 0.22	5.97 ± 0.76
J183902−083023$^{\dagger\odot}$	23.95	−1.14	+526.6 ± 0.4	−119.6 ± 5.5	12.63 ± 0.09	8.40 ± 0.22	6.67 ± 0.42
J182104−060915	23.98	+3.90	−6.0 ± 4.2	—	4.44 ± 0.30	—	3.71 ± 0.54
J183321−073121$^{\odot}$	24.18	+0.56	+776.8 ± 3.1	—	1.23 ± 0.06	—	0.69 ± 0.13
J183409−071802$^{\odot}$	24.47	+0.49	—	−10.0 ± 4.4	(0.02)	0.85 ± 0.02	0.16 ± 0.05
J185030−090659	24.70	−3.94	+172.0 ± 0.8	+151.3 ± 5.7	6.53 ± 0.09	5.65 ± 0.15	3.15 ± 0.19
J184249−075604$^{\dagger\odot}$	24.89	−1.71	+935.2 ± 2.0	+160.8 ± 5.2	6.18 ± 0.20	2.13 ± 0.06	0.62 ± 0.06
J182351−052429	24.96	+3.63	+17.4 ± 5.3	—	7.32 ± 0.63	—	11.46 ± 1.49
J182111−050219	24.98	+4.39	+186.8 ± 6.2	—	2.02 ± 0.20	—	1.19 ± 0.20
J184629−081333$^{\odot}$	25.05	−2.65	+476.1 ± 1.0	—	6.09 ± 0.10	—	2.13 ± 0.40
J182013−042541	25.41	+4.89	+68.9 ± 1.0	+59.9 ± 5.5	5.04 ± 0.08	4.19 ± 0.11	4.35 ± 0.18
J184511−060146$^{\odot}$	26.85	−1.36	+117.4 ± 2.3	—	7.61 ± 0.29	—	4.67 ± 0.84
J183253−042628$^{\odot}$	26.86	+2.09	+188.8 ± 1.7	—	3.60 ± 0.10	—	2.06 ± 0.40
J182634−030927	27.27	+4.08	+225.5 ± 1.7	+164.7 ± 9.5	3.96 ± 0.11	3.42 ± 0.14	1.84 ± 0.18
J183847−040042$^{\odot}$	27.92	+0.98	+312.3 ± 0.6	+287.1 ± 8.2	4.08 ± 0.04	2.82 ± 0.08	0.54 ± 0.09
J183400−030340$^{\odot}$	28.22	+2.48	+162.8 ± 9.7	—	0.33 ± 0.05	—	0.71 ± 0.16
J185054−050942$^{\odot}$	28.27	−2.23	+583.9 ± 1.1	—	4.48 ± 0.08	—	2.14 ± 0.25
J184415−041757$^{\odot}$	28.29	−0.36	+51.8 ± 7.1	—	0.41 ± 0.05	—	0.83 ± 0.17
J185523−053804$^{\odot}$	28.36	−3.44	+173.7 ± 1.2	—	12.03 ± 0.23	—	6.16 ± 1.00
J183652−024606$^{\odot}$	28.81	+1.97	+571.5 ± 2.8	—	1.06 ± 0.05	—	0.99 ± 0.24
J185744−052527	28.81	−3.87	+232.7 ± 1.5	+222.8 ± 13.5	11.12 ± 0.27	9.14 ± 0.68	3.64 ± 0.62
J183939−030047$^{\odot}$	28.91	+1.24	+675.0 ± 0.8	+639.4 ± 10.7	9.59 ± 0.13	4.41 ± 0.22	5.03 ± 0.47
J183717−015034	29.68	+2.30	+307.8 ± 0.9	+284.2 ± 9.1	3.53 ± 0.05	1.90 ± 0.08	0.39 ± 0.15
J182900−002018	30.07	+4.84	−56.8 ± 3.3	—	2.00 ± 0.11	—	1.67 ± 0.34
J184124−015255$^{?}$	30.11	+1.37	+20.4 ± 2.0	+338.7 ± 10.7	0.87 ± 0.03	1.10 ± 0.06	0.22 ± 0.14
J183840−012957	30.14	+2.16	+345.9 ± 1.1	+326.6 ± 7.1	6.56 ± 0.11	8.33 ± 0.25	0.38 ± 0.38
J183551−005941	30.27	+3.01	+157.2 ± 0.7	+152.5 ± 11.6	6.94 ± 0.08	5.65 ± 0.28	3.54 ± 0.35
J190014−033504	30.74	−3.59	+554.9 ± 1.8	—	3.05 ± 0.09	—	1.42 ± 0.34
J184959−013256$^{?}$	31.39	−0.38	+216.9 ± 3.5	−7.5 ± 9.9	0.37 ± 0.02	0.77 ± 0.03	0.25 ± 0.04
J183838+000858	31.60	+2.92	+115.3 ± 1.8	—	3.56 ± 0.10	—	2.34 ± 0.38
J183418+004852	31.70	+4.18	+80.3 ± 0.6	+58.6 ± 6.4	6.82 ± 0.07	7.44 ± 0.23	6.73 ± 0.45
J183931+001447	31.79	+2.76	+216.7 ± 1.8	—	8.97 ± 0.26	—	5.17 ± 0.86
J183307+011535	31.97	+4.65	+372.7 ± 1.3	+315.4 ± 11.7	1.66 ± 0.03	1.97 ± 0.10	0.23 ± 0.14
J183437+010519	31.98	+4.24	+72.3 ± 1.5	—	5.61 ± 0.14	—	3.59 ± 0.70
J185822−013654	32.28	−2.28	+558.9 ± 2.0	—	1.11 ± 0.04	—	0.68 ± 0.15
J184704−000446	32.36	+0.93	+62.1 ± 1.7	+54.1 ± 15.3	2.30 ± 0.06	2.11 ± 0.13	2.21 ± 0.24
J190833−023000	32.65	−4.95	+124.3 ± 1.6	—	3.19 ± 0.08	—	1.92 ± 0.39
J183511+014620	32.66	+4.42	+209.7 ± 0.3	+196.9 ± 4.4	9.74 ± 0.05	6.29 ± 0.14	3.53 ± 0.18
J183337+020355	32.74	+4.91	+194.0 ± 6.7	—	0.27 ± 0.03	—	0.87 ± 0.15
J184821+001108	32.75	+0.77	−145.3 ± 1.3	−107.2 ± 5.2	5.13 ± 0.11	11.26 ± 0.32	11.32 ± 0.64
J185351−002508†	32.84	−0.73	+374.0 ± 0.8	−341.3 ± 10.0	6.21 ± 0.09	4.62 ± 0.22	−0.11 ± 0.34
J185751−004817†	32.95	−1.80	+737.0 ± 4.3	−26.6 ± 10.8	0.37 ± 0.03	1.94 ± 0.10	0.49 ± 0.09

$^{\odot}$ Situated behind the prominent H II structure G26.5

† Suffers from $n\pi$-ambiguity in TSS09

$^{?}$ Poor correspondence between ϕ and RM$_{\rm TSS09}$

Table 5.4: (Continued) RM-Synthesis Results from New Broadband Observations

Target Source (NVSS)	ℓ (°)	b (°)	ϕ (rad m^{-2})	RM$_{\rm TSS09}$ (rad m^{-2})	$p_{\rm VLA}$ (%)	$p_{\rm TSS09}$ (%)	$p_{\rm NVSS}$ (%)
On-axis Targets							
J190042−005151	33.22	−2.46	+411.1 ± 1.2	+373.4 ± 19.6	3.47 ± 0.07	2.63 ± 0.22	0.90 ± 0.29
J190407−011342	33.29	−3.38	+277.8 ± 1.0	+211.4 ± 12.3	3.59 ± 0.06	3.28 ± 0.19	1.05 ± 0.24
J185146+003532	33.50	+0.19	−273.8 ± 0.6	−313.1 ± 3.4	2.82 ± 0.03	3.02 ± 0.05	0.84 ± 0.09
J190832−011929	33.70	−4.41	+188.0 ± 1.7	—	4.87 ± 0.14	—	3.16 ± 0.64
J184755+012221	33.75	+1.41	+138.0 ± 3.8	—	3.93 ± 0.24	—	4.26 ± 0.67
J185857+000727	33.90	−1.61	+267.9 ± 1.3	+240.5 ± 10.6	4.78 ± 0.10	3.79 ± 0.18	0.82 ± 0.28
J190017+000355	34.00	−1.94	+547.3 ± 1.0	—	2.07 ± 0.03	—	0.85 ± 0.18
J184435+020933	34.07	+2.51	+43.5 ± 2.7	—	7.25 ± 0.32	—	7.14 ± 1.13
J190831−004855	34.16	−4.17	−13.2 ± 2.8	—	7.97 ± 0.36	—	6.70 ± 1.57
J191010−005622	34.23	−4.60	−55.5 ± 2.7	—	8.91 ± 0.39	—	8.44 ± 2.11
J190532−000941	34.40	−3.21	+126.6 ± 1.3	+114.7 ± 11.9	4.73 ± 0.10	5.30 ± 0.31	4.47 ± 0.47
J190559+000721	34.70	−3.18	+20.2 ± 1.7	—	2.95 ± 0.08	—	2.50 ± 0.40
J190655+000339	34.75	−3.42	+9.6 ± 2.5	—	5.42 ± 0.22	—	9.41 ± 2.13
J190741+000038	34.80	−3.61	−73.3 ± 0.8	−74.2 ± 13.1	5.38 ± 0.07	4.37 ± 0.33	4.17 ± 0.32
J183848+040424	35.13	+4.66	+146.0 ± 1.3	+129.8 ± 16.1	2.57 ± 0.05	1.15 ± 0.09	0.57 ± 0.10
J185515+021054†	35.31	+0.15	+92.2 ± 1.7	−553.2 ± 12.5	10.79 ± 0.30	6.38 ± 0.41	7.25 ± 0.69
J191133+001449	35.45	−4.36	−38.2 ± 1.8	—	6.38 ± 0.19	—	5.37 ± 0.82
J190426+011036	35.46	−2.36	−68.5 ± 2.3	—	4.89 ± 0.19	—	6.35 ± 1.18
J185114+025939	35.57	+1.41	+177.3 ± 1.4	+34.6 ± 14.1	1.75 ± 0.04	4.46 ± 0.30	1.17 ± 0.12
J184320+040256	35.62	+3.65	+31.1 ± 2.0	—	4.08 ± 0.14	—	3.36 ± 0.59
J190944+005558	35.85	−3.65	+35.5 ± 3.1	—	3.54 ± 0.18	—	3.63 ± 0.67
J191417+002421	35.91	−4.90	−20.9 ± 1.7	—	16.10 ± 0.45	—	7.76 ± 1.60
J190712+012709	36.02	−2.84	+194.5 ± 0.6	+134.7 ± 9.4	2.70 ± 0.03	1.68 ± 0.08	0.91 ± 0.11
J185213+033255†	36.18	+1.44	+185.7 ± 0.9	−458.4 ± 8.7	7.03 ± 0.10	5.89 ± 0.22	3.63 ± 0.27
J185837+024518	36.20	−0.34	+161.3 ± 2.8	—	5.63 ± 0.26	—	3.21 ± 0.67
J184500+043812	36.33	+3.54	+2.9 ± 2.0	—	14.33 ± 0.47	—	9.34 ± 1.60
J184604+043450	36.40	+3.28	+34.8 ± 3.0	—	6.92 ± 0.33	—	4.39 ± 0.70
J185802+031316†	36.55	+0.00	+424.1 ± 0.3	−241.0 ± 3.6	4.75 ± 0.03	2.17 ± 0.03	0.79 ± 0.05
J185306+044052†	37.29	+1.76	+294.2 ± 0.8	−367.1 ± 10.6	14.53 ± 0.20	11.22 ± 0.61	3.24 ± 1.19
J184718+055022	37.67	+3.57	+123.4 ± 6.4	—	3.09 ± 0.32	—	5.43 ± 1.18
J184438+062651	37.91	+4.44	+200.6 ± 2.1	+179.0 ± 16.1	5.32 ± 0.18	4.34 ± 0.31	2.16 ± 0.34
J191406+025549	38.13	−3.70	+545.8 ± 3.1	—	5.30 ± 0.27	—	3.09 ± 0.78
J184432+064257	38.14	+4.58	+213.7 ± 0.5	+183.7 ± 6.3	2.75 ± 0.02	2.47 ± 0.07	1.35 ± 0.08
J185513+052158†	38.14	+1.60	+369.9 ± 0.9	−325.5 ± 10.5	7.68 ± 0.12	6.29 ± 0.31	−0.16 ± 0.52
J184919+063211	38.52	+3.44	+21.9 ± 2.4	—	12.72 ± 0.49	—	9.67 ± 2.35
J191325+034308†	38.76	−3.18	+348.1 ± 1.2	−331.6 ± 5.3	4.84 ± 0.09	7.45 ± 0.18	−0.12 ± 0.27
J191849+030442	38.81	−4.67	+70.3 ± 2.0	−66.1 ± 18.0	1.48 ± 0.05	2.01 ± 0.17	0.29 ± 0.13
J184753+071538	39.00	+4.09	+181.0 ± 1.9	+169.6 ± 15.7	3.95 ± 0.12	4.75 ± 0.33	3.86 ± 0.47
J190343+055256	39.56	−0.04	+445.6 ± 2.9	—	1.10 ± 0.05	—	0.76 ± 0.12
J190043+064546†	40.01	+1.03	+384.4 ± 1.1	−252.3 ± 13.4	7.69 ± 0.13	6.30 ± 0.39	1.70 ± 0.46
J191725+044236	40.10	−3.61	+83.5 ± 1.5	—	2.94 ± 0.07	—	1.97 ± 0.33
J192049+042052	40.17	−4.52	+77.3 ± 1.2	—	5.68 ± 0.11	—	3.41 ± 0.34
J190734+060446†	40.18	−0.80	+409.6 ± 0.9	−226.7 ± 15.2	4.11 ± 0.06	2.84 ± 0.19	0.79 ± 0.22
J191840+043932	40.20	−3.91	−18.9 ± 5.1	—	6.32 ± 0.52	—	9.23 ± 2.24
J184731+090047	40.53	+4.96	+228.0 ± 1.0	+211.7 ± 8.2	10.07 ± 0.16	10.71 ± 0.40	3.54 ± 0.68
J192258+044354	40.76	−4.82	+125.2 ± 2.2	—	6.65 ± 0.24	—	2.89 ± 0.72
J192243+045126	40.84	−4.71	+129.7 ± 1.7	—	0.83 ± 0.02	—	0.59 ± 0.08
J191310+064158	41.37	−1.75	+17.5 ± 3.3	—	4.30 ± 0.23	—	3.34 ± 0.75
J184951+094850	41.51	+4.81	+567.5 ± 1.4	—	7.45 ± 0.17	—	2.74 ± 0.62
J191917+061942	41.75	−3.27	+35.6 ± 2.6	—	1.48 ± 0.06	—	1.20 ± 0.23
J190614+084226	42.36	+0.70	+124.8 ± 2.5	—	7.38 ± 0.29	—	7.16 ± 1.39
J185557+102011	42.66	+3.70	+569.4 ± 2.3	—	1.08 ± 0.04	—	0.72 ± 0.16
J192233+071048	42.88	−3.59	+196.8 ± 4.0	—	1.67 ± 0.11	—	2.14 ± 0.45
J190741+090717	42.90	+0.57	+706.5 ± 0.8	—	3.52 ± 0.05	—	1.51 ± 0.13
J192245+073933	43.33	−3.40	+231.1 ± 2.1	+187.9 ± 16.3	5.10 ± 0.18	6.46 ± 0.42	2.96 ± 1.04
J192820+070355	43.46	−4.91	+45.6 ± 3.5	—	2.21 ± 0.13	—	1.97 ± 0.35
J191906+081920	43.49	−2.30	+220.5 ± 0.9	+191.5 ± 15.7	9.85 ± 0.15	8.82 ± 0.62	4.31 ± 0.69
J185728+111021	43.57	+3.75	+524.3 ± 0.5	—	10.91 ± 0.09	—	3.12 ± 0.53
J191641+090147	43.84	−1.44	+509.9 ± 2.1	—	14.29 ± 0.49	—	7.99 ± 1.70
J185952+112514	44.06	+3.34	+659.8 ± 2.4	—	6.11 ± 0.23	—	2.55 ± 0.57
J190323+112905†	44.51	+2.60	+833.6 ± 0.3	+141.3 ± 7.4	17.12 ± 0.07	4.52 ± 0.19	3.56 ± 0.26
J192840+084849†	45.04	−4.15	+528.3 ± 1.0	−153.4 ± 16.1	2.56 ± 0.04	1.59 ± 0.10	1.56 ± 0.15
J192355+094424	45.31	−2.68	+299.0 ± 1.3	+282.2 ± 8.7	4.24 ± 0.09	4.29 ± 0.19	0.69 ± 0.23
J185923+125912	45.41	+4.15	+263.6 ± 0.4	+154.3 ± 2.6	1.87 ± 0.01	1.46 ± 0.02	0.57 ± 0.03
J191005+114748†	45.54	+1.28	+844.8 ± 0.9	+149.5 ± 11.4	4.26 ± 0.06	1.46 ± 0.07	0.67 ± 0.18
J191000+122524	46.09	+1.59	+772.6 ± 2.3	—	3.48 ± 0.13	—	1.31 ± 0.30
J192922+095808†	46.14	−3.76	+20.0 ± 0.5	+686.6 ± 7.0	4.56 ± 0.04	3.73 ± 0.12	5.40 ± 0.21
J191733+114215†	46.31	−0.38	−124.7 ± 1.4	+529.2 ± 11.6	6.68 ± 0.15	7.98 ± 0.43	7.75 ± 0.72
J190501+132047	46.35	+3.09	+587.4 ± 1.0	—	4.95 ± 0.08	—	1.90 ± 0.28
J193434+104340	47.43	−4.52	−286.1 ± 5.3	—	1.23 ± 0.10	—	1.62 ± 0.40

$^{\odot}$ Situated behind the prominent H II structure G26.5

† Suffers from $n\pi$-ambiguity in TSS09

$^{?}$ Poor correspondence between ϕ and RM$_{\rm TSS09}$

Table 5.4: (Continued) RM-Synthesis Results from New Broadband Observations

Target Source (NVSS)	ℓ (°)	b (°)	ϕ (rad m^{-2})	RM$_{\mathrm{TSS09}}$ (rad m^{-2})	p_{VLA} (%)	p_{TSS09} (%)	p_{NVSS} (%)
On-axis Targets							
J190247+145137†	47.46	+4.26	$+541.3 \pm 1.5$	-143.1 ± 14.7	4.48 ± 0.11	4.15 ± 0.25	2.64 ± 0.35
J193357+105642	47.54	−4.28	-158.8 ± 1.1	—	4.36 ± 0.08	—	2.56 ± 0.37
J191025+140125†	47.56	+2.24	$+541.6 \pm 1.5$	-125.1 ± 5.9	3.61 ± 0.09	9.29 ± 0.23	8.24 ± 0.65
J192540+122738	47.91	−1.77	$+60.2 \pm 2.8$	—	1.76 ± 0.08	—	2.23 ± 0.44
J190451+152148†	48.13	+4.05	$+545.8 \pm 0.4$	-117.1 ± 5.1	4.11 ± 0.03	2.10 ± 0.05	1.65 ± 0.09
J190414+153638	48.28	+4.29	$+662.3 \pm 1.9$	—	2.08 ± 0.07	—	1.03 ± 0.18
J192458+130033	48.31	−1.36	$+524.2 \pm 6.1$	—	1.77 ± 0.18	—	1.78 ± 0.43
J190655+152342†	48.39	+3.62	$+636.8 \pm 0.5$	-37.5 ± 10.1	12.55 ± 0.10	7.27 ± 0.34	6.66 ± 0.46
J193335+120844	48.56	−3.62	-36.9 ± 2.7	—	7.24 ± 0.32	—	4.91 ± 1.10
J190355+160147†	48.62	+4.55	$+439.8 \pm 0.6$	-240.1 ± 12.9	5.99 ± 0.06	3.89 ± 0.21	1.75 ± 0.27
J191644+150349†	49.19	+1.37	$+534.5 \pm 0.9$	-145.5 ± 8.8	3.15 ± 0.05	2.36 ± 0.10	1.85 ± 0.13
J192517+135919	49.21	−0.97	$+451.6 \pm 2.0$	$+442.5 \pm 3.6$	3.75 ± 0.12	3.78 ± 0.06	1.19 ± 0.09
J190516+163706†	49.30	+4.53	$+489.9 \pm 0.8$	-219.6 ± 9.2	3.64 ± 0.05	2.19 ± 0.11	1.55 ± 0.13
J193302+131335	49.44	−2.98	-75.2 ± 0.7	-76.7 ± 4.9	4.17 ± 0.05	3.03 ± 0.07	2.98 ± 0.19
J191133+161431†	49.65	+3.02	$+617.0 \pm 1.5$	$+7.4 \pm 14.7$	1.64 ± 0.04	1.03 ± 0.06	0.37 ± 0.09
J191158+161147	49.66	+2.91	$+712.0 \pm 1.2$	—	1.32 ± 0.02	—	0.86 ± 0.13
J190901+163944†	49.75	+3.75	$+446.4 \pm 0.5$	-235.4 ± 7.9	3.54 ± 0.03	2.71 ± 0.10	1.28 ± 0.12
J191219+161628†	49.77	+2.87	$+751.5 \pm 0.6$	$+41.7 \pm 8.2$	5.41 ± 0.05	2.23 ± 0.09	1.86 ± 0.13
J192835+142156	49.92	−1.49	$+126.4 \pm 3.2$	—	12.16 ± 0.63	—	14.25 ± 2.27
J192910+141952	49.96	−1.63	$+124.7 \pm 1.4$	—	8.68 ± 0.19	—	6.06 ± 0.73
J191649+155836†	50.00	+1.77	$+393.6 \pm 0.8$	-284.9 ± 6.7	6.12 ± 0.08	5.21 ± 0.15	0.76 ± 0.23
J191549+160834	50.04	+2.06	$+471.4 \pm 1.1$	—	5.81 ± 0.10	—	2.44 ± 0.42
J194012+125809	50.06	−4.64	-156.7 ± 2.1	-142.3 ± 11.5	2.63 ± 0.09	4.42 ± 0.24	3.04 ± 0.41
J191414+163640†	50.28	+2.62	$+556.8 \pm 0.8$	-123.7 ± 15.9	4.79 ± 0.06	3.16 ± 0.25	2.85 ± 0.25
J192439+154043†	50.63	−0.03	$+419.9 \pm 0.6$	-178.8 ± 14.9	5.27 ± 0.05	1.74 ± 0.10	0.29 ± 0.16
J193939+134604	50.70	−4.13	-183.2 ± 2.9	—	3.81 ± 0.18	—	3.28 ± 0.72
J192032+162557	50.82	+1.20	$+534.5 \pm 1.3$	—	9.64 ± 0.20	—	5.14 ± 0.81
J192203+162243†	50.95	+0.85	$+457.9 \pm 1.1$	-228.1 ± 10.7	3.78 ± 0.07	2.89 ± 0.16	1.30 ± 0.24
J193306+145624	50.95	−2.17	$+145.2 \pm 1.3$	$+137.0 \pm 11.8$	2.32 ± 0.05	2.10 ± 0.11	1.68 ± 0.16
J193321+150446†	51.10	−2.16	$+352.5 \pm 2.6$	-238.9 ± 14.3	1.14 ± 0.05	1.39 ± 0.09	—
J193052+153235	51.22	−1.41	$+139.4 \pm 1.5$	—	1.43 ± 0.03	—	1.30 ± 0.09
Off-axis Targets							
J183756−112202	21.28	−2.21	—	—	(0.77)	—	2.11 ± 2.65
J184555−115813	21.64	−4.22	-126.1 ± 2.7	—	13.74 ± 0.60	—	2.32 ± 2.64
J182535−083948	22.28	+1.74	$+4.8 \pm 7.3$	—	9.39 ± 1.12	—	0.91 ± 2.26
J183931−101336	22.48	−2.03	$+141.2 \pm 7.5$	—	2.50 ± 0.31	—	-0.57 ± 0.90
J184906−111430	22.64	−4.59	$+42.2 \pm 4.3$	—	5.40 ± 0.38	—	-0.56 ± 1.49
J184808−105535	22.82	−4.23	$+16.9 \pm 4.0$	—	7.08 ± 0.46	—	2.28 ± 2.72
J184541−093643	23.72	−3.10	$+190.3 \pm 1.9$	—	2.74 ± 0.08	—	1.14 ± 2.13
J185027−091037	24.64	−3.96	$+98.0 \pm 5.9$	—	0.70 ± 0.07	—	0.62 ± 0.21
J182058−050223	24.95	+4.44	$+67.4 \pm 3.4$	—	4.79 ± 0.26	—	0.53 ± 0.28
J184617−081126☉	25.05	−2.59	$+620.3 \pm 6.1$	—	4.46 ± 0.44	—	1.65 ± 1.48
J182644−030952	27.29	+4.04	$+250.3 \pm 8.7$	—	4.85 ± 0.69	—	-0.75 ± 1.64
J183414−030119☉	28.28	+2.44	$+481.0 \pm 0.9$	—	4.28 ± 0.06	—	0.69 ± 0.23
J183701−015140	29.63	+2.36	$+307.9 \pm 6.8$	—	1.48 ± 0.16	—	0.32 ± 0.48
J183827−013111	30.10	+2.19	$+290.1 \pm 3.2$	—	10.03 ± 0.53	—	-0.21 ± 2.53
J183603−005747	30.32	+2.98	$+34.3 \pm 4.4$	—	1.84 ± 0.13	—	1.58 ± 0.71
J183415+004451	31.64	+4.16	$+52.0 \pm 6.9$	—	2.51 ± 0.28	—	1.85 ± 0.93
J183935+001547	31.81	+2.76	$+167.0 \pm 2.7$	—	6.37 ± 0.28	—	2.02 ± 0.81
J183433+010127	31.92	+4.22	—	—	(0.49)	—	0.33 ± 2.33
J185807−004834	32.97	−1.86	$+302.7 \pm 10.1$	—	1.15 ± 0.19	—	0.77 ± 2.25
J190832−005319	34.09	−4.21	$+6.3 \pm 4.1$	—	11.43 ± 0.77	—	-1.15 ± 9.39
J190721+012341	35.99	−2.90	$+109.9 \pm 6.9$	—	2.08 ± 0.23	—	-0.52 ± 1.83
J185222+033347	36.21	+1.42	$+162.9 \pm 7.3$	—	5.46 ± 0.65	—	-0.09 ± 2.03
J191833+043928	40.18	−3.88	$+88.6 \pm 4.8$	—	6.45 ± 0.50	—	0.73 ± 1.99
J190616+083858	42.31	+0.67	$+473.8 \pm 10.1$	—	1.30 ± 0.21	—	0.74 ± 1.18
J192802+070219	43.40	−4.85	$+131.3 \pm 2.7$	—	8.07 ± 0.36	—	—
J191630+090223	43.83	−1.39	$+544.0 \pm 2.6$	—	6.63 ± 0.28	—	2.71 ± 1.06
J190319+112950	44.51	+2.62	$+786.8 \pm 2.4$	—	2.11 ± 0.08	—	0.65 ± 0.24
J190235+145023	47.41	+4.30	$+551.6 \pm 4.2$	—	3.74 ± 0.26	—	1.46 ± 1.01
J190653+152650	48.43	+3.65	$+506.6 \pm 4.2$	—	2.08 ± 0.14	—	-0.10 ± 0.66
J193328+120953	48.56	−3.59	-92.7 ± 3.3	—	12.08 ± 0.65	—	2.16 ± 2.40
J192030+162333	50.78	+1.19	—	—	(0.45)	—	1.72 ± 2.66
J192032+162429	50.80	+1.19	—	—	(0.45)	—	1.57 ± 1.92
J192157+162501	50.97	+0.89	—	—	(0.07)	—	-0.22 ± 0.39

☉ Situated behind the prominent H II structure G26.5

† Suffers from $n\pi$-ambiguity in TSS09

? Poor correspondence between ϕ and RM$_{\mathrm{TSS09}}$

in Brentjens & de Bruyn 2005)

$$\delta\phi_0 \approx \frac{2\sqrt{3}}{\Delta\lambda^2} \approx 123\,\mathrm{rad\,m^{-2}}, \tag{5.2}$$

$$\text{max-scale} \approx \frac{\pi}{\lambda^2_{\mathrm{min}}} \approx 144\,\mathrm{rad\,m^{-2}}, \text{ and} \tag{5.3}$$

$$||\phi_{\mathrm{max}}|| \approx \frac{\sqrt{3}}{\delta\lambda^2} \approx (6\text{–}20) \times 10^3\,\mathrm{rad\,m^{-2}}, \tag{5.4}$$

respectively. The range in $||\phi_{\mathrm{max}}||$ is due to the difference in the widths of the 4 MHz channels in λ^2 space at the two ends of the observed frequency.

The final Faraday spectra amplitudes ($||\mathbf{F}||$) are shown in Figures D.1 and D.2 in Appendix D. Only polarised components that are above 6σ in polarisation fraction are considered, since below this cutoff any apparent polarisation signals in Faraday spectra could just be manifestations of the polarisation bias (see George et al. 2012). We extracted the ϕ values of the target sources by considering only the highest peak in $||\mathbf{F}||$ for each source (see e.g., Heald et al. 2009; Mao et al. 2010; Betti et al. 2019). A parabola is fitted to the seven highest points of each spectrum to extract the central ϕ value of the brightest polarised component, with the uncertainty obtained by $\frac{\delta\phi_0}{2\cdot(S/N)}$ (e.g., Mao et al. 2010; Iacobelli et al. 2013). The polarisation fraction (p) of the sources are obtained by fitting the same parabola to the q_ϕ and u_ϕ Faraday spectra, but with the x-offsets and widths fixed to those obtained from the fit to the corresponding amplitude spectrum (i.e. the only free variable is the amplitude). The p value is then obtained from adding the q and u values in quadrature, with the Ricean polarisation bias *not* being corrected for since its effect would be negligible in the S/N regime of > 6 (Wardle & Kronberg 1974; George et al. 2012). The resulting p and ϕ for each source, along with the listed p and RM in the NVSS and TSS09 catalogues wherever applicable, are listed in Table 5.4 and illustrated in Figure 5.6. Out of the total of 171 on-axis and 33 off-axis targets, we found that three on-axis and five off-axis targets are unpolarised in our new observations (i.e., p being below our 6σ cutoff). For these sources, we list the 1σ values in p_{VLA} within parentheses in Table 5.4.

Before moving on to the scientific interpretation of the data, we verified that none of the off-axis targets (with a mean distance of 3.′2 from the pointing centre) have been significantly affected by the off-axis polarisation leakage in the new Jansky VLA observations. Specifically, we checked that none of these targets are (1) at polarisation levels of $p \lesssim 0.5$ per cent, (2) have ϕ peaking at $\approx 0\,\mathrm{rad\,m^{-2}}$, and (3) at NVSS polarisation levels of $p \lesssim 0.3$ per cent. The first two criteria are based on the expected signatures of the off-axis polarisation leakage for the Jansky VLA in L-band (Jagannathan et al. 2017, see also Chapter 5.3), while sources that are listed as $p > 0.3$ per cent in the original NVSS catalogue are likely truly polarised[3]. We therefore conclude that the FD values of the off-axis targets are reliable.

[3]The residual off-axis instrumental polarisation of the original NVSS catalogue is $p \approx 0.3$ per cent (Condon et al. 1998).

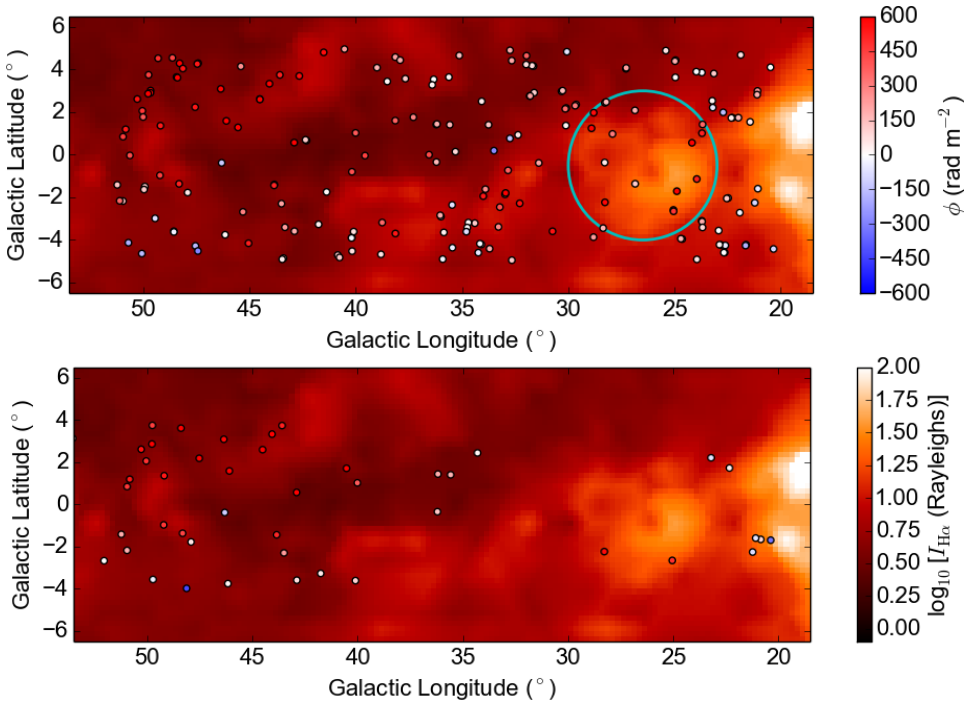

Figure 5.6: **(Top)** New FD measurements from this project and **(Bottom)** RM measurements from Van Eck et al. (2011) (both as colour dots) overlaid on the WHAMSS Hα map (Haffner et al. 2003, 2010). The typical uncertainty of the new FD is about 2 rad m^{-2}, while that of the Van Eck et al. (2011) RM is about 10 rad m^{-2}. Note that the 17 target sources situated behind the H II structure G26.5 as enclosed by the cyan circle in the top panel will not be considered in the consequent analysis stages.

5.5 Discussion

5.5.1 Comparisons with Existing RM Measurements

Out of the 168 polarised on-axis targets, 87 have reported RM values in the TSS09 catalogue. A comparison between our newly derived FD and the TSS09 RMs (Figure 5.7) has revealed 32 sources with these two sets of values being discrepant by more than 500 rad m^{-2}. This is almost certainly due to the $n\pi$-ambiguity in the TSS09 catalogue (see Chapter 3). This high fraction (almost 40 per cent) of $n\pi$-ambiguity sources in the region of interest is consistent with the remark in Chapter 3.4.1.7 that the TSS09 RM values in this particular sky region can be highly unreliable, likely linked to the complex large-scale magnetic field structure of the Milky Way here. Moreover, we identified two TSS09 sources (J183220−103510 and J183409−071802) that are unpolarised in our new Jansky VLA observations, with fractional polarisation lower than the 6σ cutoffs of 0.24 and 0.12 per cent, respectively. However, these two sources are respectively listed as 1.01 ± 0.05 and 0.85 ± 0.02 per cent polarised in TSS09. As suggested in Chapter 4, differences in p between broadband on-axis Jansky VLA observations and TSS09 can be attributed to the off-axis polarisation leakage of the NVSS observations.

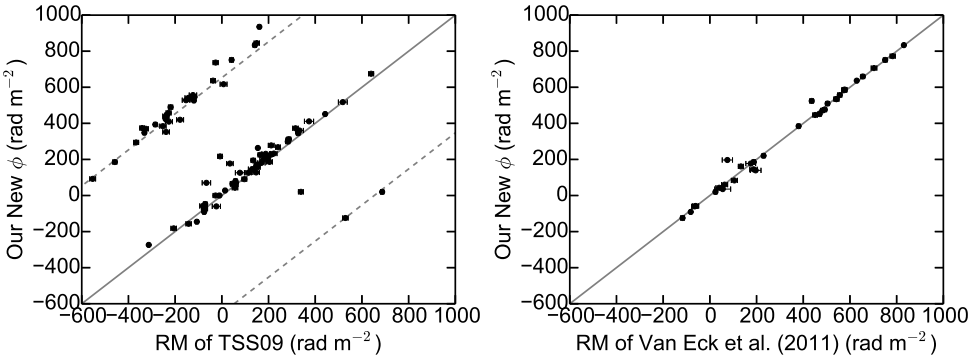

Figure 5.7: Comparisons between our newly derived FD with the RM values from **(Left)** TSS09 and **(Right)** Van Eck et al. (2011). The grey solid lines in both panels show where the x- and y-values agree, and the dashed lines in the left panel show where the measurements differ by $\pm 652.9\,\mathrm{rad\,m^{-2}}$ due to the $n\pi$-ambiguity in TSS09.

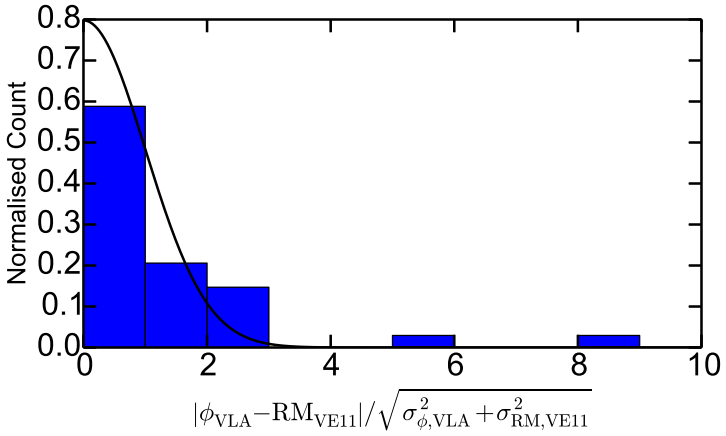

Figure 5.8: Histogram of the difference between our new FD and the Van Eck et al. (2011, VE11) RM, normalised by the two sets of measurement uncertainty added in quadrature. The black solid line shows a folded normal distribution with $\mu = 0$ and $\sigma = 1$, which is the expected distribution of the histogram if the differences in the two measurements are because of the Gaussian measurement errors only (see Chapter 4.5.4).

To summarise, if one solely rely on the TSS09 RM values for studying the magnetic fields in the Galactic disk in the $20^\circ \leq \ell \leq 52^\circ$ region, the reliability of the results can be impacted.

We further compare the new FD values with the Van Eck et al. (2011) RM values (Figures 5.6 and 5.7) for the 34 cross-matched targets. It is evident that the two sets of measurements agree with each other within uncertainties, with the distribution of their differences following the expected folded normal distribution (Figure 5.8). The only two sources with significant differences between the new FD and the Van Eck et al. (2011) RM (at $> 3\sigma$) are J192233+071048 ($\phi = +196.8 \pm 4.0\,\mathrm{rad\,m^{-2}}$; ${\rm RM}_{\rm VE11} =$

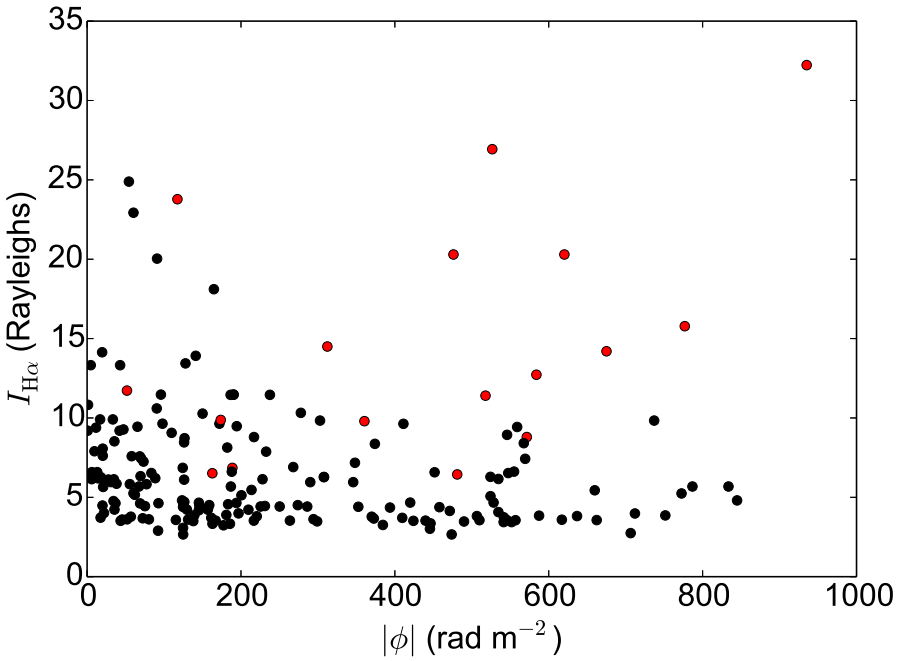

Figure 5.9: Hα intensities from WHAMSS against the newly derived $|\phi|$ for our polarised target sources. The 17 discarded sources due to their positioning behind G26.5 are marked in red.

$+75.0 \pm 22.0\,\mathrm{rad\,m^{-2}}$) and J192458+130033 ($\phi = +524.2 \pm 6.1\,\mathrm{rad\,m^{-2}}$; $\mathrm{RM_{VE11}} = +436.0 \pm 8.0\,\mathrm{rad\,m^{-2}}$), with both exhibiting complex Faraday spectra from our new data. The discrepant RMs can therefore be due to the Faraday complexities of these two sources. Our study clearly has a much higher polarised source density than that of Van Eck et al. (2011), as can be seen in Figure 5.6. Specifically, the overall source density has increased by almost a factor of five (from their previous one source per $7.3\,\mathrm{deg^2}$ to our one source per $1.6\,\mathrm{deg^2}$), with the Galactic longitude range of $20^\circ \leq \ell \leq 40^\circ$ seeing the most pronounced improvement from one source per $16.6\,\mathrm{deg^2}$ (12 sources total) to one source per $1.6\,\mathrm{deg^2}$ (126 sources total: 106 on-axis plus 20 off-axis). The increase in polarised source count has enabled our investigation of the latitude dependence of the FD due to the large-scale magnetic fields of the Milky Way in Chapter 5.5.3.

5.5.2 Contamination by Galactic H II Structures

From the WHAMSS Hα map in Figure 5.6, a large (diameter $\approx 7^\circ$) H II structure centred at $(\ell, b) = (26.5^\circ, -0.5^\circ)$ which encompasses smaller H II regions such as Sh 2-59 and Sh 2-60 has been identified. This H II structure, designated as G26.5 below, is notable because the target EGSs behind it appear to show an excess in FD of $\approx +300\,\mathrm{rad\,m^{-2}}$ compared to the surrounding EGSs that are directly outside of it. Individual Galactic H II structures are known to be able to contribute significantly to

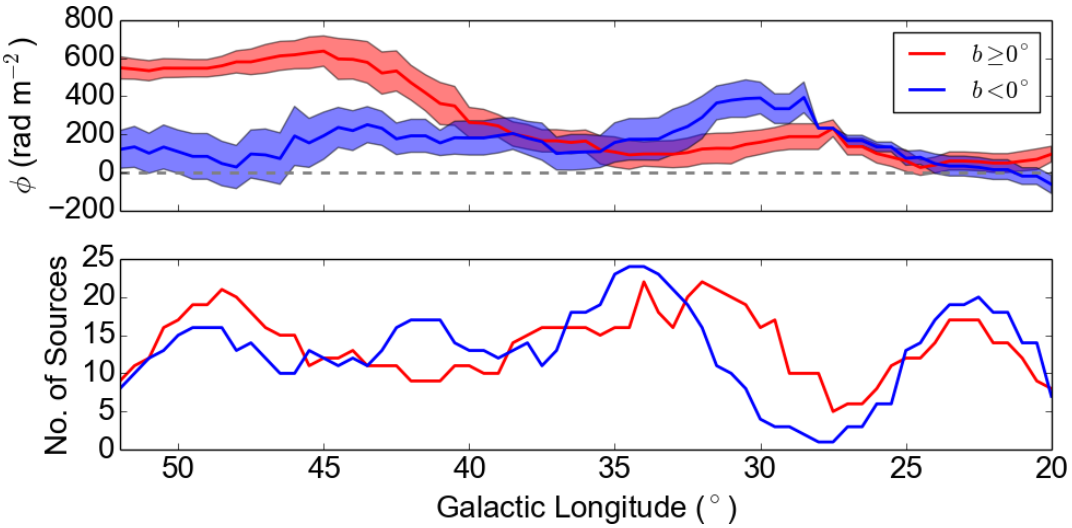

Figure 5.10: **(Top)** Boxcar-binned FD of the targets across ℓ, separated into sources above (red) and below (blue) the Galactic plane. A boxcar binning width of 5° in ℓ has been used. The shaded area encloses 1σ of the FD values within the corresponding bin. **(Bottom)** The number of sources in each ℓ-bin.

the observed FD of background EGSs (e.g., Harvey-Smith et al. 2011; Purcell et al. 2015), since they are magnetised entities with enhanced free electron densities. For the case of G26.5, it is highly likely that the FD values of the polarised target sources (15 on-axis and two off-axis) behind it are contaminated by this H II structure, and as a precaution these sources are not included in the analysis of the large-scale magnetic fields below. The Hα intensity against $|\phi|$ for the polarised target sources are plotted in Figure 5.9 as reference.

5.5.3 The Latitude Asymmetry of Faraday Depth in $40° \lesssim \ell \lesssim 52°$

A feature in the spatial FD distribution can be directly seen from Figure 5.6 — a clear disparity within the $40° \lesssim \ell \lesssim 52°$ region across $b = 0°$. Hints of such structures were already present in the Van Eck et al. (2011) data (lower panel of Figure 5.6), but were not explicitly noted nor discussed in their paper. We present in the upper panel of Figure 5.10 the boxcar-binned FD across ℓ with our target sources separated into above or below the Galactic plane. The median FD within the longitude range of 40°–52° above the Galactic plane is $+543.7\,\mathrm{rad\,m^{-2}}$, and that below the Galactic plane is $+125.0\,\mathrm{rad\,m^{-2}}$. It should be noted that these two FD values have the same (positive) sign, and are not symmetric about $\phi = 0\,\mathrm{rad\,m^{-2}}$. Although there is also an apparent FD disparity at $28° \lesssim \ell \lesssim 32°$, this feature has less statistical significance because of the low source count at that region — only four below the Galactic plane in $27.5° \leq \ell \leq 32.5°$ (lower panel of Figure 5.10).

Furthermore, we found that this FD disparity starts at Galactic latitude of very close to 0°. This is reflected by the clearly asymmetric FD profile along Galactic

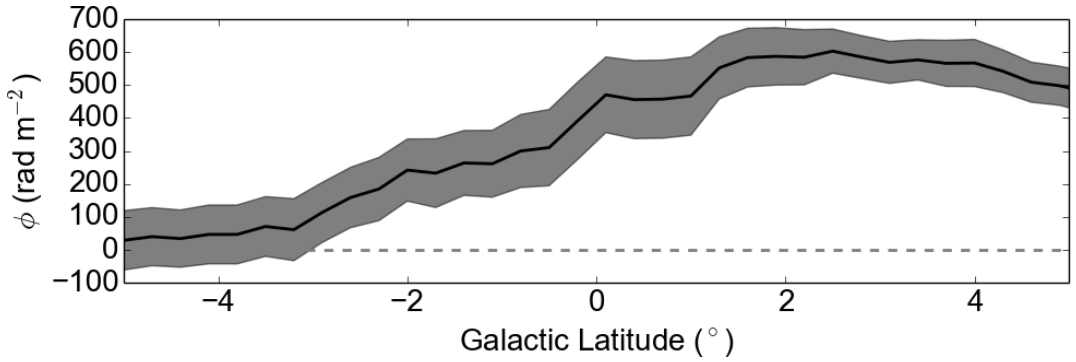

Figure 5.11: Boxcar-binned FD of the targets within $40° \leq \ell \leq 52°$ across b. A boxcar binning width of 3° in b has been used. The shaded area encloses 1σ of the FD values within the corresponding bin.

latitude about $b = 0°$, and also by its slope being the steepest at $b \approx 0°$ (Figure 5.11). If the FD disparity begins at some higher Galactic latitudes, we would expect to see a symmetric, or even flat, FD profile near $b = 0°$ instead.

The FD profiles presented above, if not affected by local structures, are representative of the large-scale magnetic fields of the Milky Way, since the FD contributions from within the EGSs and from the small-scale Galactic magnetic fields are expected to be smoothed out from the spatial binning. It should be noted that the 1σ error regions shown are the standard deviations of FD within each boxcar bin, and are dominated by the statistical spread in FD due to the small-scale Galactic magnetic fields ($\sim 100\,\mathrm{rad\,m^{-2}}$ over $\sim 1°$; e.g. Haverkorn et al. 2008) and the intrinsic FD of the EGSs ($\sigma \sim 10\,\mathrm{rad\,m^{-2}}$; e.g. Schnitzeler 2010; Oppermann et al. 2015), meaning that the actual uncertainties in the FD contributions by the large-scale fields are expected to be much smaller. The FD profiles across longitude (top panel of Figure 5.10) show that the disparity between above and below the Galactic plane is only seen at $40° \lesssim \ell \lesssim 52°$, but not at $20° \lesssim \ell \lesssim 40°$. The direct implication of this observed difference in FD is that the distributions of the large-scale magnetic fields and/or the Galactic free electron density are different across $b = 0°$ within the Galactic longitude range of 40°–52°. Below, we first supplement our EGS FD results with existing pulsar FD measurements, and then consider three possible scenarios that can explain the observed FD disparity.

5.5.3.1 Faraday Depths of Galactic Pulsars

We retrieved the FD values and distances of Galactic pulsars within $40° \leq \ell \leq 52°$ and $|b| \leq 5°$ from the ATNF Pulsar Catalogue (version 1.60; Manchester et al. 2005)[4]. These pulsar measurements allow one to probe how FD changes along a certain sight line (e.g., Noutsos et al. 2008; Han et al. 2018, see also Chapter 1.4.5.2), and for our case allow us to estimate where along our line of sight does the FD disparity occur. A total of 55 pulsars have been considered, with 10 having distances determined from

[4]Available on http://www.atnf.csiro.au/research/pulsar/psrcat/.

independent measurements (e.g., parallax or H I measurements; see Lorimer & Kramer 2012; Han 2017), and the remaining 45 pulsars have distances estimated from their DM values combined with the Galactic free electron density model of Yao et al. (2017). The FD against distance of these pulsars are plotted in Figure 5.12. The pulsars above and below the Galactic plane both follow the same FD trend up to a distance of $\approx 5\,\mathrm{kpc}$, where the FD trends begin to deviate. The FD of pulsars above the Galactic plane continues to rise and eventually reconcile with the EGS FD, suggesting that the Perseus and the Outer arms, both at distances $\gtrsim 10\,\mathrm{kpc}$ in this sky region (Figure 5.13), do not contribute significantly to the EGS FDs. The situation below the Galactic plane appears to be more complex, with the pulsars further divided into two trends — one group continues to rise up to $\phi \approx +600\,\mathrm{rad\,m^{-2}}$, while the other falls to $\phi \approx 0\,\mathrm{rad\,m^{-2}}$ and roughly matching the EGS FD.

We draw a division between these two classes at $\phi = +300\,\mathrm{rad\,m^{-2}}$, and plotted their spatial distributions in the top panel of Figure 5.14. The pulsars below the Galactic plane at distances of $\geq 5\,\mathrm{kpc}$ with $\phi \geq +300\,\mathrm{rad\,m^{-2}}$ (magenta points) are clearly concentrated spatially at $40^\circ \lesssim \ell \lesssim 46^\circ$ and $-1\overset{\circ}{.}5 \lesssim b \lesssim 0^\circ$, suggesting that the abnormally high FD values of those pulsars are due to peculiarities in the free electron densities and/or the magnetic fields along those sight lines at distances of $\approx 5\,\mathrm{kpc}$. Meanwhile, pulsars with $\phi < +300\,\mathrm{rad\,m^{-2}}$ (cyan points) are situated outside of the above peculiar region, but since there are only five such pulsars, we cannot draw useful conclusions.

Finally, we divide our EGSs in the same sky region at also $\phi = +300\,\mathrm{rad\,m^{-2}}$. This is to attempt to uncover similar spatial distributions seen in pulsars above, as would be expected if the Perseus and the Outer arms do not contribute significantly to our EGS FDs. The results are plotted in the lower panel of Figure 5.14 under the same colour scheme, and we find that the EGSs below the Galactic plane with $\phi \geq +300\,\mathrm{rad\,m^{-2}}$ are scattered throughout the sky region, unlike the spatial concentration seen from pulsars. Note, however, that the absence of a spatial concentration of EGSs with $\phi \geq +300\,\mathrm{rad\,m^{-2}}$ in the peculiar region identified above (i.e., $40^\circ \lesssim \ell \lesssim 46^\circ$ and $-1\overset{\circ}{.}5 \lesssim b \lesssim 0^\circ$) can be attributed to the lack of target EGSs within that region to begin with (only three; all with $\phi \geq +300\,\mathrm{rad\,m^{-2}}$). Outside of this region, the five EGSs with $\phi \geq +300\,\mathrm{rad\,m^{-2}}$ could be explained by FD contributions of $\sim 100\,\mathrm{rad\,m^{-2}}$ by small-scale magnetic fields along those sight lines, though it is challenging to draw concrete conclusions with currently available data.

We conclude the investigation with pulsar FD values here that (1) the FD disparity at $40^\circ \lesssim \ell \lesssim 52^\circ$ above versus below the plane can be occurring at a distance of $\approx 5\,\mathrm{kpc}$ away from us, (2) along these sight lines (at least for the case above the Galactic plane), it is likely that the Perseus and the Outer arms do not contribute significantly to the EGS FD, and (3) the magneto-ionic medium in this sky region can be even more complex than that revealed by our EGS data, with the region at $40^\circ \lesssim \ell \lesssim 46^\circ$ and $-1\overset{\circ}{.}5 \lesssim b \lesssim 0^\circ$ showing peculiar pulsar FD behaviours. Our study here is limited by the number of available pulsars (especially at distances $\gtrsim 5\,\mathrm{kpc}$) as well as polarised EGSs. Both are expected to see drastic improvements in source number with future polarisation surveys with the Square Kilometre Array (SKA) and its pathfinders (see

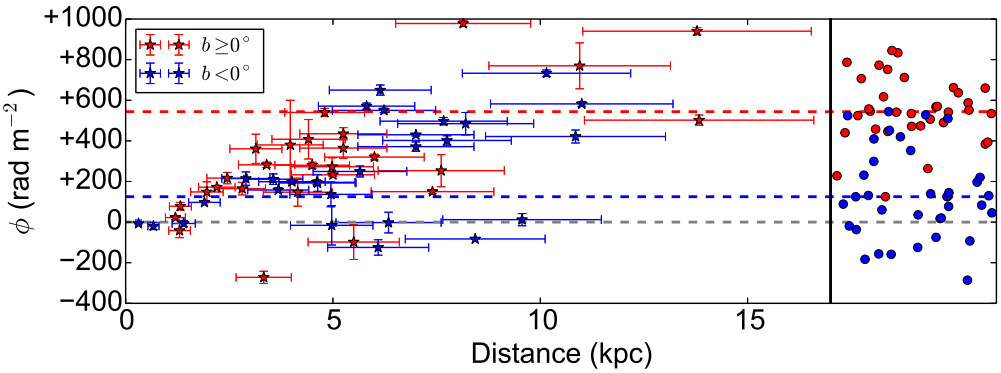

Figure 5.12: Pulsar FD values across distances within $40° \leq \ell \leq 52°$ and $|b| \leq 5°$, retrieved from the ATNF Pulsar Catalogue (Manchester et al. 2005). Sources above and below the Galactic plane are marked as red and blue, respectively. A typical pulsar distance uncertainty of 20 per cent has been adopted (e.g., Han 2017). The EGS FD values from our new observations are plotted beyond the black solid line at 17 kpc, with the x-values randomised to facilitate visualisation of the vast number of data points. The median FD values of EGSs above ($+543.7\,\mathrm{rad\,m^{-2}}$) and below ($+125.0\,\mathrm{rad\,m^{-2}}$) the Galactic plane are shown as the red and blue dashed lines, respectively.

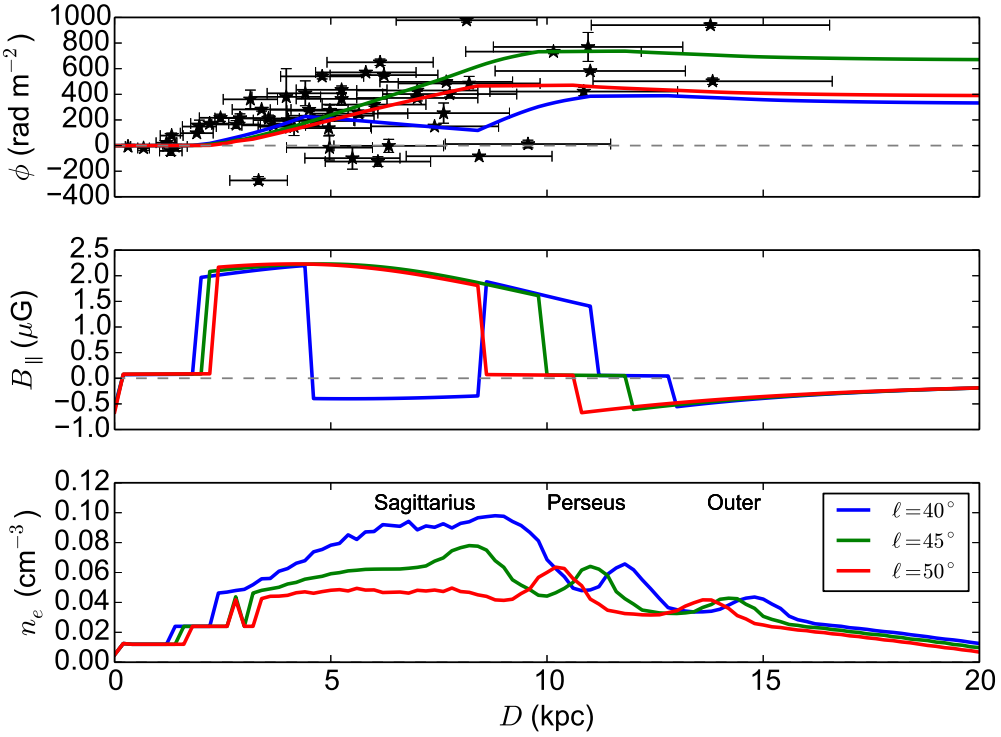

Figure 5.13: Profiles of predicted ϕ, $B_\parallel$, and n_e across distance at Galactic longitudes of $\ell = 40°, 45°, 50°$ at $b = 0°$. $B_\parallel$ and n_e profiles are adopted from the Van Eck et al. (2011) and Cordes & Lazio (2002) models, respectively. The large-scale field reversals exhibit as positive $B_\parallel$ here, and the peaks in n_e corresponding to the Sagittarius, Perseus, and Outer spiral arms are labelled. The FD against distance of pulsars within $40° \leq \ell \leq 52°$ and $|b| \leq 5°$ retrieved from the ATNF Pulsar Catalogue (Manchester et al. 2005) are plotted as black data points in the top panel (see Figure 5.12).

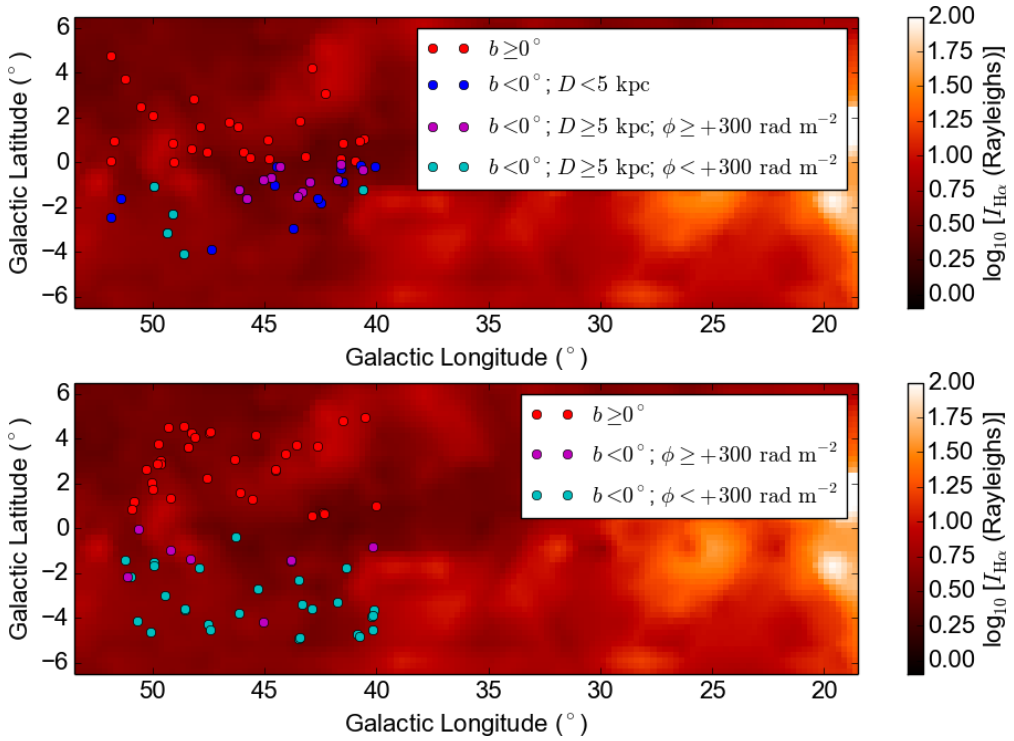

Figure 5.14: Spatial distribution of **(Top)** pulsars retrieved from the ATNF Pulsar Catalogue (Manchester et al. 2005) and **(Bottom)** our target EGSs, within $40° \leq \ell \leq 52°$ and $|b| \leq 5°$. Sources situated above the Galactic plane are marked as red, and those below the Galactic plane with distances less than 5 kpc are marked as blue. For sources further than 5 kpc from us (including EGSs), they are separated by their FD values — magenta for $\phi \geq +300\,\mathrm{rad\,m^{-2}}$ and cyan for $\phi < +300\,\mathrm{rad\,m^{-2}}$. The background heat map is the WHAMSS Hα map (Haffner et al. 2003, 2010).

Chapters 6.2.1 and 6.4.1.1).

5.5.3.2 Scenario I: Large-scale Galactic Disk Field with Odd Parity

The first scenario that can explain the EGS FD disparity is that some parts of the large-scale Galactic disk field have odd parity — the plane-parallel magnetic field changes direction across the Galactic mid-plane. This is in contrast to an even-parity field, where the plane-parallel field direction is preserved across the Galactic plane. Both odd- and even-parity fields are possible solutions according to the α-Ω dynamo theory (e.g., Beck et al. 1996), although even parity is preferred for flat astrophysical systems such as the Galactic disk (e.g., Ruzmaikin et al. 1988b) and has been determined to be the case for the local Galactic volume (Frick et al. 2001) and for the Perseus arm (Mao et al. 2012). An even-parity Galactic disk field has also been assumed in global field modelling (e.g., Sun et al. 2008; Jansson & Farrar 2012). Nonetheless, an odd-parity field can emerge if the Galactic disk is thick enough (i.e. tending towards a spherical morphology), the α-effect is strong (i.e. significant Galactic outflows), and/or

the effect of differential rotation is weak (e.g., Stepinski & Levy 1988; Meinel et al. 1990; Sokoloff & Shukurov 1990; Brandenburg et al. 1992; Ferrière 2005).

In our case, the change in the magnetic field direction across the mid-plane from an odd-parity field could have led to a disparity in the FD above versus below $b = 0°$. This requires the assumption that both the free electron density and the magnetic field strength (but not necessarily the direction) are the same across the Galactic plane. However, we argue that the disk field cannot have odd parity everywhere in the longitude range considered, but instead some regions have to host even-parity fields. This is because a purely odd parity field would produce FD profiles symmetric about $0\,\mathrm{rad\,m^{-2}}$, which is not seen anywhere over the Galactic longitude range that we have probed ($20° \leq \ell \leq 52°$). Within the longitude range of 40°–52°, the median FD above and below the mid-plane are about $+540$ and $+120\,\mathrm{rad\,m^{-2}}$, respectively. This could be decomposed into an even-parity field contribution of $\approx +330\,\mathrm{rad\,m^{-2}}$ to both above and below the plane, and an odd-parity field contribution of $\approx \pm 210\,\mathrm{rad\,m^{-2}}$ that caused the split in the FD profiles. The odd-parity field would have directions pointing towards and away from us above and below the Galactic plane, respectively.

A schematic picture of the magnetic field configuration of this scenario is shown in Figure 5.15. The sight lines in the Galactic longitude range of $40° \lesssim \ell \lesssim 52°$ pass through three spiral arms — the Sagittarius arm, the Perseus arm, and the Outer arm (Figure 5.13). As we found from the pulsar FD analysis above (Chapter 5.5.3.1), the FD trends for both above and below the plane are similar for distances of $\lesssim 5\,\mathrm{kpc}$, indicative of an even-parity field there. The FD disparity most likely occurred at a distance of $\approx 5\,\mathrm{kpc}$ from us, coinciding with the large-scale field reversal of the Sagittarius arm (Thomson & Nelson 1980; Sun et al. 2008; Van Eck et al. 2011). This suggests that the Sagittarius arm can have an odd-parity disk magnetic field. We are unable to draw concrete conclusions about the magnetic fields in the more distant (at $\gtrsim 10\,\mathrm{kpc}$) Perseus and Outer arms, since (1) the number of available pulsars at such distances is currently limited, and (2) the FD contributions by these arms, at least for above the Galactic plane, are likely not significant (see Chapter 5.5.3.1).

5.5.3.3 Scenario II: FD Contributions from the Odd-parity Galactic Halo Fields

The second possible scenario is that the differences in the FD profiles are caused by the large-scale halo field with odd parity. A schematic picture of the magnetic field configuration of this scenario is shown in Figure 5.16. Such field geometry in the Galactic halo has already been suggested from all-sky RM distribution of EGSs and pulsars (e.g., Han et al. 1997; Sun et al. 2008; Jansson & Farrar 2012) and is the preferred magnetic field configuration of spherical objects such as galactic halos (e.g., Sokoloff & Shukurov 1990; Moss et al. 2010). In this case, assuming again that both the free electron density and the magnetic field strength are identical on both sides across the Galactic plane, the even-parity disk field could have led to an FD contribution of $\approx +330\,\mathrm{rad\,m^{-2}}$, while the split in the FD profiles by $\pm 210\,\mathrm{rad\,m^{-2}}$ can be explained by the odd-parity halo field.

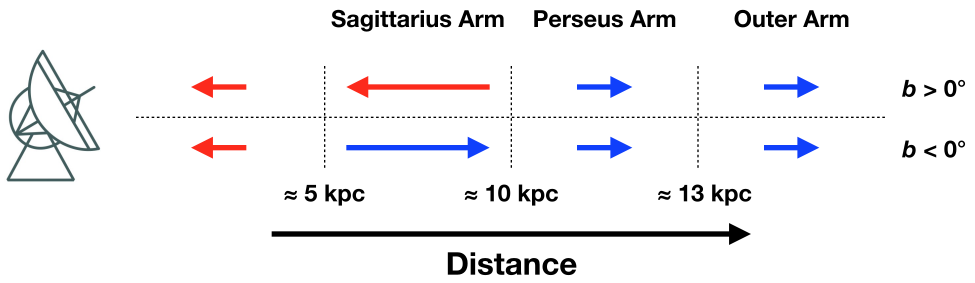

Figure 5.15: Schematic picture of magnetic fields along lines of sight towards $40° \lesssim \ell \lesssim 52°$ under Scenario I: an odd-parity disk field in the Sagittarius arm. The solid colour arrows represent the directions of the disk magnetic fields in each of the segments along the line of sight, with their lengths showing approximately the relative magnetic field strengths. Segments corresponding to Galactic spiral arms are indicated, and the Galactic mid-plane is represented by the horizontal black dashed line. The disk magnetic field directions in the Perseus and Outer arms are as suggested by the Van Eck et al. (2011) model. Image courtesy of MPIfR (MPIfR logo).

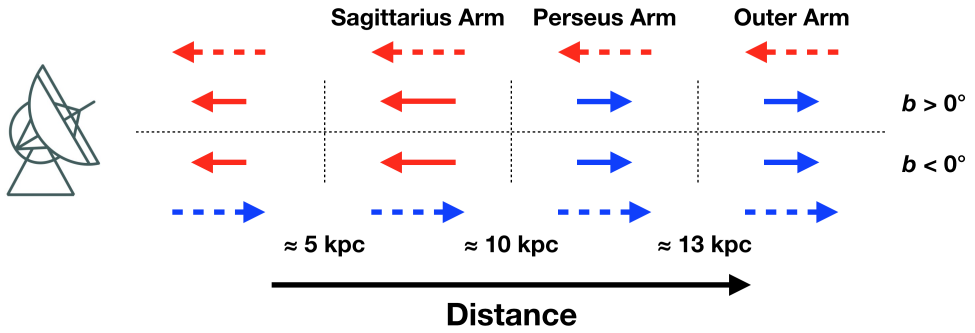

Figure 5.16: Schematic picture of Scenario II: large-scale Galactic halo field with odd parity. This Figure is similar to Figure 5.16. The disk and halo magnetic fields are represented by solid and dashed colour arrows, respectively. Image courtesy of MPIfR (MPIfR logo).

Since we do not see significant differences in the FD for above and below the Galactic plane at $20° \leq \ell \leq 40°$, we require the halo field in this scenario to have negligible FD contribution in this longitude range[5]. Furthermore, it is challenging to reconcile this scenario with the measured EGS RM towards the Perseus arm by Mao et al. (2012): their study involved 641 EGSs within $100° \leq \ell \leq 117°$ and $|b| \leq 30°$, and from the RM against b profile they suggested that the measured RMs at $|b| \lesssim 15°$ are dominated by the Galactic disk field, while the halo field dominates in $|b| \gtrsim 15°$. By assuming that the majority of Faraday rotation along their sight lines occurred in the Perseus arm at a distance of about 2 kpc (Xu et al. 2006), this translates to a disk-halo transition

[5]Apart from the uncertain range of $28° \lesssim \ell \lesssim 32°$, although if the FD disparity there is truly astrophysical, the magnetic field structure required to explain it will be even more complicated, as the FD disparity here has an opposite sense compared to that at $40° \lesssim \ell \lesssim 52°$.

height of ~ 540 pc. We apply the same disk-halo transition height to test whether the Galactic halo field is expected to have significant contributions to our measured FDs at $|b| \leq 5°$. By adopting a distance of 5 kpc for the region where the FD disparity occurs (Chapter 5.5.3.1), the $|z| \sim 540$ pc transition height of Mao et al. (2012) would occur at $\sim 6.^{\circ}2$ for our case. Meanwhile, our newly discovered FD disparity starts at $b \approx 0°$ and saturates at $b \approx \pm 2°$ (Chapter 5.11). This either suggest that our observed differences in the FD profiles cannot be attributed to the Galactic halo field, or that the disk-halo transition height along our sight lines at $\ell \approx 45°$ is much closer to the Galactic mid-plane than towards the outer Galaxy. In Chapter 5.5.4.6, we will further investigate this scenario by comparing our results with the Galactic halo field prescriptions of the Sun et al. (2008) and Jansson & Farrar (2012) models.

5.5.3.4 Scenario III: Contamination by Ionised Structures

In the two scenarios above, we attributed the FD disparity to changes in magnetic field structures across the Galactic mid-plane. In this final scenario, we consider the possibility that the FD disparity is caused by differences in free electron densities across the Galactic plane, produced by extended ($\gtrsim 10°$ along the Galactic longitude) ionised structures either above or below the Galactic plane that cannot be clearly identified from the WHAMSS Hα map. The absence of obvious Hα structures could be attributed to dust extinction. However, no obvious structures could be located upon consulting the Finkbeiner (2003) extinction-corrected Hα map. The mean extinction-corrected Hα intensities in Galactic longitudes of 40°–52° within $|b| \leq 5°$ are 4.40 and 4.35 Rayleighs for above and below the mid-plane, respectively. Furthermore, we inspected the H I map of the Effelsberg-Bonn H I Survey (EBHIS; Winkel et al. 2016) and the total intensity map of the Sino-German 6 cm Polarization Survey (Sun et al. 2011) to look for signatures of the warm neutral medium, but could not locate any corresponding structures. There are also no corresponding listed H II regions from the *WISE* catalogue (Anderson et al. 2014).

Nonetheless, if the FD disparity is indeed caused by an enhanced free electron density by some ionised structures invisible in Hα, H I, and radio continuum, it would pose as a challenge to the study of the large-scale magnetic field reversal within the same longitude ranges using ϕ of EGSs, since the measured ϕ values either above or below the Galactic plane can be altered by the said ionised structure. However, with the currently available information, we can neither support nor rule out this possibility.

5.5.3.5 Summary on the Faraday Depth Disparity

In Chapter 5.5.3, we reported our discovery of a clear FD disparity across the Galactic mid-plane in longitude range of 40°–52°. The median FD above the Galactic plane ($0° \leq b \leq +5°$) is $+543.7\,\mathrm{rad\,m^{-2}}$, while that below the plane ($-5° \leq b < 0°$) is $+125.0\,\mathrm{rad\,m^{-2}}$. By considering pulsars with measured FD values in this region, we suggest that this FD disparity is caused by some magneto-ionic structures at a distance of ≈ 5 kpc, coinciding with the Sagittarius arm that was known to host the large-scale magnetic field reversal.

Such feature cannot be explained by an even-parity magnetic field in the Galactic disk alone. Thus, we have proposed three possible scenarios to explain the observed FD trends: (I) the disk field in the Sagittarius arm has an odd parity; (II) the presence of an odd-parity halo field at low Galactic latitude; or (III) the observed FD is contaminated by an enhancement in free electron density due to some ionised structures. Given the currently available information, we favour Scenario I since Scenario II would require the dominance of the halo field at a much lower Galactic height than expected, and we did not find obvious Hα, H I, or radio continuum structures supporting Scenario III. Future increase in the number of pulsars with accurately determined distances and FD values (see Chapter 6.4.1.1), combined with focus case studies of specific spiral arms (e.g., Mao et al. 2012), will allow us to confidently distinguish these scenarios.

5.5.4 Comparisons with Existing Galactic Magnetic Field Models

The performance of large-scale magnetic field models of the Milky Way can be tested using the newly derived FD values of the 196 EGSs. In this work, we consider three recent major Galactic magnetic field models, namely Sun et al. (2008), Van Eck et al. (2011) and Jansson & Farrar (2012). The azimuthal components of the Galactic disk fields of the three models are illustrated in Figure 5.17, with their key features described below.

5.5.4.1 A Brief Review on the Galactic Magnetic Field Models

Firstly, the Sun et al. (2008) model[6] was developed using the EGS RM measurements reported in the CGPS (Taylor et al. 2003; Brown et al. 2003) and the Southern Galactic Plane Survey (SGPS; Gaensler et al. 2001; Brown et al. 2007). Specifically, they adopted the NE2001 free electron density model (Cordes & Lazio 2002), and determined the values of the free parameters of their large-scale magnetic field model by fitting the predicted RM to the observed RM values. The Galactic large-scale field reversal has been represented by a ring at Galacto-centric radius of $6 < R\,(\mathrm{kpc}) \leq 7.5$, and the disk field strength diminishes exponentially at increasing Galactic height z. Furthermore, the disk field is assumed to have an even parity in their model. They also included a toroidal halo field component with opposite field directions across the Galactic disk (i.e. odd-parity halo fields). The vertical magnetic field has been assumed to be negligible in their model.

Next, the Van Eck et al. (2011) model used their RM measurements of 194 EGSs on the Galactic plane, in addition to the CGPS (Brown et al. 2003) and SGPS (Brown et al. 2007) RMs, to determine the parameters of their field model of the Galactic disk. The NE2001 electron density model (Cordes & Lazio 2002) has again been used. In their work, only the Galactic disk field (which is assumed to have an even parity) has been considered. Their model consists of three independent sectors with vastly different

[6] In this work, we consider their ASS+RING model for the disk field, since it has been found to give the best fit to observations compared to their ASS+ARM and BSS models (Sun et al. 2008; Van Eck et al. 2011).

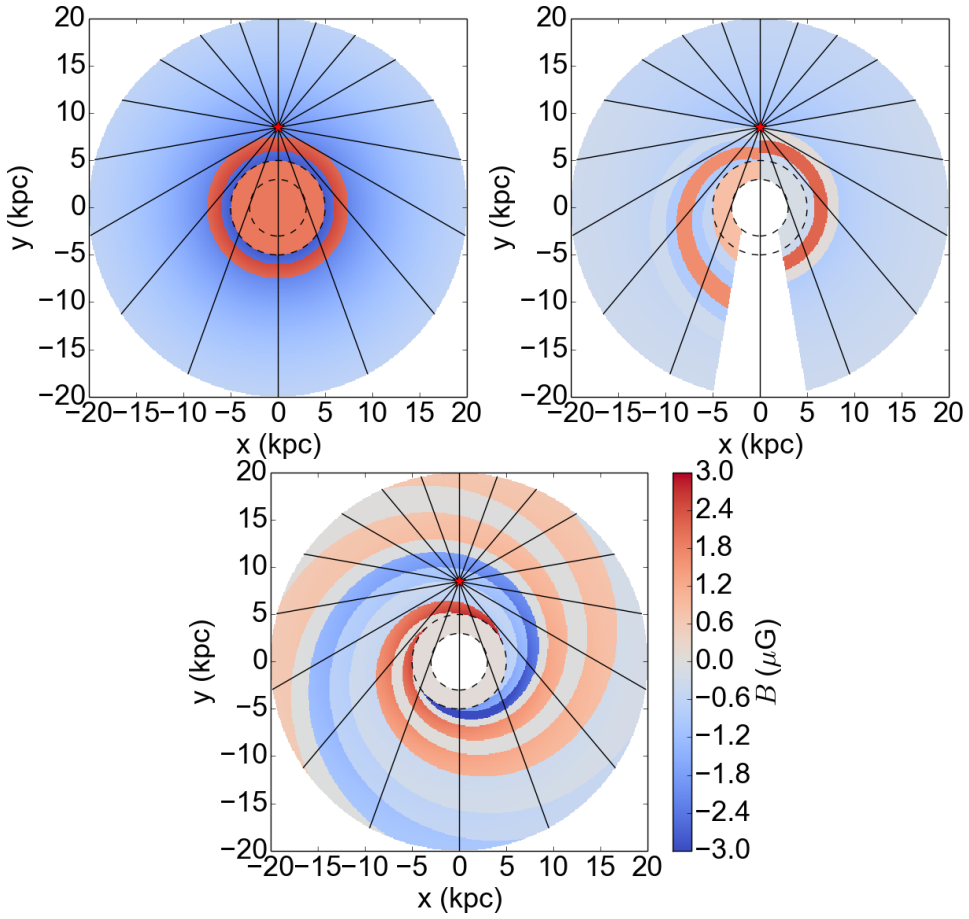

Figure 5.17: The azimuthal components of the large-scale magnetic fields of the Milky Way on the Galactic disk (i.e. $z = 0$) according to the **(Top left)** Sun et al. (2008), **(Top right)** Van Eck et al. (2011), and **(Bottom)** Jansson & Farrar (2012) models, looking down from the Galactic north pole. The magnetic field strengths are shown in colour, with blue and red representing regions with clockwise and anti-clockwise fields, respectively. The location of the Sun is marked by the red stars, and the dashed black lines enclose the molecular ring of the Milky Way. Black solid lines are drawn to mark the Galactic longitudes at a 20° interval starting from $\ell = 0°$.

geometries. Within the region of interest of this Chapter, the Galactic large-scale field reversal occurs at $5.8 < R\,(\mathrm{kpc}) \leq 8.4$. The magnetic fields are assumed to be constant along z up till $\pm 1.5\,\mathrm{kpc}$ beyond which the field strength is assumed to be zero, and they also ignored the vertical field component.

Finally, the Jansson & Farrar (2012) model is distinctive from the other two models because their model is fully 3D. It is separated into the disk, the toroidal halo, and the X halo components, with the vertical magnetic field also implemented. Furthermore, their field model is more physically motivated, with the divergenceless condition of magnetic fields applied and the X-shaped halo field implemented as motivated by the observational results from external edge-on galaxies (e.g., Krause 2009; Wiegert et al.

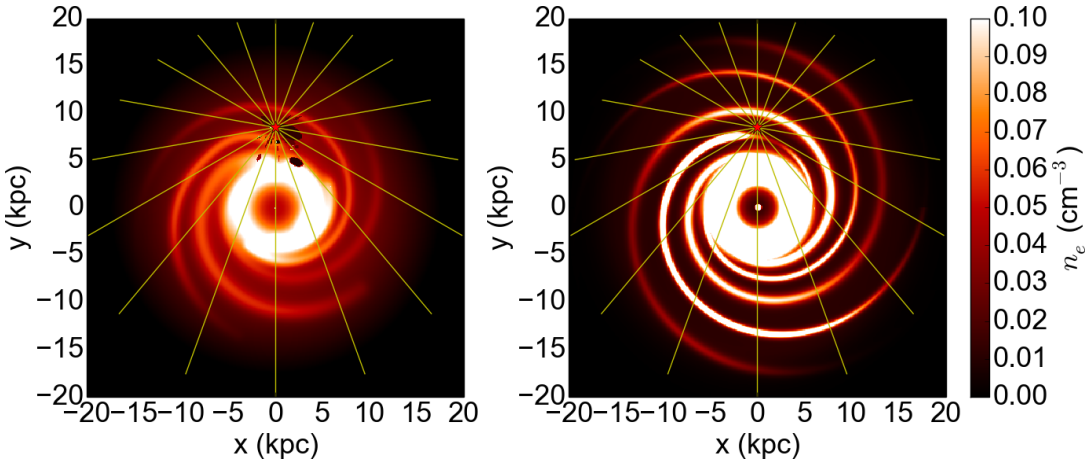

Figure 5.18: The Galactic free electron densities on the Galactic disk (i.e. $z = 0$) according to the **(Left)** NE2001 (Cordes & Lazio 2002) and **(Right)** YMW16 (Yao et al. 2017) models, looking down from the Galactic north pole. The location of the Sun is marked by the red stars, and the yellow solid lines are drawn to mark the Galactic longitudes at a 20° interval starting from $\ell = 0°$.

2015). They used (1) an extensive list of RM measurements from the literature covering the entire sky, (2) the K-band (22 GHz) WMAP polarised synchrotron data of the Galactic foreground (Gold et al. 2011)[7], (3) the NE2001 free electron density model (Cordes & Lazio 2002), and (4) the Galactic cosmic ray density models from GALPROP (Strong et al. 2009) and WMAP (Page et al. 2007) as the input data to determine the best-fit parameters of their Galactic magnetic field model. The disk field component, which is the focus of this study, is mostly determined by the RM values from the CGPS (Brown et al. 2003), SGPS (Brown et al. 2007), Van Eck et al. (2011), and the TSS09 catalogue.

5.5.4.2 Remarks on the Free Electron Density Models

With the large-scale Galactic magnetic field models above, maps of the predicted FD along lines of sight through the Milky Way can be generated given a Galactic free electron density model. We consider below two commonly adopted models of the electron density, namely the NE2001 (Cordes & Lazio 2002) and the YMW16 (Yao et al. 2017) models. The newer YMW16 model has been claimed to be more reliable in predicting the distances to pulsars by their DM values than NE2001 (see Yao et al. 2017), meaning that the former can be a more accurate representation of the free electron density distribution of the Milky Way than the latter. Nonetheless, all three large-scale field models that are examined in this work adopted the NE2001 model when fitting to the observed RM values. Moreover, NE2001, Sun et al. (2008), Van Eck et al. (2011) and Jansson & Farrar (2012) have all adopted the same solar distance

[7]They masked certain regions of the WMAP data that can be contaminated by individual polarised Galactic objects.

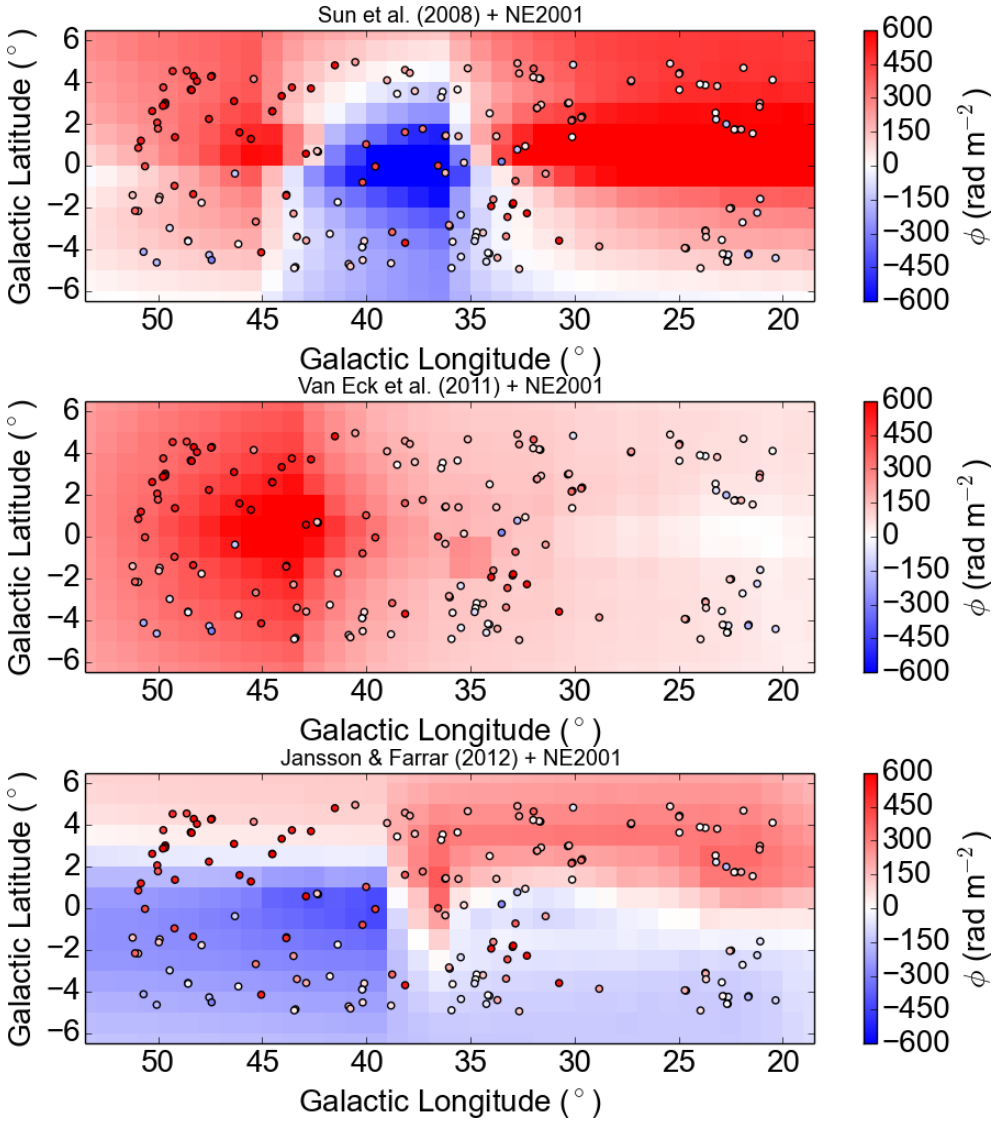

Figure 5.19: Our new FD measurements (colour dots) overlaid on the predicted FD maps of **(Top)** Sun et al. (2008), **(Middle)** Van Eck et al. (2011), and **(Bottom)** Jansson & Farrar (2012) models of the large-scale magnetic fields of the Milky Way. The free electron density model of NE2001 (Cordes & Lazio 2002) has been used.

from the Galactic centre of 8.5 kpc (Kerr & Lynden-Bell 1986), while YMW16 has used 8.3 kpc (Brunthaler et al. 2011). The different adopted distances will clearly lead to mismatches in the physical locations of Galactic structures (e.g. spiral arms). We can therefore expect the predicted FD values using NE2001 to be more consistent with the observed FD values than that when using YMW16.

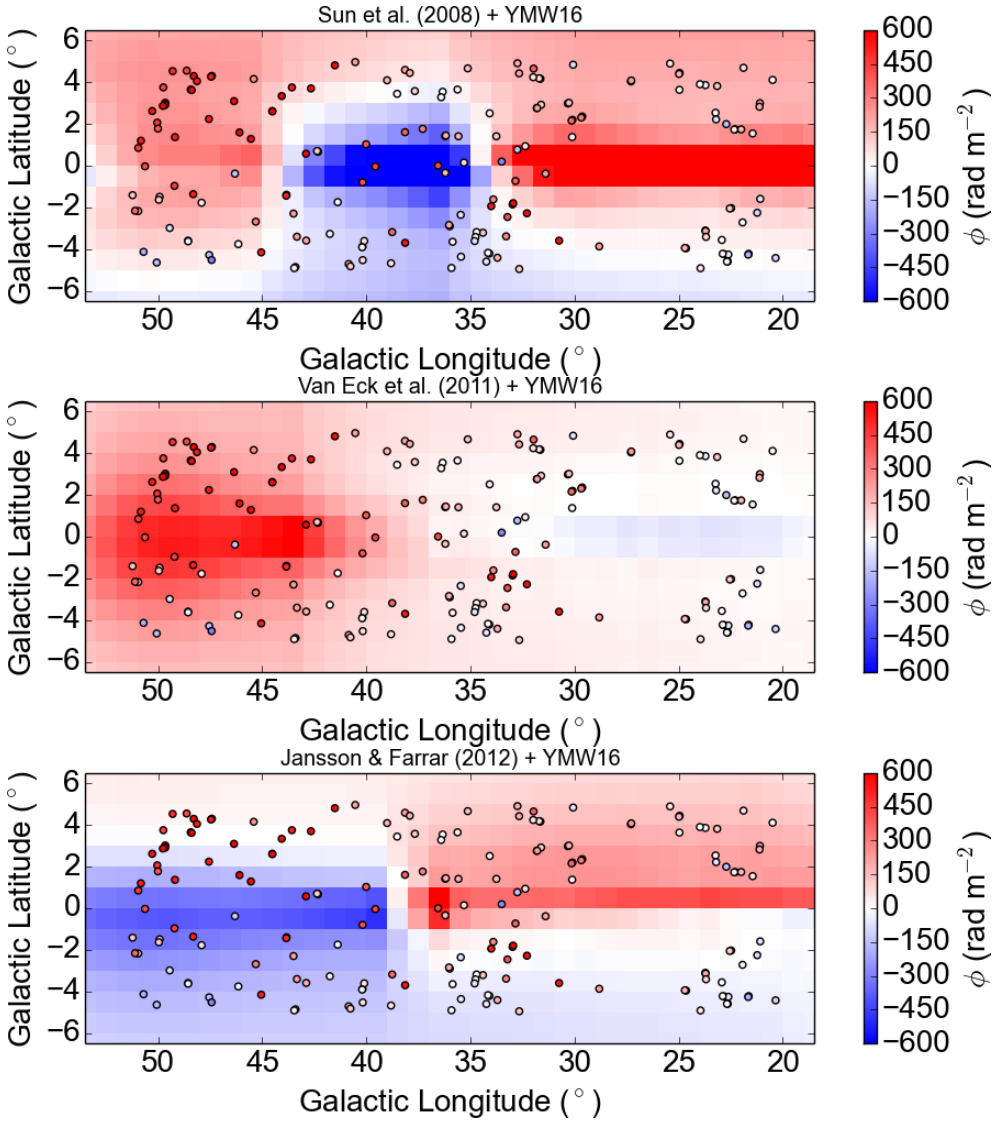

Figure 5.20: Same as Figure 5.19, but using instead the free electron density model of YMW16 (Yao et al. 2017).

5.5.4.3 Predicted Faraday Depth Maps

The predicted FD maps of the three magnetic field models within the region of interest are shown in Figure 5.19, using the NE2001 electron density model. Among the predictions made by these field models, striking differences can be noted. The Van Eck et al. (2011) model predicts mostly symmetric FD distributions about $b = 0°$, with same signs and similar amplitudes. This is because their model has only considered a disk field that is symmetric about the Galactic plane. Any subtle deviations of FD from symmetry are therefore due to asymmetries in the electron density model. On the other hand, both Sun et al. (2008) and Jansson & Farrar (2012) predicted FDs are highly asymmetric about the Galactic mid-plane, often with different signs and

amplitudes. Although their disk field components are symmetric about $b = 0°$, that is not the case for the halo fields. Specifically, the plane-parallel fields of the halo components in both models switch direction as one moves along z through $b = 0°$, while the direction of the vertical fields of the X halo component of Jansson & Farrar (2012) remains unchanged. All these features of the halo fields are imprinted as the asymmetries seen in the predicted FD across $b = 0°$. As noted in Chapter 5.5.3, the newly derived FD values above versus below the Galactic plane are found to differ in the $40° \lesssim \ell \lesssim 52°$ region, meaning that the symmetric magnetic field model of Van Eck et al. (2011) would not be adequate in matching the observed FD above and below the Galactic plane simultaneously (see below).

As we move along the Galactic plane at increasing ℓ, the predicted FD of the Sun et al. (2008) model shows rapid changes from about $+600\,\mathrm{rad\,m^{-2}}$ in $20° \lesssim \ell \lesssim 30°$ down to about $-400\,\mathrm{rad\,m^{-2}}$ at $\ell \approx 40°$, and finally back up to about $+300\,\mathrm{rad\,m^{-2}}$ in $40° \lesssim \ell \lesssim 52°$. The minima in FD at $\ell \approx 40°$ can be attributed to the ring at $5 < R\,(\mathrm{kpc}) \leq 6$ with clockwise fields. On the other hand, the peaks in FD at $20° \lesssim \ell \lesssim 30°$ and $40° \lesssim \ell \lesssim 52°$ are dominated by the Galactic molecular ring region at $3 \leq R\,(\mathrm{kpc}) \leq 5$ and the field reversal region at $6 < R\,(\mathrm{kpc}) \leq 7.5$, respectively, both with anti-clockwise fields. With visual inspection of the predicted and the newly derived FD values (top panel of Figure 5.19), we find large discrepancies particularly in the $20° \lesssim \ell \lesssim 40°$ range, suggesting that the Sun et al. (2008) field model can be inadequate in this longitude range.

Next, we consider the Van Eck et al. (2011) model, which predicts a low $\phi \approx +100\,\mathrm{rad\,m^{-2}}$ at $20° \lesssim \ell \lesssim 30°$, and a peak of $\phi \approx +600\,\mathrm{rad\,m^{-2}}$ at $\ell \approx 45°$. This FD peak corresponds to the sight line passing almost tangential to the field reversal ring at $5.8 < R\,(\mathrm{kpc}) \leq 7.2$. The consistently positive predicted FD values within the entire Galactic longitude range of 20°–52° signifies that the contribution of the field reversal region is dominant throughout. Overlaying the new observed FD values on the Van Eck et al. (2011) predicted FD map (middle panel of Figure 5.19) suggests a good agreement between them, except for the region below the Galactic plane at $40° \lesssim \ell \lesssim 52°$ where the observed ϕ is consistently lower than predicted. This will be further investigated below.

Complex structures in the predicted FD map of Jansson & Farrar (2012) can be seen in the bottom panel of Figure 5.19. We find a generally poor agreement between their predicted FD with our observed FD, meaning that their global model may not perform satisfactorily within the region of interest.

Finally, we present in Figure 5.20 the predicted FD maps of the same three magnetic field models but with the YMW16 electron density model. The qualitative trends of these maps are largely similar to that with NE2001, except that (1) in all field models the predicted $|\phi|$ falls off quicker with increasing $|b|$ for YMW16 than for NE2001, and (2) the predicted FD of Van Eck et al. (2011) at $20° \lesssim \ell \lesssim 30°$ on the Galactic plane is instead slightly negative when YMW16 is used. The conclusions of this work remain unchanged if YMW16 is used instead of NE2001.

Table 5.5: χ^2 of the Different Model Combinations

Input Model	Galactic Longitude Range			
	20°–30°	30°–40°	40°–52°	Full Range
$-5° \leq b \leq +5°$				
Sun et al. (2008) + NE2001	4.3×10^4	4.0×10^5	1.5×10^5	2.2×10^5
Van Eck et al. (2011) + NE2001	$\mathbf{4.0 \times 10^3}$	$\mathbf{3.2 \times 10^4}$	$\mathbf{7.4 \times 10^4}$	$\mathbf{4.1 \times 10^4}$
Jansson & Farrar (2012) + NE2001	1.5×10^4	3.8×10^4	4.4×10^5	1.9×10^5
Sun et al. (2008) + YMW16	6.0×10^3	8.2×10^5	2.3×10^5	3.9×10^5
Van Eck et al. (2011) + YMW16	6.3×10^3	5.8×10^4	1.6×10^5	8.4×10^4
Jansson & Farrar (2012) + YMW16	6.4×10^3	7.4×10^4	4.7×10^5	2.1×10^5
$0° \leq b \leq +5°$				
Sun et al. (2008) + NE2001	6.8×10^4	6.6×10^5	2.5×10^5	3.7×10^5
Van Eck et al. (2011) + NE2001	$\mathbf{3.6 \times 10^3}$	4.1×10^4	$\mathbf{9.9 \times 10^4}$	$\mathbf{5.3 \times 10^4}$
Jansson & Farrar (2012) + NE2001	1.7×10^4	$\mathbf{2.2 \times 10^4}$	7.6×10^5	2.9×10^5
Sun et al. (2008) + YMW16	4.9×10^3	1.5×10^6	4.2×10^5	7.1×10^5
Van Eck et al. (2011) + YMW16	7.8×10^3	8.0×10^4	2.8×10^5	1.4×10^5
Jansson & Farrar (2012) + YMW16	5.9×10^3	9.8×10^4	8.2×10^5	3.4×10^5
$-5° \leq b \leq 0°$				
Sun et al. (2008) + NE2001	1.6×10^4	8.6×10^4	6.4×10^4	6.0×10^4
Van Eck et al. (2011) + NE2001	$\mathbf{4.5 \times 10^3}$	$\mathbf{2.0 \times 10^4}$	5.0×10^4	2.9×10^4
Jansson & Farrar (2012) + NE2001	1.3×10^4	5.8×10^4	1.3×10^5	7.6×10^4
Sun et al. (2008) + YMW16	7.1×10^3	8.6×10^4	5.6×10^4	5.5×10^4
Van Eck et al. (2011) + YMW16	4.8×10^3	3.1×10^4	$\mathbf{3.7 \times 10^4}$	$\mathbf{2.7 \times 10^4}$
Jansson & Farrar (2012) + YMW16	6.9×10^3	4.6×10^4	1.4×10^5	7.4×10^4

NOTE — For each combination of Galactic longitude and latitude ranges, the lowest χ^2 value is bold-faced.

5.5.4.4 Quantitative Comparisons between Models

We further perform quantitative comparisons between the Galactic magnetic field models, combined with the two free electron density models, by evaluating the goodness-of-fit of their predicted FD values to the newly derived FDs. For each model combination, we define a measure of the goodness-of-fit as

$$\chi^2 = \sum_j^N \frac{(\phi_{\mathrm{obs},j} - \phi_{\mathrm{model},j})^2}{N \cdot \sigma_{\phi,j}^2}, \tag{5.5}$$

where j is an index for the N data points, ϕ_{obs} is the observed FD value from our new observations, ϕ_{model} is the predicted FD value at the exact Galactic coordinates of the observed EGS, and σ_ϕ is the FD measurement uncertainty from RM-Synthesis. Note that the scatter in FD of $\sim 100\,\mathrm{rad\,m^{-2}}$ introduced by the combination of EGS intrinsic FD and small-scale Galactic magnetic fields (see Chapter 5.5.3), has not been accounted for in this analysis, and its magnitude is much larger than our typical measurement

uncertainty in FD of $\approx \ 2\,\mathrm{rad\,m^{-2}}$. Therefore, the χ^2 values are not expected to converge to unity, but nonetheless they can be used to evaluate the relative goodness-of-fit among the model combinations considered.

The χ^2 values of each model combination for different Galactic longitude and latitude ranges are listed in Table 5.5, with a lower value indicating a better fit. In almost all cases, the FD predictions by the Van Eck et al. (2011) field model combined with the NE2001 model yielded the lowest χ^2 values among the model combinations, and even for cases otherwise its χ^2 value is still close to that of the best model combination (within a factor of two). This suggests that the Van Eck et al. (2011) plus NE2001 model combination, despite its inability to predict the observed FD disparity across the Galactic mid-plane (Chapter 5.5.4.3), can best reproduce the observed FDs among those considered in this work.

5.5.4.5 Boxcar-binned Faraday Depth Across Galactic Longitude

Finally, we collapse the Galactic latitude axis and compare between the predicted and observed FD profiles across Galactic longitude, with the goals to (1) qualitatively compare the FD trends to identify potential areas of weaknesses of the Galactic magnetic field models, and (2) to further verify the conclusions drawn in the previous two Chapters (5.5.4.3 and 5.5.4.4) regarding the effectiveness of the models. Boxcar binning of the FD of the target sources across ℓ has been performed to minimise the effects of the intrinsic FD of the EGSs as well as that of the spatially fluctuating FD due to turbulence in the Faraday rotating warm ionised medium of the Milky Way (e.g., Gaensler et al. 2005; Mao et al. 2010; Van Eck et al. 2011; Mao et al. 2012). In particular, turbulence in the Galactic disk can lead to FD fluctuations of $\sim 100\,\mathrm{rad\,m^{-2}}$ on an angular scale of $\sim 1^\circ$ (e.g., Haverkorn et al. 2008).

Since the observed FDs were noted to exhibit different distributions above and below the Galactic plane (Chapter 5.5.3), three boxcar-binning results from our observations have been generated, considering sources within (1) $-5^\circ \leq b \leq +5^\circ$, (2) $0^\circ \leq b \leq +5^\circ$, and (3) $-5^\circ \leq b < 0^\circ$, with a binning width of 5° in ℓ used in all cases[8]. Similarly, equivalent plots of FD across ℓ as predicted by the three field models combined with the two free electron density models have been created. For each case, the expected FDs at the exact sky positions of the target sources have been calculated according to the different model combinations. The lists of expected FDs are then boxcar-averaged in the same way as did to the observed FDs. This will mitigate any potential biases from the uneven spatial sampling due to the random positions where our polarised target EGSs are located at. The comparisons between the models and our new observations are shown in Figure 5.21 with NE2001, and Figure 5.22 with YMW16.

Considering the full Galactic latitude range with NE2001, one can notice the striking resemblance between the observed FD and the prediction of the Van Eck et al. (2011) model. The two only show moderate deviations in the longitude range of $25^\circ \lesssim \ell \lesssim 30^\circ$.

[8]This binning width must be larger than the outer scale of turbulence of the Galactic warm ionised medium ($\gtrsim 1^\circ$; e.g. Haverkorn et al. 2008) for the spatial averaging to be effective. The final choice of 5° is dictated by the sparse spatial sampling at $25 \lesssim \ell \lesssim 30^\circ$ below the Galactic plane.

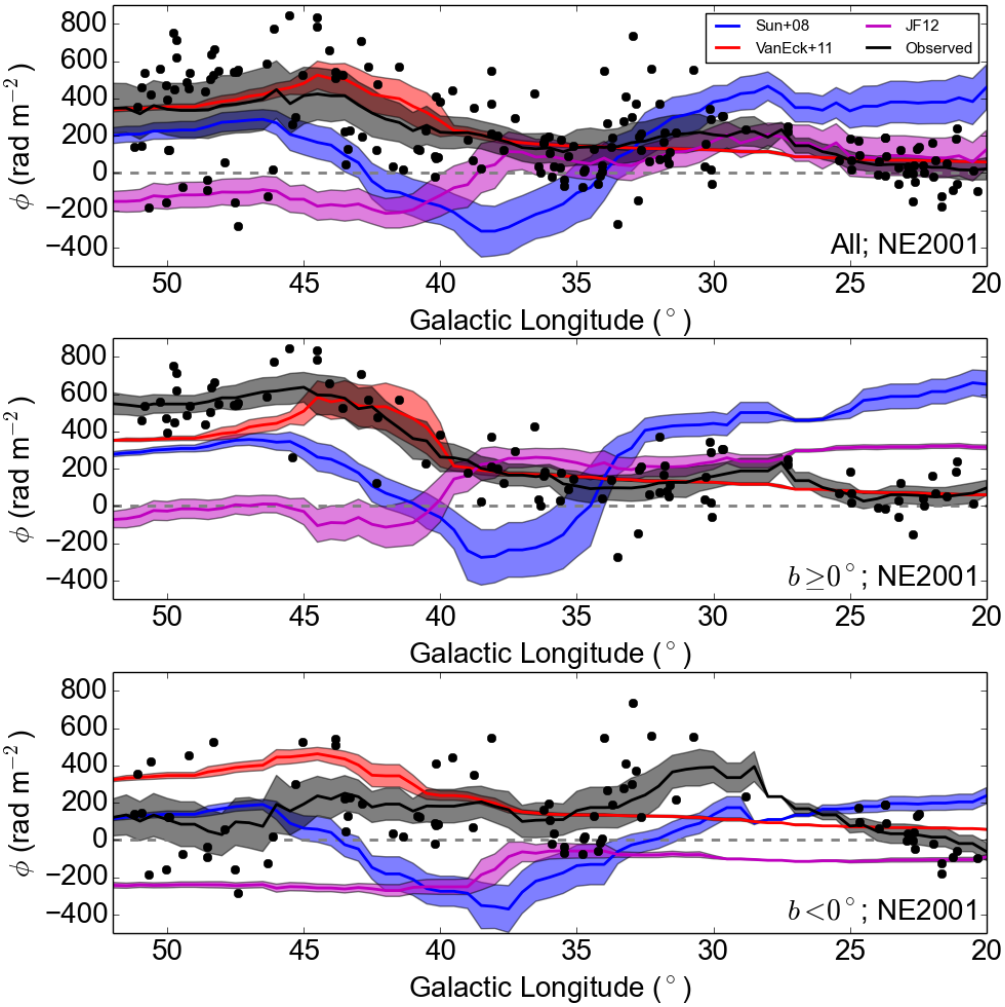

Figure 5.21: Comparisons between the boxcar-binned observed FD (black lines) and the predictions of the Sun et al. (2008) (Sun+08; blue lines), Van Eck et al. (2011) (VanEck+11; red lines), and Jansson & Farrar (2012) (JF12; magenta lines) models. The three panels show the results from considering Galactic latitude ranges of **(Top)** $-5° \leq b \leq +5°$, **(Middle)** $0° \leq b \leq +5°$, and **(Bottom)** $-5° \leq b < 0°$. The shaded areas enclose 1σ of the FD values within the corresponding bin, and the observed FD values of the individual sources are marked as the black data points. The free electron density model of NE2001 (Cordes & Lazio 2002) has been used.

The model also fits the new observations well for sources above the Galactic plane ($b \geq 0°$) up to $\ell \approx 45°$ beyond which the predicted and the observed FD deviate: the predicted FD falls off gradually to $\approx +350\,\mathrm{rad\,m^{-2}}$, while the observed FD stays at the $\approx +500\,\mathrm{rad\,m^{-2}}$ level. As the sight lines in $45° \lesssim \ell \lesssim 52°$ run tangentially through the field reversal region in the Van Eck et al. (2011) model, this discrepancy suggests that the parameters of the field reversal region in the model were not adequately constrained, particularly the spatial extent and/or the magnetic field strength. Finally, we note that

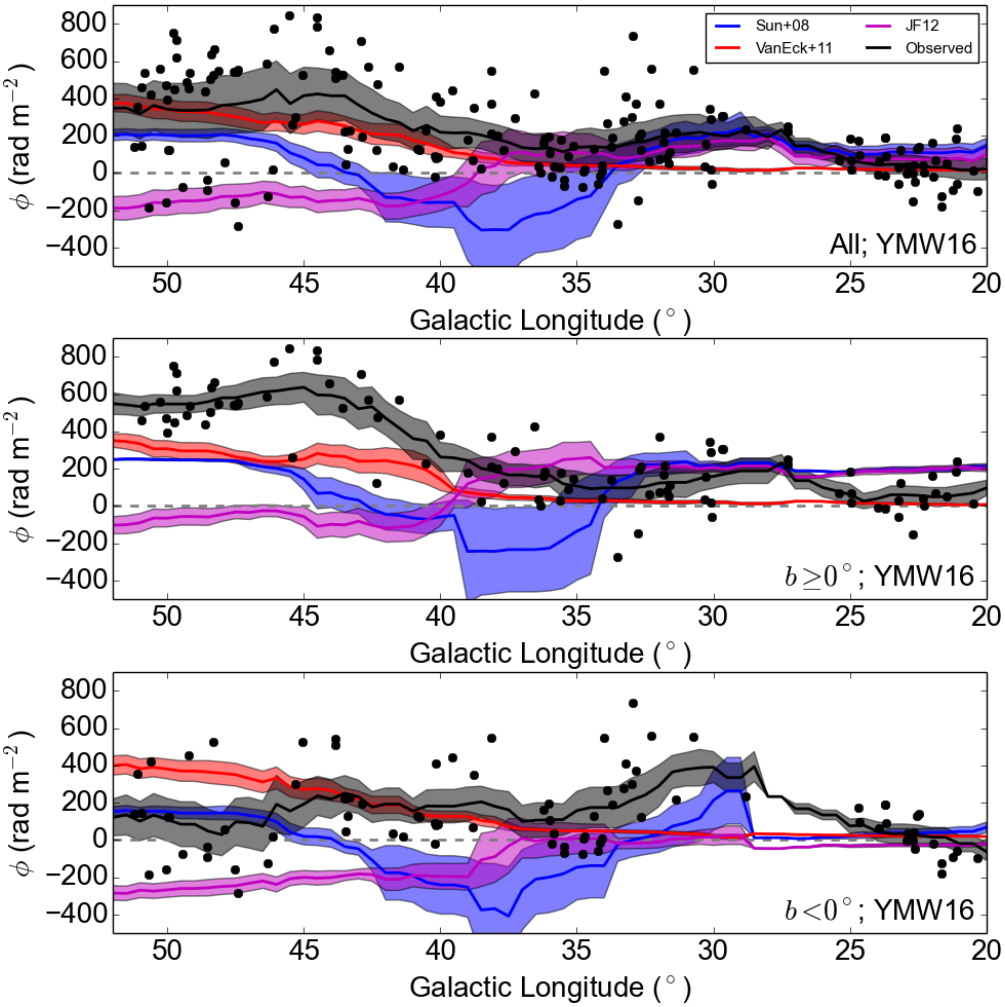

Figure 5.22: Same as Figure 5.21, but using instead the free electron density model of YMW16 (Yao et al. 2017).

the Van Eck et al. (2011) model cannot satisfactorily predict the new ϕ values below the Galactic plane, since the model assumes a-priori that the magnetic field strength and direction remains the same across the Galactic mid-plane. This clearly calls for a new Galactic magnetic field model that considers the observed FD values above and below the Galactic mid-plane separately.

We find that both Sun et al. (2008) and Jansson & Farrar (2012) predicted FD fails to match the new FD values, regardless of the Galactic latitude ranges considered. Furthermore, if the YMW16 electron density model is adopted, none of the three field models give satisfactory fit to the observations. This is as expected, since all three field models were constructed assuming the NE2001 model (see Chapter 5.5.4.2).

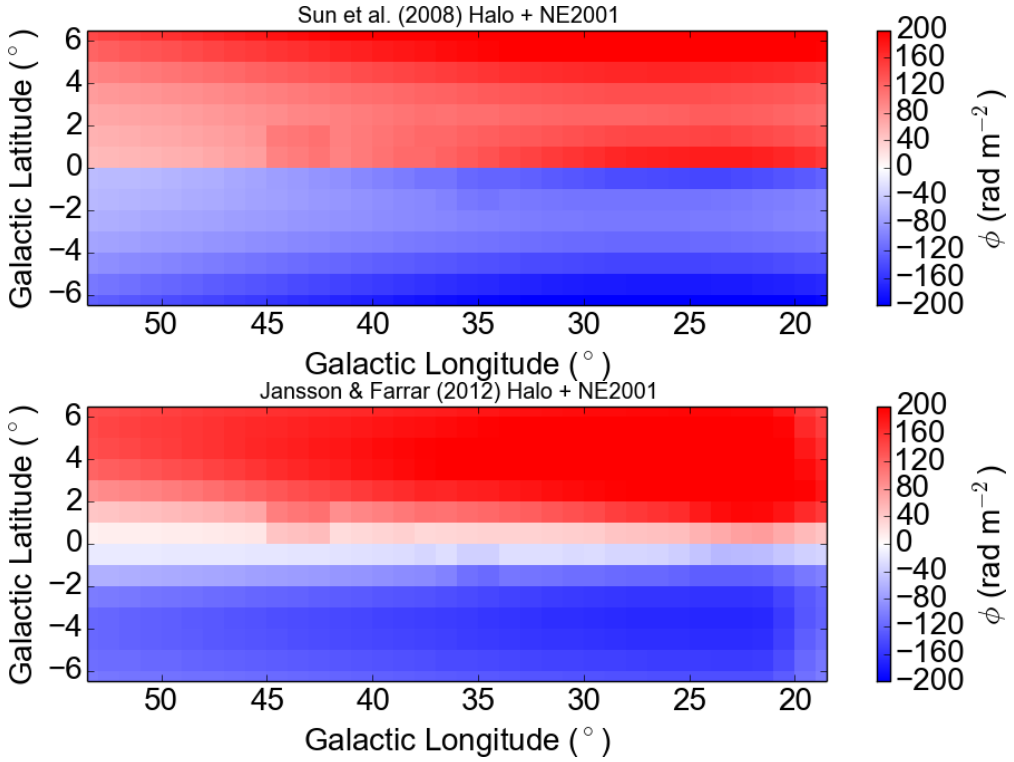

Figure 5.23: Predicted FD contribution maps of the Galactic halo field of **(Top)** Sun et al. (2008) and **(Bottom)** Jansson & Farrar (2012) models. Note the different colour scales compared to previous Figures in this Chapter. The free electron density model of NE2001 (Cordes & Lazio 2002) has been used.

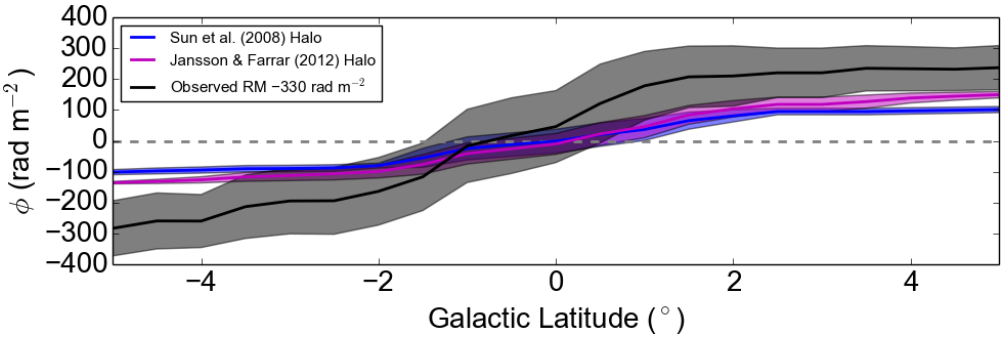

Figure 5.24: Boxcar-binned FD of the targets (black line) across b within the longitude range of 40°–52° only, plus a y-offset of $-330\,\mathrm{rad\,m^{-2}}$. The predictions by the halo components of Sun et al. (2008) and Jansson & Farrar (2012) models are shown in blue and magenta, respectively. A boxcar binning width of 5° in b has been used. The shaded area encloses 1σ of the FD values within the corresponding bin.

5.5.4.6 Can the Halo Field Explain the Faraday Depth Disparity?

Finally, we return to investigate whether the Galactic halo field, at least according to the prescriptions of the Sun et al. (2008) and Jansson & Farrar (2012) models,

can explain the observed FD disparity across the Galactic plane in $40^\circ \lesssim \ell \lesssim 52^\circ$ (Chapter 5.5.3). Both halo field models have odd-parity magnetic fields that fill the entire volume of the Milky Way. At a Galacto-centric radius of 8.5 kpc and at 500 pc above the Galactic mid-plane, the Sun et al. (2008) and Jansson & Farrar (2012) halo field models predict magnetic field strengths of 0.3 and 0.9 μG, respectively. Predicted FD maps have been generated by using the halo field components of these two models (i.e., the disk field components have been removed), combined with the NE2001 model (Figure 5.23).

Indeed, both halo field models can create disparities in FD of $\approx$ 200–300 rad m^{-2} along Galactic latitudes within the $40^\circ \leq \ell \leq 52^\circ$ range, but the same is also predicted for the longitude range of 20°–40°. This predicted FD disparity in $20^\circ \leq \ell \leq 40^\circ$ is not seen from our newly derived FDs. Nonetheless, we generated the boxcar-binned FD profiles but this time along Galactic latitude by considering sources within $40^\circ \leq \ell \leq 52^\circ$ only, which is shown in Figure 5.24 along with the predictions by the halo fields of Sun et al. (2008) and Jansson & Farrar (2012). A y-offset of -330 rad m^{-2} has been added to the observed FD profile to centre it at $\phi \approx 0$ rad m^{-2} to facilitate comparisons with the model predictions. In the scenario that we investigate here (i.e. the disk field has an even parity while the halo field has an odd parity), this -330 rad m^{-2} will correspond to the FD contribution by the even-parity disk field. The similarities in the functional forms between the observed and predicted profiles suggest that the Galactic halo field remains a plausible candidate to explaining the observed FD disparity, though the implementations of neither of the two halo models can (1) reproduce the amplitude of this disparity in the 40°–52° longitude range, or (2) explain the absence of FD disparity at the 20°–40° longitude range.

5.6 Conclusion

In this Chapter, we have conducted new broadband spectro-polarimetric observations with the Jansky VLA to investigate the large-scale magnetic fields near the Milky Way mid-plane ($|b| \leq 5^\circ$) within the Galactic longitude range of $20^\circ \leq \ell \leq 52^\circ$. The FD values of a total of 196 EGSs (168 on-axis plus 28 off-axis) were determined, out of which 179 (153 on-axis plus 26 off-axis sources) were used for this study. Our new data have marked a significant increase in the number of sight lines with reliably determined FD values by a factor of five when compared with Van Eck et al. (2011) in the above longitude range. Upon comparison between our newly derived FDs and the RM values in the TSS09 catalogue, we found that almost 40 per cent of the TSS09 RM values suffer from the $n\pi$-ambiguity, which leads to deviations of the listed RM in TSS09 from the true values by ± 652.9 rad m^{-2}. This means the TSS09 catalogue is not optimal for the study of the Galactic magnetic field within the above region of interest, and the magnetic field models derived using those RM values can be negatively impacted.

By inspecting the spatial distribution of FD, we found a clear disparity in the FD values within the Galactic longitude range of $40^\circ \lesssim \ell \lesssim 52^\circ$ across the Galactic mid-plane, while the FD values above and below the plane in $20^\circ \lesssim \ell \lesssim 40^\circ$ agree with

each other. By incorporating the existing pulsar FD measurements, we suggest that the FD disparity occurs at a distance of ≈ 5 kpc away from us, corresponding to the Sagittarius arm known to also host a large-scale magnetic field reversal. We considered three scenarios that could have led to the newly discovered FD disparity:

- Scenario I: The large-scale magnetic field in the Galactic disk in the Sagittarius arm can have an odd parity, meaning that the plane-parallel magnetic field changes in direction as one crosses the Galactic plane;
- Scenario II: A large-scale odd-parity Galactic halo field contributes significantly to the observed FD, leading to the FD disparity; or
- Scenario III: The difference in FD values of the target EGSs either above or below the Galactic plane have been contaminated by an enhanced free electron density due to some Galactic ionised structures.

Given the currently available information, we favour Scenario I, since Scenario II requires the halo field to dominate at a very low Galactic height of $\ll 500$ pc, while we could not locate corresponding structures in Hα, H I, or 6 cm radio continuum maps, nor in the *WISE* H II region catalogue that would support Scenario III. Furthermore, we found that pulsars within the sky region of $40^\circ \lesssim \ell \lesssim 46^\circ$ and $-1\overset{\circ}{.}5 \lesssim b \lesssim 0^\circ$ have peculiar FD values.

Finally, we performed rigorous comparisons between the observed FD values with the predictions by three major large-scale magnetic field models — Sun et al. (2008), Van Eck et al. (2011), and Jansson & Farrar (2012), combined with the free electron density models of NE2001 (Cordes & Lazio 2002) and YMW16 (Yao et al. 2017). We conclude that the model combination of Van Eck et al. (2011) and NE2001 can best reproduce our measured FD values. However, we noted potential short-comings of the Van Eck et al. (2011) model. As a field model that has been assumed a-priori to be symmetric about the Galactic mid-plane, it fails to fit to the observed FD values below the Galactic plane within $40^\circ \lesssim \ell \lesssim 52^\circ$. In addition, the differences in the FD profiles between the model prediction and observation within the same longitude range suggests that the parameters of the field reversal region, in particular the spatial extent and/or the magnetic field strength, were not adequately constrained. We further noted that the Galactic halo field prescriptions of neither Sun et al. (2008) nor Jansson & Farrar (2012) can adequately explain our discovered FD disparity.

Our study has provided us with new insights into the large-scale magnetic fields of the Milky Way. The data portray a highly complex magneto-ionic medium along the Sagittarius arm that must be carefully taken into account in future modelling works of the large-scale magnetic fields of the Milky Way. Our results also call for similar detailed studies to be conducted on other spiral arms in attempt to identify similar FD disparities.

Chapter 6

Conclusions and Future Prospects

In the final chapter of this thesis, I will first summarise the results from Chapters 3–5. Then, I will outline the expected progresses in the near future within the field of cosmic magnetism. Finally, I will describe my role in the future development of the research field as extensions of the studies presented in this thesis.

Contents

6.1 Summary of the Thesis

Magnetic fields are ubiquitous in our Universe, showing a wide variety of field strengths and geometries at a vast range of physical scales. In the interstellar medium of spiral galaxies, the magnetic fields with strengths of $\sim 10\,\mu$G are known to be crucial to astrophysical processes such as interstellar gas dynamics, star formation, and cosmic ray propagation. An accurate knowledge of the magnetic fields of our home Galaxy, the Milky Way, is clearly essential for the studies of many branches of Galactic astrophysics.

Therefore, I have dedicated this thesis to the measurements of the magnetic fields of the Milky Way.

Astrophysical magnetic fields can be measured by performing radio polarisation observations at multiple frequencies. Such strategy exploits the Faraday rotation effect, with the observable, namely rotation measure (RM) or Faraday depth (FD), being related to the strength and direction of the magnetic field component along the sight line. By forming grids of FD (or RM) measurements of extragalactic radio sources (EGSs) covering large sky areas, one can probe the strength and geometry of the Milky Way.

Large-sky-area polarisation surveys are some of the best resources for the study of Galactic magnetism. The current state-of-the-art RM catalogue of Taylor et al. (2009, hereafter TSS09), covering the sky north of declination of $-40°$ at an RM density of higher than one per deg^2 (37,543 sources in total), has been indispensable for the study of the magnetic fields of the Milky Way. A thorough understanding in the limitations and systematics of this RM catalogue is essential for accurate characterisations of the Galactic magnetic fields, as well as for future careful comparisons or combinations with the results from future polarisation surveys (see Chapter 6.2.1.1).

In Chapter 3, I have broken the $n\pi$-ambiguity problem in the TSS09 RM catalogue. This systematic issue is present because the RM catalogue is based on polarisation measurements in two frequency bands only, and the potential wrapping of polarisation angles (PAs) lead to ambiguous RM values by $\pm 652.9\,\mathrm{rad\,m^{-2}}$ for their specific observational setup. FD values determined from radio broadband spectro-polarimetric observations are free of $n\pi$-ambiguity, as the polarisation measurements are conducted at hundreds of closely separated frequency channels, leaving no room for ambiguous PA wraps between the channels. I have exploited this capability with new broadband spectro-polarimetric observations using the Jansky VLA in L-band (1–2 GHz) to verify the RM values of 23 $n\pi$-ambiguity candidates of the TSS09 catalogue. My study has led to the identification of nine $n\pi$-ambiguity sources, in addition to 11 sources that have reliable $\mathrm{RM_{TSS09}}$ values. Furthermore, one source was found to be incompatible with neither $n\pi$-ambiguity nor reliable $\mathrm{RM_{TSS09}}$ cases, and two sources were found to be actually unpolarised. With the sources separated into the two main classes, I rigorously explored the parameter space in search for a good diagnostic of $n\pi$-ambiguity of the TSS09 RM catalogue that exhibits a clear difference in statistical distributions between the two classes. I devised a new parameter, Δ/σ, which is a measure of how much a source's RM deviates from that of its neighbours, as a good diagnostic: a large value ($\gtrsim 2.5$) is suggestive of $n\pi$-ambiguity. I further computed the Δ/σ of all TSS09 sources, and found that there are at least 50 sources suffering from the $n\pi$-ambiguity problem. This number is a lower limit to the actual figure, since my inspection of the RM catalogue of Van Eck et al. (2011) has led to the identification of a region on the Galactic plane ($35° \lesssim \ell \lesssim 52°$) with a high concentration of TSS09 $n\pi$-ambiguity sources that had not been identified by Δ/σ. The ineffectiveness of Δ/σ in this region can be attributed to the highly complex magnetic field structure, which I have studied in Chapter 5 of this thesis (see below). To conclude, I found that the TSS09 RM values are mostly reliable in a broad sense, but on the individual source level, their RM values

can be erroneous and care must be taken when using them.

I continued the in-depth study of the TSS09 RM catalogue in Chapter 4, in which the new observations from Chapter 3 have been further exploited to quantify the effects of off-axis instrumental polarisation on RM_{TSS09}. Off-axis instrumental polarisation can be caused by imperfections in optical alignments or standing waves within optical parts of radio telescopes, leading to false polarisation signals for positions away from the pointing axis. This effect has not been calibrated out in the TSS09 catalogue, which is based on a blind polarisation survey and therefore its sources are in general situated off-axis. In my new observations, the target sources are placed on the pointing axis, meaning that my polarisation measurements are free of off-axis instrumental polarisation. By a rigorous comparison between the two data sets within identical frequency ranges, I found that the two sets of RM values do not agree within measurement uncertainties. This discrepancy, along with the two unpolarised sources identified in Chapter 3 that were reported as ≈ 0.5 per cent polarised in TSS09, have been attributed to the off-axis instrumental polarisation present in the TSS09 data. I further quantified its effects on RM measurements by a simulation, adopting the 0.5 per cent above as the typical off-axis instrumental polarisation amplitude. The simulation results showed that the reported TSS09 RM uncertainties have to be increased by 10 per cent on average to take into account the effect of the uncorrected off-axis instrumental polarisation. This extra RM uncertainty is a function of the source's polarisation fraction and its true RM value, and has been found to be highly non-Gaussian. I have successfully reconciled the discrepant RM values of 18 out of the 21 polarised target sources by incorporating this extra RM uncertainty, while the remaining three sources may be variable in RM, and they have been followed up by further observations (see Chapter 6.5.3). This work suggests that the TSS09 RM uncertainties have been underestimated, and must be carefully taken into account for precise studies of Galactic and cosmic magnetism. Furthermore, future polarisation surveys must properly calibrate out the effects of off-axis instrumental polarisation for high precision polarisation measurements.

Finally, in Chapter 5, I investigated in the magnetic fields in the first Galactic quadrant near the mid-plane of the Milky Way. The magnetic field geometry in this sky region is highly complex, with a known large-scale magnetic field reversal in the Sagittarius arm. However, the number of EGSs with reliably determined FD (or RM) values in this region used to derive the complicated field structure is severely lacking. This could have led to the different exact descriptions of the large-scale field reversal among Galactic magnetic field models. I have therefore performed new Jansky VLA observations in L-band (1–2 GHz) to measure the FD values of 196 EGSs within Galactic longitudes of 20°–52° and latitudes of ±5°. The resulting source number density of one per 1.6 deg^2 is a drastic increase from the one per 7.3 deg^2 of Van Eck et al. (2011), enabling my careful investigation of the large-scale magnetic fields of the Milky Way. I first showed that almost 40 per cent (32 out of 87) of TSS09 RMs within the region of interest suffer from $n\pi$-ambiguity, meaning that Galactic magnetic field models constructed using those RM values can be negatively impacted. The major finding of my work is the discovery of an intriguing feature in the spatial FD distribution —

a clear disparity in FD across the Galactic mid-plane within $40° \leq \ell \leq 52°$. The median of my newly derived FDs above and below the plane in this longitude range are $+543.7$ and $+125.0\,\mathrm{rad\,m^{-2}}$, respectively. Using existing pulsar data from the ATNF Pulsar Catalogue (Manchester et al. 2005), I constrained that this FD disparity occurs at a distance of $\approx 5\,\mathrm{kpc}$, corresponding to the Sagittarius arm that also hosts a large-scale magnetic field reversal. The FD disparity cannot be explained by an even-parity Galactic disk field alone, and can be due to (1) an odd-parity disk field in the Sagittarius arm, (2) an odd-parity halo field with significant contributions to the observed FD at low Galactic latitudes of $|b| \ll 5°$, or (3) the sight lines are contaminated by an enhanced free electron density due to some ionised structures. Given the currently available information, I favour the first scenario above (i.e. odd-parity disk field). This is because the odd-parity halo field scenario requires the dominance of the halo field to start at a much lower Galactic height of $\ll 500\,\mathrm{pc}$ than expected, while the hypothetical ionised structure in the third scenario could not be identified from Hα, H I, or 6 cm radio continuum maps, nor from the *WISE* H II region catalogue. Moreover, I compared my newly derived FD values with the predictions of three major Galactic magnetic field models —Sun et al. (2008), Van Eck et al. (2011), and Jansson & Farrar (2012), each combined with the free electron density models of NE2001 (Cordes & Lazio 2002) and YMW16 (Yao et al. 2017). I concluded that the model combination of Van Eck et al. (2011) with NE2001 can best match my observed FD values, though the symmetric magnetic fields across the Galactic plane of the Van Eck et al. (2011) model obviously cannot match the FD disparity. Finally, I found that the Galactic halo field prescriptions of neither Sun et al. (2008) nor Jansson & Farrar (2012) can explain the observed FD disparity, since both of them (1) underestimate the amplitude of the FD disparity by a factor of two to three, and (2) predict the presence of a similar FD disparity in the Galactic longitude range of 20°–40° as well that is absent in my data. To summarise, my findings demand the construction of a new global magnetic field model of the Milky Way that can capture the newly discovered FD disparity in the Sagittarius arm.

6.2 Future Faraday Depth Grids

6.2.1 On-going and Future Polarisation Surveys

6.2.1.1 Future Goldmines for Cosmic Magnetism

The TSS09 RM catalogue, despite its limitations (see Chapters 3 and 4), has led to significant advances in our understanding of the magnetic fields in the Universe, especially for that in the Milky Way (e.g., Stil et al. 2011; Jansson & Farrar 2012; Oppermann et al. 2012; Terral & Ferrière 2017). Its polarised source density of about one per square degree has resulted in our current knowledge of the RM contributions of the Milky Way at an angular resolution of $\approx 3°$ (e.g., Oppermann et al. 2012, 2015), and has allowed studies of turbulence in the Galactic warm ionised medium down to an angular scale of $\approx 10'$ (e.g., Stil et al. 2011). On-going and future polarisation

surveys are anticipated to further revolutionise our view of the magnetised Universe, by virtue of (1) their broadband spectro-polarimetric capabilities that will allow Faraday complexities to be taken into account using RM-Synthesis or QU-fitting (see below), (2) their expected drastic increase in polarised source densities because of improvements in sensitivities of radio instruments, and (3) their higher angular resolution. These new broadband surveys will also be immune to the $n\pi$-ambiguity problem, which I showed to be a limitation in the TSS09 RM catalogue (Chapters 3 and 5).

The study of large-scale magnetic fields of the Milky Way can greatly benefit from the increases in the polarised source densities. In such studies, the goal is to accurately recover the FD contributions by the large-scale fields throughout the entire sky, and the FD contributions by both the small-scale Galactic magnetic fields and the EGSs themselves can be regarded as variance introduced to our measurements. With increases in the polarised source densities, more EGS FDs will be encompassed within the same spatial scale. Therefore, the resulting spatially binned FD values over the same scale are expected to have less contributions by the above variance. This will lead to more accurate measurements of the FDs by the large-scale Galactic magnetic fields.

The new survey data can also be analysed in several different ways to investigate the Galactic small-scale magnetic fields. Firstly, the regime of $\gtrsim 1'$ can be probed by the structure function analysis (e.g., Haverkorn et al. 2008; Mao et al. 2010; Stil et al. 2011), which measures the spatial fluctuation of FD at various angular scales by considering the FD values *between* individual EGSs. The smallest angular scale that the structure function analysis is sensitive to is determined by the polarised source density of the survey, which is expected to see enormous improvements in the coming years (see below). Secondly, at angular scales $\lesssim 1'$ but larger than the resolution of the survey, the effects of the small-scale magnetic fields of the Milky Way are imprinted in the spatial fluctuation of FD *within* spatially resolved EGSs (e.g., Leahy et al. 1986; Minter & Spangler 1996). The improvements in the angular resolution from the $60''$ of TSS09 to 1–$10''$ of the new surveys will open up possibilities for future works at such angular scales. However, this will first require a deeper understanding in the intrinsic FD of EGSs (see Chapter 6.3). Finally, the new broadband spectro-polarimetric surveys will further allow us to "resolve" the small-scale magnetic fields that cannot be spatially resolved by the surveys (see Chapter 2.2.4), but again would require a prior knowledge in the intrinsic FD of EGSs.

Some on-going interferometric polarisation surveys are the Polarisation Sky Survey of the Universe's Magnetism (POSSUM; Gaensler et al. 2010) with the Australian Square Kilometre Array Pathfinder (ASKAP), the Very Large Array Sky Survey (VLASS: Myers et al. 2014; Mao et al. 2014; Lacy et al. 2019) with the Jansky VLA, the Max-Planck-Institut für Radioastronomie (MPIfR) MeerKAT S-band Galactic plane survey (Barr, Kramer, Mao et al. in prep.), and the APERture Tile In Focus (APERTIF) survey with the Westerbork Synthesis Radio Telescope (WSRT)[1]. The basic parameters of the former two surveys, along with those of TSS09 as comparisons, are listed in Table 6.1. The four surveys are individually discussed below.

[1]See https://old.astron.nl/sites/astron.nl/files/cms/OTHER/ApertifSurveyPlanII.v2.2.pdf.

Table 6.1: Parameters of the Taylor et al. (2009), POSSUM, and VLASS Surveys

	TSS09[a]	POSSUM	VLASS
Instrument	Legacy VLA	ASKAP	Jansky VLA
Central Frequency (MHz)	1400	1280	3000
Bandwidth (MHz)	2×42	300	2000
Sky Coverage	$\delta > -40°$	$\delta < +30°$	$\delta > -40°$
Epochs	1993–1997	2019–	2017–
Source Count	37,543	10^6	2×10^5
Source Density (deg^{-2})	1	25	5
Sensitivity ($\mu\mathrm{Jy\,beam}^{-1}$)	300	10	70
Angular Resolution	$45''$	$10''$	$2\farcs5$

[a] Original data from the NVSS (Condon et al. 1998).

6.2.1.2 POSSUM Survey with ASKAP

Thanks to the wide field-of-view of up to $\approx 30\,\mathrm{deg}^2$ granted by the phased array feed (PAF), the ASKAP telescope is a potent instrument for radio all-sky surveys. This will indeed be exploited by the POSSUM survey (Gaensler et al. 2010). The third roll axis of the ASKAP antennas mean the off-axis instrumental polarisation pattern can be fixed with respect to the sky, allowing for a relatively straightforward removal of this instrumental effect in the image plane[2]. With all the 36 antennas operational since just several months ago as of the time of writing[3], the POSSUM pilot survey is expected to commence in the coming months, with the full survey anticipated to start in 2020. The southern polarised sky has been relatively sparsely sampled, with the Southern Galactic Plane Survey (SGPS; Gaensler et al. 2001; Brown et al. 2007) covering the Galactic longitude and latitude ranges of $253° < \ell < 358°$ and $|b| < 1.5°$ and the S-PASS/ATCA survey (Schnitzeler et al. 2019) covering the entire southern sky ($\delta < 0°$) being the only notable large-area surveys. The SGPS has resulted in RM measurements of 148 EGSs ($\approx 0.5\,\mathrm{deg}^{-2}$), while the S-PASS/ATCA reported more than 3,800 FD measurements ($\approx 0.2\,\mathrm{deg}^{-2}$). This southern polarised source count is expected to see a significant improvement with POSSUM's projected $\approx 10^6$ sources south of $\delta = +30°$ ($\approx 25\,\mathrm{deg}^{-2}$), and will result in a crisp view into the magnetism in the southern sky.

6.2.1.3 The VLASS with the Jansky VLA

The VLASS (Myers et al. 2014; Mao et al. 2014; Lacy et al. 2019) will be the first large-area polarisation survey conducted in S-band (2–4 GHz). This unique frequency range will be well suited for studying Galactic regions[4] with peculiar physical conditions that would lead to severe depolarisation in L-band. Specifically, S-band

[2] See http://www.atnf.csiro.au/projects/askap/documents/ASKAP_sci_obs_guide%20(002).pdf.
[3] See https://www.atnf.csiro.au/content/askap-36-antenna-integration-complete/.
[4] Similarly for extragalactic regions; see Chapter 6.3.

measurements with the Jansky VLA are less prone to Faraday depolarisation effects: considering the external Faraday dispersion case (Chapter 2.2.4), a σ_ϕ of $10\,\mathrm{rad\,m^{-2}}$ will lead to a decrease in the measured polarisation by 34 per cent in L-band (assumed 1.4 GHz), while that in S-band (assumed 3 GHz) will only be about 2 per cent. Furthermore, S-band observations are more resilient against bandwidth depolarisation, with the measured polarisation decrease by 50 per cent for a polarised source with a high $|\phi| \approx 1.4 \times 10^5\,\mathrm{rad\,m^{-2}}$ (assuming a frequency of 3 GHz and a native channel width of 2 MHz), while the same occurs to L-band observations (assuming a frequency of 1.5 GHz and a native channel width of 1 MHz) at a lower $|\phi| \approx 3.6 \times 10^4\,\mathrm{rad\,m^{-2}}$. This means the VLASS can facilitate studies of Galactic volumes with enhanced turbulence (e.g. the "polarisation shadows"; Stil & Taylor 2007) or with extreme values of FD (e.g. the Galactic centre; Schnitzeler et al. 2016). Finally, the Jansky VLA off-axis instrumental polarisation will be calibrated out for the final VLASS data products[5], granting a clean data set for rigorous polarisation studies.

6.2.1.4 The MPIfR MeerKAT S-band Galactic Plane Survey

A total of about 2,000 hours of observing time of the South African Square Kilometre Array (SKA) pathfinder, the MeerKAT radio telescope (Jonas & MeerKAT Team, 2016), will be dedicated to the MPIfR MeerKAT S-band Galactic plane survey (Barr, Kramer, Mao et al. in prep.). This survey is planned to cover the southern Galactic plane within longitudes of $-65°$ to $+15°$ and latitudes of $\pm 1°$ at an angular resolution of $\approx 3'$. The expected polarised EGS number density is $\gtrsim$ 20–30 per deg^2, much higher than that of the current state-of-the-art TSS09 (one per deg^2) and the SGPS (0.5 per deg^2; Gaensler et al. 2001; Brown et al. 2007). The results from this survey will be influential to the understanding of the magnetic fields of the Milky Way, as it covers critical Galactic regions in the southern sky that are at present poorly sampled by EGS RM grids. Such regions include the highly complex Galactic centre region (e.g., Law et al. 2011b, see also Han 2017) hosting intriguing non-thermal filaments (Yusef-Zadeh et al. 1984), and the tangential sight lines to the Norma and Crux-Scutum spiral arms. There are indications that the large-scale magnetic field reversal of the Sagittarius arm extends to either the Crux-Scutum (e.g., Van Eck et al. 2011) or the Carina arm (e.g., Frick et al. 2001). The resulting data from this S-band survey will allow us to verify if this is the case for the Crux-Scutum arm. Furthermore, this survey can be utilised as excellent continuation of my work presented in Chapter 5. Specifically, it is possible to identify FD disparities towards the above spiral arms across the Galactic mid-plane, similar to the one I discovered in the Sagittarius arm. The parallel pulsar search programme stemming from the same survey can lead to a high number of known pulsars towards those southern spiral arms. The FD values of these pulsars can be determined by follow-up observations, and can be used for more accurate constraints on the distances to the potential FD disparities.

[5] See http://www.aoc.nrao.edu/~fschinze/VLASS/memos/memo_teccor.pdf.

6.2.1.5 APERTIF Survey with the WSRT

The APERTIF survey will exploit the PAF of the WSRT to observe sections in the northern sky in the frequency range of 1130–1430 MHz, with a very narrow channel width of 12.2 kHz. The shallow survey regions covering $\sim 3500\,\mathrm{deg}^2$ have been defined to overlap with surveys in optical wavelengths such as the Sloan Digital Sky Survey (SDSS), and the Galactic plane within right ascension of 2–5 h, with a target sensitivity of $\sim 15\,\mu\mathrm{Jy\,beam}^{-1}$. Several medium-deep survey areas covering $\sim 450\,\mathrm{deg}^2$ have also been defined, with an expected sensitivty of $\sim 6\,\mu\mathrm{Jy\,beam}^{-1}$. The expected angular resolution of the APERTIF survey will be $\approx 15''$.

6.2.1.6 Future Polarisation Surveys

In the mid-late 2020s, upcoming radio telescopes such as the SKA[6] and the next-generation Very Large Array (ngVLA)[7] promise even greater leaps forward in our understanding of cosmic magnetism (e.g., Mao 2018). The former is expected to be operational starting from the next decade with a frequency coverage of 50–1760 MHz and 4.6–15.3 GHz, while the latter may be available for scientific uses starting from year 2034 and is expected to cover 1.2–160 GHz. The expected substantial increase in the sensitivity of both telescopes will provide us with even denser FD grids — up to 14 million polarised sources ($\approx 400\,\mathrm{deg}^{-2}$; Johnston-Hollitt et al. 2015) with the SKA and potentially even more with polarisation surveys with the ngVLA.

6.2.2 Optimisation of Broadband Spectro-polarimetric Algorithms

As we invest our efforts into obtaining the wealth of data to be brought by on-going and future polarisation surveys, parallel works in optimising the broadband spectro-polarimetric algorithms are warranted. Despite the wide usage of these algorithms in recent studies (e.g., Heald et al. 2009; O'Sullivan et al. 2012; Anderson et al. 2015; Mao et al. 2015; Kim et al. 2016; Pasetto et al. 2018; Betti et al. 2019), the best method to convert the observational data into the FD contributions of the foreground magneto-ionic media has yet to be determined. Further tests on actual observational data (e.g., Schnitzeler 2018), as well as by simulations (e.g., Sun et al. 2015; Schnitzeler & Lee 2017), are needed to refine the current algorithms, or even to develop new tools, to fully exploit the broadband capabilities of the new surveys.

6.2.2.1 Rotation Measure Synthesis or QU-fitting?

The effectiveness of RM-Synthesis compared to that of Stokes QU-fitting has yet to be fully explored. Studies done on simulated observations at 1.1–1.4 GHz have shown that QU-fitting can be more reliable for sources that are best represented by two Faraday thin components at a polarisation S/N ratio of about 30 (Sun et al. 2015). It has also been independently demonstrated that QU-fitting can be more robust in

[6] http://www.skatelescope.org/.
[7] http://ngvla.nrao.edu/.

identifying multiple polarised components with similar FD values (Schnitzeler 2018). Similar comparisons can be done for (1) sources composed of other Faraday components, (2) different S/N regimes, and (3) different frequency coverages for a complete understanding of the relative strengths and weaknesses between the two algorithms.

6.2.2.2 An Optimised Characterisation of the Foreground Magneto-ionic Medium

The key goal of FD-grid experiments is to represent the characteristics of the foreground magneto-ionic volumes of interest by a few parameters (e.g., ϕ and σ_ϕ; see Chapter 2.2.4). A commonly adopted strategy is to locate, for each target EGS seen in the sky plane, the highest peak in the Faraday spectrum and report the corresponding FD value as the FD along that sight line (e.g., Mao et al. 2010; Betti et al. 2019, see also Chapter 5). This implicitly assumes that for cases with multiple polarised components, the FD of the component with the highest PI or p is the best representation of the foreground along that sight line. However, without prior knowledge of the intrinsic polarisation properties of the EGSs themselves, it is not trivial to verify this assumption. In fact, one can argue that the FD values of all polarised components can be equally good (or, bad) representations of the foreground magneto-ionic medium. The determination of the optimal procedure to incorporate the extra information granted by multiple polarised components in FD-grid experiments is overdue, and is tightly linked to deeper understanding of the EGS source properties (Chapter 6.3). This can be tested with the new data I obtained for Chapter 5 (see Chapter 6.5.4).

6.2.2.3 Faraday Synthesis — A New Approach

The Faraday synthesis algorithm (also referred to as "3D RM-Synthesis"; Bell & Enßlin 2012) has been invented as a new approach to processing broadband spectro-polarimetric data. The traditional RM-Synthesis method is to first form (deconvolved) channel images from the visibility data, and then perform RM-Synthesis individually for each pixel in the sky plane to obtain the final Faraday cubes. The two independent steps of imaging and RM-Synthesis have been proposed to be combined in the Faraday synthesis algorithm, with the deconvolution performed in the 3D space of the Faraday cubes. It has been shown that Faraday synthesis can improve the fidelity and dynamic range of the final Faraday cube, and can perform better in low S/N scenarios (Bell & Enßlin 2012). However, the current plan for both the ASKAP and the SKA surveys is to release calibrated channel images instead of keeping the visibility data, meaning that the traditional RM-Synthesis analysis has to be followed unless Faraday synthesis will be performed at the observatory level.

6.3 Polarisation Properties of Extragalactic Radio Sources

Not only do broadband spectro-polarimetric observations of EGSs allow studies of the magneto-ionic medium in the foreground, but also of the intrinsic polarisation

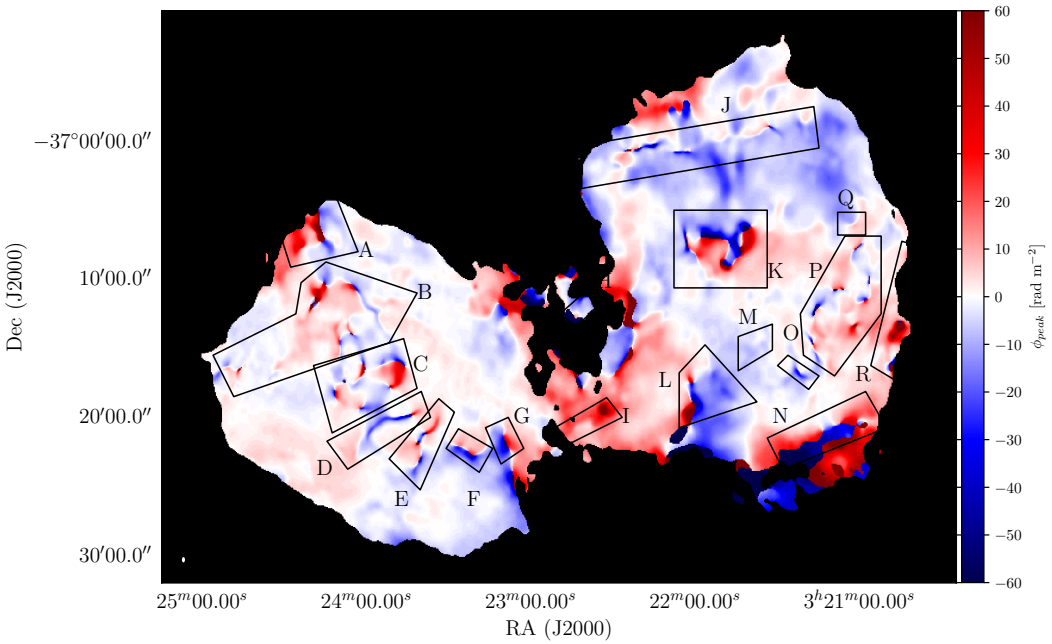

Figure 6.1: The FD map of the radio galaxy Fornax A from broadband spectro-polarimetric observations at 1.28–3.1 GHz (Anderson et al. 2018). The Galactic FD contribution of $-6\,\mathrm{rad\,m^{-2}}$ has been removed. The size of the synthesised beam is shown as the white ellipse to the lower left. Image courtesy of Anderson et al. (2018).

properties of the EGSs themselves. In fact, since the observed FD value is the sum of all components along a sight line, including the contributions from the EGS itself, a better understanding in the intrinsic polarisation properties of the EGSs is necessary for accurate quantifications of the FD contributions by the targets (e.g., the Milky Way) in future FD-grid experiments (see e.g., Rudnick 2019).

EGSs are known to have FD contributions originating from within themselves, as well as from their immediate vicinities (e.g., Zavala & Taylor 2001; Pasetto et al. 2018). The magnitudes of such intrinsic FD values when observed at deci- and centimetre wavelengths are typically $\sim 10\,\mathrm{rad\,m^{-2}}$ (e.g., Schnitzeler 2010; Oppermann et al. 2015), but for some cases can reach $\sim 10^3\,\mathrm{rad\,m^{-2}}$ (e.g., Pasetto et al. 2018). Furthermore, a recent broadband (1.28–3.1 GHz) spectro-polarimetric study at high spatial resolution ($25'' = 2.2\,\mathrm{kpc}$) of a nearby ($D \approx 18\,\mathrm{Mpc}$) radio galaxy, Fornax A, has revealed rich and complex structures in the FD map of its radio lobes, with spatial variations in FD of $\approx 100\,\mathrm{rad\,m^{-2}}$ (see Figure 6.1; Anderson et al. 2018). If this system is instead not spatially resolved (e.g., situated at a much larger distance), the intricate structures of its magneto-ionic medium could manifest as a broadening in the Faraday spectrum that would be difficult to be distinguished from, for instance, the turbulence in the interstellar medium of the Milky Way at the angular scale of this radio galaxy. To mitigate the effects of the intrinsic FD of EGSs in FD-grid experiments, we need to better our knowledge in the typical broadband polarisation properties of these EGSs.

Specifically, the relationships between the intrinsic FD along with its spatial spread with parameters such as redshifts[8], source types (e.g., AGNs[9], radio relics, etc.), and physical scales shall be studied in details.

One on-going project aiming to further our understanding in the broadband spectro-polarimetric properties of EGSs is QU Observations at Cm wavelength with Km baselines using ATCA (QUOCKA; Principal investigator: G. Heald)[10], which will utilise new broadband (1–8.5 GHz) ATCA observations of polarised EGSs identified in ASKAP early-science images. At an even larger survey scale, the VLASS, thanks to its unique frequency coverage and high angular resolution (Chapter 6.2.1.3), can also uncover new classes of EGSs that are situated in highly turbulent magneto-ionic media that cause severe depolarisation in L-band but not in S-band (see Chapter 6.2.1.3; Mao et al. 2014). The VLASS data in S-band can also be combined with the L-band data from POSSUM and/or the APERTIF survey in the overlapping regions to obtain a broad λ^2 coverage for such studies.

Furthermore, I show in Appendix B that for spatially resolved EGSs, the flux-integrated QU-fitting results may not match satisfactorily with those from the spatially resolved analysis. This highlights the gap between the Stokes QU-fitting models generally considered in the literature and the actual physical conditions of the magneto-ionic medium of the EGSs. As illustrated by the Fornax A example above, high spatial resolution studies of EGSs can reveal the rich structures of their magneto-ionic media. One direction to pursue is therefore high angular resolution studies of EGSs to spatially resolve the Faraday complexities of EGSs. This can lead to a better understanding in the physical properties of the EGSs that are causing the observed Faraday complexities, paving towards more realistic QU-fitting models that can better capture the intrinsic polarisation properties of the EGSs. The enhanced Multi Element Remotely Linked Interferometer Network (e-MERLIN) telescope can be utilised for such studies by exploiting its broadband (1.25–1.75 GHz for L-band and 4.5–7.5 GHz for C-band, with bandwidth of 512 MHz for each band) capabilities combined with its high angular resolution ($0\farcs2$ and $0\farcs05$ for L- and C-bands, respectively)[11].

Finally, the polarisation properties of EGSs can be explored in the time domain. Recent pioneering work in broadband polarisation variabilities of blazars by Anderson et al. (2019) with the ATCA at 1.1–3.1, 4.5–6.5, and 8.0–10.0 GHz has revealed that all nine of their targets showed significant changes in polarisation properties. The variabilities over five years are interpreted as changes in the jet structures of the blazars. One could also study the broadband time variabilities of the polarisation properties of the 23 EGSs that I studied in Chapters 3 and 4 (preliminary results are shown in Chapter 6.5.3).

[8] See the unpublished work of Hammond et al. (2012) as an example of studies of intrinsic FD as a function of redshift and p by using the narrowband results of Taylor et al. (2009).

[9] See O'Sullivan et al. (2017) as an example of studies of the polarisation properties of AGNs segregated into radiative- and jet-modes with their broadband (1–3 GHz) observations.

[10] See https://research.csiro.au/quocka/.

[11] A large number of EGSs can be spatially resolved at an angular resolution of $\approx 10''$ at 1.4 GHz (e.g., Rudnick & Owen 2014).

6.4 Towards a Coherent Picture of the Milky Way Magnetic Fields

Apart from the efforts towards a next-generation EGS FD grid covering the entire sky by the on-going polarisation surveys, the magnetic fields of the Milky Way can be further constrained by other observational tracers. By combining the strengths of the different techniques in probing the Galactic magnetic fields through robust statistical methods, we can anticipate significant advances in the understanding of the Galactic magnetic fields, which is of critical importance to many astrophysical branches (see Chapter 1.2).

6.4.1 Other Observational Tracers of Galactic Magnetic Fields

6.4.1.1 Faraday Depths of Galactic Pulsars

The FD-grid experiments described in this thesis mainly involved using EGSs to probe the Galactic magnetic field. In this case, the measured FD values are the results from integrating along the sight lines through the entire Milky Way and even beyond. Similar FD-grid experiments can be performed with Galactic pulsars as well to obtain a 3D-view of the magnetic fields of the Milky Way (see Chapter 1.4.5.2). Although at present the number of pulsars suitable for such studies are rather limited (e.g. 150 pulsars in Noutsos et al. 2008; 477 pulsars in Han et al. 2018; 1134 pulsars in the ATNF Pulsar Catalogue version 1.60 — Manchester et al. 2005) and the accessible pulsars are mostly nearby (most with distances $\lesssim 10\,\mathrm{kpc}$; Han et al. 2018), the SKA is expected to increase the number of known pulsars to $(1\text{–}3) \times 10^4$ spread over the entire Milky Way (Keane et al. 2015; Kramer & Stappers 2015), many of which can be used for the study of the Galactic magnetic fields (Han et al. 2015; Haverkorn et al. 2015). This, combined with the expected 14 million polarised EGSs from the SKA surveys (Chapter 6.2.1), will certainly grant us a detailed and complete view of the magnetic fields of the Milky Way.

6.4.1.2 Galactic Diffuse Synchrotron Emission

The diffuse synchrotron emission from the Milky Way can trace the Galactic magnetic fields in two ways (see, e.g., Heiles & Haverkorn 2012; Beck & Wielebinski 2013; Haverkorn & Spangler 2013; Beck 2016) — the intrinsic polarisation properties can tell us about the magnetic fields perpendicular to the line of sight in the emitting volume (Chapter 1.4.2), while the FD of such emission allows us to infer the magnetic fields along the sight lines in the intervening media.

However, the interpretation of the results from such diffuse emission can be challenging for several reasons. Firstly, the intrinsic polarisation angles are ambiguous by $\pm 180°$, meaning that we can only infer the *orientation* but not the *direction* of the magnetic fields in the emission volume. The consequence of this limit is that we cannot directly identify magnetic field reversals from the intrinsic polarisation properties, and also we cannot distinguish between regular and ordered magnetic fields. Secondly,

this method has diminished sensitivity to the polarised emission coming from beyond a certain distance called the "polarisation horizon", because of the Faraday dispersion effects. The distance to the polarisation horizon can be frequency, resolution, and direction dependent, and is expected to be $\sim$ kpc for observations performed at $\lesssim 2$ GHz on the Galactic plane (e.g., Uyaniker et al. 2003; Hill 2018). Finally, since the synchrotron emission is integrated along the sight lines before being measured, it can be difficult to trace back to the physical distances at which the emission originated from[12]. Despite these challenges, recent studies of the diffuse Galactic synchrotron emission have revealed complex polarisation structures that are not identified by other magnetic field tracers (e.g., Gaensler et al. 2011; Van Eck et al. 2017), demonstrating its importance in obtaining a complete picture of the Galactic magnetic fields.

Some key narrowband experiments probing the Galactic diffuse synchrotron emission include the Wilkinson Microwave Anisotropy Probe (WMAP) at 23–94 GHz (Page et al. 2007; Bennett et al. 2013), the *Planck* mission at 20–100 GHz (upper panel of Figure 6.2; Planck Collaboration et al. 2016d), the Sino-German 6 cm survey with the Urumqi 25 m telescope at 4.8 GHz (Sun et al. 2007), and the S-band Polarization All Sky Survey (S-PASS) with Parkes radio telescope at 2.3 GHz (Carretti et al. 2019). In the coming years, broadband spectro-polarimetric data coming from on-going surveys such as the C-Band All-Sky Survey (C-BASS) at 4500–5500 MHz (King et al. 2010), the G-ALFA Continuum Transit Survey (GALFACTS) at 1225–1525 MHz (Taylor & Salter 2010), the Global Magneto-Ionic Medium Survey (GMIMS)[13] at 300–1800 MHz (Wolleben et al. 2009), and the LOFAR Two-metre Sky Survey (LoTSS) at 120-168 MHz (Shimwell et al. 2017, 2019) can be expected to bring new exciting results to the field of Galactic magnetism.

6.4.1.3 Starlight Polarisation

The continuum emission of stars in the optical and infrared wavelengths is intrinsically unpolarised. However, if such starlight traverses through the interstellar medium occupied by asymmetric dust particles, the resulting starlight will be polarised, serving as a tracer of the magnetic fields in the interstellar medium (e.g., Clemens et al. 2012; Pavel et al. 2012). Specifically, the magnetic moment vector (and therefore the spin axis) of an asymmetric dust grain is aligned along the local magnetic field, and is perpendicular to the long axis of the grain itself (see e.g., Andersson et al. 2015; Hoang & Lazarian 2016; Boulanger et al. 2018). This would lead to an enhanced dust extinction along the long axis, resulting in a final starlight polarisation to its orthogonal orientation.

One strength of using starlight polarisation to study the Galactic magnetic fields is that, similar to FD grids of pulsars (Chapter 6.4.1.1), the 3D magnetic field structure

[12]There are cases, however, where the measured synchrotron emission is believed to be dominated by the contributions of Galactic spiral arms (e.g., Gaensler et al. 2001; Haverkorn et al. 2004), meaning that some physical distances can be assumed.

[13]Including the Southern Twenty-centimeter All-sky Polarization Survey (STAPS) observed with the Parkes radio telescope at 1300–1800 MHz simultaneously with S-PASS (see, e.g., Haverkorn 2015).

of the Milky Way can be constructed by polarisation measurements of numerous stars with measured distances (see, e.g., Boulanger et al. 2018). In fact, since pulsar FD measurements are only sensitive to the magnetic fields along the lines of sight while starlight polarisation measurements are only sensitive to that perpendicular to the sight lines, the two probes are complementary to each other. Relevant on-going optical and infrared stellar polarisation surveys include the SOUTH-POL (Magalhães 2014) and the Polar-Areas Stellar Imaging in Polarization High-Accuracy Experiment (PASIPHAE; Tassis et al. 2018), and can be combined with high accuracy parallax measurements of stellar distances from *Gaia* (Gaia Collaboration et al. 2016; Luri et al. 2018).

6.4.1.4 Polarised Dust Emission

As the interstellar dust particles absorb the ambient starlight (Chapter 6.4.1.3), the energy can be re-emitted in sub-millimetre to far-infrared regimes. Such emission can be polarised along the long axis of the asymmetric dust grains and perpendicular to the local magnetic fields (e.g., Stein 1966; Andersson et al. 2015; Boulanger et al. 2018), and therefore serve as a tracer to the Galactic magnetic fields. The dust emission from the interstellar medium of the Milky Way has been measured at 353 GHz by the *Planck* mission, and is shown in the lower panel of Figure 6.2 (Planck Collaboration et al. 2014a, 2016b, 2019).

6.4.2 The IMAGINE Consortium

The recently established Interstellar MAGnetic field INference Engine (IMAGINE) Consortium (Boulanger et al. 2018) aims to combine the observational, theoretical, and numerical efforts of research groups towards significant improvements in the model of the Galactic magnetic fields. The core of the Consortium is the IMAGINE code (Steininger et al. 2018), which iteratively generate instances of the 3D Galactic magnetic fields as well as the corresponding predicted observables. These predictions are then compared with the actual observed values of the tracers of Galactic magnetic fields (see above), and the likelihood of the field models are determined with Bayesian methods. In other words, the IMAGINE code serves as a platform to apply rigorous statistical methods to combine knowledge from various observational results and theoretical progresses to optimise the Galactic magnetic field model.

The results presented in Chapters 3 and 4 on evaluating the robustness of the Taylor et al. (2009) RM catalogue are highly relevant to the IMAGINE Consortium, since it will remain as the largest RM catalogue until the arrival of the results from on-going polarisation surveys (namely, POSSUM, VLASS, the MPIfR MeerKAT survey, and the APERTIF survey) in a few years up to a decade. I propose to continue the study to create a refined TSS09 RM catalogue incorporating the effects of both $n\pi$-ambiguity and off-axis instrumental polarisation (see Chapter 6.5.2). Furthermore, the study in Chapter 5 has shown that the magnetic fields near the Galactic plane within longitude range of $20^\circ \leq \ell \leq 52^\circ$ are more complex than previously expected. This will be an important information for the Consortium towards an improved Galactic magnetic field

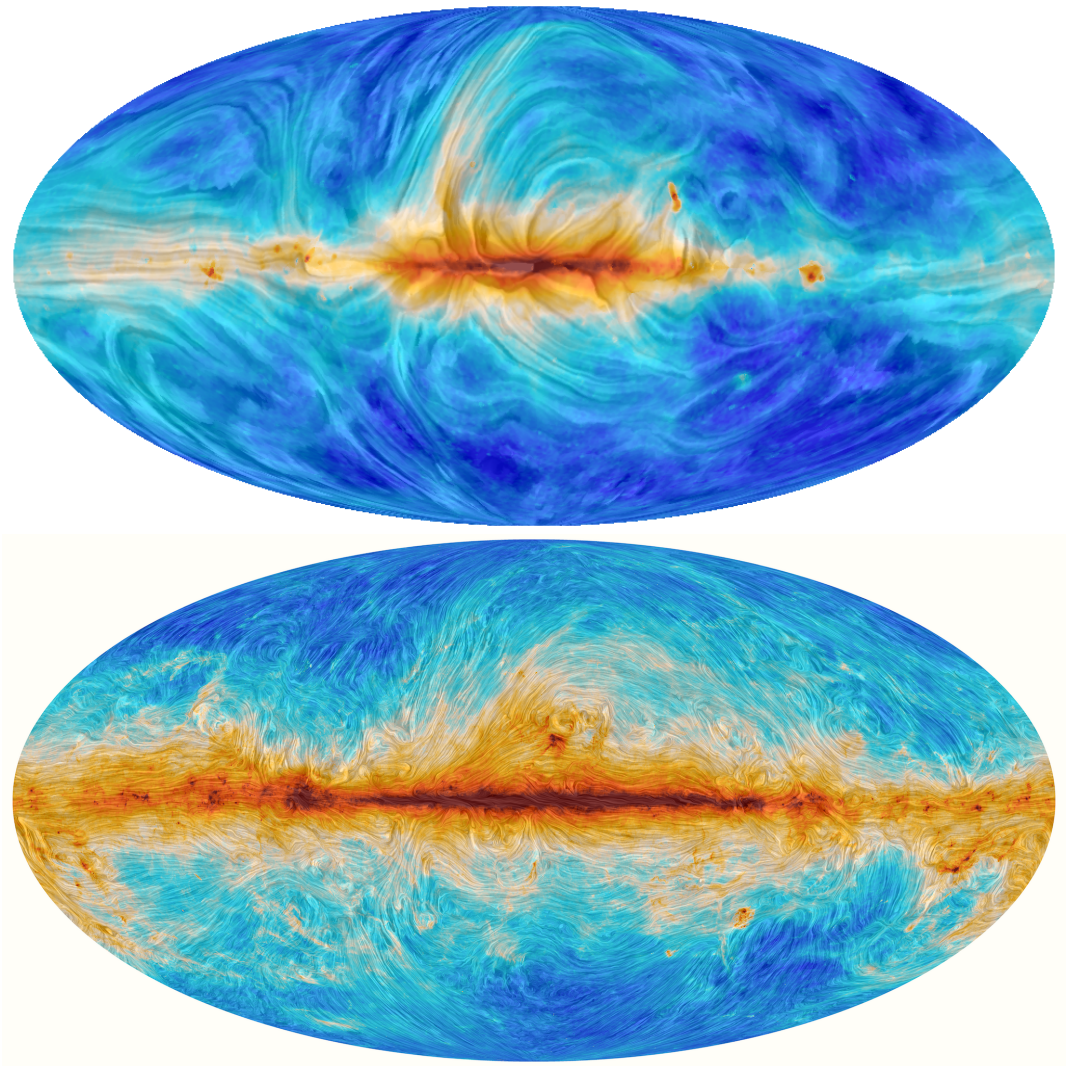

Figure 6.2: All-sky maps produced by the *Planck* mission in Galactic coordinates for (Top) synchrotron emission at 30 GHz and (Bottom) dust emission at 353 GHz (Planck Collaboration et al. 2016b,d). The intensity of the emission are shown by the colours, and the magnetic field orientation in the plane of sky is traced by the textures. Image courtesy of ESA and the Planck Collaboration.

model.

6.4.3 Knowledge from Studies of External Galaxies

Our perspective of the Milky Way galaxy from within poses a major challenge to the study of the Galactic magnetic fields. In contrast, the less complicated viewing geometries to nearby external galaxies make the interpretations of their magnetic field configurations easier at the expense of lower resolution in physical scale. Nonetheless, the study of the magnetic fields of the Milky Way is closely related to those of external

galaxies, as the astrophysical processes that amplify and shape the magnetic fields of other spiral galaxies should also apply to the Milky Way.

Currently, the magnetic field structures of at least 117 external galaxies have been investigated with radio polarimetric observations (Beck & Wielebinski 2013)[14]. Studies of face-on systems have revealed that the large-scale disk field of almost all spiral galaxies have ASS configuration as the dominant component, with no large-scale field reversals. A possible exception is M81, which was suggested to be hosting a dominant BSS configuration and hence two large-scale field reversals (Krause et al. 1989). However, their polarimetric observations with the legacy VLA at 21 cm suffered from the missing flux issue of radio interferometers, which could have affected the interpretation of the large-scale magnetic field geometry of this galaxy. Verification of the large-scale magnetic field structure of M81 would certainly be interesting, and could shed light on the true magnetic field structure of the Milky Way should the BSS-dominant large-scale field be confirmed. On the other hand, studies of edge-on galaxies (see, e.g., Krause 2009; Wiegert et al. 2015) have shown that (1) the disk fields are parallel to the galactic plane, (2) galactic halos can be commonly found in spiral galaxies, and (3) the halo field structures exhibit X-shaped morphologies. Such features of the magnetic fields of spiral galaxies are expected to be present in the Milky Way as well, and have been incorporated in recent modelling works of the Galactic magnetic fields (e.g., Jansson & Farrar 2012).

The broadband spectro-polarimetric capabilities of modern radio telescopes allow detailed investigations of the magnetic fields of nearby external galaxies, thanks to the increase in both the sensitivity and the λ^2-coverage of the observations. The Continuum Halos in Nearby Galaxies — an EVLA Survey (CHANG-ES; Irwin et al. 2012) project has observed 35 edge-on galaxies in L- (1247–1503 and 1647–1903 MHz) and C-bands (4979–7021 MHz). One goal of their systematic study of edge-on systems is to deepen our understanding in the origin and physical conditions of the galactic halos. In comparison, broadband observational efforts on studying nearby face-on spiral galaxies are relatively lacking, with M51 (Mao et al. 2015, see also PhD thesis of Maja Kierdorf) and M74 (NGC628; Mulcahy et al. 2017) being the only two examples. Multi-frequency polarimetric observations allow one to study the magnetic fields in the disk and halo of face-on spirals separately (see Figure 6.3; Fletcher et al. 2011, for the case of M51). Observations at high frequency (about 5–10 GHz) are sensitive to the magneto-ionic media in both the galactic disk and halo, while those at lower frequencies (about 1.4 GHz) are sensitive to the galactic halo only. The recent broadband study of M51 at 1–2 GHz has demonstrated the power of spectro-polarimetric analysis in extracting the properties of the magnetic fields and turbulence in face-on systems (Mao et al. 2015). In the future, one should study the magnetic fields of other nearby face-on galaxies with new broadband spectro-polarimetric observations to increase the currently sparse sample (see Chapter 6.5.6 for the case of the barred spiral galaxy M83).

[14] According to the updated version on February 2018, available from: http://www.mpifr-bonn.mpg.de/staff/rbeck/PSSS18.pdf.

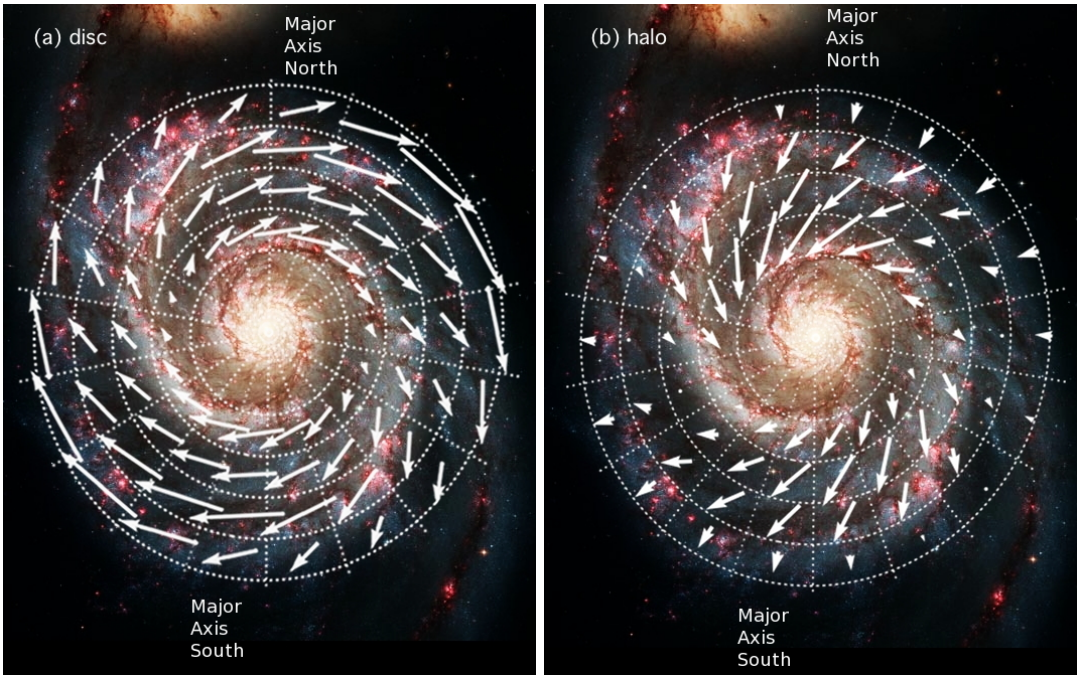

Figure 6.3: The large-scale magnetic fields of a nearby face-on spiral galaxy M51, derived from multi-frequency polarimetric observations at 20, 18, 6, and 3 cm (Fletcher et al. 2011). The magnetic fields are separated into the components in (a) the galactic disk and (b) the galactic halo. The lengths of the vectors represent the regular magnetic field strengths. The background colour map shows a *Hubble Space Telescope* optical image of M51 [Credit: NASA, ESA, S. Beckwith (STScI) and The Hubble Heritage Team (STScI/AURA)]. Image courtesy of Fletcher et al. (2011).

6.5 My Future Involvements

As part of the thesis conclusion, I outline here the research projects that I propose and am currently leading, as extensions to the studies presented in this thesis.

6.5.1 Expanding the Census of nπ-ambiguity Sources in TSS09

In Chapter 3, I identified the parameter Δ/σ as a good diagnostic of $n\pi$-ambiguity sources in the TSS09 catalogue. This can be further tested by observing new $n\pi$-ambiguity candidates selected this way. I have obtained new L-band spectro-polarimetric data with the Jansky VLA in C array configuration, in collaboration with A. Basu, C. Heiles, S. A. Mao, and J. West. The main goal of this project is to expand my census of $n\pi$-ambiguity sources, and eventually to further correct for the $n\pi$-ambiguity issue in the TSS09 catalogue. A total of 14 new $n\pi$-ambiguity candidates were selected by their Δ/σ and $|\mathrm{RM}_{\mathrm{TSS09}} - \mathrm{RM}_{3^\circ}|$ values (see Chapter 3.4.1.6), and were observed in 2017 May (Project ID: 17A-327; 2.5 hours granted with A-priority).

Apart from the primary goal of verifying whether these candidates indeed suffer

from the $n\pi$-ambiguity in the TSS09 catalogue, this data set can also be used to study the Faraday complexities in EGSs. The angular resolution of L-band C-array observations is $\approx 14''$, much higher than the $\approx 45''$ of the previous observations reported in Chapters 3 and 4. This high angular resolution can grant crisp views into the Faraday complexities of the spatially resolved EGSs, allowing comparisons between the flux-integrated and the spatially-resolved results similar to Appendix B.1.

6.5.2 Towards a Revised NVSS Rotation Measure Catalogue

From my investigations of the TSS09 RM catalogue, I estimated that there can be more than 50 $n\pi$-ambiguity sources (Chapter 3), and their RM measurements are affected by the off-axis instrumental polarisation (Chapter 4). These findings can be applied to correct for the RM values (for the $n\pi$-ambiguity cases; see also Appendix A) and the RM uncertainties (for all sources due to the instrumental polarisation) to create a revised TSS09 RM catalogue. The major work required would be to properly quantify the effects of the off-axis instrumental polarisation, including using the TSS09 listed values as the outputs instead of the inputs to the simulation (Chapter 4.5.1), applying Monte Carlo methods to carefully propagate the measurement uncertainties to obtain the non-Gaussian RM distribution, and finding the optimal way to present such highly non-Gaussian distributions in the final RM catalogue. Some further findings regarding the reliability of TSS09 RM values, presented in the Appendix A, can also be included. Such work will be indispensible to future studies of cosmic magnetism, and will be critical to the upcoming master RM catalogue (Van Eck et al. in prep.) that aims to combine all existing FD / RM measurements.

6.5.3 Broadband Polarisation Variabilities of Extragalactic Radio Sources

In Chapter 4.5.4, I identified three sources that showed hints of RM time variabilities out of the 21 polarised targets upon comparing the TSS09 and my new RM values in matching frequency ranges. Such variabilities can be attributed to changes in the physical conditions of the Faraday rotating volumes along the AGN jets (e.g., Zavala & Taylor 2001; Anderson et al. 2019).

To study such variabilities in details, I obtained new Jansky VLA data in 2017 May (Project ID: 17A-328; 7 hours granted with A-priority) of the same 23 sources that I studied in Chapters 3 and 4. Combined with my 2014 data, the radio time variabilities (in both total intensities and polarisation) of these objects over three years can be studied. The new observations were conducted in L- (1–2 GHz) and S-bands (2–4 GHz) in C-array configuration, resulting in an angular resolution of $\approx 14''$ and $\approx 7''$ in L- and S-bands, respectively. With these new data, one can even better characterise the Faraday complexities present in the targets than in Chapter 3 (see Chapter 6.3), as the data obtained in both epochs are from broadband spectro-polarimetric observations with the Jansky VLA..

The data reduction of the 2017 L-band data has already been completed, allowing

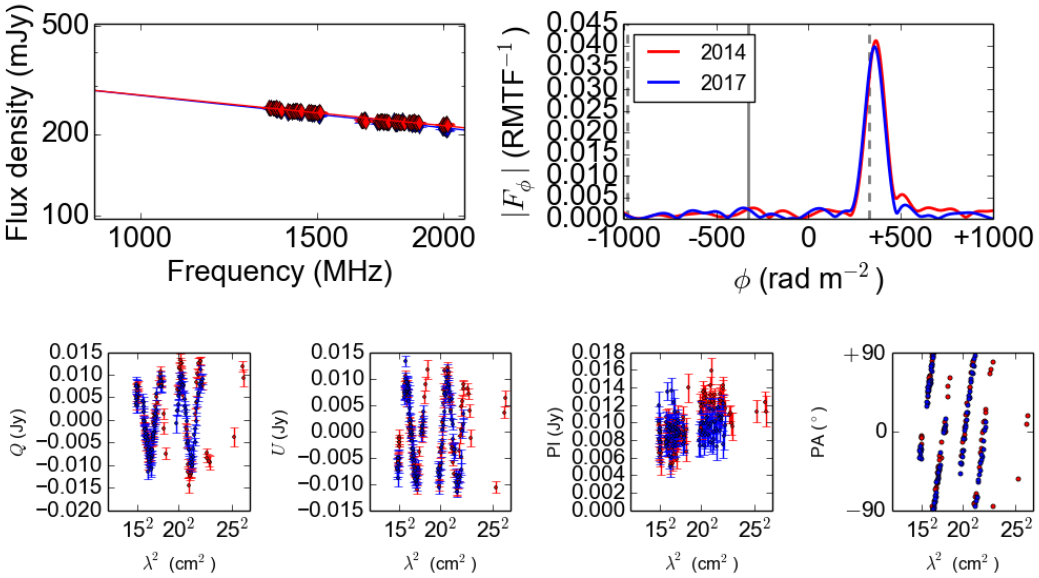

Figure 6.4: Total intensity and polarisation measurements of NVSS J094808−344010 from my 2014 and 2017 observations (Chapter 6.5.3). This source does not show obvious variabilities in neither total intensities nor polarisation over the three years. In particular, the Faraday spectra shown in the upper right panel are in units of fractional polarisation, with the solid grey line showing the TSS09 RM and the dashed grey lines showing the RM values with $\pm 1\pi$-ambiguity.

us to detect any polarisation time variabilities of the targets. Note that the use of multi-epochs broadband spectro-polarimetric data to study polarisation time variabilities is a new technique, with Anderson et al. (2019) being the only published example to date. I show the preliminary results comparing the 2014 and 2017 data in Figures 6.4–6.6. In particular, the radio spectra, Faraday spectra, as well as Stokes Q, Stokes U, PI, and PA against λ^2 at the two epochs are shown. One example of sources that do not show significant variabilities in neither total intensities nor polarisation properties, NVSS J094808−344010, is shown in Figure 6.4. I also show two sources that exhibit both Stokes I and polarisation variabilities — NVSS J111857+123442 (Figure 6.5) and NVSS J170934−172853 (Figure 6.6). In the future, these 2017 L-band data can be further combined with the S-band observations for a careful study of the Faraday complexities in these EGSs.

6.5.4 Towards an Improved Galactic Magnetic Field Model

The new broadband spectro-polarimetric data from the Jansky VLA have shown complexities of the magneto-ionic medium within $20° \leq \ell \leq 52°$ and $|b| \leq 5°$ that has never been noted before (Chapter 5). My study of the large-scale magnetic fields is currently limited by the knowledge in the small-scale magnetic fields in the same sky region. Such small-scale fields lead to fluctuations of the measured FD of $\sim 100\,\mathrm{rad\,m^{-2}}$

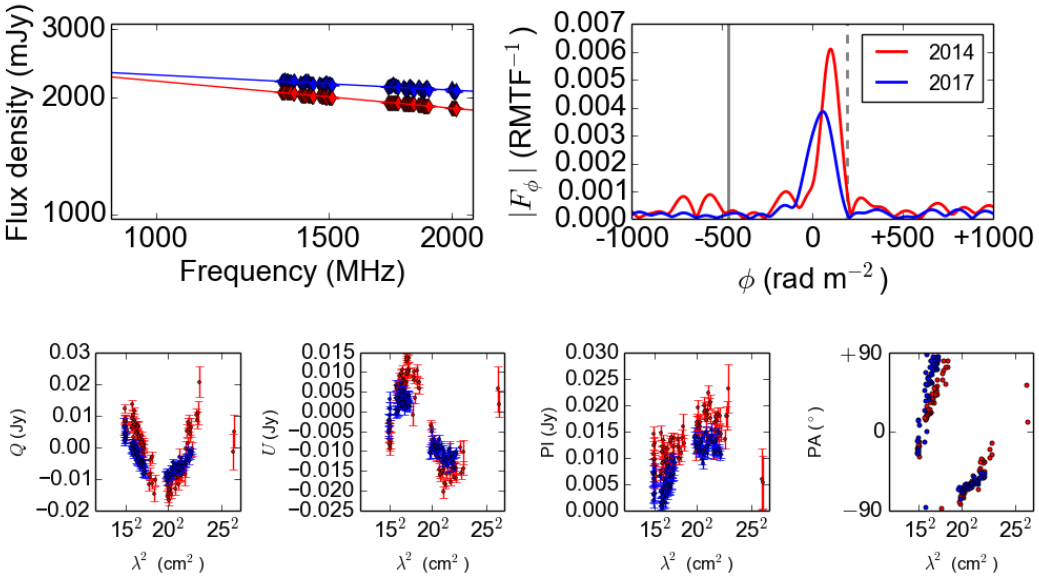

Figure 6.5: Same as Figure 6.4, but for NVSS J111857+123442, which shows significant variabilities in both total intensities and polarisation.

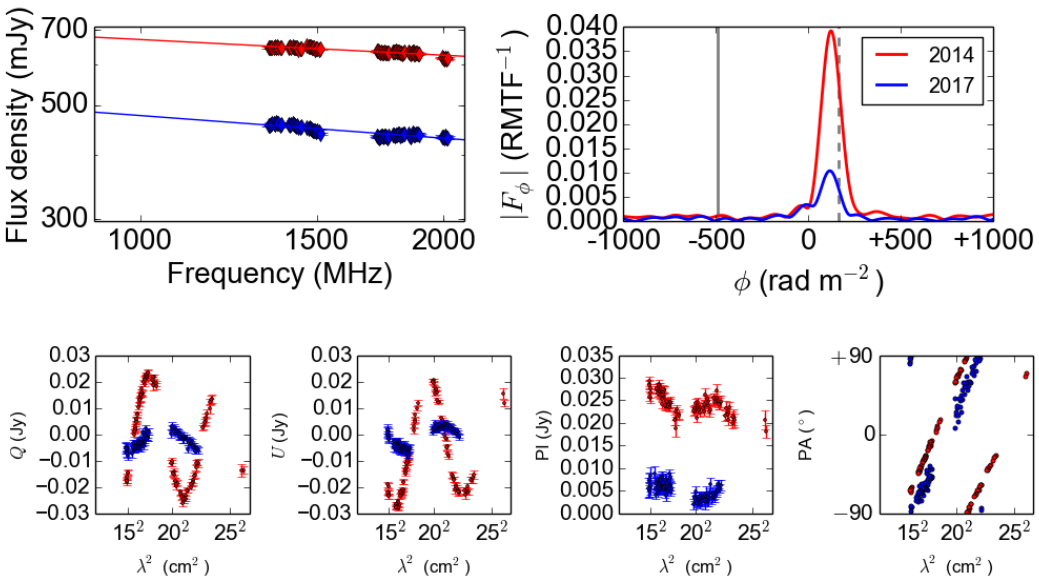

Figure 6.6: Same as Figure 6.4, but for NVSS J170934−172853, which shows significant variabilities in both total intensities and polarisation.

over angular scales of $\sim 1^\circ$ (e.g., Haverkorn et al. 2008) superimposed on the expected smooth spatial distribution of FD due to the large-scale fields. Carefully quantifying the contributions of the small-scale fields will be useful towards the construction of more realistic error bars of my spatially binned FD values. This will be vital to the careful comparisons of the FD profiles above versus below the Galactic mid-plane

(Chapter 5.5.3), and the comparisons between my FD values with those predicted from the existing field models (Chapter 5.5.4). Furthermore, the study of the small-scale fields within the region of interest is also compelling in its own right. The turbulence power spectra along a few lines of sight through the Galactic disk in the fourth Galactic quadrant were presented in Haverkorn et al. (2004, 2008), but otherwise remain poorly constrained. Within the region of interest in this project, there are suggestions for enhanced turbulence (Stil & Taylor 2007) as inferred from the lower polarised source densities there in the original NVSS catalogue (Condon et al. 1998). The broadband data presented in Chapter 5 can be repurposed for a complementary (and complimentary) study of the small-scale magnetic fields towards the inner Galaxy in the first quadrant.

The small-scale magnetic field contributions to FD can be extracted from my broadband data in two ways. At angular scales of $\gtrsim 10'$, the spatial fluctuations of FD due to the small-scale fields can be quantified by the structure function analysis (e.g, Minter & Spangler 1996; Haverkorn et al. 2008; Stil et al. 2011; Mao et al. 2012). On the other hand, at small angular scales of $\lesssim 1'$ one can fully exploit the broadband spectro-polarimetric data to measure the same spatial FD fluctuations, but this time manifested as Faraday depolarisation behaviours that can be captured by, e.g., Stokes QU-fitting analysis (Chapter 2.2.4). These techniques will allow a more direct measurement of the small-scale magnetic fields tied to the turbulent interstellar medium.

My new data set is also ideal for tests in preparation for the on-going and future broadband polarisation surveys such as POSSUM and the VLASS (Chapter 6.2.1). Most FD-grid experiments in the literature thus far determine the FD values of the target sources by considering the highest peak in Faraday spectra only (e.g., Mao et al. 2010; Betti et al. 2019, also Chapter 5). Given the wealth of information brought by new broadband spectro-polarimetric observations, this choice may not be optimal (see Chapter 6.2.2). For example, incorporating all peaks in Faraday spectra could improve the results from FD-grid experiments. By attempting different methods of extracting FD values using my new data, one can shed light on the most ideal way to exploit broadband spectro-polarimetric data for FD-grid experiments. Such knowledge would be invaluable for on-going and future polarisation surveys, as this can determine the details of the advanced data products produced by these new surveys.

Finally, the eventual goal would be to construct an improved magnetic field model of the Milky Way. My work presented in Chapter 5 has shown, for the first time, the complexities in the large-scale Galactic magnetic fields within the sky region that have been discussed. Specifically, my newly derived FD values revealed a clear disparity in the FD above versus below the Galactic plane at Galactic longitudes of $40^\circ \lesssim \ell \lesssim 52^\circ$, but not at $20^\circ \lesssim \ell \lesssim 40^\circ$. There can be physical connections between this FD disparity with the diagonal $\phi = 0\,\mathrm{rad\,m^{-2}}$ structure within $56^\circ \lesssim \ell \lesssim 68^\circ$ and $-2^\circ \lesssim b \lesssim +4^\circ$ (Ordog et al. 2017). A joint analysis of the two data sets may reveal such physical connections (if any). Furthermore, a careful look into pulsar data from the ATNF Pulsar Catalogue (Manchester et al. 2005) has revealed peculiar FD behaviours in the sky region of $40^\circ \lesssim \ell \lesssim 47^\circ$ and $-2^\circ \lesssim b \lesssim 0^\circ$ at a distance of $\approx 5\,\mathrm{kpc}$. All the above information will be critical towards the eventual goal of an improved Galactic magnetic

field model.

6.5.5 Zooming In to the Magnetohydrodynamic Turbulence in the Interstellar Medium

The small-scale Galactic magnetic fields, especially in the sub-pc regime, remain poorly understood. Such small-scale fields driven by turbulence in the interstellar medium are manifested as spatial FD fluctuations, and can be quantified by structure function analysis of FD measurements. The FD values can be those of EGSs (e.g., Haverkorn et al. 2008; Mao et al. 2010; Stil et al. 2011, see also Chapter 6.5.4), with which the resulting structure functions will reflect the turbulence along the entire sight line through the Milky Way, and are only sensitive to angular scales of $\gtrsim 10'$ limited by the EGS source density. On the other hand, the FDs of the diffuse Galactic synchrotron emission can be used (e.g., Haverkorn et al. 2004), which is sensitive to angular scales of $\gtrsim 1'$ but it is often difficult to accurately assign a single physical distance to the origin of such emission.

The power spectrum of interstellar turbulence can be represented by the remarkable "Big Power Law in the Sky" (Armstrong et al. 1995), which showed using other turbulence tracers such as DM fluctuations and interstellar scintillations that the electron density power spectrum follows the classic Kolmogorov spectrum from at least 10^{14} m ($\sim 10^{-3}$ pc) down to 10^{8} m ($\sim 10^{-3}$ AU). At scales larger than pc, the same power spectrum as probed by FD structure functions exhibit a wide range of spectral slopes (0.32–1.36; e.g. Minter & Spangler 1996; Haverkorn et al. 2004, 2008; Stil et al. 2011, see also Xu & Zhang 2016), all flatter than the Kolmogorov slope of 5/3. This slope reflects the physics of turbulence cascade, which can be affected by the local magnetic field strength, as well as the energy regime of the turbulence itself (see Kowal et al. 2007; Xu & Zhang 2016). To reconcile with the Big Power Law above, the FD structure function must turn over in the unexplored sub-pc regime.

I plan to perform structure function analysis of the FD of Galactic pulsar wind nebulae (PWNe) to study the magnetohydrodynamic turbulence in the interstellar medium. PWNe are highly polarised and typically have centrally filled morphologies at radio wavelengths (e.g., Kothes 2017). In addition, their emission originates from a single, well-defined distance that can be measured accurately (e.g., Dodson et al. 2003; Kothes 2013). These make PWNe potent background illuminating screens for the study of the turbulence in the foreground, with the resulting structure functions probing the turbulence from the nebula extent ($\approx 10'$) down to the angular resolution of the observations ($2''$ in the case below). The angular scales can be translated into physical scales easily, given that the distances to the target PWNe are known.

I will propose for new Jansky VLA observations in L-band in all (D to A) array configurations to observe three Galactic PWNe. The closest target is at a distance of 2 kpc away from us, translating the $2''$ angular resolution to ≈ 0.02 pc in physical scale. This allows the turbulence in the interstellar medium in the sub-pc regime to be explored. With this project, the aim is to answer key questions such as (1) what astrophysical processes govern the physical conditions of the turbulent interstellar

medium, which led to the variety of structure function slopes above, (2) at what physical scale does the flat spectrum at $\gtrsim$ pc turn over to reconcile with the Big Power Law, and (3) what is the physical meaning of such spectral turnovers. I have been granted 4.2 hours of observing time in D-array configuration as a pilot survey.

6.5.6 Reconcile with External Galaxies

Finally, I propose to continue my study in galactic magnetism with broadband spectro-polarimetric observations of external galaxies. One prime candidate is the nearby face-on spiral galaxy M83. This galaxy has been suggested to have strong outflows from the active star-forming disk, as inferred from its extended surrounding X-ray halo (Ehle et al. 1998). Previous efforts of Neininger et al. (1993) to determine the large-scale magnetic field configuration of M83 were not conclusive, as the only data available to them were discrete narrowband measurements at 3, 6, 13, and 20 cm.

I have been granted a total of 82 hours with the ATCA for an in-depth study of the magnetic fields of M83[15], with the observations conducted at 1.1–3.1, 4.5–6.5, and 8.0–10.0 GHz. The final angular resolution of 10″ translates to a physical scale of ≈ 500 pc for M83. The multi-frequency broadband spectro-polarimetric observational campaign will allow separation of the disk and halo components of the large-scale fields (see Chapter 6.4.3), and will allow a careful quantification of the turbulence that leads to depolarisation at lower frequencies. This work will add to the currently sparse sample of face-on spiral galaxies with magnetic field structures studied using broadband spectro-polarimetric observations, and will pave towards a much improved understanding in galactic magnetism. The knowledge can be applied to the case of the Milky Way for a better idea in the Galactic magnetic fields (Chapter 6.4.3).

6.6 Final Remarks

Magnetic fields of the Milky Way are essential for many Galactic astrophysical processes. In this thesis, I have furthered our knowledge in Galactic magnetic fields from the perspective of FD-grid experiments. In Chapters 3 and 4, I have quantified the systematic issues that affect the reliability of the current state-of-the-art RM catalogue of TSS09. These must be taken into account for precise studies of astrophysical magnetic fields. In Chapter 5, I have discovered a new magneto-ionic structure in the Sagittarius arm that also hosts a large-scale magnetic field reversal. My findings demand a new global Galactic magnetic field model that can capture the observed structures. This also demonstrates the expected capabilities for the study of Galactic magnetism with on-going polarisation surveys, including POSSUM, the VLASS, the MPIfR MeerKAT S-band Galactic plane survey, and the APERTIF survey, as well as future surveys by the SKA and the ngVLA. With such high quality polarisation data, the research field of Galactic and cosmic magnetism will be full of exciting prospects. We will certainly further unravel the mystery of magnetic fields in our Universe in the coming years.

[15] In collaboration with E. Lenc, S. A. Mao, and X. H. Sun,

Bibliography

Aab A., et al., 2015, ApJ, 804, 15 (Cited on pages 6 and 7.)

Abolfathi B., et al., 2018, ApJS, 235, 42 (Cited on pages 76 and 90.)

Ackermann M., et al., 2011, ApJ, 743, 171 (Cited on pages 76 and 90.)

Adgie R. L., Crowther J. H., Gent H., 1972, MNRAS, 159, 233 (Cited on page 93.)

Adriani O., et al., 2017, Phys. Rev. Lett., 119, 181101 (Cited on page 12.)

Aller H. D., 1970, ApJ, 161, 1 (Cited on page 95.)

Amenomori M., et al., 2006, Science, 314, 439 (Cited on page 6.)

Anderson L. D., Bania T. M., Balser D. S., Cunningham V., Wenger T. V., Johnstone B. M., Armentrout W. P., 2014, ApJS, 212, 1 (Cited on page 135.)

Anderson C. S., Gaensler B. M., Feain I. J., Franzen T. M. O., 2015, ApJ, 815, 49 (Cited on pages 37, 42, 51, 76, 79, 80 and 156.)

Anderson C. S., Gaensler B. M., Feain I. J., 2016, ApJ, 825, 59 (Cited on pages 37, 52, 76, 77, 80 and 95.)

Anderson C. S., Gaensler B. M., Heald G. H., O'Sullivan S. P., Kaczmarek J. F., Feain I. J., 2018, ApJ, 855, 41 (Cited on pages 37 and 158.)

Anderson C. S., O'Sullivan S. P., Heald G. H., Hodgson T., Pasetto A., Gaensler B. M., 2019, MNRAS, 485, 3600 (Cited on pages 95, 109, 159, 166 and 167.)

Andersson B.-G., Lazarian A., Vaillancourt J. E., 2015, ARA&A, 53, 501 (Cited on pages 161 and 162.)

Armstrong J. W., Rickett B. J., Spangler S. R., 1995, ApJ, 443, 209 (Cited on page 170.)

Arshakian T. G., Beck R., Krause M., Sokoloff D., 2009, A&A, 494, 21 (Cited on page 8.)

Baars J. W. M., Genzel R., Pauliny-Toth I. I. K., Witzel A., 1977, A&A, 61, 99 (Cited on page 92.)

Baiesi-Pillastrini G. C., Palumbo G. G. C., Vettolani G., 1984, A&AS, 56, 363 (Cited on page 76.)

Balbus S. A., Hawley J. F., 1998, Rev. Mod. Phys., 70, 1 (Cited on page 6.)

Basu A., Mao S. A., Kepley A. A., Robishaw T., Zweibel E. G., Gallagher III J. S., 2017, MNRAS, 464, 1003 (Cited on pages 4, 37 and 50.)

Beck R., 2016, A&A Rev., 24, 4 (Cited on pages 4, 5, 7, 8, 10, 50, 84, 108, 110 and 160.)

Beck R., Krause M., 2005, Astronomische Nachrichten, 326, 414 (Cited on page 14.)

Beck R., Wielebinski R., 2013, in Oswalt T. D., Gilmore G., eds, Planets, Stars and Stellar Systems. Vol. 5: Galactic Structure and Stellar Populations. Springer, Berlin, p. 641 (Cited on pages 10, 11, 50, 84, 110, 160 and 164.)

Beck R., Brandenburg A., Moss D., Shukurov A., Sokoloff D., 1996, ARA&A, 34, 155 (Cited on page 132.)

Beck R., Shukurov A., Sokoloff D., Wielebinski R., 2003, A&A, 411, 99 (Cited on page 22.)

Beck R., Fletcher A., Shukurov A., Snodin A., Sokoloff D. D., Ehle M., Moss D., Shoutenkov V., 2005, A&A, 444, 739 (Cited on page 5.)

Beck A. M., Lesch H., Dolag K., Kotarba H., Geng A., Stasyszyn F. A., 2012, MNRAS, 422, 2152 (Cited on page 8.)

Becker R. H., White R. L., Edwards A. L., 1991, ApJS, 75, 1 (Cited on page 93.)

Becker R. H., White R. L., Helfand D. J., 1995, ApJ, 450, 559 (Cited on pages 78, 92 and 94.)

Bell M. R., Enßlin T. A., 2012, A&A, 540, A80 (Cited on page 157.)

Bennett C. L., et al., 2013, ApJS, 208, 20 (Cited on page 161.)

Beresnyak A., Lazarian A., 2015, in Lazarian A., de Gouveia Dal Pino E. M., Melioli C., eds, Astrophysics and Space Science Library Vol. 407, Magnetic Fields in Diffuse Media. Springer-Verlag, Berlin, p. 163 (Cited on page 108.)

Betti S. K., Hill A. S., Mao S. A., Gaensler B. M., Lockman F. J., McClure-Griffiths N. M., Benjamin R. A., 2019, ApJ, 871, 215 (Cited on pages 18, 47, 50, 71, 72, 85, 96, 101, 102, 103, 104, 109, 124, 156, 157 and 169.)

Bhatnagar S., Cornwell T. J., Golap K., Uson J. M., 2008, A&A, 487, 419 (Cited on pages 35 and 86.)

Bhatnagar S., Rau U., Golap K., 2013, ApJ, 770, 91 (Cited on pages 35 and 86.)

Biermann L., 1950, Zeitschrift für Naturforschung A, 5, 65 (Cited on page 8.)

Birnboim Y., Balberg S., Teyssier R., 2015, MNRAS, 447, 3678 (Cited on page 6.)

Biskamp D., 2008, Magnetohydrodynamic Turbulence. (Cambridge Univ. Press, Cambridge) (Cited on page 5.)

Black A. R. S., Baum S. A., Leahy J. P., Perley R. A., Riley J. M., Scheuer P. A. G., 1992, MNRAS, 256, 186 (Cited on page 203.)

Bonafede A., et al., 2009, A&A, 503, 707 (Cited on pages 75 and 109.)

Boulanger F., et al., 2018, J. Cosmology Astropart. Phys., 8, 049 (Cited on pages 4, 110, 161 and 162.)

Boulares A., Cox D. P., 1990, ApJ, 365, 544 (Cited on page 5.)

Brandenburg A., 2015, in Lazarian A., de Gouveia Dal Pino E. M., Melioli C., eds, Astrophysics and Space Science Library Vol. 407, Magnetic Fields in Diffuse Media. Springer-Verlag, Berlin, p. 529 (Cited on page 9.)

Brandenburg A., Subramanian K., 2005, Phys. Rep., 417, 1 (Cited on pages 8 and 10.)

Brandenburg A., Donner K. J., Moss D., Shukurov A., Sokolov D. D., Tuominen I., 1992, A&A, 259, 453 (Cited on page 133.)

Brandenburg A., Donner K. J., Moss D., Shukurov A., Sokoloff D. D., Tuominen I., 1993, A&A, 271, 36 (Cited on page 108.)

Brentjens M. A., de Bruyn A. G., 2005, A&A, 441, 1217 (Cited on pages 38, 39, 41, 51, 55, 58, 109, 119 and 124.)

Briggs D. S., 1995, BAAS, 27, 1444 (Cited on pages 54, 88 and 116.)

Broten N. W., MacLeod J. M., Vallee J. P., 1988, Ap&SS, 141, 303 (Cited on page 22.)

Brown J. C., Taylor A. R., Jackel B. J., 2003, ApJS, 145, 213 (Cited on pages 19, 22, 111, 136 and 138.)

Brown J. C., Haverkorn M., Gaensler B. M., Taylor A. R., Bizunok N. S., McClure-Griffiths N. M., Dickey J. M., Green A. J., 2007, ApJ, 663, 258 (Cited on pages 19, 22, 108, 136, 138, 154 and 155.)

Brunthaler A., et al., 2011, Astronomische Nachrichten, 332, 461 (Cited on page 139.)

Burlaga L. F., Ness N. F., 2014, ApJ, 784, 146 (Cited on page 4.)

Burn B. J., 1966, MNRAS, 133, 67 (Cited on pages 42, 51 and 62.)

Carretti E., et al., 2019, MNRAS, accepted (Cited on page 161.)

Charbonneau P., 2014, ARA&A, 52, 251 (Cited on page 4.)

Chen W. P., Lee H. T., 2008, in Reipurth B., ed., Handbook of Star Forming Regions, Vol. I. ASP, San Francisco, CA, p. 124 (Cited on page 74.)

Chiuderi C., Velli M., 2015, Basics of Plasma Astrophysics. (Springer-Verlag, Berlin) (Cited on page 5.)

Chow-Martínez M., Andernach H., Caretta C. A., Trejo-Alonso J. J., 2014, MNRAS, 445, 4073 (Cited on page 75.)

Chyży K. T., Weżgowiec M., Beck R., Bomans D. J., 2011, A&A, 529, A94 (Cited on page 4.)

Clemens D. P., Pinnick A. F., Pavel M. D., Taylor B. W., 2012, ApJS, 200, 19 (Cited on page 161.)

Cohen A. S., Lane W. M., Cotton W. D., Kassim N. E., Lazio T. J. W., Perley R. A., Condon J. J., Erickson W. C., 2007, AJ, 134, 1245 (Cited on page 93.)

Condon J. J., Cotton W. D., Greisen E. W., Yin Q. F., Perley R. A., Taylor G. B., Broderick J. J., 1998, AJ, 115, 1693 (Cited on pages 23, 28, 32, 34, 35, 36, 52, 85, 86, 87, 90, 93, 95, 98, 112, 117, 124, 154, 169 and 214.)

Contopoulos G., Jappel A., 1974, Transactions of the International Astronomical Union, Vol. 15. (Reidel, Dordrecht) (Cited on pages 29 and 30.)

Cooper B. F. C., Price R. M., 1962, Nature, 195, 1084 (Cited on page 17.)

Cordes J. M., Lazio T. J. W., 2002, NE2001. I. A New Model for the Galactic Distribution of Free Electrons and Its Fluctuations (arXiv:astro-ph/0207156) (Cited on pages 17, 18, 22, 131, 136, 138, 139, 144, 146, 148 and 152.)

Costa A. H., Spangler S. R., Sink J. R., Brown S., Mao S. A., 2016, ApJ, 821, 92 (Cited on pages 50 and 85.)

Cotton W. D., 1994, Widefield Polarization Correction of VLA Snapshot Images at 1.4 GHz. (NRAO, Charlottesville, VA) (Cited on pages 35, 86 and 98.)

Coziol R., Andernach H., Caretta C. A., Alamo-Martínez K. A., Tago E., 2009, AJ, 137, 4795 (Cited on page 75.)

Crutcher R. M., 1999, ApJ, 520, 706 (Cited on page 5.)

Crutcher R. M., 2012, ARA&A, 50, 29 (Cited on page 4.)

Dickey J. M., et al., 2019, ApJ, 871, 106 (Cited on page 37.)

Dodson R., Legge D., Reynolds J. E., McCulloch P. M., 2003, ApJ, 596, 1137 (Cited on page 170.)

Dolag K., Vogt C., Enßlin T. A., 2005, MNRAS, 358, 726 (Cited on page 38.)

Dougherty M. K., et al., 2018, Science, 362 (Cited on page 4.)

Douglas J. N., Bash F. N., Bozyan F. A., Torrence G. W., Wolfe C., 1996, AJ, 111, 1945 (Cited on page 93.)

Draine B. T., 2011, Physics of the Interstellar and Intergalactic Medium. (Princeton Univ. Press, Princeton, NJ) (Cited on pages 5 and 6.)

Durrer R., Neronov A., 2013, A&A Rev., 21, 62 (Cited on page 8.)

Ehle M., Pietsch W., Beck R., Klein U., 1998, A&A, 329, 39 (Cited on page 171.)

Faraday M., 1846, On the Magnetization of Light and the Illumination of Magnetic Lines of Force. Experimental Researches in Electricity, The Royal Society (Cited on page 16.)

Farnsworth D., Rudnick L., Brown S., 2011, AJ, 141, 191 (Cited on pages 37, 42, 51, 62, 77 and 109.)

Ferrière K., 1996, A&A, 310, 438 (Cited on page 8.)

Ferrière K. M., 2001, Reviews of Modern Physics, 73, 1031 (Cited on page 5.)

Ferrière K., 2005, in Chyzy K. T., Otmianowska-Mazur K., Soida M., Dettmar R.-J., eds, The Magnetized Plasma in Galaxy Evolution. p. 147 (Cited on page 133.)

Fey A. L., Charlot P., 1997, ApJS, 111, 95 (Cited on page 78.)

Fey A. L., Charlot P., 2000, ApJS, 128, 17 (Cited on page 78.)

Finkbeiner D. P., 2003, ApJS, 146, 407 (Cited on pages 17 and 135.)

Finlay C. C., et al., 2010, Geophysical Journal International, 183, 1216 (Cited on page 3.)

Fletcher A., 2010, in Kothes R., Landecker T. L., Willis A. G., eds, Astronomical Society of the Pacific Conference Series Vol. 438, The Dynamic Interstellar Medium: A Celebration of the Canadian Galactic Plane Survey. ASP, San Francisco, CA, p. 197 (Cited on page 11.)

Fletcher A., Beck R., Shukurov A., Berkhuijsen E. M., Horellou C., 2011, MNRAS, 412, 2396 (Cited on pages 14, 15, 37, 84, 164 and 165.)

Frick P., Stepanov R., Shukurov A., Sokoloff D., 2001, MNRAS, 325, 649 (Cited on pages 110, 132 and 155.)

Gaensler B. M., Slane P. O., 2006, ARA&A, 44, 17 (Cited on page 20.)

Gaensler B. M., Dickey J. M., McClure-Griffiths N. M., Green A. J., Wieringa M. H., Haynes R. F., 2001, ApJ, 549, 959 (Cited on pages 22, 32, 75, 136, 154, 155 and 161.)

Gaensler B. M., Haverkorn M., Staveley-Smith L., Dickey J. M., McClure-Griffiths N. M., Dickel J. R., Wolleben M., 2005, Science, 307, 1610 (Cited on pages 4, 19, 37, 50, 71, 85, 109 and 143.)

Gaensler B. M., Madsen G. J., Chatterjee S., Mao S. A., 2008, PASA, 25, 184 (Cited on page 112.)

Gaensler B. M., Landecker T. L., Taylor A. R., POSSUM Collaboration 2010, BAAS, 42, 515 (Cited on pages 52, 86, 153 and 154.)

Gaensler B. M., et al., 2011, Nature, 478, 214 (Cited on page 161.)

Gaia Collaboration et al., 2016, A&A, 595, A1 (Cited on page 162.)

Gardner F. F., Whiteoak J. B., 1966, ARA&A, 4, 245 (Cited on page 32.)

George S. J., Stil J. M., Keller B. W., 2012, PASA, 29, 214 (Cited on pages 36, 58, 60 and 124.)

Gießübel R., Heald G., Beck R., Arshakian T. G., 2013, A&A, 559, A27 (Cited on pages 50, 84 and 85.)

Ginzburg V. L., Syrovatskii S. I., 1965, ARA&A, 3, 297 (Cited on page 12.)

Girichidis P., Seifried D., Naab T., Peters T., Walch S., Wünsch R., Glover S. C. O., Klessen R. S., 2018, MNRAS, 480, 3511 (Cited on page 6.)

Gold B., et al., 2011, ApJS, 192, 15 (Cited on page 138.)

Govoni F., Feretti L., 2004, International Journal of Modern Physics D, 13, 1549 (Cited on pages 12 and 75.)

Govoni F., et al., 2010, A&A, 522, A105 (Cited on pages 75 and 109.)

Gower J. F. R., Scott P. F., Wills D., 1967, MmRAS, 71, 49 (Cited on page 93.)

Gregory P. C., Condon J. J., 1991, ApJS, 75, 1011 (Cited on page 93.)

Griffith M. R., Wright A. E., Burke B. F., Ekers R. D., 1994, ApJS, 90, 179 (Cited on page 93.)

Guidetti D., Laing R. A., Bridle A. H., Parma P., Gregorini L., 2011, MNRAS, 413, 2525 (Cited on page 205.)

Haffner L. M., Reynolds R. J., Tufte S. L., Madsen G. J., Jaehnig K. P., Percival J. W., 2003, ApJS, 149, 405 (Cited on pages 19, 73, 115, 125 and 132.)

Haffner L. M., Reynolds R. J., Madsen G. J., Hill A. S., Barger K. A., Jaehnig K. P., Mierkiewicz E. J., Percival J. W., 2010, BAAS, 42, 265 (Cited on pages 73, 115, 125 and 132.)

Hales C. A., 2017, AJ, 154, 54 (Cited on pages 34 and 86.)

Hammond A. M., Robishaw T., Gaensler B. M., 2012, A New Catalog of Faraday Rotation Measures and Redshifts for Extragalactic Radio Sources (`arXiv:1209.1438`) (Cited on page 159.)

Han J. L., 2017, ARA&A, 55, 111 (Cited on pages 20, 22, 111, 130, 131 and 155.)

Han J. L., Manchester R. N., Berkhuijsen E. M., Beck R., 1997, A&A, 322, 98 (Cited on page 133.)

Han J. L., Beck R., Berkhuijsen E. M., 1998, A&A, 335, 1117 (Cited on page 50.)

Han J. L., Manchester R. N., Lyne A. G., Qiao G. J., 2002, ApJ, 570, L17 (Cited on page 20.)

Han J. L., Manchester R. N., Lyne A. G., Qiao G. J., van Straten W., 2006, ApJ, 642, 868 (Cited on page 110.)

Han J. L., et al., 2015, Advancing Astrophysics with the Square Kilometre Array (AASKA14), p. 41 (Cited on page 160.)

Han J. L., Manchester R. N., van Straten W., Demorest P., 2018, ApJS, 234, 11 (Cited on pages 20, 21, 22, 109, 111, 129 and 160.)

Hanayama H., Takahashi K., Kotake K., Oguri M., Ichiki K., Ohno H., 2005, ApJ, 633, 941 (Cited on page 8.)

Harvey-Smith L., Madsen G. J., Gaensler B. M., 2011, ApJ, 736, 83 (Cited on pages 4, 5, 17, 18, 19, 23, 50, 74, 75, 85, 109 and 128.)

Harwood J. J., et al., 2017, MNRAS, 469, 639 (Cited on pages 203 and 205.)

Haverkorn M., 2015, in Lazarian A., de Gouveia Dal Pino E. M., Melioli C., eds, Astrophysics and Space Science Library Vol. 407, Magnetic Fields in Diffuse Media. Springer-Verlag, Berlin, p. 483 (Cited on pages 7, 11, 108, 110 and 161.)

Haverkorn M., Spangler S. R., 2013, Space Sci. Rev., 178, 483 (Cited on pages 5 and 160.)

Haverkorn M., Gaensler B. M., McClure-Griffiths N. M., Dickey J. M., Green A. J., 2004, ApJ, 609, 776 (Cited on pages 161, 169 and 170.)

Haverkorn M., Brown J. C., Gaensler B. M., McClure-Griffiths N. M., 2008, ApJ, 680, 362 (Cited on pages 108, 109, 129, 143, 153, 168, 169 and 170.)

Haverkorn M., et al., 2015, Advancing Astrophysics with the Square Kilometre Array (AASKA14), p. 96 (Cited on page 160.)

Heald G. H., 2012, ApJ, 754, L35 (Cited on page 108.)

Heald G., Braun R., Edmonds R., 2009, A&A, 503, 409 (Cited on pages 37, 39, 50, 55, 120, 124 and 156.)

Heiles C., Crutcher R., 2005, in Wielebinski R., Beck R., eds, Lecture Notes in Physics Vol. 664, Cosmic Magnetic Fields. Springer-Verlag, Berlin, p. 137 (Cited on page 5.)

Heiles C., Haverkorn M., 2012, Space Sci. Rev., 166, 293 (Cited on pages 5, 73 and 160.)

Heiles C., Chu Y.-H., Troland T. H., 1981, ApJ, 247, L77 (Cited on page 75.)

Hennessy G. S., Owen F. N., Eilek J. A., 1989, ApJ, 347, 144 (Cited on page 22.)

Hewitt A., Burbidge G., 1987, ApJS, 63, 1 (Cited on pages 79 and 90.)

Hewitt A., Burbidge G., 1991, ApJS, 75, 297 (Cited on page 90.)

Hill A., 2018, Galaxies, 6, 129 (Cited on page 161.)

Hill A. S., Mao S. A., Benjamin R. A., Lockman F. J., McClure-Griffiths N. M., 2013, ApJ, 777, 55 (Cited on pages 50 and 85.)

Hoang T., Lazarian A., 2016, ApJ, 831, 159 (Cited on page 161.)

Hou L. G., Han J. L., 2014, A&A, 569, A125 (Cited on page 21.)

Hovatta T., Lister M. L., Aller M. F., Aller H. D., Homan D. C., Kovalev Y. Y., Pushkarev A. B., Savolainen T., 2012, AJ, 144, 105 (Cited on page 95.)

Huchra J. P., et al., 2012, ApJS, 199, 26 (Cited on pages 75 and 90.)

Iacobelli M., Haverkorn M., Katgert P., 2013, A&A, 549, A56 (Cited on pages 58 and 124.)

Irwin J., et al., 2012, AJ, 144, 43 (Cited on page 164.)

Jagannathan P., Bhatnagar S., Rau U., Taylor A. R., 2017, AJ, 154, 56 (Cited on pages 35, 86, 117 and 124.)

Jagannathan P., Bhatnagar S., Brisken W., Taylor A. R., 2018, AJ, 155, 3 (Cited on pages 35 and 86.)

Jansson R., Farrar G. R., 2012, ApJ, 757, 14 (Cited on pages 23, 71, 110, 111, 132, 133, 135, 136, 137, 138, 139, 140, 141, 142, 144, 145, 146, 147, 148, 152 and 164.)

Johnston-Hollitt M., 2003, PhD thesis, University of Adelaide (Cited on pages ix, 22 and 25.)

Johnston-Hollitt M., et al., 2015, Advancing Astrophysics with the Square Kilometre Array (AASKA14), p. 92 (Cited on page 156.)

Jonas J., MeerKAT Team, 2016, in Proceedings of MeerKAT Science: On the Pathway to the SKA. p. 1 (Cited on page 155.)

Jones D. H., et al., 2009, MNRAS, 399, 683 (Cited on pages 90 and 203.)

Kaczmarek J. F., Purcell C. R., Gaensler B. M., McClure-Griffiths N. M., Stevens J., 2017, MNRAS, 467, 1776 (Cited on pages 4, 18, 42, 50 and 85.)

Kaczmarek J. F., Purcell C. R., Gaensler B. M., Sun X., O'Sullivan S. P., McClure-Griffiths N. M., 2018, MNRAS, 476, 1596 (Cited on pages 37 and 52.)

Kahniashvili T., Brandenburg A., Kosowsky A., Mandal S., Roper Pol A., 2018, PIAU, accepted (Cited on page 4.)

Kalberla P. M. W., Haud U., 2015, A&A, 578, A78 (Cited on pages 73 and 75.)

Kalberla P. M. W., Kerp J., 2009, ARA&A, 47, 27 (Cited on page 6.)

Kazantsev A. P., 1968, ZhETF, 53, 1806 (Cited on page 108.)

Keane E., et al., 2015, Advancing Astrophysics with the Square Kilometre Array (AASKA14), p. 40 (Cited on page 160.)

Kerr F. J., Lynden-Bell D., 1986, MNRAS, 221, 1023 (Cited on page 139.)

Kierdorf M., Beck R., Hoeft M., Klein U., van Weeren R. J., Forman W. R., Jones C., 2017, A&A, 600, A18 (Cited on pages 4, 15 and 84.)

Kim W.-T., Stone J. M., 2012, ApJ, 751, 124 (Cited on page 5.)

Kim C.-G., Kim W.-T., Ostriker E. C., 2006, ApJ, 649, L13 (Cited on pages 8 and 108.)

Kim K. S., Lilly S. J., Miniati F., Bernet M. L., Beck R., O'Sullivan S. P., Gaensler B. M., 2016, ApJ, 829, 133 (Cited on pages 52 and 156.)

King O. G., et al., 2010, in Holland W. S., Zmuidzinas J., eds, SPIE Conf. Ser. Vol. 7741, Millimeter, Submillimeter, and Far-Infrared Detectors and Instrumentation for Astronomy V. SPIE, Bellingham (Cited on page 161.)

Kothes R., 2013, A&A, 560, A18 (Cited on page 170.)

Kothes R., 2017, in Torres D. F., ed., ASSL Vol. 446, Modelling Pulsar Wind Nebulae. Springer International Publishing, p. 1 (Cited on pages 4 and 170.)

Kothes R., Landecker T. L., Reich W., Safi-Harb S., Arzoumanian Z., 2008, ApJ, 687, 516 (Cited on pages 37 and 50.)

Kowal G., Lazarian A., Beresnyak A., 2007, ApJ, 658, 423 (Cited on page 170.)

Krall N. A., Trivelpiece A. W., 1973, Principles of Plasma Physics. (McGraw-Hill Kogakusha, Tokyo) (Cited on page 5.)

Kramer M., Stappers B., 2015, Advancing Astrophysics with the Square Kilometre Array (AASKA14), p. 36 (Cited on page 160.)

Krause M., 2009, in Revista Mexicana de Astronomia y Astrofisica Conference Series. p. 25 (Cited on pages 137 and 164.)

Krause M., 2019, Galaxies, 7, 54 (Cited on page 108.)

Krause M., Beck R., Hummel E., 1989, A&A, 217, 17 (Cited on pages 11, 37, 110 and 164.)

Kronberg P. P., 2016, Cosmic Magnetic Fields. (Cambridge Univ Press, Cambridge) (Cited on pages 8 and 10.)

Kronberg P. P., Newton-McGee K. J., 2011, PASA, 28, 171 (Cited on page 112.)

Kuehr H., Witzel A., Pauliny-Toth I. I. K., Nauber U., 1981, A&AS, 45, 367 (Cited on page 93.)

Kulsrud R. M., 2005, in Wielebinski R., Beck R., eds, Lecture Notes in Physics Vol. 664, Cosmic Magnetic Fields. Springer-Verlag, Berlin, p. 69 (Cited on pages 9 and 10.)

Lacy M., et al., 2019, The Karl G. Jansky Very Large Array Sky Survey (VLASS). Science Case, Survey Design and Initial Results (arXiv:1907.01981) (Cited on pages 153 and 154.)

Large M. I., Mills B. Y., Little A. G., Crawford D. F., Sutton J. M., 1981, MNRAS, 194, 693 (Cited on page 93.)

Law C. J., et al., 2011a, ApJ, 728, 57 (Cited on pages 37, 51, 68, 71, 80 and 81.)

Law C. J., Brentjens M. A., Novak G., 2011b, ApJ, 731, 36 (Cited on pages 111 and 155.)

Lawler J. M., Dennison B., 1982, ApJ, 252, 81 (Cited on page 22.)

Lazar M., Schlickeiser R., Wielebinski R., Poedts S., 2009, ApJ, 693, 1133 (Cited on page 8.)

Leahy J. P., Jagers W. J., Pooley G. G., 1986, A&A, 156, 234 (Cited on page 153.)

Licquia T. C., Newman J. A., 2015, ApJ, 806, 96 (Cited on page 6.)

Longair M. S., 2011, High Energy Astrophysics. (Cambridge Univ. Press, Cambridge) (Cited on pages 6 and 7.)

Lorimer D. R., Kramer M., 2012, Handbook of Pulsar Astronomy. (Cambridge Univ. Press, Cambridge) (Cited on pages 4, 17, 20, 22, 109 and 130.)

Luri X., et al., 2018, A&A, 616, A9 (Cited on page 162.)

Ma Y. K., Ng C.-Y., Bucciantini N., Slane P. O., Gaensler B. M., Temim T., 2016, ApJ, 820, 100 (Cited on pages 13, 15, 37 and 50.)

Mac Low M.-M., Klessen R. S., 2004, Reviews of Modern Physics, 76, 125 (Cited on page 108.)

MacLow M.-M., 2004, Ap&SS, 289, 323 (Cited on page 6.)

Madsen G. J., Reynolds R. J., Haffner L. M., 2006, ApJ, 652, 401 (Cited on page 17.)

Magalhães A. M., 2014, in Revista Mexicana de Astronomia y Astrofisica Conference Series. p. 209 (Cited on page 162.)

Manchester R. N., Hobbs G. B., Teoh A., Hobbs M., 2005, AJ, 129, 1993 (Cited on pages 129, 131, 132, 152, 160 and 169.)

Mao S. A., 2018, PIAU, accepted (Cited on page 156.)

Mao S. A., Gaensler B. M., Stanimirović S., Haverkorn M., McClure-Griffiths N. M., Staveley-Smith L., Dickey J. M., 2008, ApJ, 688, 1029 (Cited on pages 50 and 85.)

Mao S. A., Gaensler B. M., Haverkorn M., Zweibel E. G., Madsen G. J., McClure-Griffiths N. M., Shukurov A., Kronberg P. P., 2010, ApJ, 714, 1170 (Cited on pages 19, 23, 50, 58, 71, 72, 85, 104, 109, 124, 143, 153, 157, 169 and 170.)

Mao S. A., et al., 2012, ApJ, 759, 25 (Cited on pages 23, 29, 50, 71, 85, 108, 109, 132, 134, 135, 136, 143 and 169.)

Mao S. A., et al., 2014, A Wideband Polarization Survey of the Extragalactic Sky at 2-4 GHz: A Science White Paper for the VLA Sky Survey (`arXiv:1401.1875`) (Cited on pages 153, 154 and 159.)

Mao S. A., Zweibel E., Fletcher A., Ott J., Tabatabaei F., 2015, ApJ, 800, 92 (Cited on pages 37, 42, 47, 84, 156 and 164.)

Mao S. A., et al., 2017, Nature Astronomy, 1, 621 (Cited on pages 20, 47, 50, 85 and 109.)

Massardi M., et al., 2008, MNRAS, 384, 775 (Cited on page 93.)

Mauch T., Murphy T., Buttery H. J., Curran J., Hunstead R. W., Piestrzynski B., Robertson J. G., Sadler E. M., 2003, MNRAS, 342, 1117 (Cited on page 93.)

McClure-Griffiths N. M., et al., 2009, ApJS, 181, 398 (Cited on pages 73 and 75.)

McClure-Griffiths N. M., Madsen G. J., Gaensler B. M., McConnell D., Schnitzeler D. H. F. M., 2010, ApJ, 725, 275 (Cited on pages 4, 23, 50 and 85.)

McMullin J. P., Waters B., Schiebel D., Young W., Golap K., 2007, in Shaw R. A., Hill F., Bell D. J., eds, ASP Conf. Ser. Vol. 376, Astronomical Data Analysis Software and Systems XVI. ASP, San Francisco, CA, p. 127 (Cited on pages 54, 87 and 113.)

Meinel R., Elstner D., Ruediger G., 1990, A&A, 236, L33 (Cited on page 133.)

Minter A. H., Spangler S. R., 1996, ApJ, 458, 194 (Cited on pages 37, 109, 153, 169 and 170.)

Miyashita Y., Ideguchi S., Nakagawa S., Akahori T., Takahashi K., 2019, MNRAS, 482, 2739 (Cited on page 77.)

Moss D., Sokoloff D., 2013, Geophysical and Astrophysical Fluid Dynamics, 107, 497 (Cited on page 110.)

Moss D., Sokoloff D., Beck R., Krause M., 2010, A&A, 512, A61 (Cited on page 133.)

Moss D., Stepanov R., Arshakian T. G., Beck R., Krause M., Sokoloff D., 2012, A&A, 537, A68 (Cited on page 110.)

Mulcahy D. D., Beck R., Heald G. H., 2017, A&A, 600, A6 (Cited on page 164.)

Murphy T., et al., 2010, MNRAS, 402, 2403 (Cited on page 93.)

Myers S. T., Baum S. A., Chandler C. J., 2014, BAAS, 223, 236.01 (Cited on pages 52, 86, 153 and 154.)

Neininger N., Beck R., Sukumar S., Allen R. J., 1993, A&A, 274, 687 (Cited on page 171.)

Ness N. F., Acuna M. H., Lepping R. P., Burlaga L. F., Behannon K. W., Neubauer F. M., 1979, Science, 204, 982 (Cited on page 4.)

Norman C. A., Ferrara A., 1996, ApJ, 467, 280 (Cited on page 108.)

Noutsos A., Johnston S., Kramer M., Karastergiou A., 2008, MNRAS, 386, 1881 (Cited on pages 20, 109, 129 and 160.)

O'Sullivan S. P., et al., 2012, MNRAS, 421, 3300 (Cited on pages 37, 42, 46, 51, 62, 64, 109 and 156.)

O'Sullivan S. P., Gaensler B. M., Lara-López M. A., van Velzen S., Banfield J. K., Farnes J. S., 2015, ApJ, 806, 83 (Cited on page 37.)

O'Sullivan S. P., Purcell C. R., Anderson C. S., Farnes J. S., Sun X. H., Gaensler B. M., 2017, MNRAS, 469, 4034 (Cited on pages 37, 52, 61, 72, 76, 77, 80 and 159.)

O'Sullivan S. P., Lenc E., Anderson C. S., Gaensler B. M., Murphy T., 2018, MNRAS, 475, 4263 (Cited on pages 4, 19 and 37.)

O'Sullivan S. P., et al., 2019, A&A, 622, A16 (Cited on page 109.)

Opher M., Bibi F. A., Toth G., Richardson J. D., Izmodenov V. V., Gombosi T. I., 2009, Nature, 462, 1036 (Cited on page 4.)

Oppermann N., et al., 2012, A&A, 542, A93 (Cited on pages 19, 52, 85 and 152.)

Oppermann N., et al., 2015, A&A, 575, A118 (Cited on pages 19, 23, 73, 85, 129, 152 and 158.)

Ordog A., Brown J. C., Kothes R., Landecker T. L., 2017, A&A, 603, A15 (Cited on pages 111 and 169.)

Osterbrock D. E., Ferland G. J., 2006, Astrophysics of Gaseous Nebulae and Active Galactic Nuclei. (University Science Books) (Cited on page 6.)

Owens M. J., Forsyth R. J., 2013, Living Reviews in Solar Physics, 10, 5 (Cited on page 4.)

Pacholczyk A. G., 1970, Radio Astrophysics. Nonthermal Processes in Galactic and Extragalactic Sources. (W. H. Freeman, San Francisco, CA) (Cited on page 12.)

Page L., et al., 2007, ApJS, 170, 335 (Cited on pages 138 and 161.)

Pakmor R., Marinacci F., Springel V., 2014, ApJ, 783, L20 (Cited on page 8.)

Parker E. N., 1971, ApJ, 163, 255 (Cited on page 108.)

Pasetto A., Carrasco-González C., O'Sullivan S., Basu A., Bruni G., Kraus A., Curiel S., Mack K.-H., 2018, A&A, 613, A74 (Cited on pages 19, 37, 52, 80, 156 and 158.)

Paturel G., Fouque P., Bottinelli L., Gouguenheim L., 1989, A&AS, 80, 299 (Cited on page 203.)

Pavel M. D., Clemens D. P., Pinnick A. F., 2012, ApJ, 749, 71 (Cited on page 161.)

Peimbert M., Peimbert A., Delgado-Inglada G., 2017, PASP, 129, 082001 (Cited on page 74.)

Perley R. A., Butler B. J., 2013a, ApJS, 204, 19 (Cited on pages 54 and 92.)

Perley R. A., Butler B. J., 2013b, ApJS, 206, 16 (Cited on page 54.)

Perley R., et al., 2009, IEEE Proceedings, 97, 1448 (Cited on pages 28 and 29.)

Perlman E. S., Padovani P., Giommi P., Sambruna R., Jones L. R., Tzioumis A., Reynolds J., 1998, AJ, 115, 1253 (Cited on page 90.)

Piro A. L., Gaensler B. M., 2018, ApJ, 861, 150 (Cited on page 20.)

Planck Collaboration et al., 2014a, A&A, 571, A11 (Cited on page 162.)

Planck Collaboration et al., 2014b, A&A, 571, A29 (Cited on page 75.)

Planck Collaboration et al., 2016a, A&A, 586, A138 (Cited on page 6.)

Planck Collaboration et al., 2016b, A&A, 594, A10 (Cited on pages 162 and 163.)

Planck Collaboration et al., 2016c, A&A, 594, A13 (Cited on page 52.)

Planck Collaboration et al., 2016d, A&A, 594, A25 (Cited on pages 161 and 163.)

Planck Collaboration et al., 2019, A&A, in press (Cited on page 162.)

Popping A., Braun R., 2008, A&A, 479, 903 (Cited on page 35.)

Price D. J., Bate M. R., 2008, MNRAS, 385, 1820 (Cited on page 6.)

Purcell C. R., et al., 2015, ApJ, 804, 22 (Cited on pages 18, 23, 50, 52, 74, 85 and 128.)

Rand R. J., Lyne A. G., 1994, MNRAS, 268, 497 (Cited on pages 110 and 111.)

Rawes J., Birkinshaw M., Worrall D. M., 2018, MNRAS, 480, 3644 (Cited on page 71.)

Reynolds R. J., 1988, ApJ, 333, 341 (Cited on page 17.)

Reynolds S. P., Gaensler B. M., Bocchino F., 2012, Space Sci. Rev., 166, 231 (Cited on page 4.)

Richards J. L., et al., 2011, ApJS, 194, 29 (Cited on page 93.)

Rodrigues L. F. S., Shukurov A., Fletcher A., Baugh C. M., 2015, MNRAS, 450, 3472 (Cited on page 8.)

Rodríguez L. F., Gómez Y., Tafoya D., 2012, MNRAS, 420, 279 (Cited on page 75.)

Rudnick L., 2019, PIAU, accepted (Cited on pages 19 and 158.)

Rudnick L., Jones T. W., 1983, AJ, 88, 518 (Cited on page 22.)

Rudnick L., Owen F. N., 2014, ApJ, 785, 45 (Cited on page 159.)

Rudnick L., et al., 1985, ApJS, 57, 693 (Cited on page 95.)

Rusin D., Norbury M., Biggs A. D., Marlow D. R., Jackson N. J., Browne I. W. A., Wilkinson P. N., Myers S. T., 2002, MNRAS, 330, 205 (Cited on page 20.)

Russeil D., 2003, A&A, 397, 133 (Cited on page 74.)

Ruzmaikin A., Sokolov D., Shukurov A., 1988a, Magnetic Fields of Galaxies. (Springer-Verlag Berlin Heidelberg) (Cited on page 8.)

Ruzmaikin A., Sokolov D., Shukurov A., 1988b, Nature, 336, 341 (Cited on page 132.)

Rybicki G. B., Lightman A. P., 1986, Radiative Processes in Astrophysics. (Wiley-VCH-Verlag, Weinheim) (Cited on page 12.)

Schleicher D. R. G., Banerjee R., Sur S., Arshakian T. G., Klessen R. S., Beck R., Spaans M., 2010, A&A, 522, A115 (Cited on page 8.)

Schlickeiser R., 2012, Phys. Rev. Lett., 109, 261101 (Cited on page 8.)

Schlickeiser R., Felten T., 2013, ApJ, 778, 39 (Cited on page 8.)

Schnitzeler D. H. F. M., 2010, MNRAS, 409, L99 (Cited on pages 19, 129 and 158.)

Schnitzeler D. H. F. M., 2018, MNRAS, 474, 300 (Cited on pages 46, 64, 77, 78, 156 and 157.)

Schnitzeler D. H. F. M., Lee K. J., 2017, MNRAS, 466, 378 (Cited on pages 39, 58, 120 and 156.)

Schnitzeler D. H. F. M., Eatough R. P., Ferrière K., Kramer M., Lee K. J., Noutsos A., Shannon R. M., 2016, MNRAS, 459, 3005 (Cited on page 155.)

Schnitzeler D. H. F. M., Carretti E., Wieringa M. H., Gaensler B. M., Haverkorn M., Poppi S., 2019, MNRAS, 485, 1293 (Cited on pages 23, 26, 37, 52 and 154.)

Seta A., Beck R., 2019, Galaxies, 7, 45 (Cited on page 15.)

Seta A., Shukurov A., Wood T. S., Bushby P. J., Snodin A. P., 2018, MNRAS, 473, 4544 (Cited on page 15.)

Shimmins A. J., Wall J. V., 1973, Australian Journal of Physics, 26, 93 (Cited on page 93.)

Shimwell T. W., et al., 2017, A&A, 598, A104 (Cited on page 161.)

Shimwell T. W., et al., 2019, A&A, 622, A1 (Cited on page 161.)

Shneider C., Haverkorn M., Fletcher A., Shukurov A., 2014, A&A, 567, A82 (Cited on page 46.)

Shukurov A., 2004, in Dormy E., Soward A. M., eds, Mathematical Aspects of Natural Dynamos. EDP Press, p. 313 (Cited on page 15.)

Simard-Normandin M., Kronberg P. P., 1980, ApJ, 242, 74 (Cited on pages ix, 11, 19, 22, 24, 108 and 110.)

Simard-Normandin M., Kronberg P. P., Button S., 1981, ApJS, 45, 97 (Cited on pages 22 and 37.)

Sokoloff D., Shukurov A., 1990, Nature, 347, 51 (Cited on pages 108 and 133.)

Sokoloff D. D., Bykov A. A., Shukurov A., Berkhuijsen E. M., Beck R., Poezd A. D., 1998, MNRAS, 299, 189 (Cited on pages 42, 43, 51 and 62.)

Soler J. D., Hennebelle P., Martin P. G., Miville-Deschênes M.-A., Netterfield C. B., Fissel L. M., 2013, ApJ, 774, 128 (Cited on page 6.)

Stein W., 1966, ApJ, 144, 318 (Cited on page 162.)

Stein Y., et al., 2019, A&A, 623, A33 (Cited on pages 11 and 110.)

Steininger T., et al., 2018, Inferring Galactic Magnetic Field Model Parameters Using IMAGINE - An Interstellar MAGnetic field INference Engine (`arXiv:1801.04341`) (Cited on page 162.)

Stepinski T. F., Levy E. H., 1988, ApJ, 331, 416 (Cited on page 133.)

Stil J. M., Taylor A. R., 2007, ApJ, 663, L21 (Cited on pages 155 and 169.)

Stil J. M., Taylor A. R., Sunstrum C., 2011, ApJ, 726, 4 (Cited on pages 23, 52, 85, 104, 108, 109, 152, 153, 169 and 170.)

Stix M., 1975, A&A, 42, 85 (Cited on page 108.)

Stokes G. G., 1851, Transactions of the Cambridge Philosophical Society, 9, 399 (Cited on page 29.)

Strong A. W., Moskalenko I. V., Reimer O., 2000, ApJ, 537, 763 (Cited on page 15.)

Strong A. W., Moskalenko I. V., Porter T. A., Jóhannesson G., Orlando E., Digel S. W., 2009, The GALPROP Cosmic-Ray Propagation Code (arXiv:0907.0559) (Cited on page 138.)

Sun X. H., Han J. L., Reich W., Reich P., Shi W. B., Wielebinski R., Fürst E., 2007, A&A, 463, 993 (Cited on page 161.)

Sun X. H., Reich W., Waelkens A., Enßlin T. A., 2008, A&A, 477, 573 (Cited on pages 71, 109, 110, 111, 132, 133, 135, 136, 137, 138, 139, 140, 141, 142, 144, 145, 146, 147, 148 and 152.)

Sun X. H., Reich P., Reich W., Xiao L., Gao X. Y., Han J. L., 2011, A&A, 536, A83 (Cited on page 135.)

Sun X. H., et al., 2015, AJ, 149, 60 (Cited on pages 47, 62, 77 and 156.)

Tabara H., Inoue M., 1980, A&AS, 39, 379 (Cited on page 22.)

Tassis K., et al., 2018, PASIPHAE: A High-Galactic-Latitude, High-Accuracy Optopolarimetric Survey (arXiv:1810.05652) (Cited on page 162.)

Taylor A. R., Salter C. J., 2010, in Kothes R., Landecker T. L., Willis A. G., eds, Astronomical Society of the Pacific Conference Series Vol. 438, The Dynamic Interstellar Medium: A Celebration of the Canadian Galactic Plane Survey. ASP, San Francisco, CA, p. 402 (Cited on page 161.)

Taylor G. B., Carilli C. L., Perley R. A., eds, 1999, Synthesis Imaging in Radio Astronomy II. ASP Conf. Ser. Vol. 180. (ASP, San Francisco, CA) (Cited on page 27.)

Taylor G. B., Govoni F., Allen S. W., Fabian A. C., 2001, MNRAS, 326, 2 (Cited on pages 75 and 109.)

Taylor A. R., et al., 2003, AJ, 125, 3145 (Cited on pages 22, 111 and 136.)

Taylor A. R., Stil J. M., Sunstrum C., 2009, ApJ, 702, 1230 (Cited on pages ix, x, xiii, 19, 21, 23, 26, 32, 34, 35, 36, 37, 38, 52, 53, 56, 57, 59, 61, 62, 64, 65, 66, 67, 68, 70, 71, 72, 73, 81, 85, 86, 87, 88, 89, 91, 93, 94, 95, 96, 97, 98, 99, 100, 101, 102, 103, 104, 105, 108, 111, 113, 114, 121, 122, 123, 124, 125, 126, 138, 147, 150, 151, 152, 153, 154, 155, 159, 162, 165, 166, 167, 171, 191, 192, 193, 196, 197, 198, 199, 201, 202 and 213.)

Temim T., Slane P., Kolb C., Blondin J., Hughes J. P., Bucciantini N., 2015, ApJ, 808, 100 (Cited on page 13.)

Terral P., Ferrière K., 2017, A&A, 600, A29 (Cited on pages 23, 50, 52, 85 and 152.)

Thompson A. R., Moran J. M., Swenson Jr. G. W., 2017, Interferometry and Synthesis in Radio Astronomy. (Springer International Publishing) (Cited on page 27.)

Thomson R. C., Nelson A. H., 1980, MNRAS, 191, 863 (Cited on pages 11, 20, 109, 110, 111 and 133.)

Thomson A. J. M., et al., 2018, MNRAS, 479, 5620 (Cited on page 4.)

Uyaniker B., Landecker T. L., Gray A. D., Kothes R., 2003, ApJ, 585, 785 (Cited on page 161.)

Vallee J. P., 1990, ApJ, 360, 1 (Cited on pages 19 and 109.)

Van Eck C. L., et al., 2011, ApJ, 728, 97 (Cited on pages ix, x, xiii, 18, 19, 23, 29, 50, 71, 85, 108, 109, 110, 111, 112, 113, 125, 126, 127, 128, 131, 133, 134, 136, 137, 138, 139, 140, 141, 142, 143, 144, 145, 147, 148, 150, 151, 152, 155, 196, 197, 198 and 202.)

Van Eck C. L., et al., 2017, A&A, 597, A98 (Cited on page 161.)

Van Eck C. L., et al., 2018, A&A, 613, A58 (Cited on page 43.)

Vernstrom T., Gaensler B. M., Rudnick L., Andernach H., 2019, ApJ, 878, 92 (Cited on pages 4, 19, 23 and 109.)

Wang C., Han J. L., Lai D., 2011, MNRAS, 417, 1183 (Cited on page 20.)

Wardle J. F. C., Kronberg P. P., 1974, ApJ, 194, 249 (Cited on pages 36, 58 and 124.)

White M. P., 1978, Astronomische Nachrichten, 299, 209 (Cited on page 108.)

Wiegert T., et al., 2015, AJ, 150, 81 (Cited on pages 137 and 164.)

Wills B. J., 1975, Australian Journal of Physics Astrophysical Supplement, 38, 1 (Cited on page 93.)

Wilson T. L., Rohlfs K., Hüttemeister S., 2013, Tools of Radio Astronomy. (Springer-Verlag Berlin Heidelberg) (Cited on page 27.)

Winkel B., Kerp J., Flöer L., Kalberla P. M. W., Ben Bekhti N., Keller R., Lenz D., 2016, A&A, 585, A41 (Cited on pages 73, 75 and 135.)

Wolleben M., et al., 2009, in Strassmeier K. G., Kosovichev A. G., Beckman J. E., eds, IAU Symposium Vol. 259, Cosmic Magnetic Fields: From Planets, to Stars and Galaxies. Cambridge Univ. Press, Cambridge, p. 89 (Cited on page 161.)

Wright A. E., Griffith M. R., Hunt A. J., Troup E., Burke B. F., Ekers R. D., 1996, ApJS, 103, 145 (Cited on page 93.)

Xu S., Zhang B., 2016, ApJ, 824, 113 (Cited on page 170.)

Xu Y., Reid M. J., Zheng X. W., Menten K. M., 2006, Science, 311, 54 (Cited on page 134.)

Yao J. M., Manchester R. N., Wang N., 2017, ApJ, 835, 29 (Cited on pages 17, 22, 130, 138, 140, 145, 148 and 152.)

Young A., Maaskant R., Ivashina M. V., de Villiers D. I. L., Davidson D. B., 2013, IEEE Transactions on Antennas and Propagation, 61, 2466 (Cited on page 35.)

Yusef-Zadeh F., Morris M., Chance D., 1984, Nature, 310, 557 (Cited on page 155.)

Zank G. P., 2015, ARA&A, 53, 449 (Cited on page 4.)

Zavala R. T., Taylor G. B., 2001, ApJ, 550, L147 (Cited on pages 95, 109, 158 and 166.)

Zwicky F., Herzog E., Wild P., Karpowicz M., Kowal C. T., 1961, Catalogue of Galaxies and of Clusters of Galaxies, Vol. I. (California Institute of Technology, Pasadena) (Cited on page 75.)

de Wijn A. G., Stenflo J. O., Solanki S. K., Tsuneta S., 2009, Space Sci. Rev., 144, 275 (Cited on page 4.)

Appendix A

Further Investigations in the NVSS Rotation Measure Catalogue

In this Appendix, I include some relevant tests and ideas regarding the reliability of the rotation measure (RM) values of the NVSS RM catalogue (Taylor et al. 2009, hereafter TSS09). These are extensions to Chapters 3 and 4, and will be included in a future publication refining this RM catalogue (see Chapter 6.5.2).

A.1 The Rotation Measure Correction Factor

A.1.1 A Quick Review

The TSS09 RM values were determined from polarisation measurements at the two intermediate frequency (IF) bands centred at 1364.9 and 1435.1 MHz, with bandwidths of 42 MHz each. In particular, the reported RM values were calculated from

$$\mathrm{RM} = C \cdot \frac{\mathrm{PA}_2 - \mathrm{PA}_1 + n\pi}{\lambda_2^2 - \lambda_1^2}, \tag{A.1}$$

where C is the correction factor that is the focus of this Appendix, PA [rad] is the polarisation position angle measured at the two IFs, n is an integer corresponding to the $n\pi$-ambiguity (see Chapter 2.2.2), λ [m] is the wavelength matching the central frequencies of the two IFs, and the subscript (1 or 2) denotes the two IFs. The correction factor C is given by (equation 2 of TSS09)

$$C = \left(1 + \frac{\Delta\lambda_2^2 - \Delta\lambda_1^2}{\lambda_2^2 - \lambda_1^2}\right)^{-1}, \tag{A.2}$$

where $\Delta\lambda^2$ [m^2] was not explicitly defined in TSS09, but can be determined by "reverse engineering" using their given value of $C = 0.96$ for the NVSS that, $\Delta\lambda^2$ is half of the bandwidth in λ^2 space of the two IFs:

$$\Delta\lambda^2 = \frac{\lambda_{\mathrm{max}}^2 - \lambda_{\mathrm{min}}^2}{2}, \tag{A.3}$$

where λ_{max}^2 and λ_{min}^2 are the upper and lower ends of an IF in λ^2 space. The values of $\Delta\lambda^2$ are listed in Table A.1. As directly quoted from TSS09, "C is a correction factor that accounts for the effect of the finite width of the bands on the effective center wavelength in λ^2 space" (p. 1231). I interpret this as addressing the different definitions of the "band centre", as explained below.

Table A.1: Parameters of the Two NVSS Bands

Parameter	IF1 Value	IF2 Value	Description
ν [MHz]	1364.9	1435.1	Central frequency
$\Delta\nu$ [MHz]	42	42	Frequency bandwidth
λ [m]	0.21964	0.20890	Wavelength matching the central frequency
$\overline{\lambda}$ [m]	0.21970	0.20894	Band centre in λ space
$\overline{\lambda^2}$ [10^{-2} m^2]	4.8278	4.3661	Band centre in λ^2 space
$\sqrt{\overline{\lambda^2}}$ [m]	0.21972	0.20897	Square root of $\overline{\lambda^2}$
$\Delta\lambda^2$ [10^{-3} m^2]	1.4852	1.2777	Half-bandwidth in λ^2 space (as per TSS09)

A.1.2 The Many Band Centres of the NVSS

Different band centres can be defined by considering different parameter spaces. The IF1 and IF2 of NVSS observations span 1343.9–1385.9 and 1414.1–1456.1 MHz in frequency space, respectively. The band centres in frequency space are therefore 1364.9 and 1435.1 MHz, respectively. These can be directly translated to wavelength by $\lambda = c/\nu$, giving $\lambda_1 = 0.21964$ m and $\lambda_2 = 0.20890$ m. Similarly in λ space, the IFs span 0.21632–0.22308 and 0.20589–0.21200 m, respectively. These give band centres in λ space of $\overline{\lambda_1} = 0.21970$ m and $\overline{\lambda_2} = 0.20894$ m. Finally, in λ^2 space, the two IFs span $(4.6793\text{–}4.9763)\times10^{-2}$ and $(4.2390\text{–}4.4932)\times10^{-2}$ m^2, respectively. The band centres in λ^2 space are therefore $\overline{\lambda_1^2} = 4.8278 \times 10^{-2}$ m^2 and $\overline{\lambda_2^2} = 4.3661 \times 10^{-2}$ m^2. These can be further converted to $\sqrt{\overline{\lambda_1^2}} = 0.21972$ m and $\sqrt{\overline{\lambda_2^2}} = 0.20897$ m. All these band centre values are summarised in Table A.1.

As inferred from the direct quote from TSS09 (see Appendix A.1.1), for their RM measurements the band centres in λ^2 space instead of ν space have been adopted, which they implemented by introducing the correction factor C to translate from the latter band centre definition to the former. The background rationale of this is stated below.

A.1.3 Background Rationale for C

In linear polarisation observations, one makes measurements of Stokes Q and U (Chapter 2.1.2). The observed values, $\tilde{Q}$ and $\tilde{U}$ [Jy], are obtained from integrating the actual values, Q and U, within the frequency bands or channels, as given by

$$\begin{aligned}
\tilde{Q}(\nu_{\rm obs}) &= \frac{1}{\nu_{\rm hi}-\nu_{\rm lo}}\int_{\nu_{\rm lo}}^{\nu_{\rm hi}} Q(\nu)\,{\rm d}\nu \\
&= \frac{1}{\nu_{\rm hi}-\nu_{\rm lo}}\int_{\nu_{\rm lo}}^{\nu_{\rm hi}} S(\nu)\cdot p(\nu)\cdot\cos[2({\rm PA}_0+{\rm RM}\lambda^2)]\,{\rm d}\nu, \qquad \text{(A.4)} \\
\tilde{U}(\nu_{\rm obs}) &= \frac{1}{\nu_{\rm hi}-\nu_{\rm lo}}\int_{\nu_{\rm lo}}^{\nu_{\rm hi}} U(\nu)\,{\rm d}\nu \\
&= \frac{1}{\nu_{\rm hi}-\nu_{\rm lo}}\int_{\nu_{\rm lo}}^{\nu_{\rm hi}} S(\nu)\cdot p(\nu)\cdot\sin[2({\rm PA}_0+{\rm RM}\lambda^2)]\,{\rm d}\nu, \qquad \text{(A.5)}
\end{aligned}$$

where $\nu_{\rm obs}$ is the frequency corresponding to the measurements $\tilde{Q}$ and $\tilde{U}$ (see below), $\nu_{\rm hi}$ and $\nu_{\rm lo}$ are the upper and lower bounds of the frequency band, respectively, S [Jy] is the total intensity, p is the polarisation fraction, and PA_0 [rad] is the intrinsic polarisation position angle.

The values of $\nu_{\rm obs}$ can be treated as the exact frequencies where the measurements have been made. Ideally, $\nu_{\rm obs}$ should be set such that the measured values equate the actual values at that frequency: $\tilde{Q}(\nu_{\rm obs}) = Q(\nu_{\rm obs})$ and $\tilde{U}(\nu_{\rm obs}) = U(\nu_{\rm obs})$. In practice, it is often simply assigned that

$$\nu_{\rm obs} = \frac{\nu_{\rm hi} + \nu_{\rm lo}}{2}, \tag{A.6}$$

i.e. the band centre in frequency space is taken as $\nu_{\rm obs}$. Strictly speaking, this choice is only valid if the observable has a linear relationship with ν: consider an observable $G(\nu) = K_0 \cdot \nu + K_1$, where K_0 and K_1 are two parameters of the astrophysical source. We then have

$$\begin{aligned}
\tilde{G}(\nu_{\rm obs}) &= \frac{1}{\nu_{\rm hi} - \nu_{\rm lo}} \int_{\nu_{\rm lo}}^{\nu_{\rm hi}} G(\nu)\,\mathrm{d}\nu \\
&= \frac{1}{\nu_{\rm hi} - \nu_{\rm lo}} \int_{\nu_{\rm lo}}^{\nu_{\rm hi}} K_0 \cdot \nu + K_1\,\mathrm{d}\nu \\
&= \frac{1}{\nu_{\rm hi} - \nu_{\rm lo}} \cdot \left[\frac{K_0}{2} \cdot (\nu_{\rm hi}^2 - \nu_{\rm lo}^2) + K_1(\nu_{\rm hi} - \nu_{\rm lo}) \right] \\
&= K_0 \cdot \frac{\nu_{\rm hi} + \nu_{\rm lo}}{2} + K_1 \\
&= G\left(\frac{\nu_{\rm hi} + \nu_{\rm lo}}{2} \right).
\end{aligned} \tag{A.7}$$

Nonetheless, this choice of $\nu_{\rm obs}$ (Equation A.6) can also be justified for other observables (e.g., Stoke I, Q, and U) given that the bandwidth is sufficiently narrow. If the bandwidths are instead wide, as pointed out to be the case for the NVSS observations by TSS09, different appropriate choices of $\nu_{\rm obs}$ should be used.

For the TSS09 RM measurements, it has been suggested that the band centres in λ^2 space should be adopted instead (see Appendix A.1.2):

$$\nu_{\rm obs} = \frac{c}{\sqrt{\overline{\lambda^2}}}. \tag{A.8}$$

However, it was not explicitly discussed why this choice is more suitable than that of Equation A.6. In fact, if this definition of Equation A.8 has indeed been used, the correction factor should instead be

$$C = \frac{\lambda_2^2 - \lambda_1^2}{\overline{\lambda_2^2} - \overline{\lambda_1^2}} = 0.99686. \tag{A.9}$$

A suitable correction factor to the TSS09 RM values is crucial, since otherwise there will be a systematic offset between their listed and the actual RM values. To test the validity of their choice of $C = 0.96$, I perform mock observations with the NVSS IF configurations as described below.

Table A.2: Input Parameters of the Mock Observations

Parameter	IF1 Value	IF2 Value
$\nu_{\rm hi}$ [MHz]	1385.9	1456.1
$\nu_{\rm lo}$ [MHz]	1343.9	1414.1
α	0.0, -0.7, and -1.0	
$p(\nu)$	Constant	
PA_0 [rad]	0.0	
$\mathrm{RM}_{\rm src}$ [rad m^{-2}]	From -1000 to $+1000$	

A.1.4 Testing C with Mock Observations

The goal of the mock observations here is to determine which definition of band centre is the most appropriate for accurate recovery of the true source RM values in NVSS observations. Specifically, a range of source RM values ($\mathrm{RM}_{\rm src}$) from -1000 to $+1000\,\mathrm{rad\,m^{-2}}$ at $5\,\mathrm{rad\,m^{-2}}$ intervals have been used systematically as the inputs, and for each case the resulting RM values determined from the observations ($\mathrm{RM}_{\rm obs}$) are calculated adopting the different band centres. The limit imposed on $\mathrm{RM}_{\rm src}$ was chosen because at $|\mathrm{RM}| > 1000\,\mathrm{rad\,m^{-2}}$, the bandwidth depolarisation effect would be severe (see Chapter 2.1.3.2), and therefore serves as a detection limit of NVSS observations.

The observed $\tilde{Q}$ and $\tilde{U}$ values are obtained from Equations A.4 and A.5. I do not consider the effects of measurement uncertainties in the mock observations here (i.e. the rms noise is infinitesimal). The flux density S is set to be proportional to ν^{α}, as should be the case for synchrotron-emitting objects (see Chapter 1.4.1). Three different values of α have been used to test its effects on RM measurements: 0.0, -0.7, and -1.0. The polarisation fraction p is taken to be constant across ν (i.e. Faraday simplicity has been assumed; see Chapter 2.2.1), while PA_0 does not affect the results here, and is set as zero for all cases. I have replaced RM by $\mathrm{RM}_{\rm src}$ in the two Equations, and chose $\nu_{\rm hi}$ and $\nu_{\rm lo}$ appropriately for the two IFs. Table A.2 summarises the parameters used for the mock observations.

The observed PA values at the two IFs are determined as usual by using

$$\mathrm{PA} = \frac{1}{2}\tan^{-1}\left(\frac{\tilde{U}}{\tilde{Q}}\right). \tag{A.10}$$

From this, the resulting RM values are calculated by adopting different band centres. First, by using the band centre in frequency space:

$$\mathrm{RM}_{\rm obs} = \frac{\mathrm{PA}_2 - \mathrm{PA}_1}{\lambda_2^2 - \lambda_1^2}, \tag{A.11}$$

which is equivalent to choosing $C = 1.00$. Next, adopting the band centre in λ space gives

$$\mathrm{RM}_{\rm obs} = \frac{\mathrm{PA}_2 - \mathrm{PA}_1}{(\overline{\lambda_2})^2 - (\overline{\lambda_1})^2}, \tag{A.12}$$

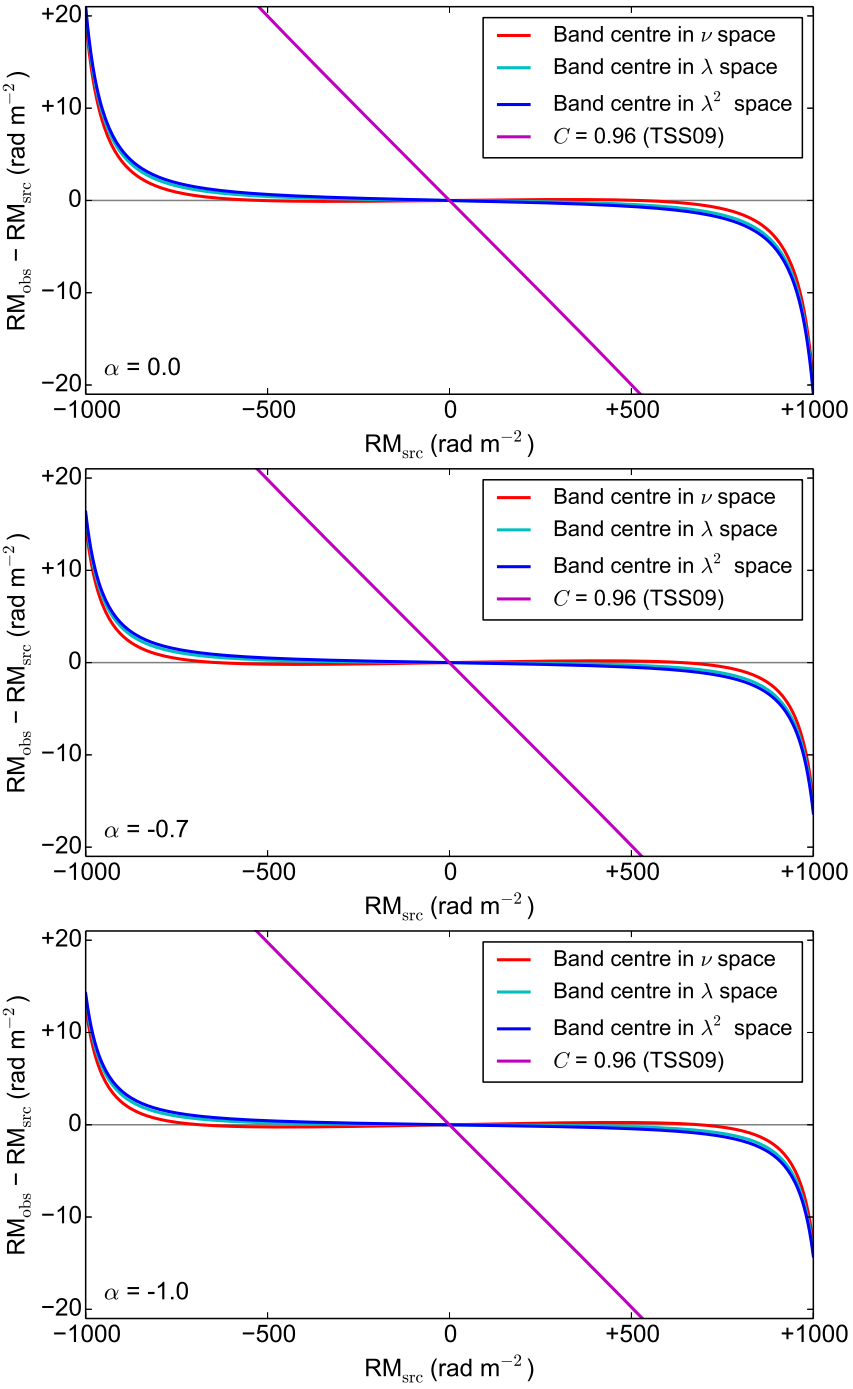

Figure A.1: Results of the mock observations testing the RM correction factor C. A curve closer to $y = 0$ means the corresponding band centre definition is more suitable. Three different choices of spectral index α have been shown: **(Top)** $\alpha = 0.0$, **(Middle)** $\alpha = -0.7$, and **(Bottom)** $\alpha = -1.0$.

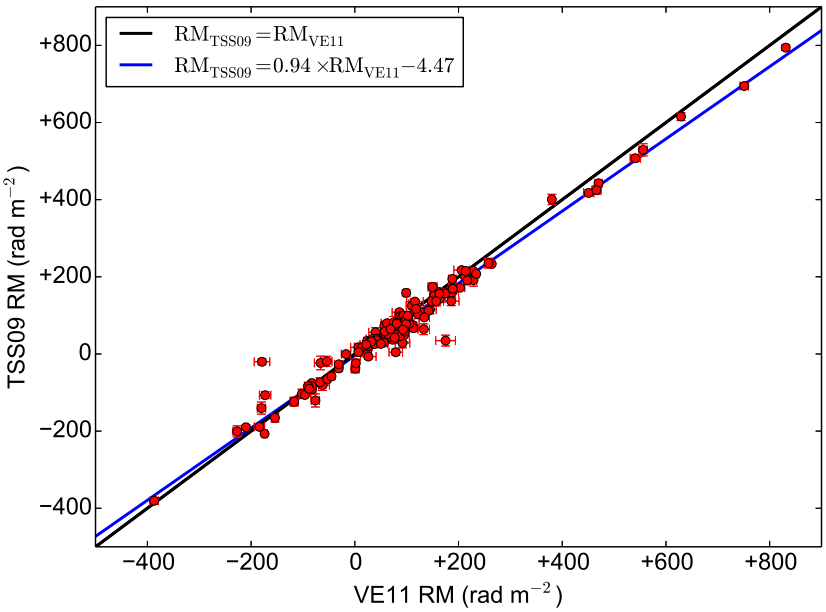

Figure A.2: Comparison between RM values of Taylor et al. (2009, TSS09) and Van Eck et al. (2011, VE11) of their 146 cross-matched sources. The TSS09 RM values of the 13 $n\pi$-ambiguity sources have been corrected.

which is identical to $C = 0.99791$. If one considers the band centre in λ^2 space, the observed RM would be

$$\mathrm{RM_{obs}} = \frac{\mathrm{PA_2} - \mathrm{PA_1}}{\sqrt{\overline{\lambda_2^2}} - \sqrt{\overline{\lambda_1^2}}}, \tag{A.13}$$

which is the same as taking $C = 0.99686$. Finally, I also attempt using $C = 0.96$ as did TSS09. For each band centre definition, I calculated $(\mathrm{RM_{obs}} - \mathrm{RM_{src}})$, with a closer value to zero meaning that band centre definition is more suitable. This is plotted against $\mathrm{RM_{src}}$, as shown in Figure A.1.

For all tested α values, I find that the orthodox choice of band centre in frequency space ($C = 1.00$) gives $\mathrm{RM_{obs}}$ values best matching $\mathrm{RM_{src}}$, with the adoption of λ and λ^2 spaces giving very similar results. This is as expected, since for all these three cases the corresponding values of C are very similar. The deviation from $y = 0$ for $|\mathrm{RM_{src}}| \gtrsim 800\,\mathrm{rad\,m^{-2}}$ with these three band centre definitions can be attributed to the significant non-linear variations of Stokes Q and U across the IFs at such high |RM| values (see Appendix A.1.3), calling for some other better choices of effective band centres for such cases. Nonetheless, since all TSS09 sources have listed $|\mathrm{RM}| < 760\,\mathrm{rad\,m^{-2}}$, I argue that the choice of band centre in frequency space would suffice for TSS09 RM measurements. To conclude, the mock observations here suggest the choice of $C = 1.00$ instead of $C = 0.96$ for the TSS09 RM measurements.

Table A.3: Evaluation of the Relationship between $\mathrm{RM_{TSS09}}$ and $\mathrm{RM_{VE11}}$

Relation	χ^2	Description
$\mathrm{RM_{TSS09}} = \mathrm{RM_{VE11}}$	5.65	Favours the choice of $C = 0.96$
$\mathrm{RM_{TSS09}} = 0.96 \times \mathrm{RM_{VE11}}$	4.30	Favours the choice of $C = 1.00$
$\mathrm{RM_{TSS09}} = 0.93 \times \mathrm{RM_{VE11}}$	4.35	Best-fit from Equation A.14 with $a = 0$
$\mathrm{RM_{TSS09}} = 0.94 \times \mathrm{RM_{VE11}} - 4.47$	3.99	Best-fit from Equation A.14

A.1.5 Testing C with Other Polarisation Observations

I further compare the RM values between TSS09 and Van Eck et al. (2011) to gain further insights into the effectiveness of the correction factor C. The Van Eck et al. (2011) observations were performed with the legacy VLA in spectral line mode in two IFs centred at 1365 and 1485 MHz. Each IF was further divided into seven channels with widths of about 3.6 MHz each, and the RM values were derived from these 14 polarisation measurements. The narrow channel width means they can safely adopt $C = 1.00$ for their RM measurements, and their RM values can be used as references to test the effectiveness of the TSS09 choice of $C = 0.96$.

There are a total of 146 cross-matched sources between Van Eck et al. (2011) and TSS09, with 13 found to suffer from $n\pi$-ambiguity in TSS09. I corrected for these erroneous values by adding the appropriate $\pm 652.9\,\mathrm{rad\,m^{-2}}$ to the TSS09 RMs. The two sets of RM values are compared in Figure A.2. If the choice of $C = 0.96$ for the TSS09 RM is suitable, the data points should be best represented by a one-to-one line: $\mathrm{RM_{TSS09}} = \mathrm{RM_{VE11}}$, where VE11 represents Van Eck et al. (2011). If $C = 1.00$ should have been used instead (Appendix A.1.4), the data points would follow $\mathrm{RM_{TSS09}} = 0.96 \times \mathrm{RM_{VE11}}$. In the most general case, the two sets of RM values can be related by

$$\mathrm{RM_{TSS09}} = b \times \mathrm{RM_{VE11}} + a. \tag{A.14}$$

I performed a least-square fit to the two sets of RM values by Equation A.14, and found the best-fit parameters to be $b = 0.94 \pm 0.01$ and $a = -4.47 \pm 2.44$. If the y-offset is fixed by $a = 0$, the best-fit parameter would then be $b = 0.93 \pm 0.01$.

The four equations above relating $\mathrm{RM_{TSS09}}$ and $\mathrm{RM_{VE11}}$ are evaluated by a measure of goodness-of-fit defined as

$$\chi^2 = \sum_j^N \frac{[\mathrm{RM_{TSS09},}_j - (b \times \mathrm{RM_{VE11},}_j + a)]^2}{N \cdot (\sigma^2_{\mathrm{TSS09},j} + b^2 \sigma^2_{\mathrm{VE11},j})}, \tag{A.15}$$

where the subscript j denotes the $N = 146$ data points. The χ^2 values are listed in Table A.3, with a lower χ^2 value meaning a better fit of the equation to the data points. From this comparison of $\mathrm{RM_{TSS09}}$ with $\mathrm{RM_{VE11}}$, I find that the choice of $C = 1.00$ is favoured over the TSS09 choice of $C = 0.96$. There are also hints of a constant offset of $4.5\,\mathrm{rad\,m^{-2}}$ between the two sets of RM values, which is outside of the scope of the study here.

Finally, I shall point out that Van Eck et al. (2011) have performed similar comparisons between their RM values with those of TSS09, but their focus was to validate their measurements rather than to evaluate the choice of $C = 0.96$ of TSS09. They found a linear correlation coefficient of 0.96, as well as an offset of about $10\,\mathrm{rad\,m^{-2}}$ between the two sets of RM values.

A.2 A Deeper Understanding in the $n\pi$-ambiguity Issue

Next, I take a deeper investigation in the $n\pi$-ambiguity issue of the TSS09 RM catalogue, which is the focus of my work presented in Chapter 3. The $n\pi$-ambiguity mitigation algorithm of TSS09 has been summarised in Chapter 3.4.1.1. In short, the most likely RM value for each source was chosen by comparing the observed amount of bandwidth depolarisation (quantified as R_0; see below) with those predicted by the few candidate RM values, and by restricting the chosen RM value to be within $\pm 520\,\mathrm{rad\,m^{-2}}$ from the median RM of neighbouring sources. Several factors that can lead to the failure of this $n\pi$-ambiguity mitigation method are explored below.

A.2.1 The Effectiveness of R_0

A.2.1.1 Challenges Due to Measurement Uncertainty

I first explore the effectiveness of the factor R_0, which was defined as (TSS09)

$$R_0 = \frac{\mathrm{PI}_1 + \mathrm{PI}_2}{2\mathrm{PI}_c}, \tag{A.16}$$

where PI_1, PI_2, and PI_c are the measured polarised intensities in IF1, IF2, and with both bands combined, respectively. All three values are functions of RM due to bandwidth depolarisation (Chapter 2.1.3.2; see Figure 2.5), and this property has been exploited in TSS09 to tackle the $n\pi$-ambiguity issue in their catalogue (see below). Here, I adopt the RM correction factor of $C = 0.96$ for consistency with TSS09 (see Appendix A.1), while the effect of choosing the "correct" $C = 1.00$ will be explored in Appendix A.2.1.2.

For each source, TSS09 considered three candidate RM values: RM_0 and $\mathrm{RM}_0 \pm 652.9\,\mathrm{rad\,m^{-2}}$, with RM_0 corresponding to the candidate RM value without any PA wraps between IF1 and IF2 (i.e., $n = 0$ in Equation A.1). These three candidate RMs will each predict a corresponding R_0 value due to bandwidth depolarisation, which are in turn compared to the actual observed R_0. From this comparison, the most likely candidate RM (that is also within $\pm 520\,\mathrm{rad\,m^{-2}}$ of the median RM of its neighbours) is reported as the RM value of the source. While in the TSS09 paper it was stated that the uncertainty of the observed R_0 has been taken into account, it was not explicitly explained how.

I explore here the effectiveness of the parameter R_0 in resolving $n\pi$-ambiguity in TSS09 under the presence of measurement uncertainties. Instead of determining the most likely RM value for each source, I looked into how many candidate RM values

Table A.4: List of Acceptable RM Values for the 20 Sources

Source (NVSS)	Observed R_0	Acceptable RM (rad m^{-2})	RM Uncertainty (rad m^{-2})	$\overline{\phi}$ (rad m^{-2})
Outliers (Reliable RM$_{\mathrm{TSS09}}$)				
J083930−240723	$7.72^{+10.30}_{-0.95}$	−316.4; +336.5	±12.5	+325.9 ± 1.0
J084701−233701	$1.84^{+0.42}_{-0.17}$	−210.4; +442.5	±15.0	+384.8 ± 2.0
J090015−281758	$4.71^{+0.49}_{-0.36}$	None	±3.9	+352.1 ± 0.2
J092410−290606	$1.77^{+0.22}_{-0.14}$	+491.4	±8.7	$+527.6^{+0.3}_{-0.3}$
J093349−302700	$8.78^{+7.89}_{-0.83}$	+317.2	±9.4	+341.6 ± 0.8
J093544−322845	$2.23^{+2.29}_{-0.26}$	−259.7; +393.2	±31.9	$+390.9^{+0.3}_{-0.3}$
J094750−371528	$2.98^{+3.22}_{-0.41}$	−372.4; +280.5	±22.3	+328.8 ± 2.2
J162706−091705	$5.22^{+8.89}_{-0.48}$	−304.6; +348.3	±15.2	−327.8 ± 0.7
J163927−124139	$6.28^{+3.29}_{-0.68}$	−311.0	±9.2	$-331.4^{+0.3}_{-0.3}$
J220205+394913	$9.92^{+6.14}_{-1.07}$	None	±6.4	−367.2 ± 0.4
J220927+415834	$13.23^{+12.04}_{-1.48}$	None	±5.7	−338.1 ± 0.2
Out-*liars* ($n\pi$-ambiguity)				
J022915+085125	$1.17^{+0.06}_{-0.08}$	−123.7	8.0	+13.6 ± 1.0
J091145−301305	$2.52^{+0.13}_{-0.17}$	−436.3	5.7	$+246.9^{+0.3}_{-0.3}$
J094808−344010	$6.03^{+8.53}_{-0.54}$	−337.0; +315.9	11.1	$+382.7^{+2.6}_{-2.4}$
J111857+123442	$1.45^{+0.12}_{-0.06}$	+185.7	5.7	$+79.4^{+2.6}_{-2.8}$
J170934−172853	$1.39^{+0.25}_{-0.11}$	+185.3; +838.2	14.1	$+106.2^{+1.8}_{-1.9}$
J190255+315942	$1.67^{+0.05}_{-0.03}$	None	3.6	$+142.2^{+1.1}_{-1.1}$
J224412+405715	$9.38^{+14.38}_{-1.13}$	−311.6; +341.3	12.4	−320.4 ± 0.6
J224549+394122	$4.69^{+0.34}_{-0.23}$	+385.6	1.1	$-278.6^{+0.8}_{-1.0}$
J235728+230226	$1.08^{+0.13}_{-0.07}$	−574.5; +78.4; +731.3	12.6	+42.3 ± 6.1

NOTE — $\overline{\phi}$ is the polarisation-weighted Faraday depth (FD) of the source (see Chapter 3.3.1).

are "acceptable", defined as having the predicted and observed R_0 agreeing within 68.3 per cent confidence intervals (corresponding to 1σ for Gaussian errors) of both the RM and the observed R_0 (explained below with examples). The $\pm 520\,\mathrm{rad\,m^{-2}}$ criterion mentioned above is not considered here. The 21 polarised sources studied in Chapters 3 and 4 are investigated here, with the exception of NVSS J154936+183500 because it can neither be categorised as an $n\pi$-ambiguity nor a reliable RM source (Chapter 3.4.1.8).

From the TSS09 cutout images, I extracted the Stokes Q and U values (along with their uncertainties) in IF1, IF2, and the combined band. The values in IF1 and IF2 were used to calculate the candidate RM values (with uncertainties computed by standard error propagation formulae), while all three sets of values were used to determine the observed R_0 (with asymmetric uncertainties propagated by Monte Carlo). As each candidate RM value actually spans a range due to measurement uncertainties, the corresponding predicted R_0 also spans a range. The acceptable RM values are then identified by checking whether the range of predicted R_0 has any overlaps with the range of observed R_0. This is illustrated by Figures A.3 and A.4, with the former Figure showing the case of NVSS J091145−301305 with only one acceptable RM and the latter showing NVSS J084701−233701 with two acceptable RM values. For each of these two sources, the three candidate RM values are marked by the orange vertical lines, and the observed R_0 is marked by the magenta horizontal line. Both of these have their uncertainties represented by the shaded areas in the same colours. The predicted R_0 as a function of |RM| is shown by the blue curve. If the three coloured lines overlap, the candidate RM value is deemed acceptable, since this means the predicted and observed R_0 values agree within uncertainties.

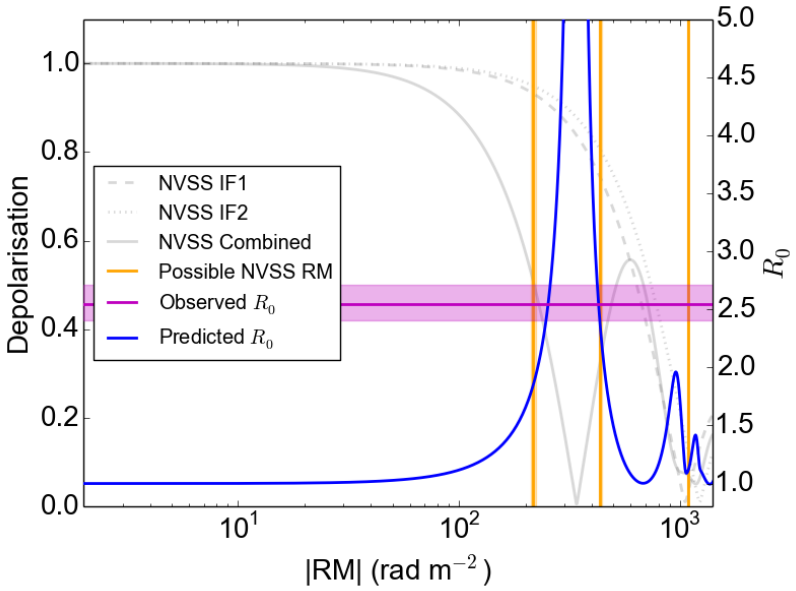

Figure A.3: Illustration of the identification of the acceptable RM values for NVSS J091145−301305. The three candidate RM values (−1089.2, −436.3, and +216.6 rad m^{-2}) are marked by the orange vertical lines, and the observed R_0 is marked by the magenta horizontal line, both with their uncertainties shown by the shaded areas. The predicted R_0 is represented by the blue curve. A candidate RM is deemed acceptable if all three coloured lines overlap, and the only acceptable RM for this source is −436.3 rad m^{-2}. The amount of bandwidth depolarisation as functions of |RM| for the NVSS setup are shown by the grey curves.

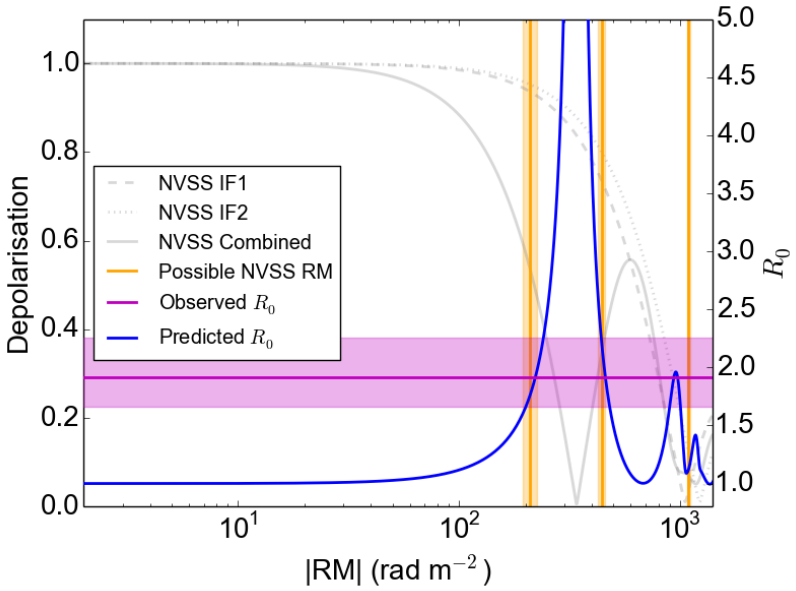

Figure A.4: Similar to Figure A.3 but for NVSS J084701−233701. The two acceptable RM values for this source are −210.4 and +442.5 rad m^{-2}, while the remaining candidate RM is +1095.4 rad m^{-2}.

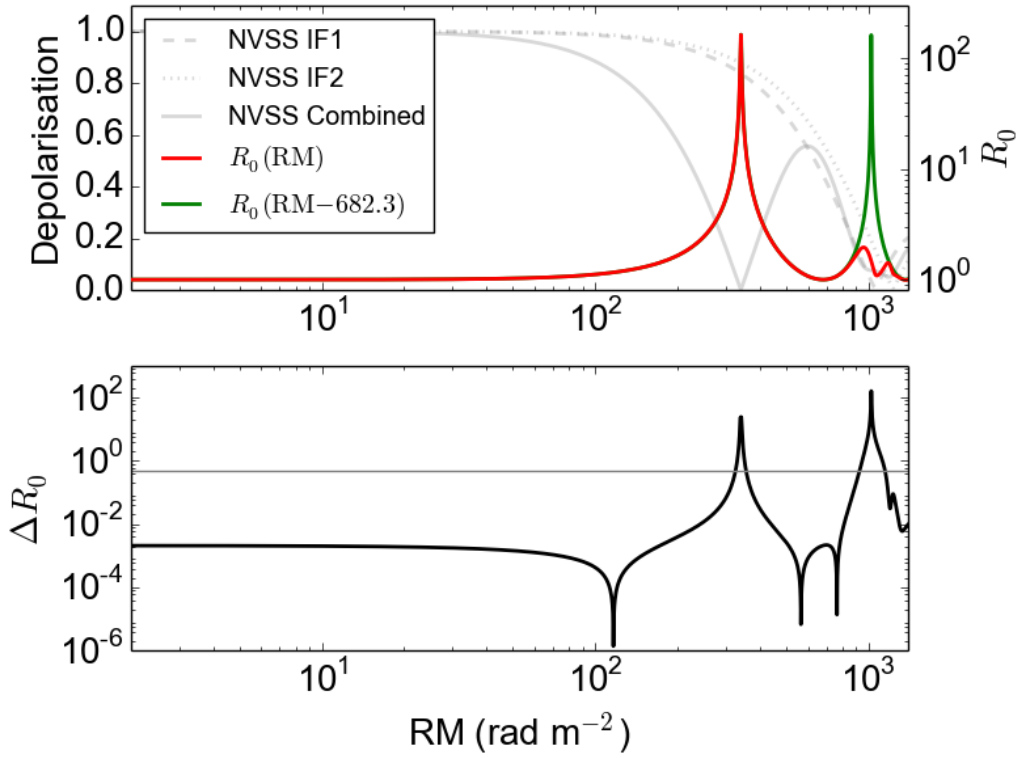

Figure A.5: Comparison of predicted R_0 against RM and its competing candidate, (RM − 682.3 rad m^{-2}), when an RM correction factor of $C = 1.00$ is adopted. **(Top)** The two competing trends of R_0 are shown as the coloured curves that overlap each other over most of the RM range shown, and the grey curves represent the amount of bandwidth depolarisation as functions of RM for the NVSS setup. **(Bottom)** Plot of $\Delta R_0(\mathrm{RM}) = |R_0(\mathrm{RM}) - R_0(\mathrm{RM} - 682.3)|$ is shown as the black curve. The grey horizontal line corresponds to the typical uncertainty in R_0 of ≈ 0.5.

The acceptable RM values for the 20 sources are listed in Table A.4, and I found that there are nine sources (45 per cent) with more than one acceptable RM values. This suggests that, at least for the sources considered here, the measurement uncertainties in RM and observed R_0 can be too large for the R_0 algorithm to be effective in resolving $n\pi$-ambiguity in the TSS09 catalogue. Whether the same conclusion holds true for the majority of TSS09 sources will require further, similar study for a larger sample.

A.2.1.2 Relationship with the Correction Factor

I further test the effectiveness of R_0 when an RM correction factor of $C = 1.00$ is chosen instead. This has been suggested to be the correct choice according to my investigations presented in Appendix A.1, and will lead to shifts in RM by ± 682.3 rad m^{-2} due to $n\pi$-ambiguity instead of the ± 652.9 rad m^{-2} with $C = 0.96$. I perform the investigation by comparing the values of R_0 as a function of RM against that for

(RM $-$ 682.3 rad m^{-2}). If these two are too similar, the R_0 algorithm may not be able to distinguish between the two candidate RM values under the presence of measurement uncertainties. I omit the comparison between RM and (RM + 682.3 rad m^{-2}) because it would be redundant.

The trends of R_0(RM) and R_0(RM $-$ 682.3 rad m^{-2}) are shown in the top panel of Figure A.5, and their difference is plotted in the bottom panel. The two trends are deemed significantly different if their predicted R_0 values deviate by more than 0.5, which is the typical uncertainty in the observed R_0 for the sources studied in Appendix A.2.1.1. As shown below, the final conclusion is not sensitive to the choice made here. It is apparent that the two trends of predicted R_0 are very similar: over most of the RM range considered, their difference is well below the cutoff of 0.5 (often even at $< 10^{-2}$ level). The only exceptions are at RM values of $\approx$ 340 rad m^{-2} and $\approx$ 1020 rad m^{-2}, but at the former RM value the combined band suffers almost complete bandwidth depolarisation, meaning that the uncertainty in observed R_0 can be much larger than the 0.5 considered above. The latter RM value leads to nearly complete bandwidth depolarisation to even the individual NVSS IFs, and may not have polarisation signals at detectable levels to begin with. I conclude that if the "correct" RM correction factor of $C = 1.00$ is chosen, the R_0 algorithm may be ineffective in resolving the $n\pi$-ambiguity problem in TSS09.

A.3 Discussion and Summary

In this Appendix, I first evaluated the suitability of the choice of RM correction factor of $C = 0.96$ adopted by TSS09. This was achieved by performing mock observations with the NVSS frequency setup, as well as by comparing between the TSS09 and Van Eck et al. (2011) RM values. I found from both approaches that the typical choice of $C = 1.00$ is favoured over the TSS09 choice of $C = 0.96$ for the determination of their RM values. This can result in a systematic underestimation in magnetic field strengths, along with the uncertainties, by 4 per cent. Furthermore, the incorrect choice of C can be indirectly tied to the $n\pi$-ambiguity issue of the TSS09 RM catalogue (see Appendix A.2.1.2).

Moreover, I explored the effectiveness of the parameter R_0 in resolving $n\pi$-ambiguity of the TSS09 RM catalogue. Using the TSS09 choice of $C = 0.96$, I found that measurement uncertainties can make it challenging to use R_0 to distinguish between RM candidates, while using $C = 1.00$ would make the predicted R_0 values at the competing candidate RM values to be too similar to be discerned.

In the future, I shall repeat the observational tests performed in this Appendix by using my data presented in Chapter 5. The 87 sources cross-matched with TSS09 will be utilised to further test the choice of the RM correction factor C, and to evaluate the effectiveness of the parameter R_0.

Appendix B

Additional Materials to Chapter 3

I include here some additional materials to my work presented in Chapter 3. Appendices B.1 and B.2 form the appendix of the paper, while Appendix B.3 here was presented as the Online Supplementary Materials of the publication.

B.1 Spatially Resolved Sources

In our new Jansky VLA D array observations, two of our target sources are spatially resolved, namely J094750−371528 and J224549+394122. The former is identified as a galaxy (PGC 626051; Paturel et al. 1989) at $z = 0.0411$ (Jones et al. 2009), while the latter is an FR II radio galaxy at $z = 0.0811$ and is well studied in the radio regime (commonly known as 3C 452; e.g. Black et al. 1992; Harwood et al. 2017). For these two sources, we formed another set of Stokes I, Q, and U images for detailed spatial analysis. Channel images were again formed by binning 4 MHz of visibilities with identical algorithm and weighting scheme as the full band data (Chapter 3.2.2). The only difference is that the images formed here are re-smoothed to a common beam size ($210'' \times 50''$ for J094750−371528 and $70'' \times 55''$ for J224549+394122) for each source. This step is necessary for the derivation of spectral index and FD maps in the following.

With the smoothed 4 MHz channel images of J094750−371528 and J224549+394122, we generated maps of Stokes I total intensity at 1.4 GHz ($S_{1.4\,\mathrm{GHz}}$) and spectral index (α_L) by fitting simple power law to each individual pixels in the maps:

$$S_\nu = S_{1.4\,\mathrm{GHz}} \cdot \left(\frac{\nu}{1.4\,\mathrm{GHz}}\right)^{\alpha_\mathrm{L}}, \tag{B.1}$$

where ν represents the observed frequency. Only pixels where the Stokes I values are larger than 6σ in all channels are fitted. In addition, we performed RM-Synthesis for each pixel as per Chapter 3.3.1. The maps of number of polarised components (N Comp.), as well as that of p, FD, and FWHM of the strongest polarised component, were created. All of the above-mentioned maps, along with their uncertainties (if applicable) are presented in Figures B.1 (for J094750−371528) and B.2 (for J224549+394122). We do not show the maps of the weaker polarised component(s), since for all cases here the secondary component is weak and can be artefacts in the Faraday spectra instead of real signals. Nonetheless, we report here the most significant secondary components for both sources. For J094750−371528, there are two pixels within the northern component of the source where secondary polarised components is seen, which has $p \approx 0.8$ per cent, $\phi \approx +502\,\mathrm{rad\,m^{-2}}$, and $\mathrm{PA}_0 \approx -36°$, while for J224549+394122, there is a finger-like patch of secondary component to the south from the eastern jet. This patch has $p \approx 0.2$ per cent, $\phi \approx -416\,\mathrm{rad\,m^{-2}}$, and $\mathrm{PA}_0 \approx +80°$.

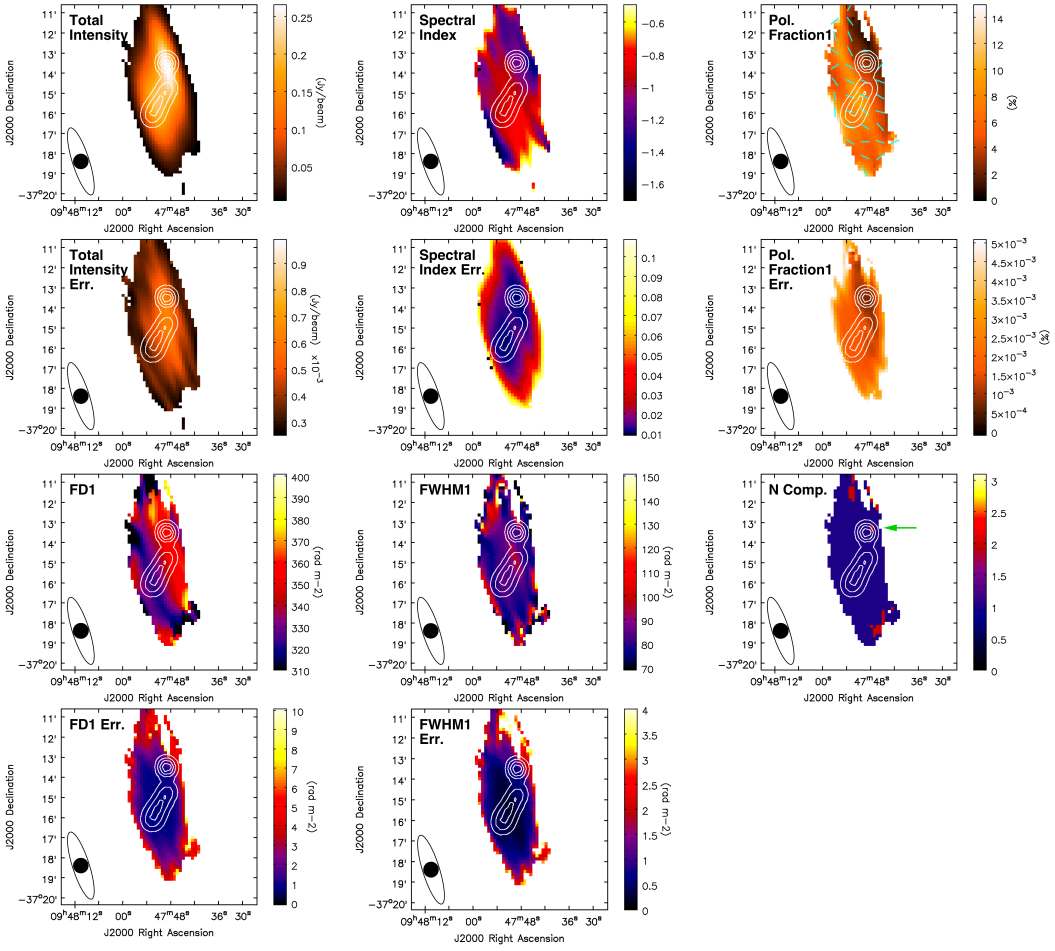

Figure B.1: Images of J094750−371528, with their associated uncertainties. Only pixels where the Stokes I values are greater than 6σ in all of the individual channels are shown. The white contours represent NVSS Stokes I map at $[0.2, 0.4, 0.6, 0.8] \times 188.6\,\mathrm{mJy\,beam^{-1}}$. The beam sizes of the maps are shown in the lower left of each panel, with the open and filled ellipses representing that of our new observation and NVSS, respectively. We also plot the intrinsic polarisation B-orientations ($B_0 = E_0 + 90°$; corrected for Faraday rotation) in the polarisation fraction panel as cyan lines. The green arrow in the "N Comp." panel points to the region with a marginal detection of a secondary polarised component as discussed in text.

The polarisation maps we obtained here allow us to make interesting comparisons with our results from the main text, where we used flux integration regions for analysis, which discarded all spatial information of these two sources. We note that J094750−371528 is mostly Faraday thin over the entire spatial extent (i.e. $\mathrm{FWHM_1} \approx \mathrm{FWHM_0} = 77\,\mathrm{rad\,m^{-2}}$). There is also a significant FD gradient from southeast ($\approx +320\,\mathrm{rad\,m^{-2}}$) to northwest ($\approx +350\,\mathrm{rad\,m^{-2}}$). This source was found to be Faraday thick in both our RM-Synthesis and QU-fitting results. The analysis here shows that the Faraday thickness is caused by spatial variations of FD across the

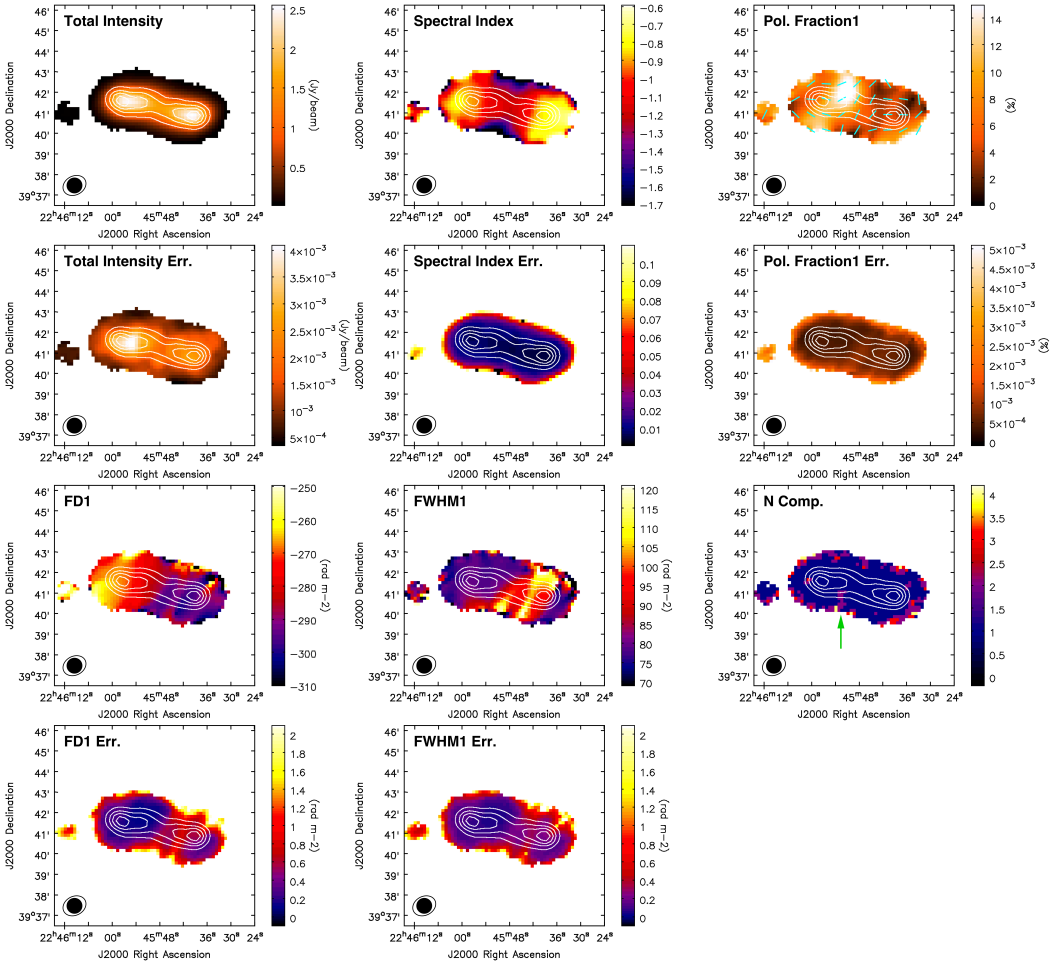

Figure B.2: Same as Figure B.1, for J224549+394122. The white contours here represent NVSS Stokes I map at $[0.2, 0.4, 0.6, 0.8] \times 1823.0\,\mathrm{mJy\,beam^{-1}}$, and the green arrow in the "N Comp." panel points to the finger-like patch with a marginal detection of a secondary polarised component as discussed in text.

sky plane (i.e. side-to-side variations in FD), but not due to Faraday rotation within the synchrotron-emitting medium (i.e. back-to-front changes in FD). The polarisation maps of J224549+394122 show much richer structures. First, we notice a bright blob in polarisation map where $p \approx 17$ per cent, which coincides spatially with a knot-like structure in the radio jet seen from Harwood et al. (2017). Second, there is an FD gradient from east ($\approx -270\,\mathrm{rad\,m^{-2}}$) to west ($\approx -300\,\mathrm{rad\,m^{-2}}$), with an FD filament with $\phi \approx -290\,\mathrm{rad\,m^{-2}}$ in the western part of the source. On this filament we also find a lower $p \approx 4$ per cent and wider $\mathrm{FWHM_1} \approx 100\,\mathrm{rad\,m^{-2}}$ than the surroundings. Similar structures in RM maps were also seen in other systems (e.g. 3C 270, 3C 353, 4C 35.03, and M84), with those "RM-bands" having differences in RM from the off-band regions of ≈ 10–$50\,\mathrm{rad\,m^{-2}}$ (Guidetti et al. 2011).

Table B.1: Comparison between RM-Synthesis and QU-fitting Results

Source (NVSS)	RM-Synthesis Results	QU-fitting Results
Sources with Differing Results		
J022915+085125	Thick	Double
J092410−290606a	Thin	Double
J092410−290606b	Thin	Thick
J093349−302700	Thin	Thick
J162706−091705b	Thin	Double
J163927−124139b	Thin	Thick
J170934−172853	Double	Double Thick
J224412+405715	Thin	Thick
J224549+394122	Double Thick	Thick
J235728+230226	Thin	Double
Sources with Agreeing Results		
J083930−240723	Thin	
J084701−233701	Thin	
J090015−281758	Thin	
J091145−301305a	Thin	
J091145−301305b	Thin	
J093544−322845a	Thin	
J093544−322845b	Thin	
J094750−371528	Thick	
J094808−344010	Double	
J111857+123442	Double	
J154936+183500	Triple	
J163927−124139a	Thin	
J190255+315942	Double	
J220205+394913	Thin	
J220927+415834	Thin	

B.2 Comparison between RM-Synthesis and QU-fitting Results

We have presented in Chapters 3.3.1 and 3.3.2 the results from RM-Synthesis and QU-fitting, respectively, and noted the discrepant results for several of our target sources from the two analysis methods. This allows comparisons of the two algorithms for the study of polarised EGSs in the frequency range of 1–2 GHz.

We have divided our RM-Synthesis and QU-fitting results into five classes — thin, double, triple, thick, and double thick. The former three corresponds to one, two, and three unresolved polarised components in RM-Synthesis, and 1T, 2T, and 3T models in QU-fitting, respectively, while the latter two (thick and double thick) maps to single

and double resolved polarised components in RM-Synthesis, and 1B, 1B+fg, 1Ed, 1Id, or 1Id+fg for thick, and 2B or 2B+fg for double thick in QU-fitting, respectively. We then compared if the two algorithms agreed on the source class, with the results listed in Table B.1. Out of the 25 polarised sources in our sample (spatial doubles are counted as two distinct sources), 15 have agreeing results, while 10 are categorised into different classes. Further studies of these sources at a wider λ^2 coverage are needed to determine whether RM-Synthesis or QU-fitting are more reliable in uncovering the Faraday complexities of these sources correctly (Ma et al. in prep). Nonetheless, we note that when RM-Synthesis identifies a source as Faraday complex, it is definitely so in QU-fitting, but the converse is not true.

B.3 Stokes QU-fitting Results

We include here plots of the QU-fitting results in Figure B.3. Plots of Stokes $q = Q/I$ and $u = U/I$, along with polarisation fraction (p) and polarisation position angle (PA) are shown.

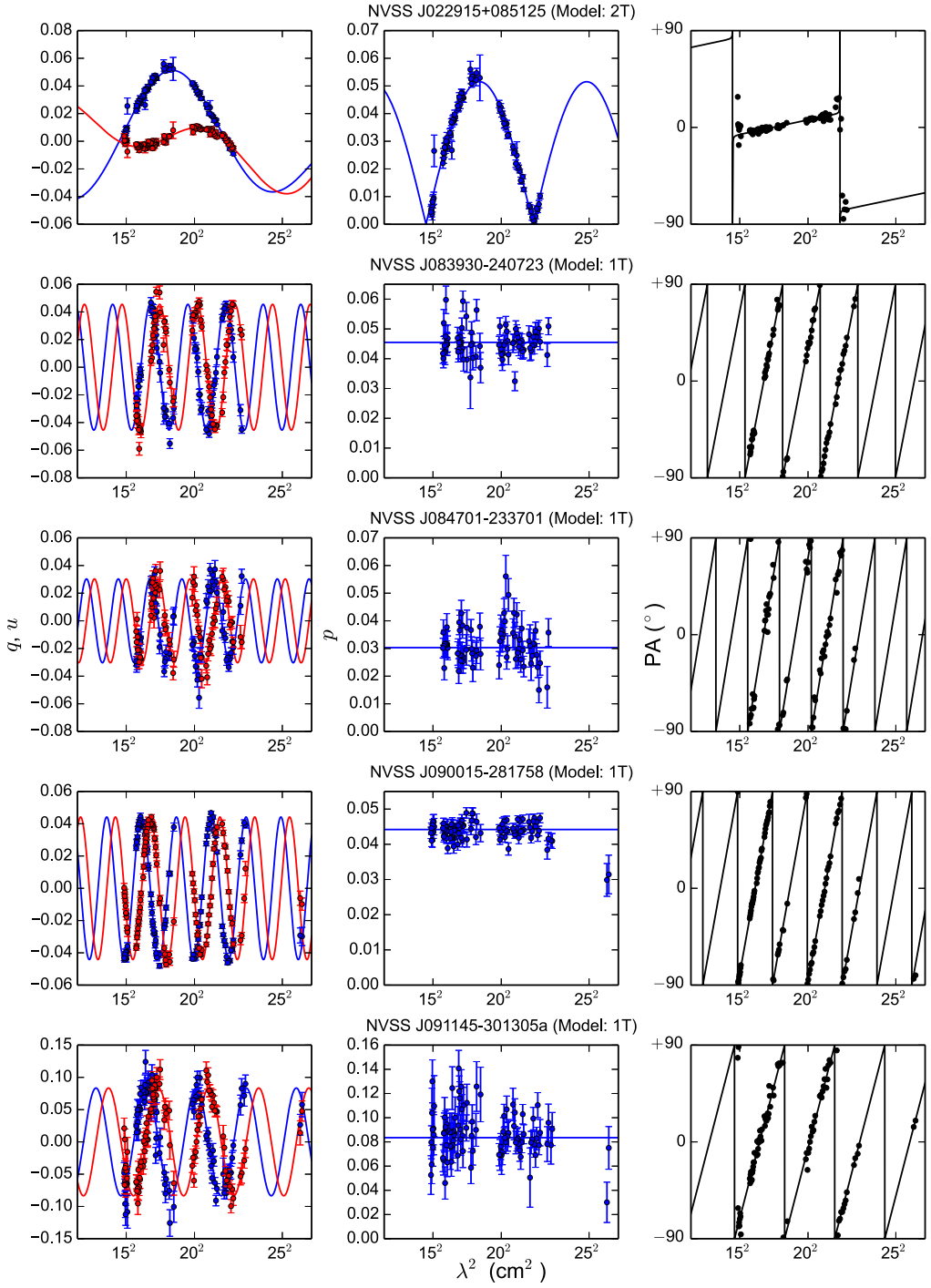

Figure B.3: QU-fitting results of our polarised target sources, showing the best-fit model from our analysis. Each source spans one of the rows in the figure. The Stokes $q = Q/I$ and $u = U/I$ values are plotted in the left column in blue and red respectively, with polarisation fraction (p) shown in the middle column, and PA in the right column. Note that the error bars in PA are not shown here.

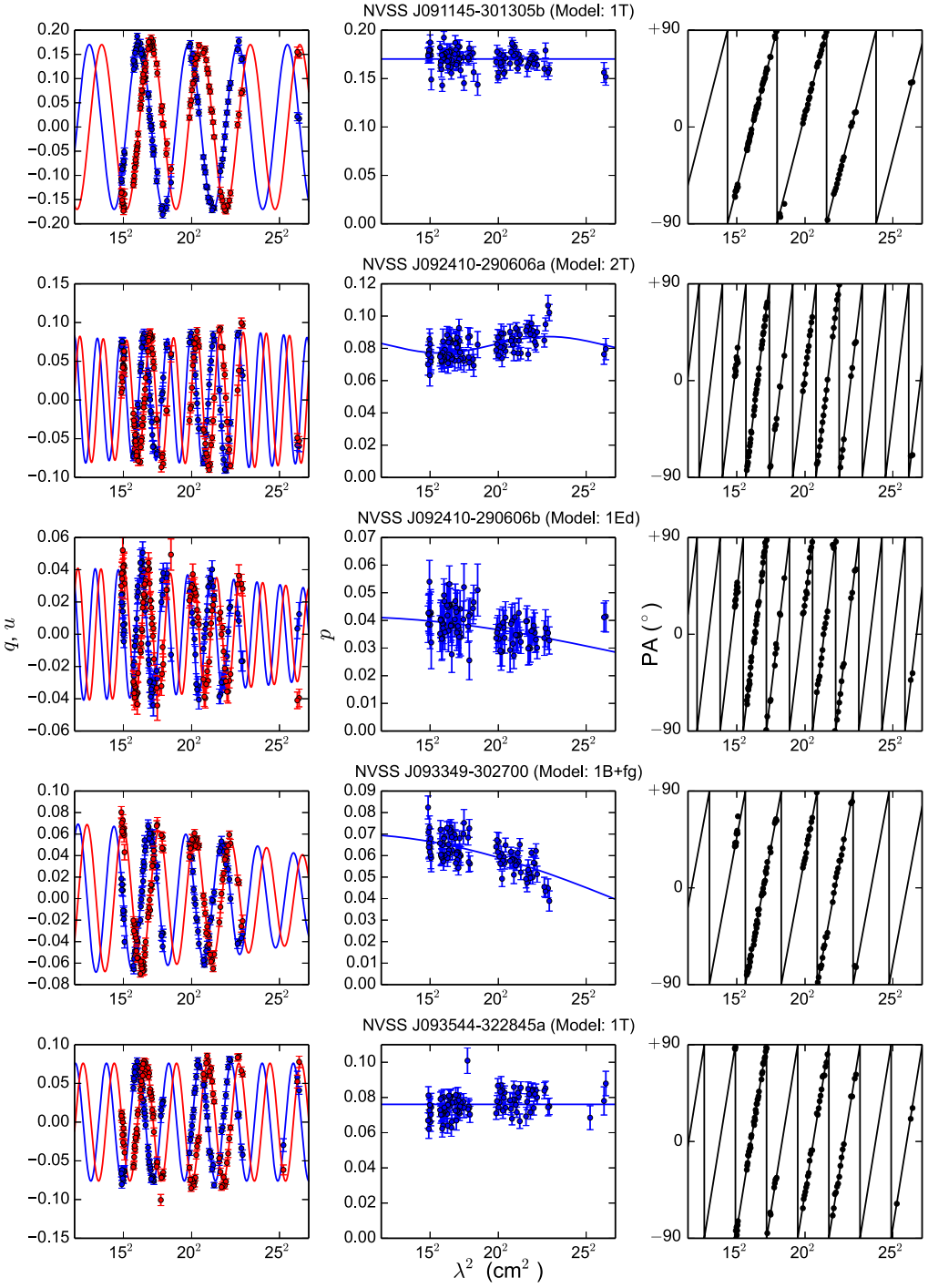

Figure B.3: (Continued) QU-fitting results of our polarised target sources.

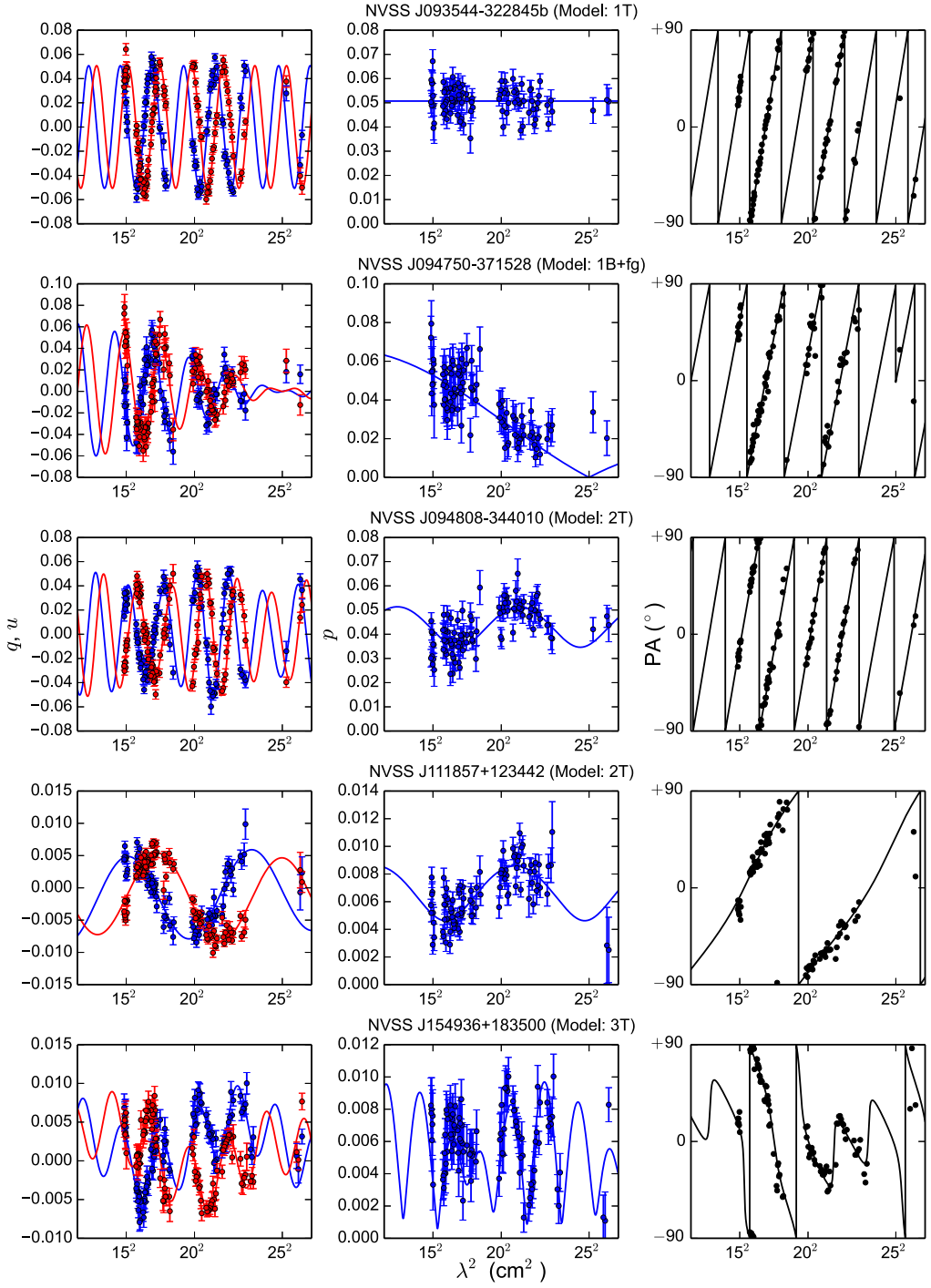

Figure B.3: (Continued) QU-fitting results of our polarised target sources.

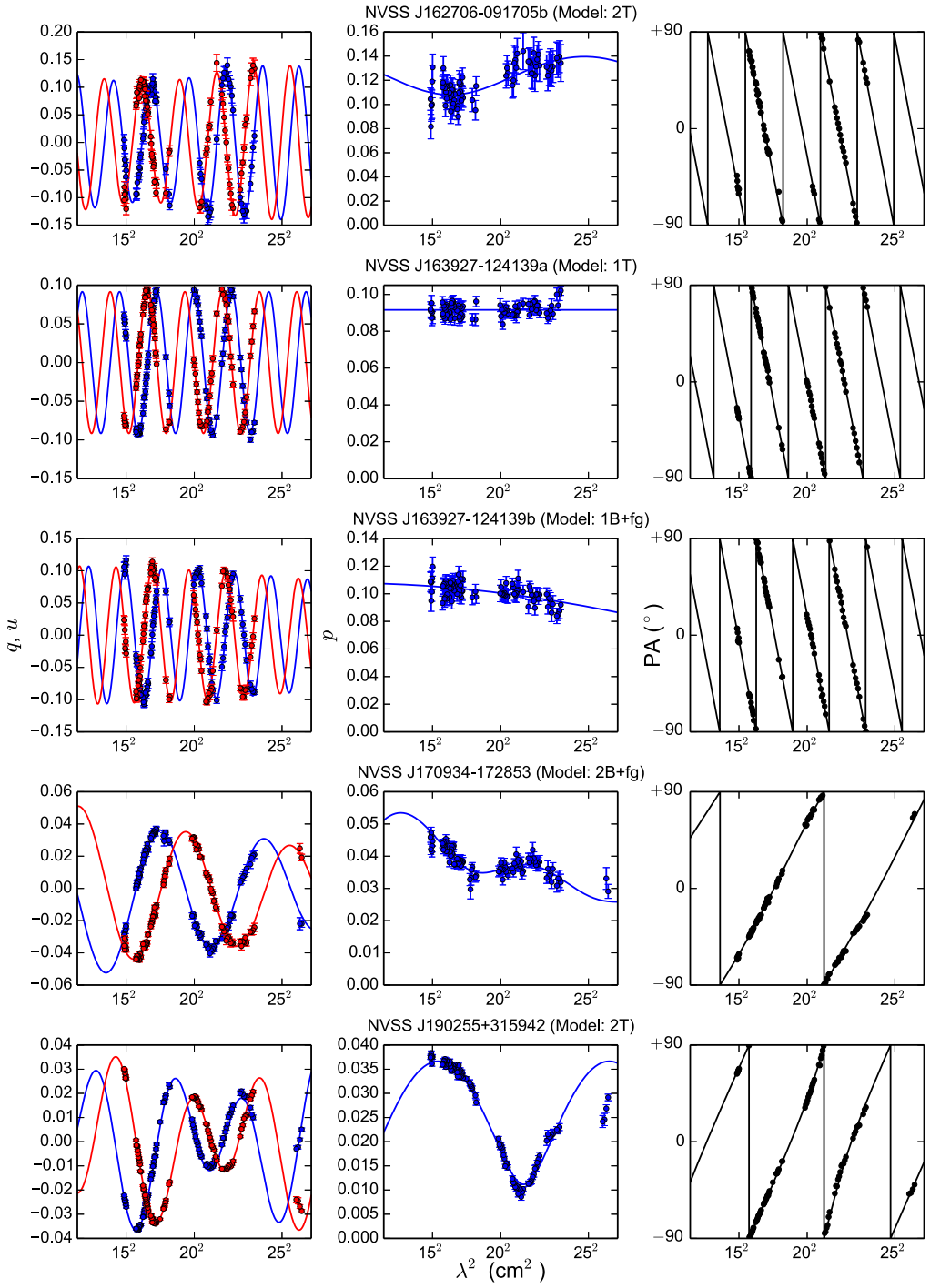

Figure B.3: (Continued) QU-fitting results of our polarised target sources.

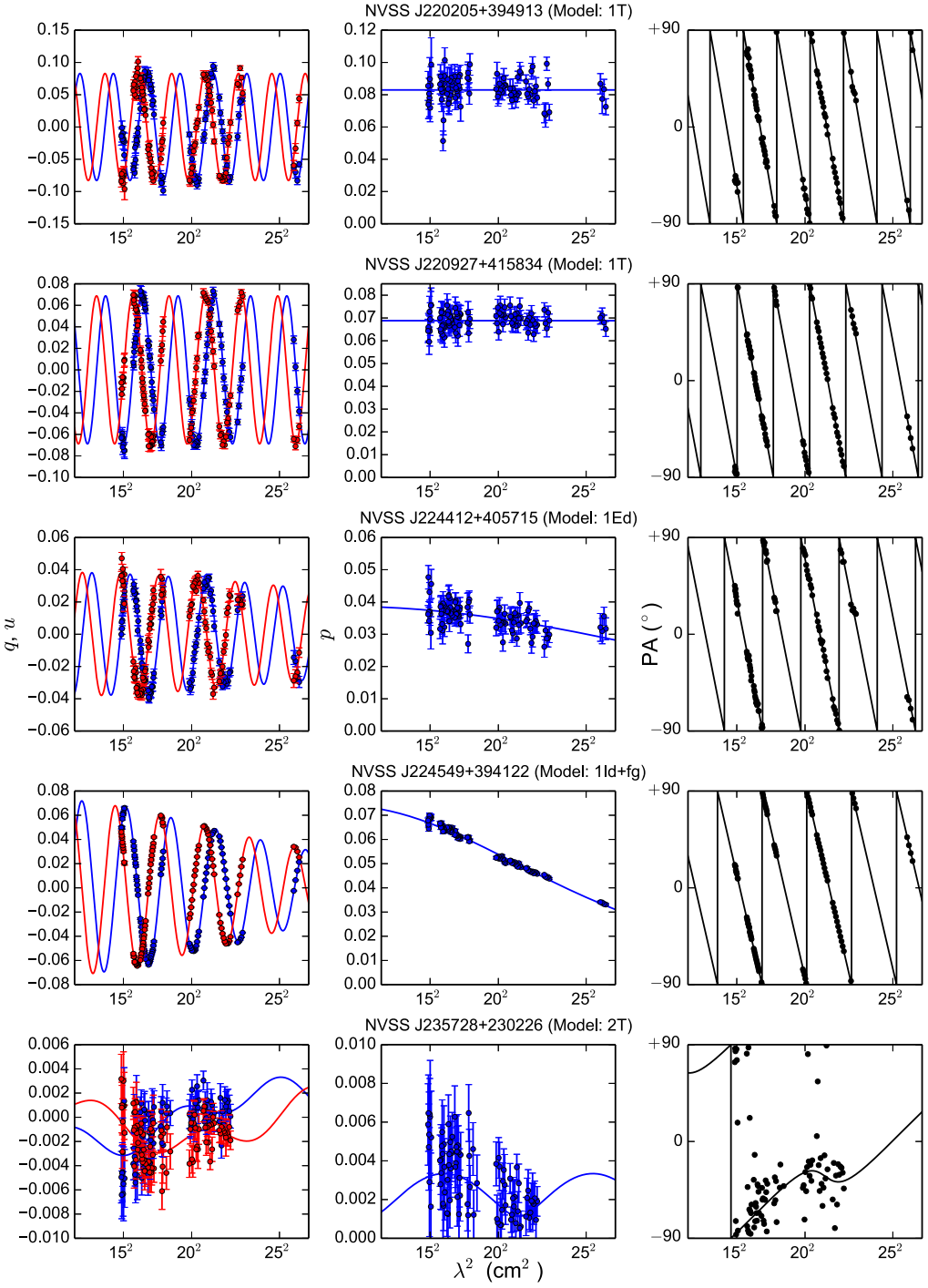

Figure B.3: (Continued) QU-fitting results of our polarised target sources.

Appendix C

Additional Materials to Chapter 4

I include here some additional materials to my work presented in Chapter 4. Both Appendices C.1 and C.2 form the appendix of the original publication.

C.1 Radio Spectra of Our Targets

We show the radio spectra of our target sources in Figure C.1. A simple power law is fitted to our broadband Jansky VLA data (from Chapter 3). For sources identified as spatial doubles, we fitted each component individually, as well as their sum (with uncertainties added in quadrature). The best-fit parameters are listed in Table 4.2.

C.2 The Role of $\mathrm{PA_{leak}}$

We further investigate here the effects of off-axis polarisation leakage in Chapter 4.5.3. Specifically, we aim to understand the cause of the asymmetric double-horn ($\mathrm{RM_{src}} - \mathrm{RM_{obs}}$) distributions seen in Figures 4.6 and 4.7. To achieve this, we repeated our simulation with the artificial sources, again with the TSS09 source properties of J091145−301305 ($S_{\mathrm{NVSS}} = 247.1\,\mathrm{mJy}$ and $\mathrm{PI} = 21.1\,\mathrm{mJy}$, as the strongly polarised case), J093349−302700 ($S_{\mathrm{NVSS}} = 272.9\,\mathrm{mJy}$ and $\mathrm{PI} = 10.3\,\mathrm{mJy}$, as the intermediately polarised case), and J235728+230226 ($S_{\mathrm{NVSS}} = 624.6\,\mathrm{mJy}$ and $\mathrm{PI} = 5.0\,\mathrm{mJy}$, as the weakly polarised case). For each case, we manually selected $\mathrm{RM_{src}}$ values of 0, +150, +300, +450, and $+600\,\mathrm{rad\,m^{-2}}$. However, instead of randomising $\mathrm{PA_0}$ and $\mathrm{PA_{leak}}$ as we did in Chapter 4.5.3, here we chose $\mathrm{PA_0}$ for each artificial source such that the source PA in the NVSS IF1 is 0°, and $\mathrm{PA_{leak}}$ is uniformly sampled within $[-\pi/2, +\pi/2]$ to see its effect on ($\mathrm{RM_{src}} - \mathrm{RM_{obs}}$). The results of this are presented in Figures C.2 and C.3, with the former showing the trend of ($\mathrm{RM_{src}} - \mathrm{RM_{obs}}$) and the latter showing that of $(\mathrm{PI_{src}} - \mathrm{PI_{obs}})/S_{\mathrm{NVSS}}$. By consulting these Figures, we can pinpoint the situations (in terms of the relative PA between the source and leakage vectors) that resulted in the double horn.

From Figure C.2, we can see that ($\mathrm{RM_{src}} - \mathrm{RM_{obs}}$) shows a nearly sinusoidal variation across $\mathrm{PA_{leak}}$, with the peaks and troughs corresponding to the two horns in Figures 4.6 and 4.7. For the strongly and intermediately polarised cases, the widths of the peaks and troughs are very similar, leading to the symmetric ($\mathrm{RM_{src}} - \mathrm{RM_{obs}}$) distributions. On the other hand, for the weakly polarised case the differences in the widths of the peaks compared to that of the troughs are much more apparent. This in turn leads to the extreme asymmetry in the double horns — the wider (or nar-

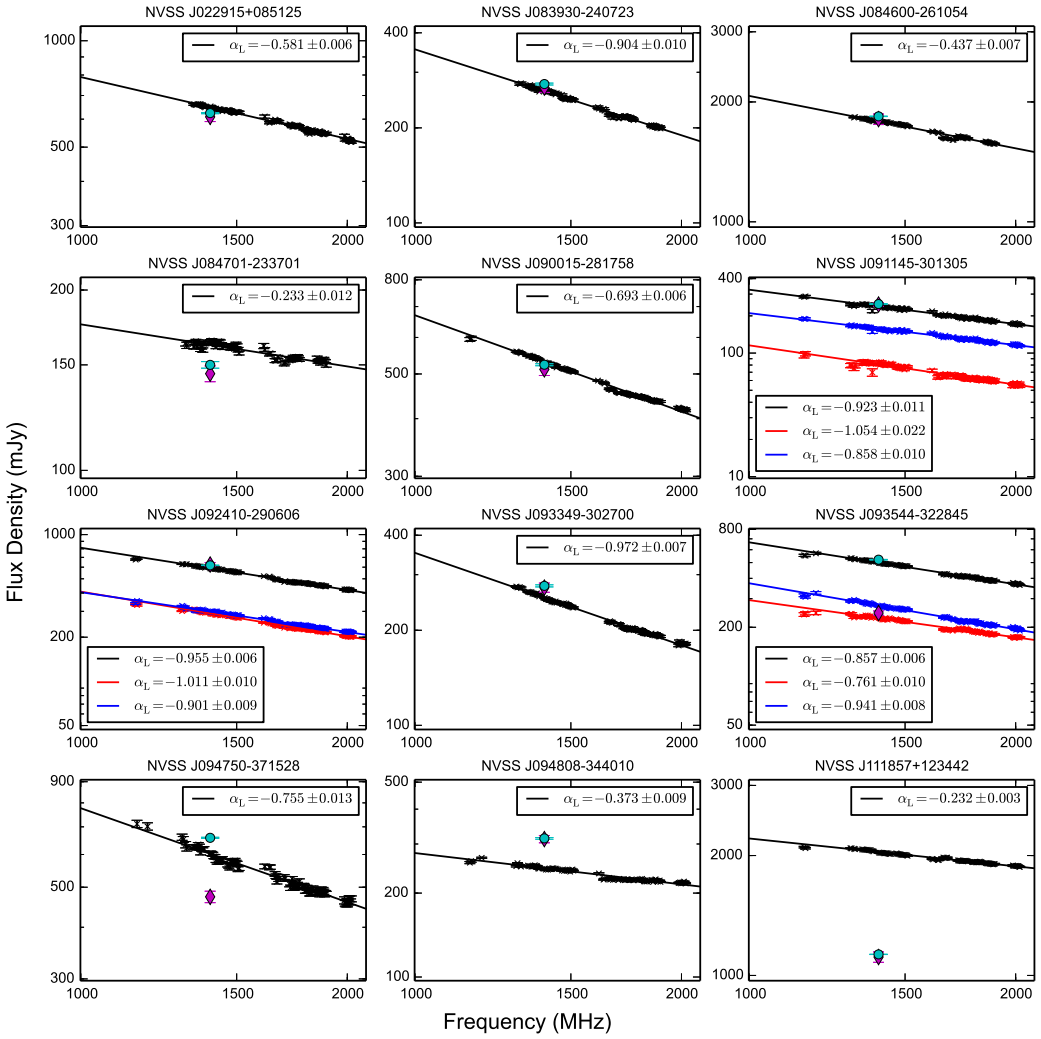

Figure C.1: Radio spectra across L-band of our target sources from the new Jansky VLA observations. The total flux densities are represented by black data points. For sources that are resolved into two spatial components, the flux densities of the individual components are plotted in red (component a) and blue (component b). The best-fit power law spectra ($S_\nu \propto \nu^{\alpha_L}$) are shown as solid lines with corresponding colours to the data points. The flux densities we determined from NVSS cutout images ($S_{\rm cutout}$) are plotted as the cyan circles, while that listed in the NVSS catalogue ($S_{\rm NVSS}$; Condon et al. 1998) are plotted as the magenta diamonds.

rower) part in ($\rm RM_{src} - RM_{obs}$) against $\rm PA_{leak}$ (Figure C.2) corresponds to the taller (or shorter) of the double horn of the histogram in Figures 4.6 and 4.7.

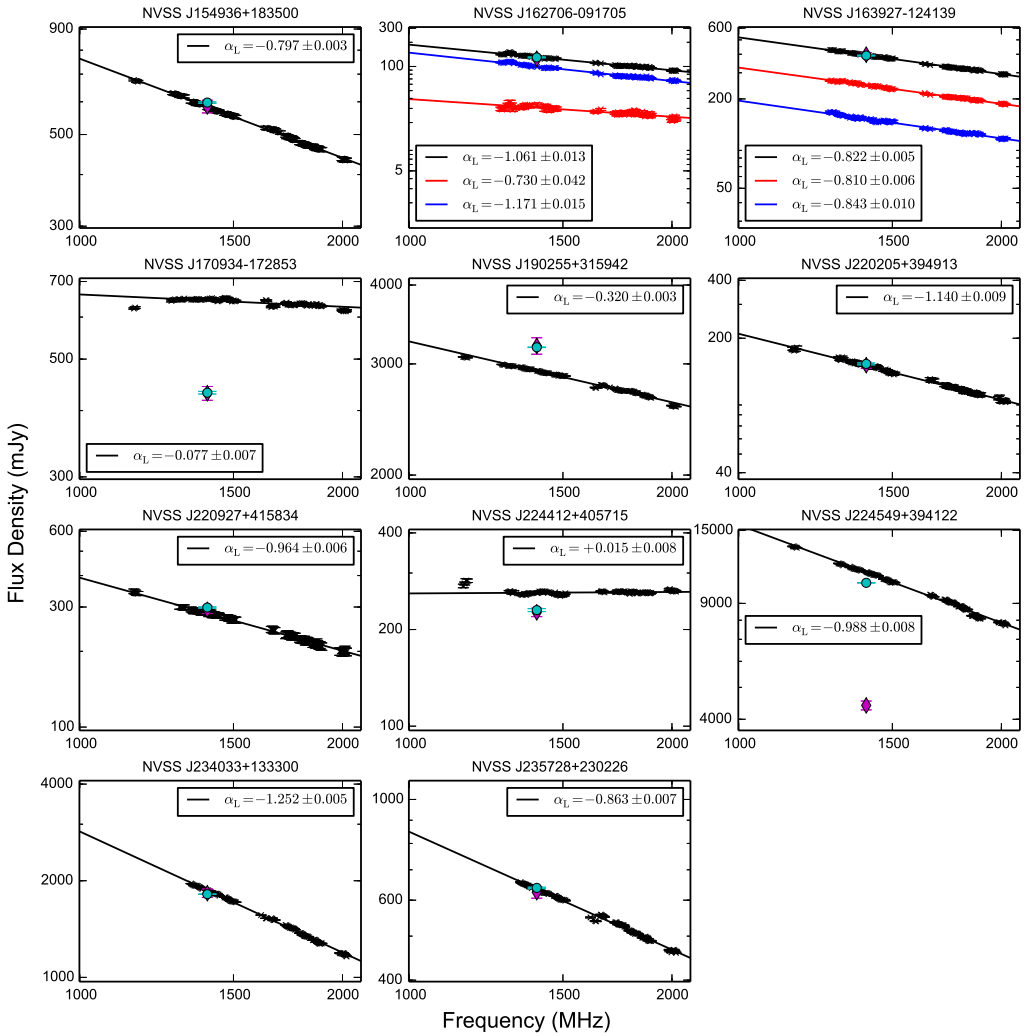

Figure C.1: (Continued) Radio spectra of our target sources from new Jansky VLA observations.

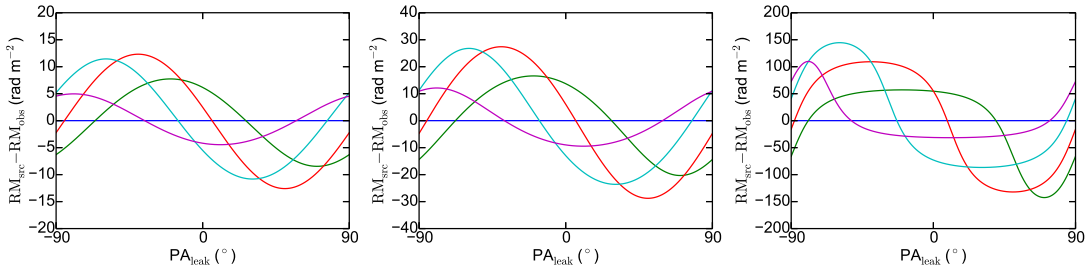

Figure C.2: Simulation results showing the relationship between $(\mathrm{RM_{src}} - \mathrm{RM_{obs}})$ and $\mathrm{PA_{leak}}$. The left, middle, and right panels show the cases where the artificial target sources are strongly ($p = 8.5$ per cent), intermediately ($p = 3.8$ per cent), and weakly ($p = 0.8$ per cent) polarised, respectively. The artificial sources with $\mathrm{RM_{in}}$ of 0, +150, +300, +450, and +600 rad m^{-2} are shown as the blue, green, red, cyan, and magenta lines, respectively. The input $\mathrm{PA_0}$ has been chosen such that the true PA at the NVSS IF1 is 0°. Note that the y-axis scales are different among the panels.

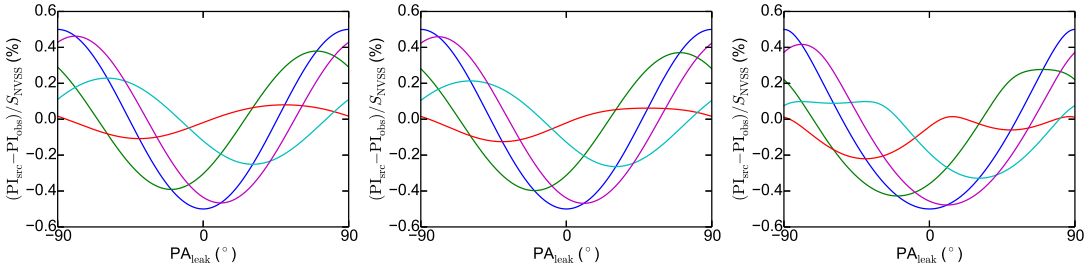

Figure C.3: Simulation results similar to those in Figure C.2, but showing $(\mathrm{PI_{src}} - \mathrm{PI_{obs}})/S_{\mathrm{NVSS}}$ instead as the y-axis.

Appendix D

Faraday Spectra from Chapter 5

I present here the Faraday spectra of the target sources observed for the study in Chapter 5. The spectra for on-axis targets are shown in Figure D.1, and those for off-axis targets are shown in Figure D.2. The results from this RM-Synthesis analysis are listed in Table 5.4.

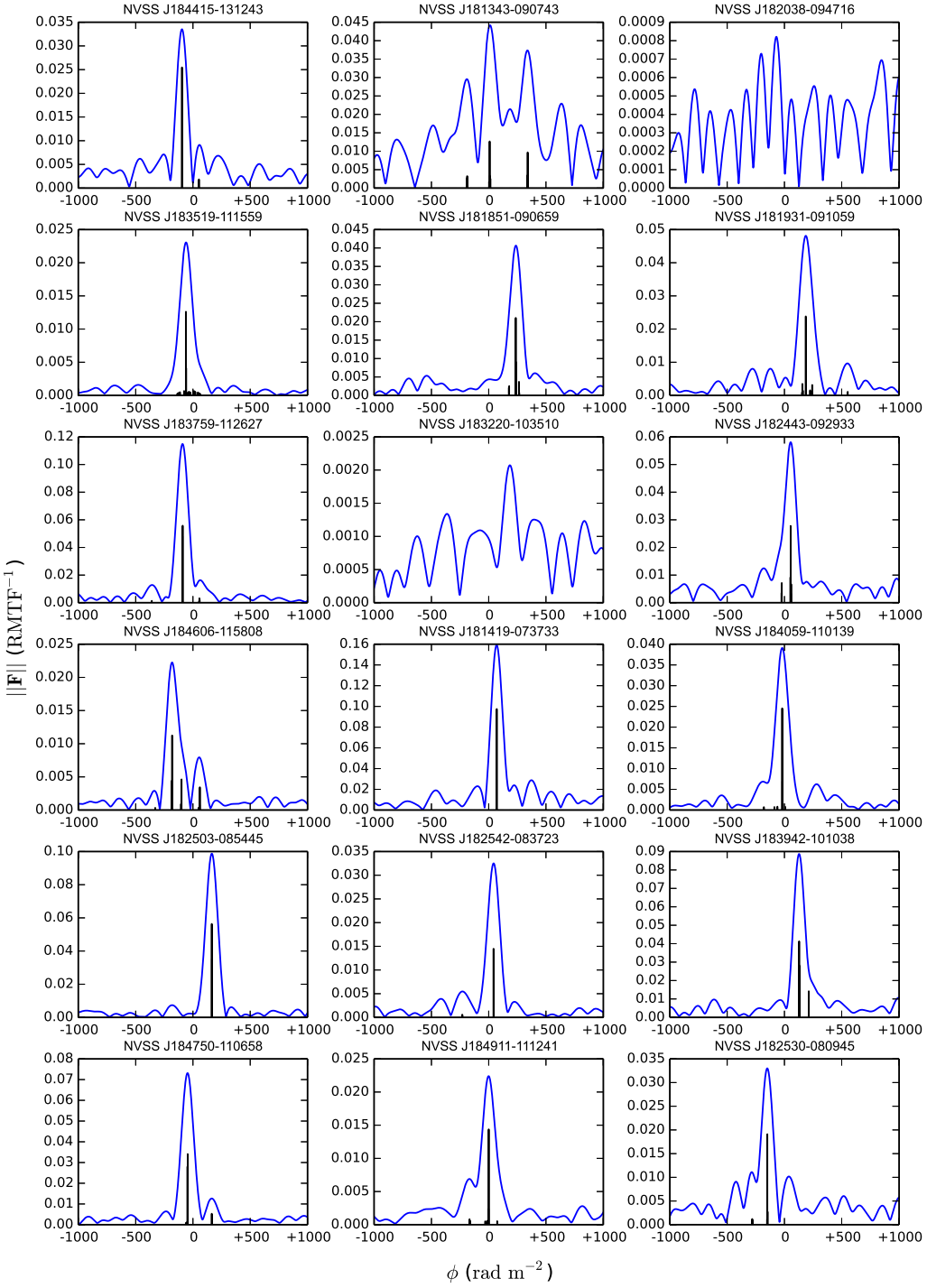

Figure D.1: Faraday spectra of the on-axis target sources, sorted by the Galactic longitude. Blue lines show the amplitudes of the deconvolved Faraday spectra, with the black bars showing the clean components.

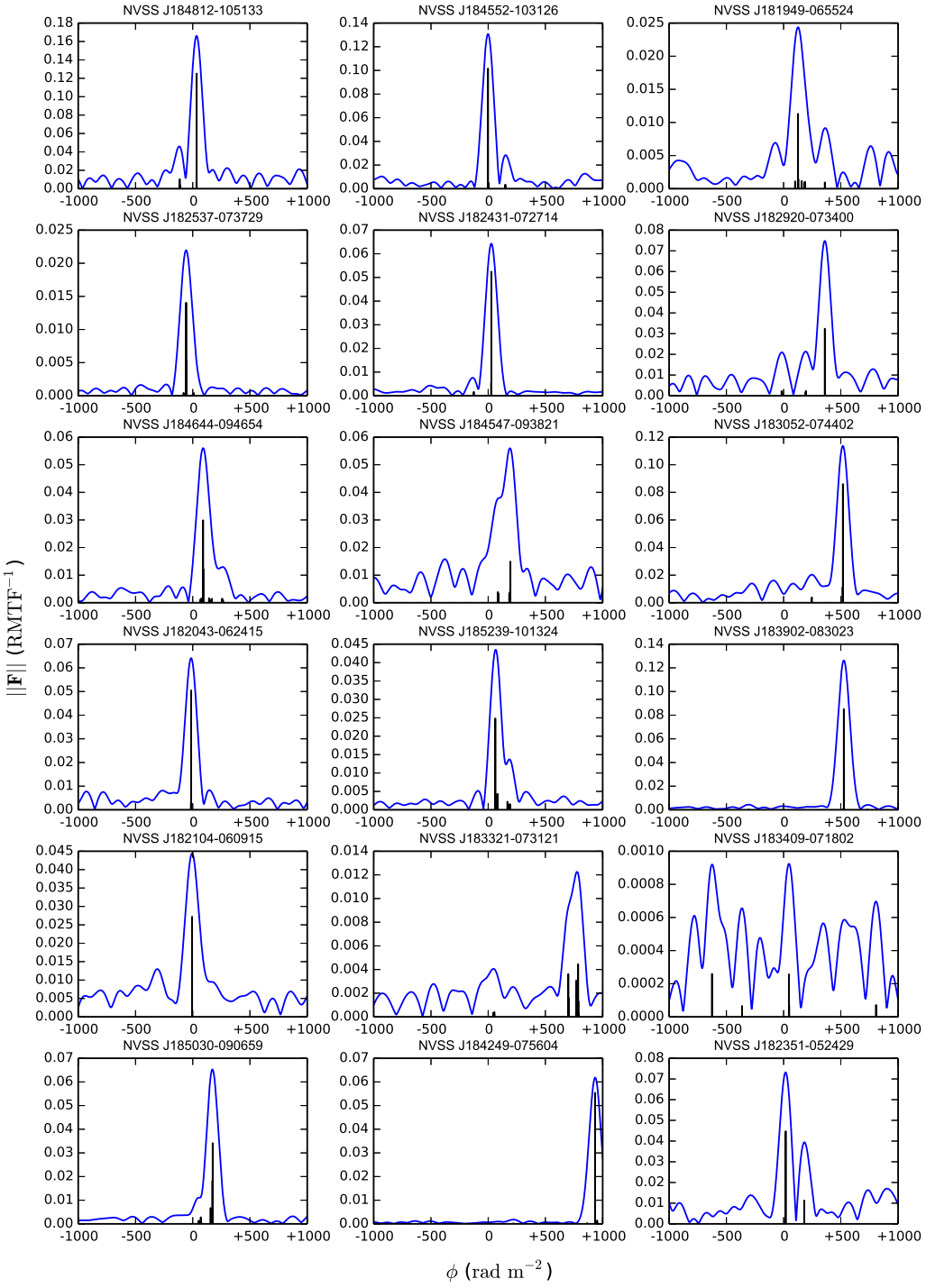

Figure D.1: (Continued) Faraday spectra of the on-axis target sources, sorted by the Galactic longitude.

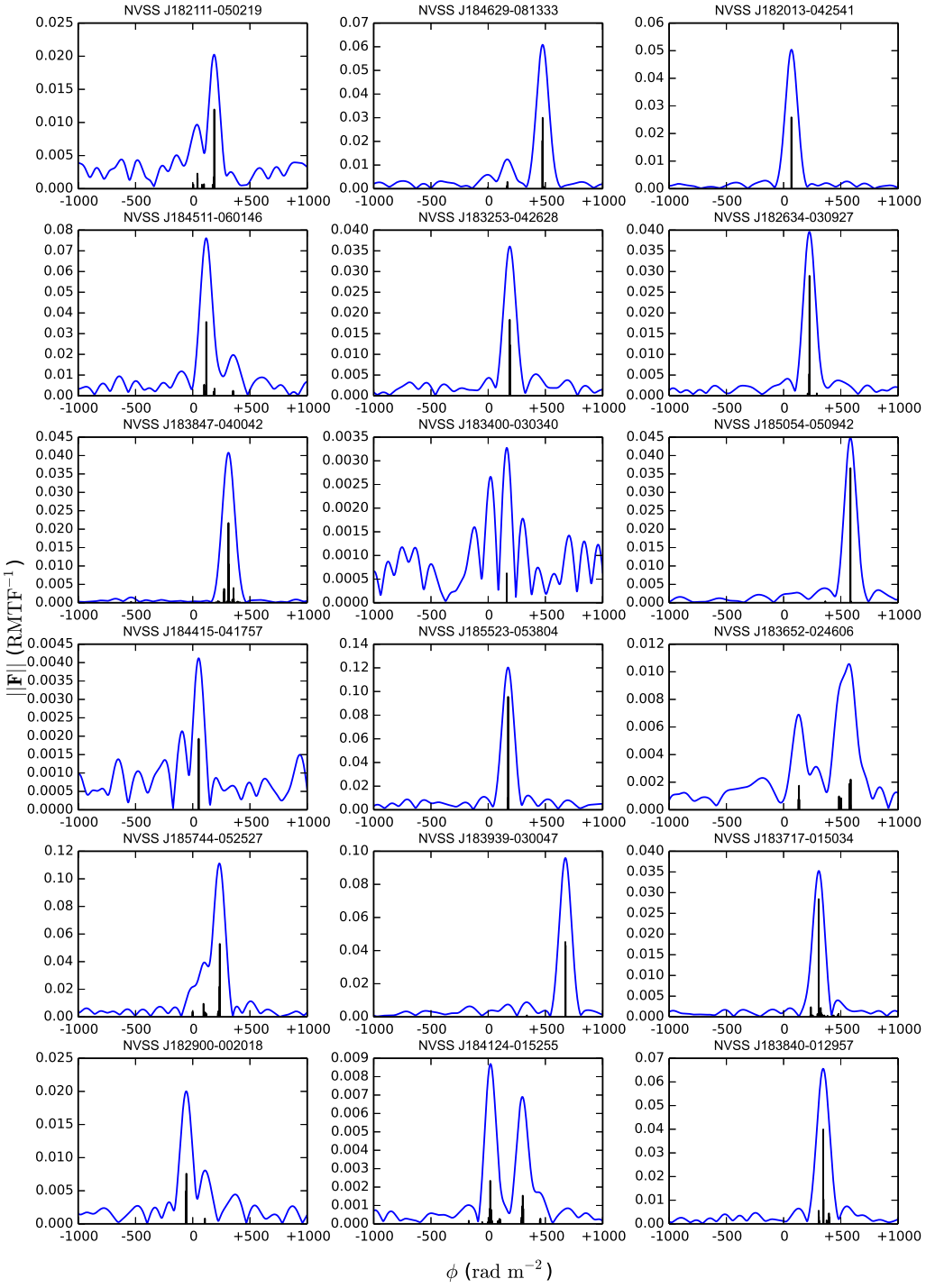

Figure D.1: (Continued) Faraday spectra of the on-axis target sources, sorted by the Galactic longitude.

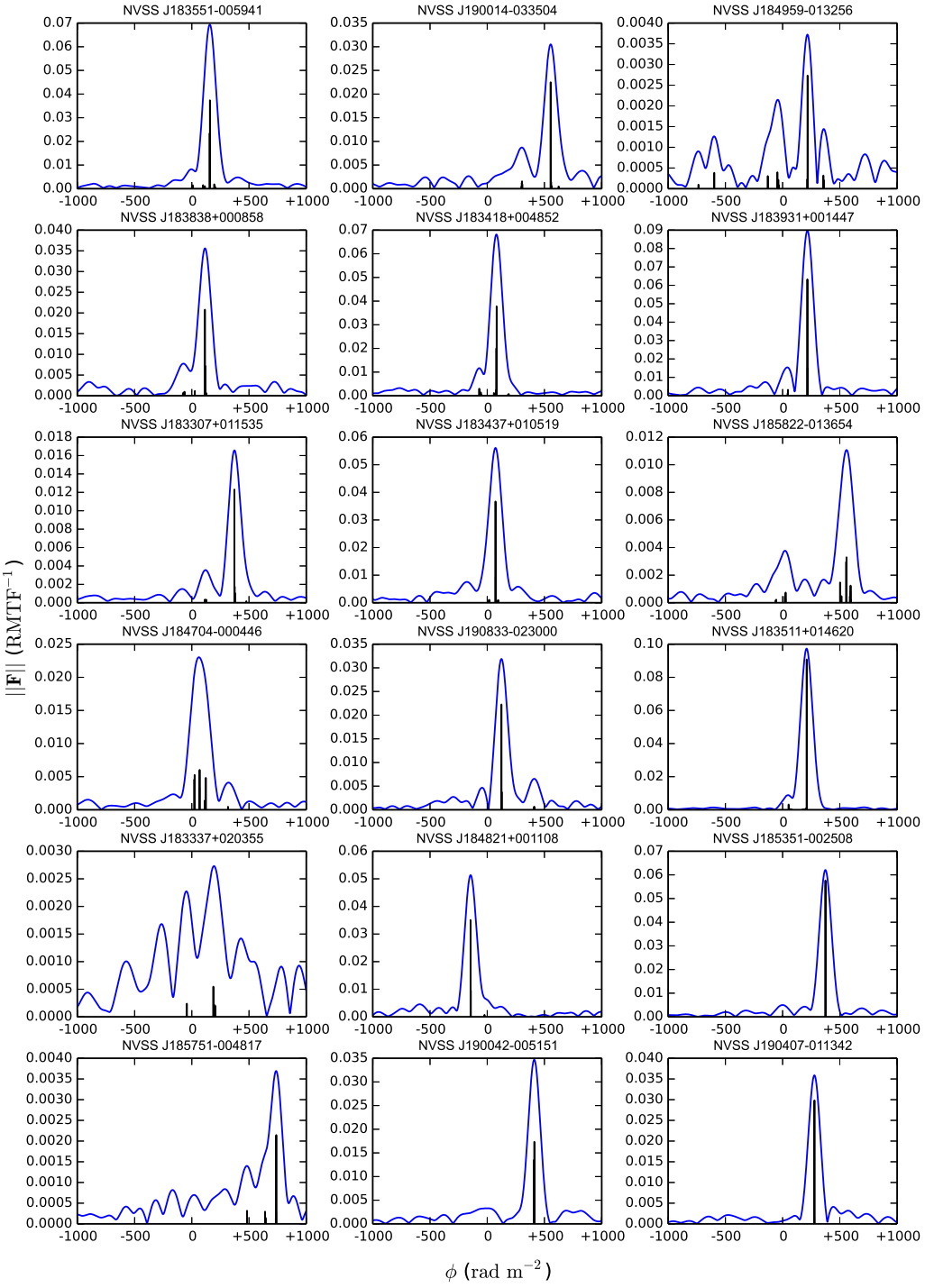

Figure D.1: (Continued) Faraday spectra of the on-axis target sources, sorted by the Galactic longitude.

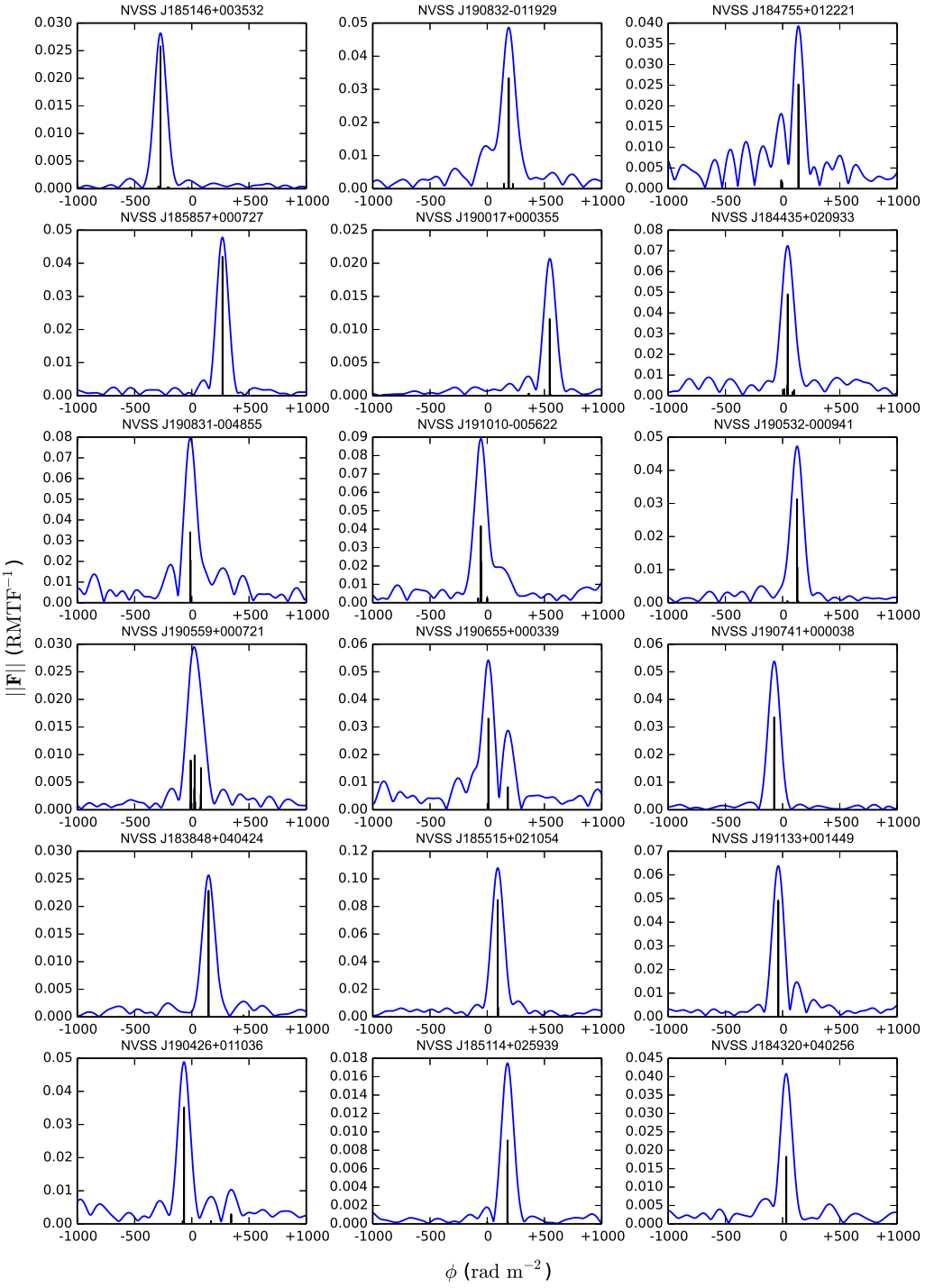

Figure D.1: (Continued) Faraday spectra of the on-axis target sources, sorted by the Galactic longitude.

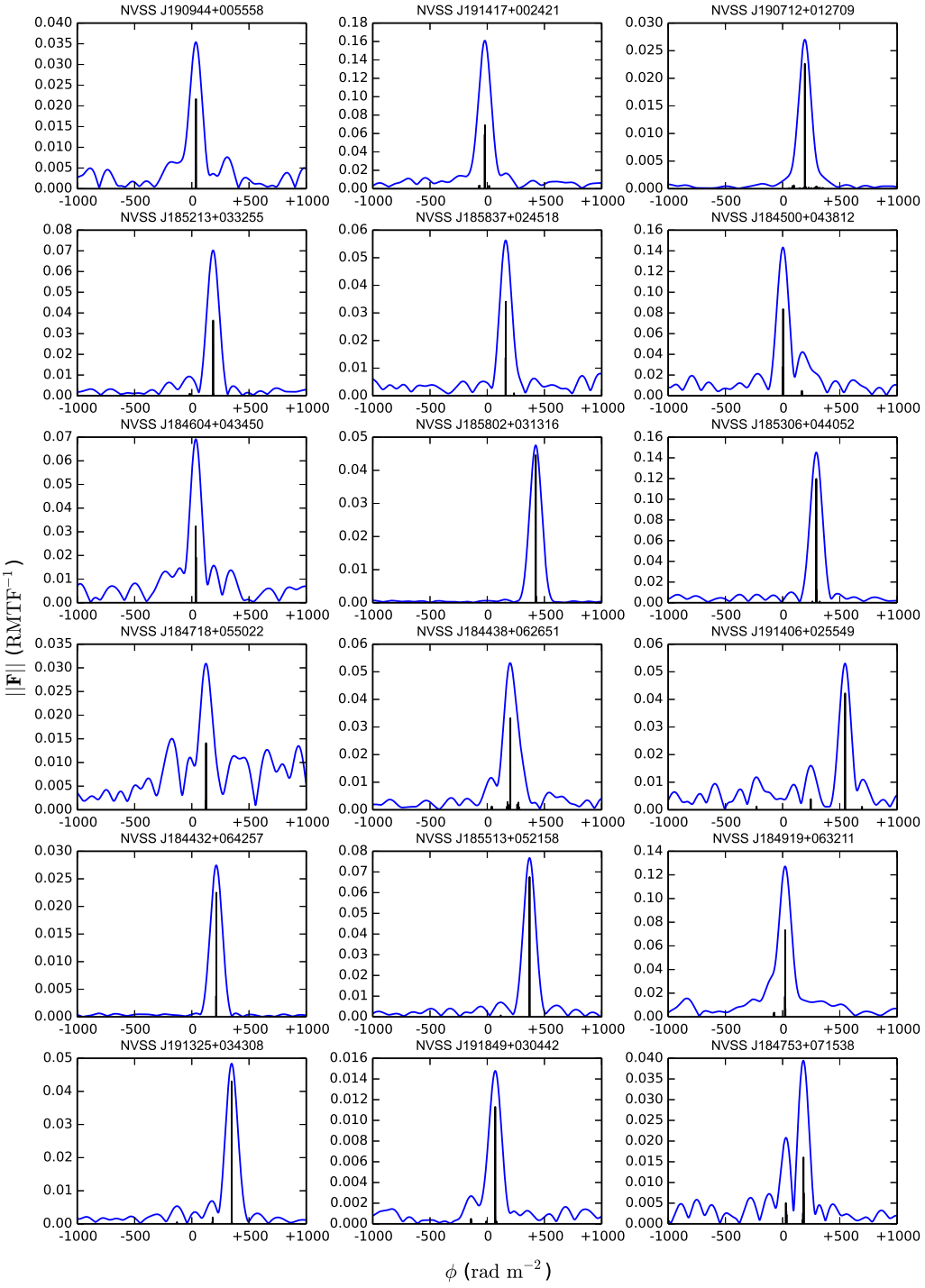

Figure D.1: (Continued) Faraday spectra of the on-axis target sources, sorted by the Galactic longitude.

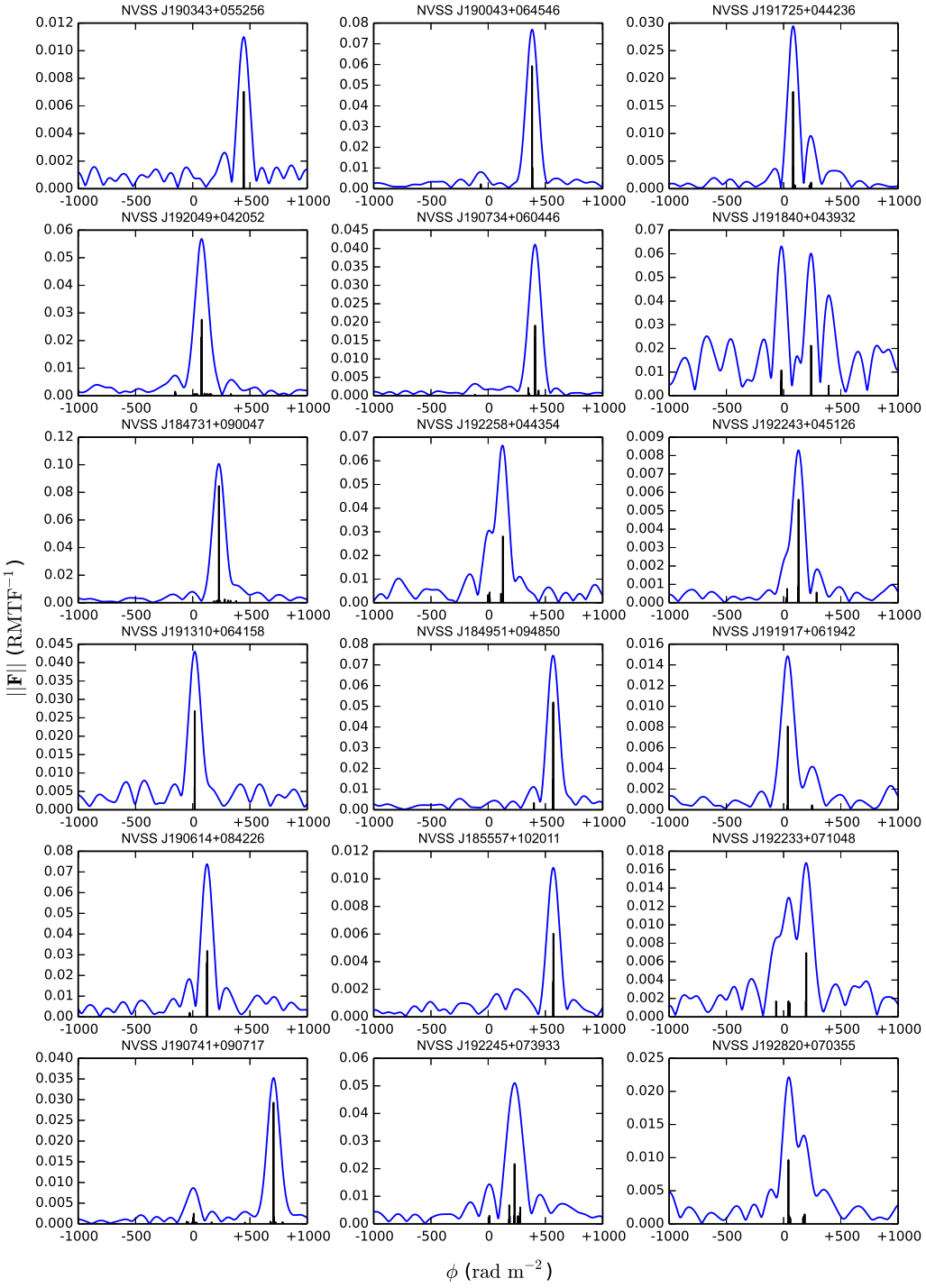

Figure D.1: (Continued) Faraday spectra of the on-axis target sources, sorted by the Galactic longitude.

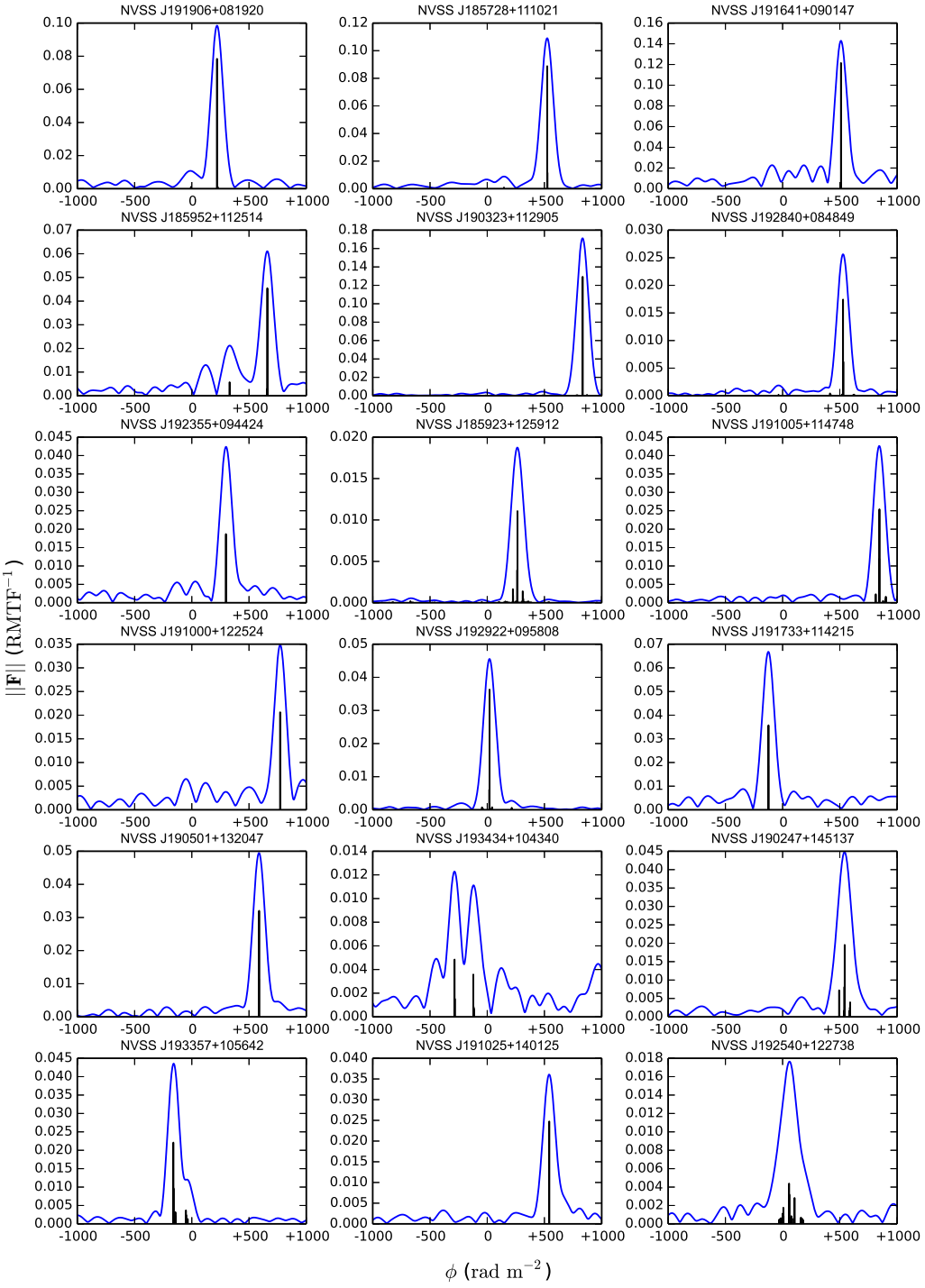

Figure D.1: (Continued) Faraday spectra of the on-axis target sources, sorted by the Galactic longitude.

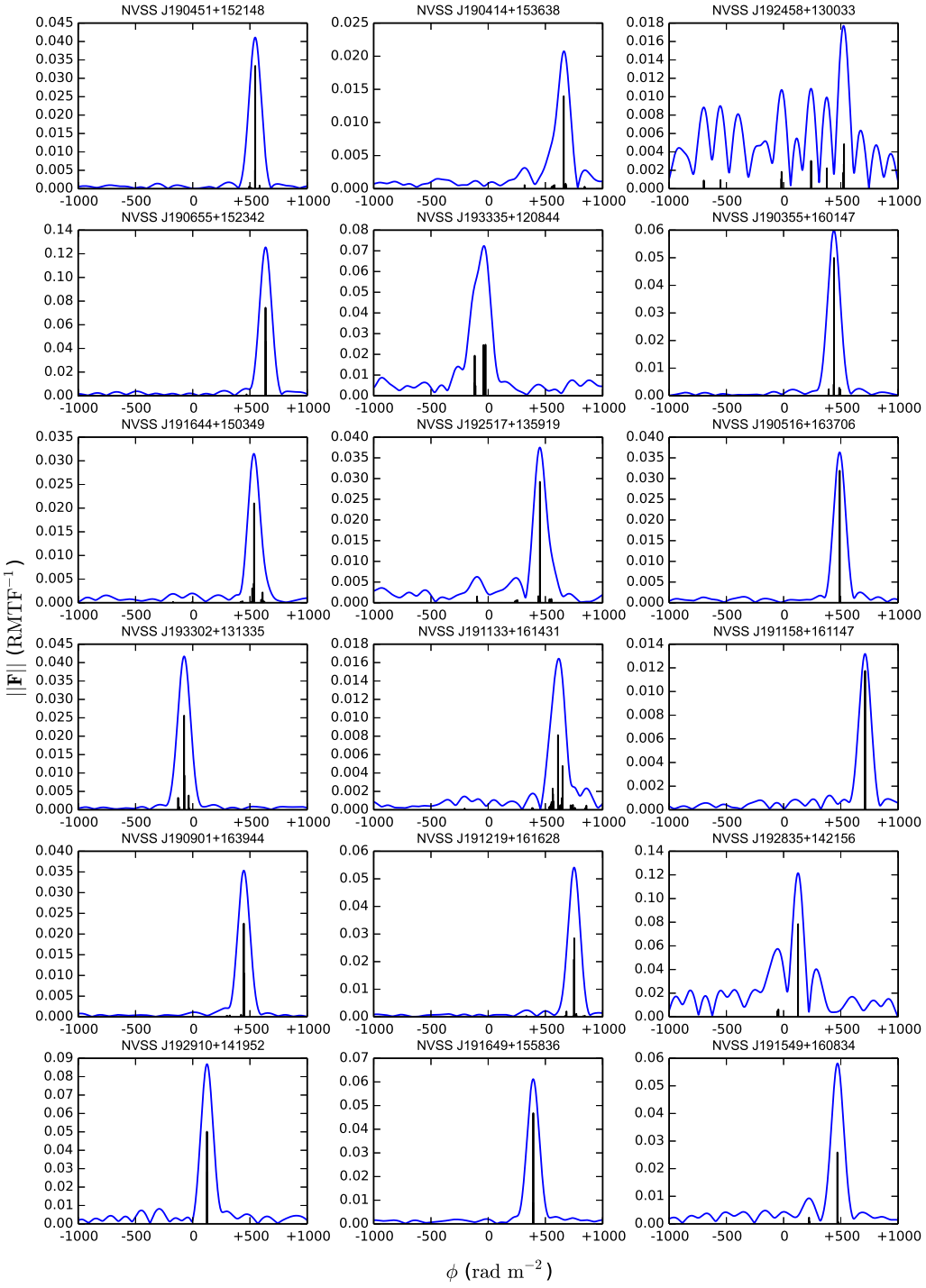

Figure D.1: (Continued) Faraday spectra of the on-axis target sources, sorted by the Galactic longitude.

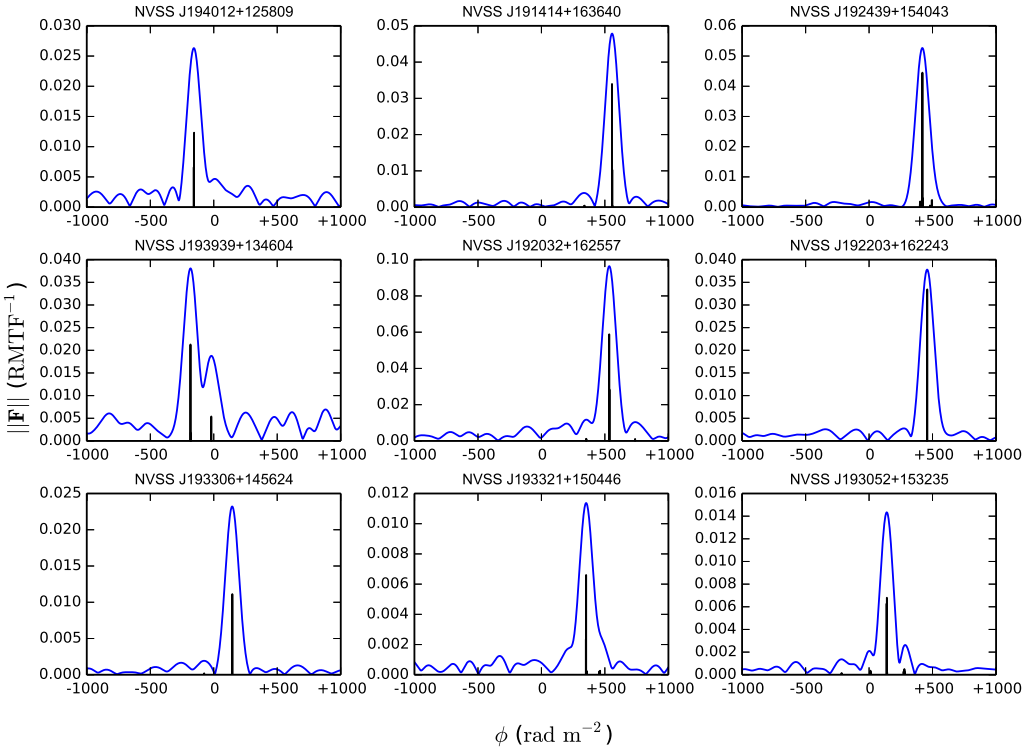

Figure D.1: (Continued) Faraday spectra of the on-axis target sources, sorted by the Galactic longitude.

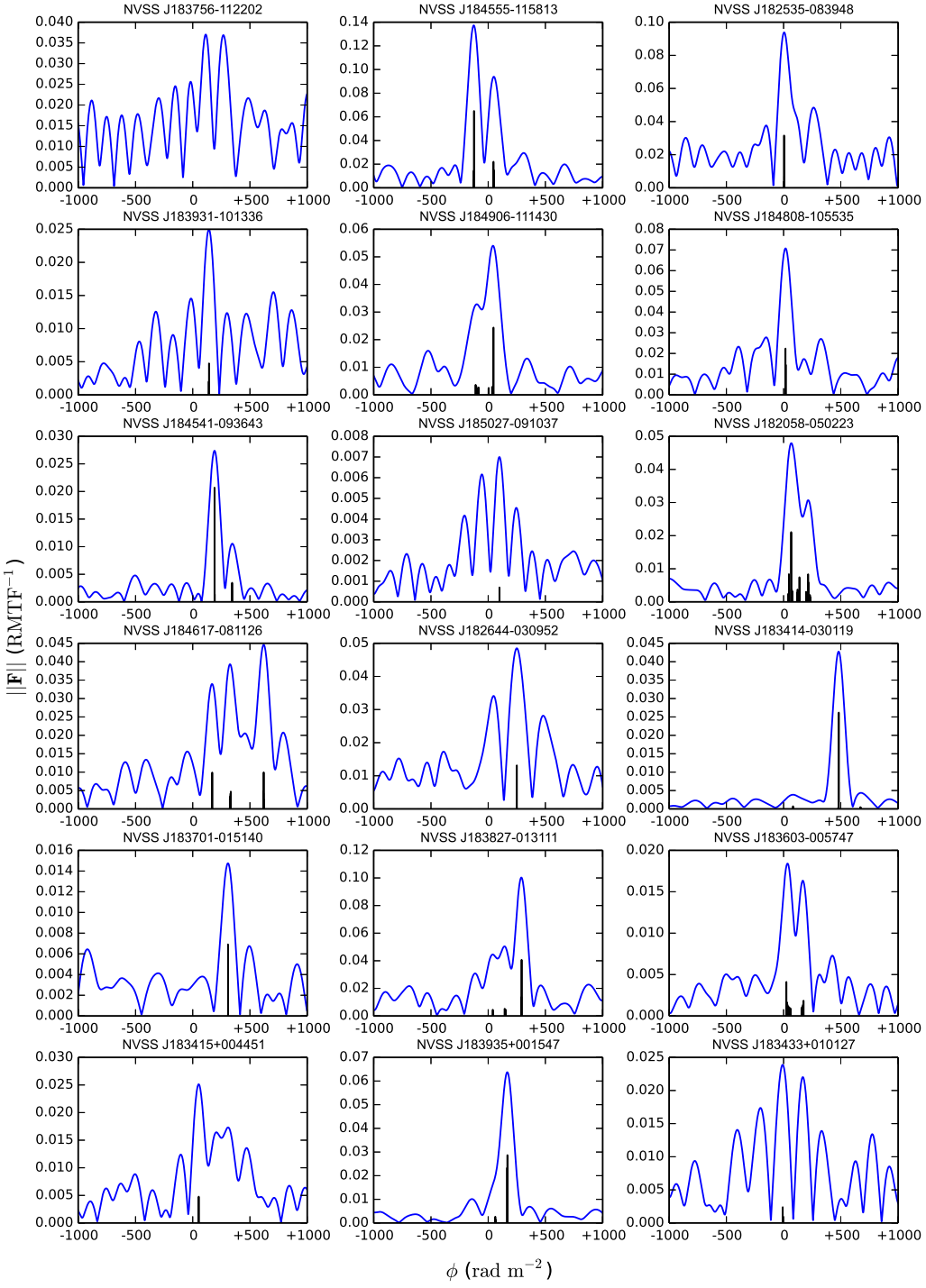

Figure D.2: Faraday spectra of the off-axis target sources, sorted by the Galactic longitude. Blue lines show the amplitudes of the deconvolved Faraday spectra, with the black bars showing the clean components.

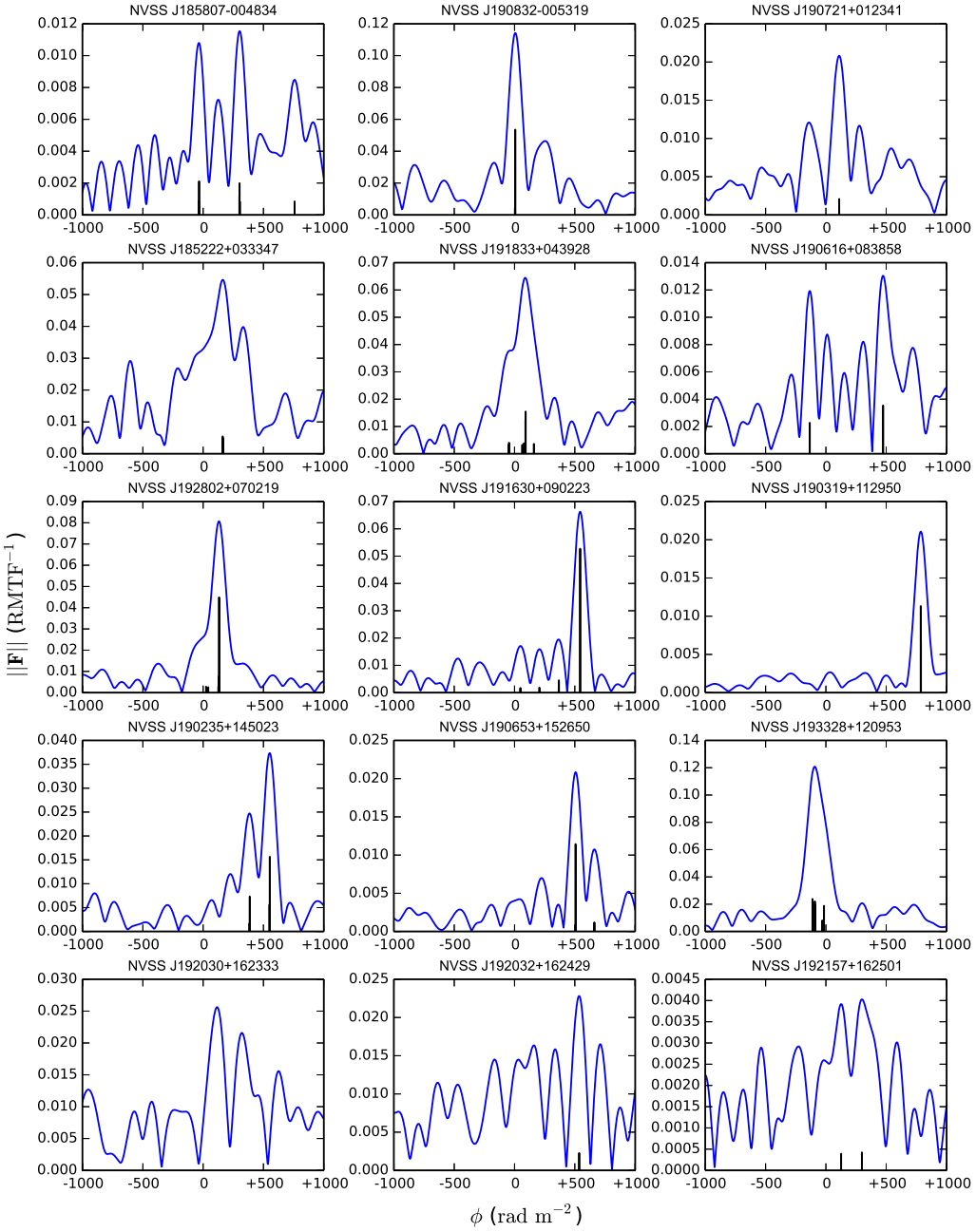

Figure D.2: (Continued) Faraday spectra of the off-axis target sources, sorted by the Galactic longitude.

Erklärung

Ich versichere, dass ich die von mir vorgelegte Dissertation selbständig angefertigt, die benutzten Quellen und Hilfsmittel vollständig angegeben und die Stellen der Arbeiteinschlielich Tabellen, Karten und Abbildungen –, die anderen Werken im Wortlaut oder dem Sinn nach entnommen sind, in jedem Einzelfall als Entlehnung kenntlich gemacht habe; dass diese Dissertation noch keiner anderen Fakultät oder Universität zur Prfung vorgelegen hat; dass sie noch nicht verffentlicht worden ist sowie, da ich eine solche Veröffentlichung vor Abschluss des Promotionsverfahrens nicht vornehmen werde. Die Bestimmungen dieser Promotionsordnung sind mir bekannt. Die von mir vorgelegte Dissertation ist von Prof. Dr. Michael Kramer betreut worden.

Unterschift:

_____

Datum:

_____

Publications Accounting for Major Parts of the Thesis

Refereed

- **Ma Y. K.**, Mao S. A., Stil J., Basu A., West J., Heiles C., Hill A. S., Betti S. K. 2019, "A Broad-band Spectro-polarimetric View of the NVSS Rotation Measure Catalogue — II. Effects of Off-axis Instrumental Polarization", Monthly Notices of the Royal Astronomical Society, Volume 487, Issue 3, p.3454–3469 (doi: 10.1093/mnras/stz1328)

- **Ma Y. K.**, Mao S. A., Stil J., Basu A., West J., Heiles C., Hill A. S., Betti S. K. 2019, "A Broad-band Spectro-polarimetric View of the NVSS Rotation Measure Catalogue — I. Breaking the $n\pi$-ambiguity", Monthly Notices of the Royal Astronomical Society, Volume 487, Issue 3, p.3432–3453 (doi: 10.1093/mnras/stz1325)

- **Ma Y. K.**, Mao S. A., Stil J., Basu A., West J., Heiles C., Hill A. S., Betti S. K. 2018, "From NVSS RM Catalogue to Future Polarisation Surveys", Astronomy in Focus, *accepted* (arXiv: 1810.03620)

- **Ma Y. K.**, Mao S. A., Basu A., Heiles C., West J. 2017, "Radio Polarisation Study of High Rotation Measure AGNs", Galaxies, Volume 5, Issue 4, p.66–71 (doi: 10.3390/galaxies5040066)